Structure Property Correlation for Selected High Performance Material

by

Joy Mittra

(Enrolment No.: ENGG01200704010)

Bhabha Atomic Research Centre, Mumbai 400085, India

A thesis submitted to the

Board of Studies in Engineering Sciences

in partial fulfillment of requirements

for the Degree of

DOCTOR OF PHILOSOPHY IN ENGINEERING SCIENCE

of

HOMI BHABHA NATIONAL INSTITUTE

February, 2014

Homi Bhabha National Institute

Recommendations of the Viva Voce Board

As members of the Viva Voce Board, we certify that we have read the dissertation prepared by Mr. Joy Mittra, entitled, "Structure Property Correlation for Selected High Performance Material" and recommend that it may be accepted as fulfilling the dissertation requirement for the Degree of Doctor of Philosophy.

Date: 07.10.2014.

P. K. Tewari
Prof., HBNI & Head, Desalination Division, BARC, Mumbai
Chairman, Doctoral Committee

Gautam Kumar Dey
Date: 7/10/14

Gautam Kumar Dey
Dean, HBNI & Associate Director, Materials Gr., BARC, Mumbai
Thesis Supervisor

Date: 7/10/14

B. S. Murty
Prof., Dept. of Metallurgical & Materials Engg, IIT, Madras
External Examiner

Date: 7/10/2014

R. C. Hubli
Prof., HBNI & Head, Materials Processing Division
Member, Doctoral Committee

Date: 7/10/14

D. Srivastava
Prof., HBNI & Head, Physical Metallurgy Section
Member, Doctoral Committee

7/10/14.

(Smt.) S. Mukhopadhyay
Prof. HBNI
Member, Doctoral Committee

Final approval and acceptance of this dissertation is contingent upon the candidate's submission of the final copies of the dissertation to HBNI. I hereby certify that I have read this dissertation prepared under my direction and recommend that it may be accepted as fulfilling the dissertation requirement.

Date: 7/10/14

Place: HBNI, Mumbai

Gautam Kumar Dey
Guide's Signature

STATEMENT BY AUTHOR

This dissertation has been submitted in partial fulfillment of requirements for an advanced degree at Homi Bhabha National Institute (HBNI) and is deposited in the library to be made available to borrowers under rules of the HBNI.

Brief quotations from this dissertation are allowable without any special permission, provided that accurate acknowledgement of source is made. Requests for permission for extended quotation from or reproduction of this manuscript in whole or in part may be granted by the competent authority of HBNI when in his or her judgment the proposed use of the material is in the interests of the scholarship. In all other instances, however, permission must be obtained from the author.

Place: : BARC, TROMBAY
Signature:

Date FEBRUARY 24, 2014
Name: Joy Mittra

Declaration

I, hereby declare that the investigation presented in this thesis has been carried out by me. The work is original and has not been submitted earlier as a whole or in part for a degree/ diploma at this or any other Institution/ University.

Place: BARC, TROMBAY Signature:

Date: FEBRUARY 24, 2014 Name: Joy Mittra

Certificate

This is to certify that the thesis entitled, "*Structure Property Correlation for Selected High Performance Material*" submitted by Shri Joy Mittra to the Homi Bhabha National Institute, Mumbai for the award of the degree of Doctor of Philosophy is a bona fide record of the research work carried out by him under my supervision and guidance. The content of the thesis, in full or parts have not been submitted to any other Institute or University for the award of any other degree or diploma.

Place: BARC, TROMBAY

Signature: Gautam Kumar Dey

Date: FEBRUARY 24, 2014

Name: Dr. Gautam Kumar Dey
Prof. HBNI & Associate Director, Materials Group,
BARC, Trombay

Dedicated to

Sri Chaitanya Mahaprabhu and His Associates

Acknowledgement

With a deep sense of gratitude, I wish to place on record the extensive help I received from many people to accomplish this dissertation. Before this noble duty, I should admit that far too many people have helped me in this task. Although I may not have acknowledged some of them through sheer oversight, I shall remain personally indebted to them all.

Prof. Gautam Kumar Dey, a Distinguished Scientist and currently the Associate Director, Materials Group, has always given due priority to this Ph.D work despite his hectic schedule. He always kept a keen eye on the progress and quality of the work. In fact, whenever the work was held up due to the unavailability of any instrument, he has personally looked into the problem. This speaks well of his friendly and generous nature. I am extremely grateful to him for all the help he has provided to me, which went beyond general guidance, technical discussion and a thorough review of the manuscript.

Next to the guide, who has helped me as a mentor, philosopher and friend was Dr. Ulhas D. Kulkarni. He has also helped me through the high-quality proof-reading of several portion of the early drafts of the thesis. I will always remember his kind gesture and remain thankful to him for his kind help.

I am grateful to Drs. Ashok K. Arya and Raghvendra Tewari for their painstaking effort in reviewing this thesis and for rendering valuable help, particularly in computational and transmission electron microscopy aspects of this work, in spite of their very busy schedule.

I am truly thankful to Mr. Jayshankar Dubey, Dr. Arijit Laik, Mr. Suman Neogy, Dr. Chandrabhanu Basak, Mrs. Suparna Banerjee, and Mr. K. V. Mani Krishna who have provided invaluable support in mechanical testing, Electron Probe Micro-Analysis, Transmission Electron Microscopy, First-Principles based Calculation, Scanning Electron Microscopy and graphical visualization work, respectively.

It would be unjust if I merely acknowledge Mr. Nirupam Das, Dr. Pranesh Sengupta, and Dr. T. S. R. C. Murthy. They were always there and ready to help me whenever help was needed. I thank them from the bottom of my heart for providing me invaluable support during the entire course of this work.

I would also like to express my sincere thanks to Dr. Jayanta Kumar Chakravartty, Director Materials Group for his constant encouragement and, also, for making the tensile testing facility available for this work.

Mr. Vaibhav Kumar, Ms. Vibhuti Duggal and Mr. Kislay Bhatt were always committed to keep the computational facility at its best, without which the computation intensive jobs in this Ph.D work could not have been completed.

I am truly grateful to Prof. Umesh V. Waghmare for inviting me as a Visiting Scientist at Jawaharlal Nehru Centre for Advance Scientific Research, Bangalore, during which he explained me several specialized of first-principles based calculations. It is at this juncture that the computational methodology of this work got its real shape. In the context of learning the ab-initio modeling, I would like to convey my special thanks to Dr. Vikas Kashid, who has literally initiated me in the computational work and in handling the Vienna Ab-initio Simulation Package.

It gives me a lot of pleasure to express my profound gratefulness to Mr. Nilangshu Kumar Das, Prof. Pravat Kumar Giri and Prof. Sudipto Ghosh, who have always been constant sources of inspiration to me for doing a good work.

It is a melancholy pleasure for me to remember the role of my late father, Mr. Manindra Kumar Mittra in my rise to this stage in life. He envisaged and made every possible effort to inculcate in us a sense of high thinking. I am sure he would have been most happy to see me acquire a Ph.D. Undoubtedly, my mother, Mrs. Sefali Devi would be equally happy for the same reason. I express my deepest gratitude to them for all the things they have done for me.

I am deeply grateful to my father-in-law, Mr. Swapan Sarkar and mother-in-law Mrs. Swapna Devi for giving us all the support that a family could need during my heavy involvement in the Ph.D work. I wish to thank my brother-in-law, Soham Ghosh and sister-in-law, Mrs. Souravi, very much for their constant encouragement during the time of my Ph.D work.

My elder brother, Mr. Jagat Jyoti Mittra played the role of my guardian, next only to my parents. He took all the trouble in tutoring me and was most happy to send me to the engineering discipline. Any amount of thanks would be insufficient to express my true gratitude for him. I would always remain obliged to him for his extreme generosity. I also thank my *Boudi*, Mrs. Shukla, and my niece, Miss. Tanisha for their good wishes.

Last but not the least, I owe a very special distinction to my wife, Mrs. Sanchali and, son, Master Bhaswat. Since long, she has been shouldering all the responsibility of the family, so that I could concentrate on my Ph.D work. Bhaswat had to sacrifice many pleasurable moments due to my heavy engagement at certain times. It would not be possible for me to return to them what they have sacrificed for my sake.

I would like to end this acknowledgement with the following quotation. "I am thankful to all those who said NO to me. It's because of them I did it myself."

(Page 54 of the book "You'll See It When You Believe" By Wayne W. Dyer.)

Contents

SYNOPSIS .... **I**

LIST OF PUBLICATIONS .... **XXV**

PUBLICATIONS IN JOURNALS XXV

PUBLICATION IN INTERNATIONAL CONFERENCES XXV

LIST OF FIGURES .... **XXVII**

LIST OF TABLES .... **XXXVII**

CHAPTER 1 .... **1**

1 INTRODUCTION **1**

1.1 BACKGROUND 1

1.2 ALLOY 625 2

1.3 MELTING PRACTICE 4

1.4 WORK-HARDENING 4

1.5 AB-INITIO MODELING OF PLANAR FAULTS 8

1.6 AIM OF THE WORK 8

1.6.1 Scope of the Work *9*

1.7 OUTLINE OF THE THESIS 10

CHAPTER 2 .... **13**

2 LITERATURE SURVEY **13**

2.1 EVOLUTION OF ALLOY 625 13

2.2 VARIOUS DERIVATIVES OF ALLOY 625 15

2.3 MAJOR ORDERED PHASES IN ALLOY 625 17

2.3.1 Ni$_2$(Cr,Mo) – D_{2h}^{25} Phase *18*

2.3.2 γ'' – DO$_{22}$ Phase *20*

2.3.3 δ – DO$_a$ phase *22*

2.4 Other Ordered Phases in Alloy 625 22

2.4.1 Carbides *22*

2.4.2 Topologically Close Packed and Other Ordered Phases *23*

2.5 Deformation of Ordered Phases 25

2.6 In- Service Changes and the Procedure for Recovery 27

2.7 Application of Alloy 625 28

CHAPTER 3 33

3 EXPERIMENTAL METHODOLOGY 33

3.1 Fabrication of Tensile Samples 33

3.2 Isothermal Treatment at Three Temperatures for Three Durations 34

3.3 Tensile Testing with Data Analysis and Hardness measurement 35

3.4 Optical Microscopy 35

3.5 Scanning Electron Microscopy of Fracture Surface 36

3.6 Transmission Electron Microscopy 36

3.7 Orientation Imaging Microscopy 37

3.8 First-principles Based Modeling 37

3.8.1 Computational Facility *37*

3.9 Instruments for Characterization 38

3.9.1 Computational Hardware *39*

3.9.2 Software for Calculations and Data Processing *39*

CHAPTER 4 41

4 MICROSTRUCTURAL CHARACTERIZATION OF ALLOY 625........... 41

4.1 INTRODUCTION 41

4.2 RESULTS 42

4.2.1 Characterization of as-received SQ Alloy 625 using EPMA................... 42

4.2.2 Microstructures of solution-quenched and Isothermally Treated Alloy 625 46

4.2.2.1 Optical Microscopy 46

4.2.2.2 Transmission Electron Microscopy 48

4.2.2.3 Orientation Imaging Microscopy.. 60

4.3 DISCUSSION 72

4.4 SUMMARY 76

CHAPTER 5.. 79

5 MECHANICAL RESPONSE OF PRECIPITATED ALLOY 625................ 79

5.1 INTRODUCTION 79

5.2 RESULTS 80

5.2.1 Mechanical Properties 80

5.2.1.1 Tensile Parameters.. 80

5.2.1.2 True-Stress – True-Strain Behavior... 83

5.2.2 Fracture Behavior 85

5.2.2.1 Visual Observations of Fractured specimens 85

5.2.2.2 Low Resolution Fractographs.. 86

5.2.2.3 High Resolution Fractographs 88

5.3 DISCUSSION 96

5.3.1.1 Solution Quenched 97

5.3.1.2 Isothermally Treated at 813 K ... 97

5.3.1.3 Isothermally Treated at 973 K ... 98

5.3.2 Isothermally Treated at 1123 K ... 100

5.4 SUMMARY ... 101

5.4.1 Mechanical Properties ... 101

5.4.2 Fracture Behavior ... 102

CHAPTER 6 ... 103

6 STUDY OF DEFORMED MICROSTRUCTURES OF ALLOY 625 ... 103

6.1 INTRODUCTION ... 103

6.2 RESULTS ... 103

6.2.1 Study of Deformed Tensile-Gauge Regions ... 103

6.2.1.1 Optical Micrographs ... 103

6.2.1.2 Transmission Electron Micrographs ... 106

6.3 DISCUSSION ... 109

6.3.1 Dislocation Interaction in $Ni_2(Cr,Mo)$ and γ'' Precipitated Alloy 625 ... 109

6.3.2 Dislocation Interaction in γ'' Precipitated Alloy 625 ... 111

6.3.3 Dislocation Interaction in δ Precipitated Alloy 625 ... 111

6.4 SUMMARY ... 112

CHAPTER 7 ... 113

7 EVALUATING WORK-HARDENING BEHAVIOR OF ALLOY 625 WITH DIFFERENT PRECIPITATED-MICROSTRUCTURES ... 113

7.1 INTRODUCTION ... 113

7.2 WORK-HARDENING ANALYSIS OF TENSILE DATA ... 114

7.2.1 Work-hardening Behavior of Alloy 625 with Intermetallic Compounds 114

7.2.2 Work-hardening Trend of Alloy 625 with Intermetallic Compounds..... 119

7.3 DISCUSSION 121

7.3.1 Work-hardening Behavior of Alloy 625 having $Ni_2(Cr,Mo)$ and γ'' phases in the Microstructure 122

7.3.2 Work-hardening Behavior of Alloy 625 having γ'' phase in the Microstructure 126

7.3.3 Work-hardening Behavior of Alloy 625 having δ phase in the Microstructure 128

7.3.4 Comparison between the interaction of dislocations with γ'' and δ....... 128

7.4 SUMMARY 130

CHAPTER 8.......... 133

8 FIRST-PRINCIPLES BASED STUDIES ON PLANAR FAULTS AND DISLOCATIONS DISSOCIATION 133

8.1 INTRODUCTION 133

8.2 LATTICE PARAMETER OPTIMIZATION (LPO) 134

8.2.1 LPO of Pure Ni 134

8.2.2 LPO of Tetragonal γ'' 135

8.2.3 LPO of Orthorhombic δ.......... 135

8.3 CALCULATIONS OF SFE 136

8.3.1 Methodology for Calculating the Precise SFE of fcc-Ni 136

8.3.2 Methodology for Calculating the SFE of $Ni_3Nb – DO_{22}$ (γ'') 141

8.3.3 Methodology for Calculating the SFE of $Ni_3Nb – DO_a$ (δ) 150

8.4 SFE'S OF NI, γ'' AND δ.......... 152

8.4.1 SFE of Ni 152

8.4.2 SFE of $\gamma''-Ni_3Nb$ 158

8.4.3 SFE of $\delta-Ni_3Nb$ 158

8.5 DISCUSSION 159

8.6 DEFORMATION MICRO-MECHANISM IN ALLOY 625 160

8.6.1 Role of Stacking Fault in Planar Slip 160

8.6.2 SFE's Governing Interactions of Dislocations with γ''-DO_{22} and δ-DO_a Ordered Phases 162

8.6.2.1 Other Factors Governing Interactions of Dislocation with the Ordered Phases 165

8.7 SUMMARY 165

CHAPTER 9 167

9 CONCLUSION 167

9.1 MICROSTRUCTURE 167

9.2 TENSILE AND FRACTURE BEHAVIOR 168

9.3 WORK-HARDENING ANALYSIS 169

9.4 FIRST PRINCIPLE BASED CALCULATIONS 170

9.5 FUTURE DIRECTION 171

REFERENCES 173

SYNOPSIS

Synopsis of the Ph.D. thesis of Shri Joy Mittra submitted to the Homi Bhabha National Institute, Mumbai for the award of the degree of Doctor of Philosophy in Engineering Sciences.

Name of the Candidate: Joy Mittra
Title of the thesis: Structure Property Correlation for Selected High Performance Material
Name of the Guide: Prof. Gautam Kumar Dey
HBNI
(Engineering Sciences)
Place of Research: Materials Science Division
Bhabha Atomic Research Centre
Mumbai – 400085
Enrolment Particulars: ENGG01200704010

Background

Ni-base alloys and their applications in high-performance areas

Application of INCONEL® Alloy 625 is widespread in high performance areas, which require various combinations of high temperature and corrosion resistance properties. Alloy 625 is recommended for a broad range of service temperatures between cryogenic and 1255 K, in which, applications calling for strength, creep and fatigue are involved. The alloy is resistant to a wide spectrum of corrosive environment, including salt-water, hydrochloric, nitric and high temperature oxidizing atmosphere and, also, to different atmospheres causing stress-corrosion. While, the alloy shows excellent ductility and toughness at cryogenic temperatures, it is also able to retain strength up to 1033 K and offers good creep and fatigue resistances [6,5].

It has been reported that prolonged use of the alloy at high temperatures results in the appearance of various second phases, which lead to an unacceptably low room temperature ductility and degradation of all important properties [21,19]. Analyses of some of the unserviceworthy Alloy 625 components, reported therein, have resulted in identification of various microstructural features responsible for variation in mechanical properties, which may be critical during service. However, Alloy 625 components, in these reports, have been subjected to high temperature operations for prolonged durations having imprecise time-temperature histories. Although the effect of aging on the alloy properties is known to be significant, systematic correlation of the structure-property of Alloy 625, delineating the role of precipitates, at various stages of their growth, on mechanical properties and fracture is yet to be established through reliable laboratory experiments.

Alloy 625 – a perspective

INCONEL® Alloy 625 is designed to provide high temperature strength due to solid solution strengthening of nickel-chromium matrix by molybdenum and niobium. However, later it has been found that a large number of ordered phases appear in the alloy during service or during high temperature aging. Work done on the characterization of this alloy, mostly above 873 K and down to 823 K, in a few cases, has revealed that depending on the time and temperature of exposure, $M_{23}C_6$, ('M' is rich in Cr), MC, M_6C ('M' is rich in Ni, Nb and Mo), γ' (rich in Ni and Nb), γ'' ($Ni_3[Nb,Al,Ti]$), δ ($Ni_3[Nb,Mo]$) and Laves phases precipitate in this alloy system [20,49]. However, sigma and γ' are not seen by some even in Alloy 625, aged for prolonged periods [49]. Most of these phases, which occur in this alloy are shown in the Time-Temperature-Transformation (TTT) diagram [20]. However, a few disagreements could be noticed there. For example, at 823 K, one study has reported the onset of γ'' precipitation after 11 h [20], while another study has reported the same after 2000 h [46]. One of the reasons for such large variation may be the ability of the techniques used for detecting the nanoscale precipitate. Apart from this, a comparatively new phase, $Ni_2(Cr,Mo)$, which has been detected in the alloy after a long service exposure below 873 K, has not been depicted on the TTT diagram in Fig. 1.1 [21]. This gives an impression that the $Ni_2(Cr,Mo)$ precipitates form after aging for time in excess of 2000 h.

Existence of the $Ni_2(Cr,Mo)$ phase in alloy 625 has first been noticed in a feed-stock super-heater of a petrochemical plant, which has been in service for about 50,000 h at around 773 K [21]. The <001> Selected area diffraction (SAD) patterns, obtained from the aged material, revealed extra reflections in addition to γ'' and parent γ. These extra reflections were correlated with $Ni_2(Nb,Mo)$ phase having Pt_2Mo type structure by Bajaj et. al., who irradiated the alloy to a fluence of 2.3 x 10^{20} neutrons/cm^2 at 633 K [39]. Later, it has been reported that a precipitate with Pt_2Mo structure, having $Ni_2(Cr,Mo)$ composition, formed in Alloy 625, when exposed to near 873K temperature for about 28,000 h and 70,000 h [21].

Formation of the second phase with the Pt_2Mo structure in Alloy 625 has been observed in the components subjected to a wide range of service exposures at temperatures below 873 K and, also, in laboratory specimen after 100 h of isothermal holding at 813 K [40]. It has also been noticed that, reflections corresponding to $Ni_2(Cr,Mo)$, in the SAD patterns from Alloy 625 have always been associated with that of γ" [40]. However, compared to the tetragonal γ", which is having three variants of ellipsoidal morphology, the orthorhombic $Ni_2(Cr,Mo)$ is seen to have six variants of snowflake morphology. Formation of ellipsoidal $Ni_2(Cr,Mo)$ has already been known in some other chromium and molybdenum bearing nickel-base alloys such as, Hastelloys [41,42] and in Haynes Alloy 242 [43], and in the latter alloy it has been seen on aging at temperatures up to 1023 K. $Ni_2(Cr,Mo)$ has been seen to completely dissolve on heating for a short duration above 873 K, leaving γ" and other precipitates in the matrix.

Formations of carbides and laves phase during the solidification of Alloy 625 and its derivatives depends upon the niobium to carbon ratio [57]. It has been observed that too high a Nb:C ratio is favorable for the Laves phase, while the opposite condition is conducive to the formation of NbC. At an intermediate Nb:C ratio, which is not so well defined, possibly due to the complex influence by other elements, presence of both carbides and laves phases is possible in this group of alloys [57]. In this regard, it has also been reported that higher Si and Fe increase the formation of Laves, especially, as the former element segregates into the topologically closed packed Laves' phase to stabilize the same [20]. Apart from NbC, $M_{23}C_6$ and M_6C type secondary carbides also form in this alloy at high-temperatures and affect the fracture properties of the alloy.

Influence of γ' precipitates on the fracture-surface morphologies of various Ni-base alloys, such as, IN738LC and CMSX-4, has been reported earlier [60,61]. It has been observed that the variations in distribution and morphology of this second-phase may result in a wide range of fracture surfaces, such as, dimple-ductile, quasi-cleavage and cleavage types. Characteristics of the fracture surfaces and the crystallographic planes of the facets are seen to depend upon the size of the precipitates and the type of the loading. It has been reported that microstructures of IN738LC with fine γ' (70 nm) and with the mixture of fine and medium sizes, of 70 nm and 450 nm, respectively, produce transgranular quasi-cleavage type fracture. The fractographs obtained from the samples tested at room temperature are reported to have facets comprising {100} type crystallographic planes [60]. However, the samples tested at high temperature are reported to also produce {111} type facets [60]. Inability of the fine precipitates to initiate voids has been reported to be responsible for such a faceted cleavage type fracture. Microstructure with γ' precipitates of medium and coarse sizes, 450 nm and 700 nm, respectively, are reported to be responsible for void nucleation, which resulted in the dimple type fracture surface. Such dimple-ductile fracture is also seen with coarser carbide precipitates, of 1 – 2 μm, at the grain boundary which resulted in the micro-crack in the region. However, during room-temperature fatigue, cracks are reported to cut through γ' precipitates and propagate along {111} planes, resulting in {111} plane type faceted fracture surface in Ni-base CMSX-4 alloy [61].

Aim of the work

In spite of the occurrence of a large number of ordered phases in the alloy matrix, Alloy 625 is continued to being used in the solid solution form. Use of the alloy in the solution quenched form has possibly been promoted by the slow kinetics of formation of major ordered second-phases. As the ordered second-phases in Alloy 625 components grow during high-temperature operation, they influence various properties of the alloy. This study aims to understand the influence of various ordered phases at various stages of their growth on the mechanical behaviors, including tensile, work hardening and fracture behaviors of the alloy and to correlate the same with the dislocation-precipitate interactions.

Scope of the Work

Scope of the study is as follows.

1. To characterize the solution quenched microstructure of the as-received Alloy 625, so as to know the starting condition that would act as a benchmark for comparison with that of isothermally treated conditions.

2. To produce various stages of growth of the ordered second phases in the intermediate temperature range through isothermal treatments and to characterize them.

3. Deforming the isothermally treated Alloy 625 specimens to understand the influence of the growth of the ordered phases on the tensile properties, stress-strain responses, work-hardening and fracture behavior.

4. Studying interactions of dislocations with various types of precipitates in Alloy 625 microstructures in order to correlate them with mechanical properties, work-hardening and fracture behaviors.

5. Density functional theory (DFT) based first-principles calculations of stacking fault energy of pure nickel, which is in close approximation to the multi-component Alloy 625 in order to understand the basic slip process that governs the deformation.

6. To explain fundamental causes for various dislocation-precipitate interactions in Alloy 625 through first-principles based calculations.

Experimental Methodology

The isothermal treatments on Alloy 625 are decided on the basis of the evolution of phases in its solid solution matrix that is known from the time-temperature-transformation (TTT) diagram provided in Fig. 1.1. The nominal composition of Alloy 625 behind such TTT behavior is given in Table 1.1.

TTT diagram

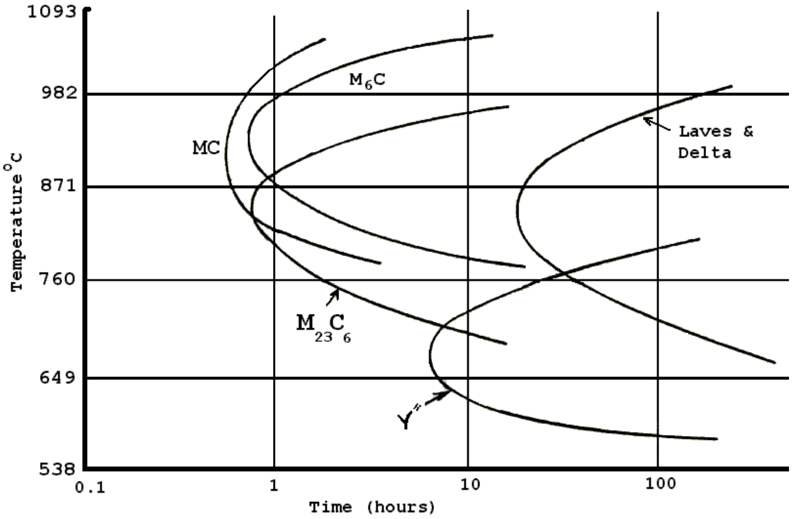

Fig. 1.1: Time-temperature-transformation diagram of Alloy 625.

Table 1.1: Nominal composition of Alloy 625 in weight %

	Ni	Cr	Mo	Nb(+Ta)	Fe	Co	Al	Ti	Si	Mn	C	P	S
Wt%	~60	20-23	8-10	3.15-5.15	5.0	1.0	0.4	0.4	0.5	0.5	0.1<	0.015<	0.015<
At% (Typical)	60.7	24.5	5.6	2.3(+0.13)	3.7	0.7	0.44	0.37	0.74	0.38	0.4	0.02	0.02

Characterization of as-received solution-quenched Alloy 625

Experimental methodologies in the present study are intended to achieve the aforementioned set of objectives. First of all, microstructural characterizations of starting material, the solution quenched (SQ) block of Alloy 625, 150 mm ×150 mm × 30 mm in dimensions have been carried out using optical microscope, 200 kV JEOL transmission electron microscope (TEM) and CAMECA SX100 electron probe micro-analyzer (EPMA).

Schedules for isothermal treatments

Threaded tensile specimens, having 28 mm gage length and 6 mm diameter have been machined out from a solution-quenched (SQ) Alloy 625 block, with the gage length oriented along the direction of maximum flow in the wrought working operation. These specimens have been held isothermally inside three different resistance-heating furnaces, which have been set at 813 K, 973 K and 1123 K. Temperature of the furnaces are controlled within ± 3 K using proportional-integral-derivative (PID) type loop feedback mechanism controller. Specimens have been taken out of the furnaces after 10 h, 100 h and 1200 h, respectively. Thus, *ten sets of samples* have been tested in the present study, *including the SQ material*. The isothermal treatments are summarized in Table 1.2.

Table 1.2: Schedules for isothermal-treatments

	813 K (540 ^{o}C)	973 K (700 ^{o}C)	1123 K (850 ^{o}C)
10 h	✓ 813 K – 10 h	✓ 973 K – 10 h	✓ 1123 K – 10 h
100 h	✓ 813 K – 100 h	✓ 973 K – 100 h	✓ 1123 K – 100 h
1200 h	✓ 813 K – 1200 h	✓ 973 K – 1200 h	✓ 1123 K – 1200 h

Tensile Testing

The tensile specimens have been tested using a screw driven INSTRON universal testing machine at a crosshead speed of 0.5 mm/minute, giving a nominal strain rate of 3.0×10^{-04} s^{-1}. Load vs. displacement data have been recorded in an attached computer, and the output has been processed for various flow properties of the material. The hardness measurements have been carried out in an automatic microhardness tester using 50 g load.

Microstructural study

Following the isothermal treatments mentioned in Table 1.2, all samples, including SQ have been prepared and viewed using optical microscope. Some samples, which have undergone isothermal treatment for longest duration, viz. 1200 h at 813 K, 973 K and 1123 K, respectively, have been investigated using 200 kV JEOL and TITAN transmission electron microscopes (TEMs).

Samples obtained from the deformed gauge regions, merely 1 mm from the fracture surfaces of broken tensile specimens have also been investigated using optical microscope and TEMs in order to study interactions of dislocations with various types of precipitates.

Orientation Imaging Microscopy and Scanning Electron Microscopy

Electron back scattered diffraction (EBSD) studies of the electropolished samples, which have undergone isothermal treatments in 973 K and 1123 K have been carried out in an orientation imaging microscope FEI Quanta 200 HV instrument. Scanning speed of electron beam has been maintained at 0.5 μs^{-1}. Grain size, grain orientation spread (GOS) and grain average misorientation (GAM) have been calculated from the EBSD data. Tensile fracture surfaces of SQ and aged samples have been investigated using Phillips XL30 scanning electron microscope.

Modeling

Ab-initio modeling approach has been used in order to understand the slip pattern, governing the dislocation precipitate interactions. Spin-polarized, plane-wave based first principles calculations have been employed in the frame work of density functional theory within the generalized-gradient-approximation (GGA), parameterized by Perdew-Burke-Ernzerhof (PBE) [66,67] scheme, as implemented in the Vienna ab initio simulation package (VASP 5.2) program [68,69,70]. The spin-polarized, ion-electron interaction has been incorporated using PAW potentials [70] as supplied in the VASP database.

Short Results and Discussion

In the present work, correlation of tensile, work-hardening (WH) and fracture behaviors of Alloy 625 with the growth of various ordered phases such as, $Ni_2(Cr,Mo)$, γ'' and δ have been attempted with the help of following results.

To benefit from the kinetics of transformation, temperatures, close to the noses of the "*C*" curves of the ordered phases in the TTT diagram have been chosen for treating the alloy isothermally. E.g. 1123 K has been chosen for the formation of δ, while 973 K has been chosen for having γ" in the Alloy 625 matrix. However, choice of 813 K, for the formation of $Ni_2(Cr,Mo)$ has been based upon a prudent guess, since "*C*" curve corresponding to $Ni_2(Cr,Mo)$ phase is not available in the existing TTT diagram. As stated earlier, too high a temperature, typically above 873 K, is reported to produce a matrix where γ" dominates, whereas, too low a temperature is likely to slow down the kinetics of transformation, per se. Also, past experience suggests that the influence of $Ni_2(Cr,Mo)$, formed at 813 K, on the microstructure and mechanical properties, is likely to dominate over that of γ", since the latter phase is known to be weaker than $Ni_2(Cr,Mo)$ initially [40]. It is also known from the literature that the strength and weldability of the alloy improves just by solutionizing $Ni_2(Cr,Mo)$ selectively at 923 K [21].

Characterization of SQ Alloy 625

Elemental analysis of SQ Alloy 625 that comprises about 99% (by weight) of the elements listed in Table 1.1, is given in Table 1.3. X-ray area mapping and line scans, carried out to reveal the distribution of Nb, Ti, Fe, Cr, Mo and Ni are not included due to the paucity of space in this report. However, the results from EPMA essentially show that solid-solution matrix contains blocky primary carbide containing Nb and Ti.

Table 1.3: Elemental analysis from EPMA in relative atom % for 8 elements of SQ Alloy 625 (comprising ~99(wt)% of its nominal composition).

	Ni	Cr	Mo	Nb	Fe	Co	Ti	Si
At%	63.45	25.87	5.9	2.95	1.4	0.65	0.1	0.3

Stress-Strain, tensile properties and work-hardening behaviors

Tensile parameters extracted from all the tests, reflecting the influence of various ordered phases, such as, $Ni_2(Cr,Mo)$, γ'' and δ are summarized in Table 1.4. The hardness values are seen to comply with the tensile parameters.

Table 1.4: Tensile parameters of SQ and aged Alloy 625 samples along with hardness values in Vicker's Hardness No. (VHN).

Condition	YS (MPa)	UTS (MPa)	Uniform Strain	Fracture Strain	Hardness (VHN)
SQ	373 ± 29	838 ± 26	0.54 ± 0.08	0.71 ± 0.04	220 ± 4
813 K - 10h	385 ± 33	853 ± 22	0.54 ± 0.067	0.68 ± 0.045	255 ± 6
813 K - 100h	422 ± 42	958 ± 47	0.40 ± 0.06	0.50 ± 0.065	285 ± 6
813 K - 1200h	557 ± 49	1045 ± 56	0.46 ± 0.04	0.61 ± 0.045	390 ± 10
973 K - 10h	372 ± 24.5	815 ± 29	0.466 ± 0.045	0.54 ± 0.06	289 ± 6
973 K - 100h	493 ± 40.5	906 ± 45	0.38 ± 0.035	0.46 ± 0.027	265 ± 6
973 K - 1200h	577 ± 49.5	961 ± 29	0.235 ± 0.022	0.31 ± 0.022	370 ± 9
1123 K- 10h	353 ± 22	836 ± 36.5	0.465 ± 0.031	0.55 ± 0.026	260 ± 6
1123 K - 100h	380 ± 42.5	803 ± 47	0.31 ± 0.027	0.38 ± 0.031	233 ± 4 (on precipitate depleted region) 350 ± 9 (on precipitate rich region)
1123 K - 1200h	484 ± 42.5	856 ± 46.5	0.23 ± 0.024	0.29 ± 0.027	368± 9

True stress (σ) - true strain (ε) behaviors of the tensile samples in the plastic region for three isothermal holding temperatures are given in Fig. 1.2. Work-hardening analyses of true stress - true strain behaviors, in terms of ($\sigma.\theta/\mu^2$) vs. σ, are given in Fig. 1.3, where θ is $\delta\sigma/\delta\varepsilon$ and μ is shear modulus. These have been effectively correlated with cutting and looping of various ordered phases in the alloy by gliding dislocations during the deformation process. The constant term, $(\sigma.\theta)_0$, and the hardening rate, θ_h, are seen to vary asymptotically with isothermal holding time and have been shown in Fig. 7.4 and Fig. 7.5, respectively. These relationships are capable of predicting the WH and true stress - true strain behaviors of the alloy for any arbitrary isothermal holding time at 973 K and 1123 K and may be extended further provided that sizes of γ'' and δ are known from the microstructural analysis.

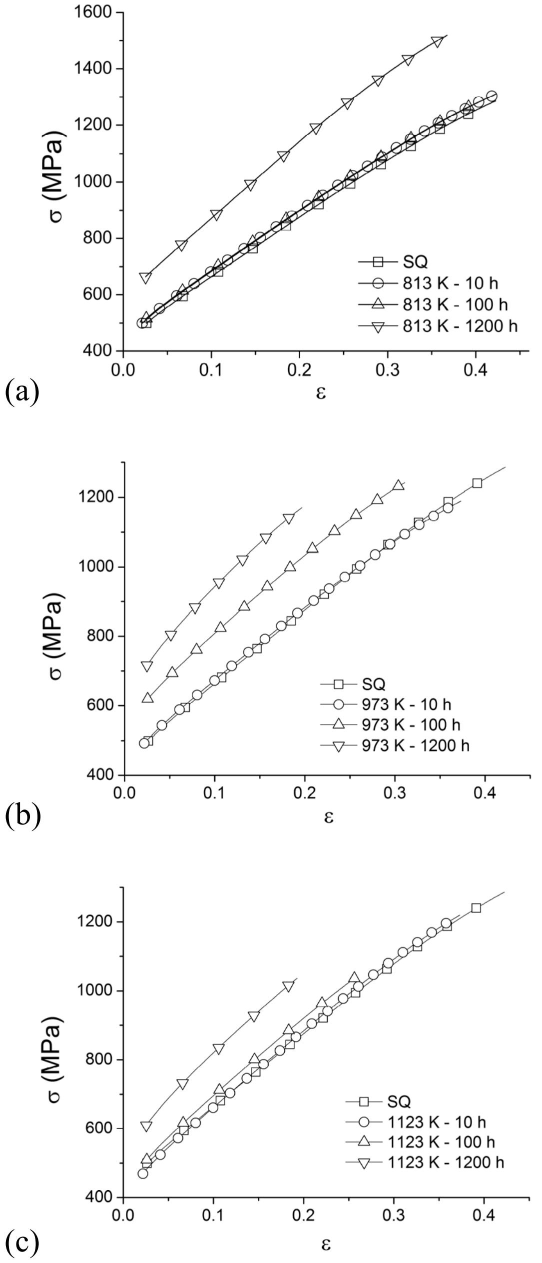

Fig. 1.2: True Stress (σ) - True Strain (ε) plot from tensile tests of Alloy 625.

(a) aged at 813 K for 10h, 100h and 1200h along with that of SQ sample.
(b) aged at 973 K for 10h, 100h and 1200h along with that of SQ sample.
(c) aged at 1123 K for 10h, 100h and 1200h along with that of SQ sample.

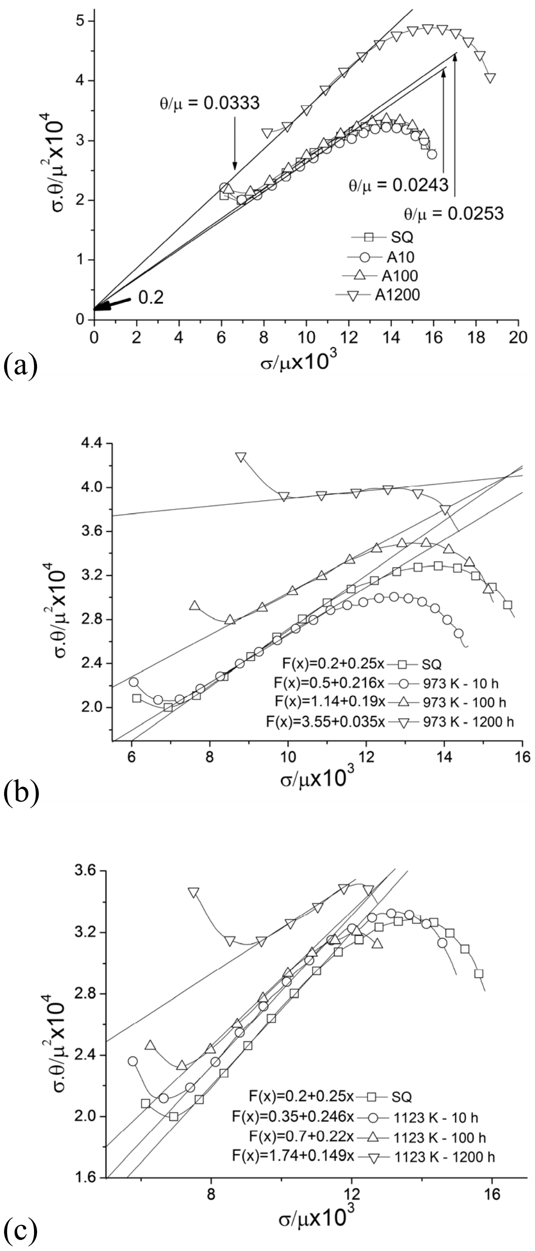

Fig. 1.3: Normalized $\sigma.\theta$ vs σ plot of Alloy 625.

(a) aged at 813 K for 10h, 100h and 1200h along with that of SQ sample.
(b) aged at 973 K for 10h, 100h and 1200h along with that of SQ sample.
(c) aged at 1123 K for 10h, 100h and 1200h along with that of SQ sample.

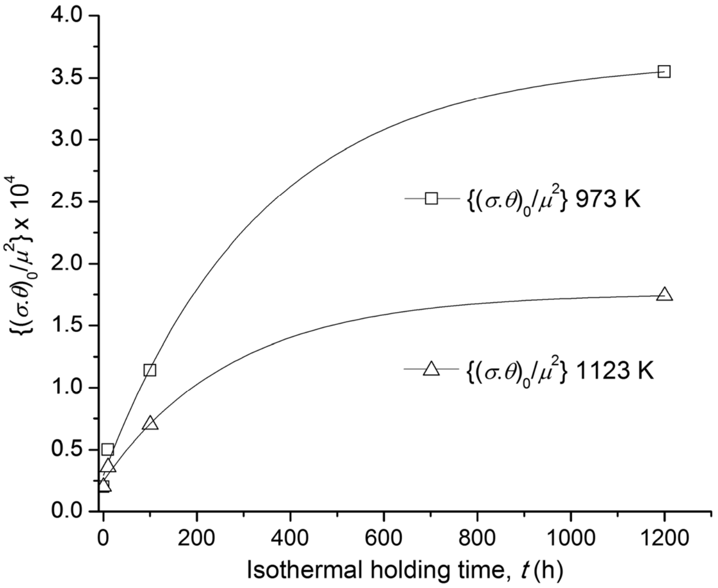

Fig. 1.4: Asymptotic rise in $(\sigma.\theta)_0$ with isothermal holding time have been noticed for two different precipitated microstructures of Alloy 625, which are generated through isothermal heating at 973 K and 1123 K.

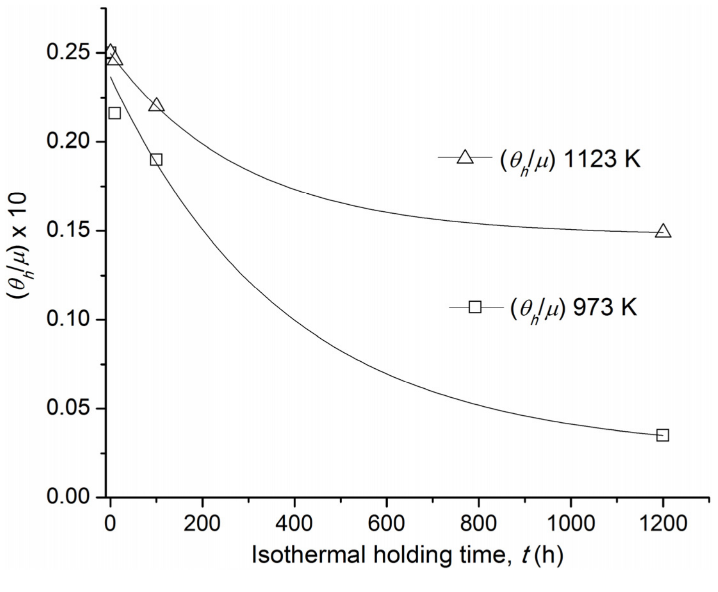

Fig. 1.5: Asymptotic drop in θ_h with isothermal holding time have been noticed for two different precipitated microstructures of Alloy 625, which are generated through isothermal heating at 973 K and 1123 K.

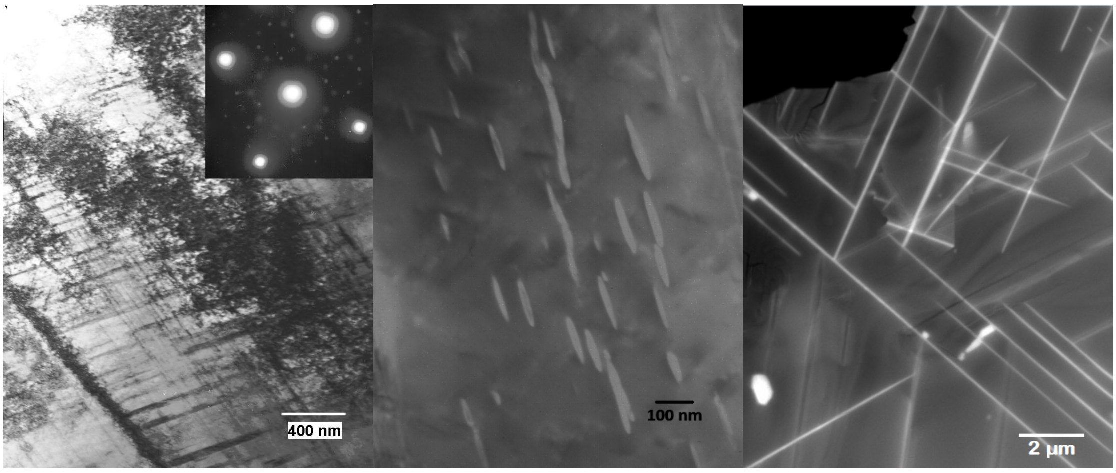

(a) (b) (c)

Fig. 1.6: (a) Dislocation density associated with the formations of $Ni_2(Cr,Mo)$ and γ" after 1200 h of isothermal holding at 813 K. (b) Dark-field image from 973 K – 1200 h sample showing lens shaped γ". (c) High angle annular dark-field image from 1123 K – 1200 h sample showing δ laths.

TEM investigation to characterize ordered phases in the aged samples and to observe dislocation-precipitate interactions in deformed samples

Only some of the TEM results have been included in Fig. 1.6 (a), (b) and (c) to show the nature of the precipitates after 1200 h of isothermal holding at 813 K, 973 K and 1123 K, respectively. Study of the deformed gauge regions, 1 mm away from the tensile fracture surfaces, are presented in Fig. 1.7.

These transmission electron micrographs have shown that even after 1200 h of growth at 813 K, γ" and $Ni_2(Cr,Mo)$ remain fully shearable and in the process they get dissolved in the matrix. Fig. 1.7 (b) and (c), respectively, shows that after 1200 h of growth at 973 K, γ" becomes completely impenetrable to the gliding dislocation, resulting in looping type of interaction, while thick δ plates after 1200 h of growth at 1123 K remains shearable. Hence, during deformation, dislocation loops around γ", while they cut δ plates in limited cases. Interactions of dislocations with various types of precipitates are seen to have a high degree of corroboration with the work hardening behaviors of the precipitated alloy.

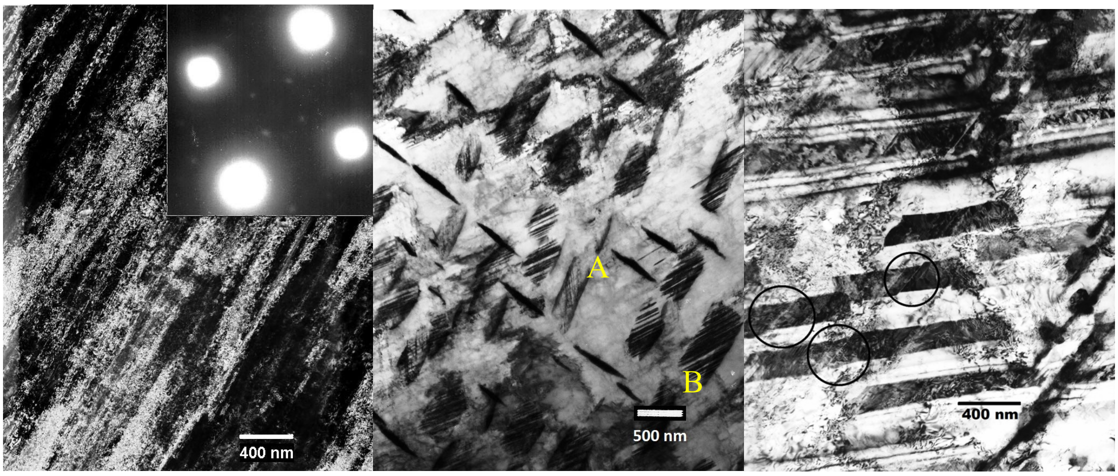

(a) (b) (c)

Fig. 1.7: TEM micrographs from deformed gauge regions. (a) 813 K - 1200 h specimen showing high density of dislocations and superlattice spots corresponding to $Ni_2(Cr,Mo)$ only, confirming the dissolution of γ". (b) 973 K - 1200 h specimen showing {111}-type planar faults on one side of γ", as a result of dislocation - γ" interaction, indicating looping of the ordered phase. (c) 1123 K - 1200 h specimen showing sheared δ laths, in the encircled region, as a result of dislocation glide.

Effect of isothermal treatment at 973 K and 1123 K on the grain sizes and boundaries

EBSD data from the samples, which have been held isothermally at 973 K and 1123 K show the effect of precipitations of γ" and δ at the respective temperatures. These data are not included to reduce the volume of this report and only some salient points are discussed here. It has been seen that precipitations of those ordered phases affect the evolution Σ1 and Σ3 coincident-site-lattice (CSL) boundaries in a quite different manner. While Σ3 is seen to disappear, possibly at the cost of Σ1 for isothermal holding at 1123 K, Σ1 is seen to increase, possibly, at the cost of Σ3, in the case of isothermal holding at 973 K. However, in both the cases of isothermal holding, the sum of these two types of boundaries, i.e. Σ1 + Σ3 isbehavior seen to remain in the range of ± 20% of Σ1 + Σ3 of the SQ.

Role of dislocations-ordered phases interactions on the fracture behaviors of Alloy 625

Three fractographs, each from one isothermal treatment after 1200 h of holding have been shown in Fig. 1.8. Fractographs showing the role of primary carbides on the fracture process and role of growing $Ni_2(Cr,Mo)$, γ" and δ are not included to keep this report concise.

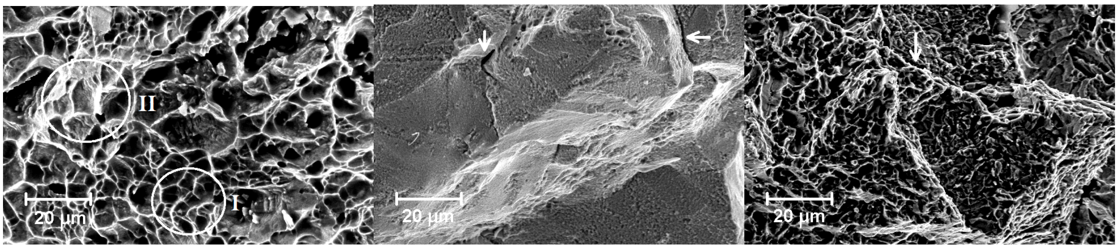

(a) (b) (c)

Fig. 1.8: Pictures in (a), (b) and (c) are the fractographs from samples, held isothermally for 1200 h at 813 K, 973 K and 1123 K, respectively. (a) Reduction of dimple sizes due to shearing of $Ni_2(Cr,Mo)$ and γ", as shown in the encircled region. (b) {100} type facets due to dislocations looping γ". Right arrow showing the boundary crack and the down-arrow in the left showing branching out of the elliptical crack in right angles. (c) {111} type facets due to dislocation cutting δ laths. Apparent crack originating region is shown by an arrow.

Shearable $Ni_2(Cr,Mo)$ and γ" result in the dimple-ductile fracture after 1200 h of holding at 813 K. However, size of the dimples come down compared to SQ Alloy 625. Looping and blocking of dislocations by γ", as seen in Fig. 1.7 (b) results in the formation of crack, as shown by the down arrow on the left side in Fig. 1.8 (b). As can be seen on the fractographs of 973 K-1200 h sample, cracks are perpendicular to each other since the cracks originating from the γ"-matrix interface run along {100} planes as a result of their orientation. However, angle between the facets in Fig. 1.8 (c) indicates that the fracture of Alloy 625 after 1200 h of holing at 1123 K is along {111} plane. This appears to be primarily due to the gliding of dislocations on the close packed plane even through the shearing of δ laths, as shown in Fig. 1.7 (c).

Ab initio calculations to determine the stacking-fault-energy (SFE) of pure Ni and energies along the path of dislocation motion in ordered γ" and δ phases

The SFE of pure nickel has been assumed to be close to that of Alloy 625. In the present study, {111}-type stacking fault energy (SFE) of *fcc*-Ni, 136.683 mJ/m^2, has been calculated using an appropriately *dilated* supercell, which is based upon a twelve {111}-plane spacing of *fcc*-Ni. The above SFE is seen to be lower by ~ 2 mJ/m^2 than the “conventional” SFE, which is also based upon a twelve {111}-plane spacing but of optimized *fcc*-Ni lattice. Occurrence of stacking fault in *fcc*-Ni at a distance of 2440.537×10^{-3} nm, which is equivalent to the SF density of 4.09746×10^5 mm^2/mm^3, is seen to be capable of decreasing the bulk density of *fcc*-Ni by 0.0895 %. The small magnitude of SFE apparently justifies small magnitude of the dilation and the reduction of SFE thereby.

In the case of γ" and δ ordered phases, energies along the path of dislocation partials, from the first-principles based calculations, are shown in Fig. 1.9. Looking into the compact planes in both the ordered phases, γ" and δ, as equivalent to the *fcc*-{111} type planes, it can be seen that <110> type dislocations are capable of restoring the order in these phases. However, they need to split into partials, as shown in Eq. 1, to make the gliding energetically feasible.

[In the case of *fcc*]

$$\frac{1}{2}\overrightarrow{[1\,1\,0]}=\frac{1}{6}\overrightarrow{[2\,1\,1]}+\frac{1}{6}\overrightarrow{[1\,2\,\bar{1}]}$$ **Eq. 1.1**

[In the case of DO_{22}]

$$\overrightarrow{[1\,1\,0]}=\underbrace{\frac{1}{12}\overrightarrow{[4\,2\,1]}+\frac{1}{12}\overrightarrow{[2\,4\,\bar{1}]}}_{\frac{1}{2}\overrightarrow{[110]}}+\underbrace{\frac{1}{12}\overrightarrow{[4\,2\,1]}+\frac{1}{12}\overrightarrow{[2\,4\,\bar{1}]}}_{\frac{1}{2}\overrightarrow{[110]}}$$ **Eq. 1.2**

i.e $\overrightarrow{[1\,1\,0]}=\frac{1}{2}\overrightarrow{[110]}+\frac{1}{2}\overrightarrow{[110]}$ **Eq. 1.3**

[In the case of DO_a]

$$\overrightarrow{[1\,0\,0]}=\underbrace{\frac{1}{12}\overrightarrow{[3\,0\,\bar{2}]}+\frac{1}{12}\overrightarrow{[3\,0\,2]}}_{\frac{1}{2}\overrightarrow{[100]}}+\underbrace{\frac{1}{12}\overrightarrow{[3\,0\,\bar{2}]}+\frac{1}{12}\overrightarrow{[3\,0\,2]}}_{\frac{1}{2}\overrightarrow{[100]}}$$ **Eq. 1.4**

i.e. $\overrightarrow{[1\,0\,0]}=\frac{1}{2}\overrightarrow{[1\,0\,0]}+\frac{1}{2}\overrightarrow{[1\,0\,0]}$ **Eq. 1.5**

In the case of DO_{22} and DO_a, the dislocations equivalent to but double the length of ½$[110]_{fcc}$ splits into the partials, as shown in Eq. 2 and Eq. 4, respectively. First-principles calculations of energies of stacking, resulting from the movement of the partials in DO_{22} and DO_a are given in Fig. 1.9. The calculation shows that these partials are not stable and combine themselves as per Eq. 3 and Eq. 5. Fig. 1.9 also shows that the energy required to move dislocations in the ordered DO$_a$ is lower than that of DO$_{22}$. This has helped to ascertain the reasons for shearing of δ and looping of γ" during the deformation.

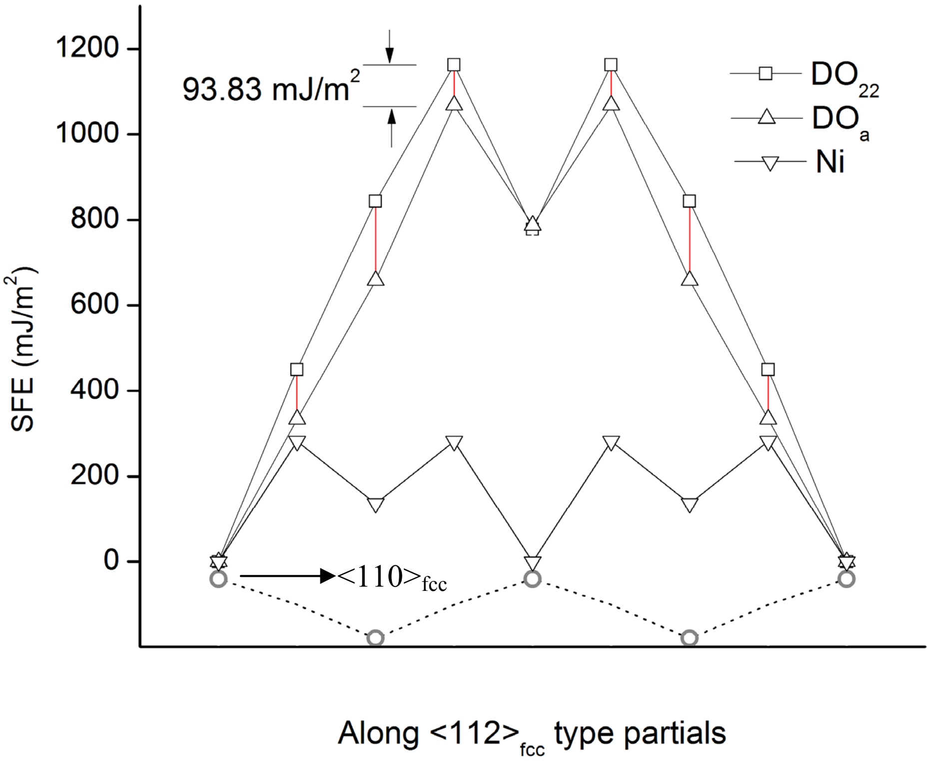

Fig. 1.9: Stacking fault energy along the path of dislocation partials in the ordered phases, Ni_3Nb-Do$_{22}$ (γ") and Ni_3Nb-DO$_a$ (δ) to show the energy required to move them. 93.83 mJ/m^2 difference in the threshold energies, which is required to form stable partials in DO$_{22}$ and DO$_a$ is marked above.

Summary of the outcome

Mechanical Properties and Fracture

In the present study, isothermal treatments of Alloy 625 samples at 813 K, 973 K and 1123 K is intended to reveal the effect of various precipitations on the room temperature mechanical properties of the alloy. While, $Ni_2(Cr,Mo)$ and γ" are formed on aging at 873 K, aging at 973 K and 1123 K have predominantly led to the formation of γ'' and δ phases, respectively. Effects of various degrees of growth of these ordered phases in the Alloy 625 microstructures have been correlated with the mechanical properties, work-hardening behavior, microstructures and fractographs. Ab-initio modeling carried out here has helped to understand and to justify the fundamental aspect of the interactions of dislocation with the selected ordered phases.

Tensile tests, investigated under three prominent microstructural conditions, which have been generated by isothermal aging at 813 K, 973 K and 1123 K for 10h, 100 h and 1200 h, have brought out the effect of carbides and ordered phases on the fracture behavior of Alloy 625. It has been found that the blocky primary-carbide particles act as nucleation sites for the large voids. The carbide in the SQ matrix contains niobium and titanium and does not show any preference for the grain boundary [77].

The ductility after 1200 h of aging at 813 K is seen to be much higher than that of all samples aged at 973 K and 1123 K [77]. Growth of fine and shearable $Ni_2(Cr,Mo)$ and γ'' phases, produced in the Alloy 625 appears to be responsible for the reduction in dimple size and depth.

Homogenously distributed, lens shaped γ'' phases, are seen to grow more than 150 nm in size on aging at 973 K for 1200 h. Growth of the γ'' phases in Alloy 625 is associated with the increase in strength and decrease in ductility and is responsible for changing the fracture surface from dimple ductile to cleavage type. After 1200 h of aging, precipitation of γ'' phases promotes intragranular cleavage fracture along {100} planes [77].

Formation of large plate-shaped δ phases at 1123 K results in lower strength but in equivalent ductility compared to that obtained during 973 K aging. Considerable amount of δ formation after 1200 h of isothermal holding is also seen to produce {111} plane facets. However, fine micro-dimples of uniform size are seen along the facets of the fractographs [77].

Work-Hardening

Various WH behaviors, noticed during the study of deformation of SQ and precipitated Alloy 625 are evaluated under the framework of Kocks-Mecking-Estrin (KME) model [29] as follows. The SQ Alloy 625 represents the case of largest starting fixed-mean-free-path, where the effect of variable MFP, based upon the dislocation density, becomes significant. With the rise in the impenetrable interactions of dislocation, as it becomes maximum with γ'' after 1200 h at 973 K, WH quotient, θ_h, continues to fall to become negligibly small. Rest of the WH responses is seen to be explainable by the combined effect of fixed and variable MFP. Hence, the *hybrid model* of KME is found suitable to describe the WH behavior of Alloy 625, since, the deformation of Alloy 625, with various degrees of growth of γ'' and δ, remains adherent to planar-slip.

Ab-initio Modeling

Role of stacking fault energy in enforcing the planar slip of dislocations, which led to cutting and looping of the ordered phases

The {111}-type stacking fault energy (SFE) of *fcc*-Ni, 136.683 mJ/m^2, calculated in the present study, is low enough to keep the partials wide apart. The low value of SFE in synergization with the lack of threshold energy at room temperature for cross-slip has apparently guided the deformation of precipitated Alloy 625 to obey the planar-slip, which has restricted the dislocation precipitate interactions to cutting and looping of the precipitates.

Difference in the cutting and looping behaviors of the ordered phases

First-principles based calculations of the ordered γ" and δ phase structures have revealed that among the possible four partials, only two partials are stable in both the ordered structures. Calculation of the energies of these ordered phases have also shown that the gliding of dislocations in γ" is more difficult than that of in δ phase. The calculations have helped to come out with the plausible explanation of the TEM observation, where massive δ plates are seen to be shearable but γ" are not during the dislocation-γ" and the dislocation-δ interactions, respectively. It has been concluded that the synergistic effect of high threshold energy required to move dislocations in γ" and its loopable size has led to the bypass of dislocations through looping. Compared to the looping of γ", the shearing of δ by gliding dislocations, in some cases, has been possible apparently due to the lower energy requirement by the partials to move through the latter in addition to the difficulty in looping the massive δ laths.

LIST OF PUBLICATIONS

Publications in Journals

1. ROLE OF DISLOCATION DENSITY IN RAISING THE STAGE II WORK-HARDENING RATE OF ALLOY 625

   Joy Mittra, J. S. Dubey, U. D. Kulkarni and G. K. Dey

   Materials Science and Engineering A 512 (2009) 87–91.
2. FRACTURE BEHAVIOR OF ALLOY 625 WITH DIFFERENT PRECIPITATE MICROSTRUCTURES

   Joy Mittra, Suparna Banerjee, Raghvendra Tewari, Gautam K.Dey

   Materials Science & Engineering A 574 (2013) 86–93.

   DOI: 10.1016/j.msea.2013.03.021
3. CONTRIBUTION OF STACKING FAULT IN LOWERING THE THEORETICAL DENSITY OF NICKEL

   Joy Mittra, Umesh V. Waghmare, Ashok Arya, Gautam K. Dey

   Computational Materials Science, 81 (2014) 249–252.
4. CORRELATING DISLOCATION-PRECIPITATE INTERACTION WITH WORK-HARDENING BEHAVIOR OF ALLOY 625

   Joy Mittra and G. K. Dey

   (Manuscript communicated)
5. MICROSTRUCTURAL EVOLUTION IN ALLOY 625 DUE TO ISOTHERMAL HOLDING AT HIGH-TEMPERATURES

   Joy Mittra and G. K. Dey

   (Manuscript ready)
6. ROLE OF SHOCKLEY PARTIALS IN THE DEFORMATION MICROMECHANISM OF ORDERED NI_3NB-(DO_{22}) AND NI_3NB-(DO_A) PHASES

   JOY MITTRA, ASHOK ARYA AND G. K. DEY

   (Manuscript under preparation)

Publication in International Conferences

1. SHOCKLEY PARTIALS IN ORDERED NI_3NB (DO_{22}) PHASE – A FIRST-PRINCIPLES STUDY
   Joy Mittra, Ashok Arya and Gautam K. Dey

   IUMRS-2013, IISc, Bangalore.

2. RELAXATION OF FORCES ON ATOMS NEAR STACKING FAULT IN FCC-NICKEL LOWERING ITS THEORETICAL DENSITY
   J. MITTRA, K. V. MANI KRISHNA, A. K. ARYA AND G. K. DEY

DAE BRNS Symposium on Current Trends in Theoretical Chemistry (CTTC-2013), September 26 – 28 , 2013, BARC, Mumbai – 900085.

3. Effect of γ" ordered phase on the planes of fracture in Alloy 625
Joy Mittra, Ashok K. Arya and Gautam K. Dey

International Conference on Electron Microscopy & XXXIV Annual Meeting of EMSI - 2013, July 3 – 5, 2013, Kolkata, India.

4. Influence of various precipitates on the deformation micromechanism in Ni base fcc alloy
J. Mittra, U. D. Kulkarni and G. K. Dey

International Conference on Electron Nanoscopy & XXXII Annual Meeting of EMSI, July 6 – 8, 2011, Hyderabad, India.

5. TEM study of various dislocation-precipitate interactions in Alloy 625
Joy Mittra, Nirupam Das, U. D. Kulkarni and G. K. Dey

International Conference on Advances in Electron Microscopy and Related Techniques & XXXI Annual Meeting of EMSI, March 8-10, 2010, Bhabha Atomic Research Centre, Mumbai, INDIA, (EMSI - 2010).

LIST OF FIGURES

Fig. 1.1: Time-temperature-transformation diagram of Alloy 625 [20]. 3

Fig. 1.2: WH behaviors of polycrystalline *fcc* alloy, based upon (a) dislocation – dislocation interaction, (b) fixed mean free path and (c) the combination of these two are schematically shown by *R*, *B* and *G* lines, respectively. 8

Fig. 2.1: Tree of descendants of Alloy 625 [5,6]. 15

Fig. 3.1: Sketch of a tensile sample showing various dimensions. 34

Fig. 4.1: X-ray line scan from 'A' to 'B' on Primary carbide particles in Alloy 625 as observed under EPMA using back scattered electron, especially to give surface topology (hence giving clarity in Z-dimension). 42

Fig. 4.2: Ni Kα, Ti Kα and Nb Lα x-ray intensities in counts per second across scanned AB line, as shown on Fig. 4.1 43

Fig. 4.3: Presence of Mo, Nb, Ti, Ni, Cr and Fe within and around the primary carbide is shown using x-ray mapping under EPMA. 44

Fig. 4.4: Optical microstructures of Alloy 625: solution-quenched and isothermally treated samples. 47

Fig. 4.5: (a) – (f) show transmission electron micrographs from 813 K – 100 h and 1200 h samples. (a) Planar array of dislocations are seen after 100 h of aging at 813 K. (b) [0 0 1] SAD pattern from 813 K – 100 h shows diffused intensities from $Ni_2(Cr,Mo)$, which has been highlighted in the inset. (c) Precipitated region showing high dislocation densities on {111} planes. (d) Thin twinned regions in 813 K – 1200

h. (e) [001] SAD pattern from the region of (c); (f) γ, γ″ and $Ni_2(Cr,Mo)$ are represented by ‘‘×’’, ‘‘o’’ and ‘‘ ■ ’’, respectively. 50

Fig. 4.6: (a) – (j) show transmission electron micrographs from samples aged at 973 K for 10h, 100 h and 1200 h. (a) and (b) Planar arrays of dislocations are seen after 10 h of aging. (c) and (d) Array of precipitations with surrounded dislocations are seen after 100 h. (e) – (h) Dark field images showing different variants of γ″ in 973 K – 1200 h sample. Circled region in (h) clearly shows the shape and size of the ordered phase. (i) [0 0 1] SAD pattern from the region of (f) is shown in (i), and the indexing of the same is shown in (j). γ and γ″ are represented by ‘‘×’’ and ‘‘o’’ respectively. 54

Fig. 4.7: HAADF – Scanning Transmission Electron micrographs at different magnifications from samples aged at 1123 K for 1200 h have been shown in (a) and (b). EDX scan along AB path is given in Fig. 4.8. 56

Fig. 4.8: Energy dispersive X-ray spectrums across the Ni_3Nb-δ phase showing distribution of Ni and Nb. 57

Fig. 4.9: High resolution transmission electron micrograph from 1123 K – 1200 h sample. 58

Fig. 4.10: High resolution transmission electron micrograph from 1123 K – 1200 h sample and the plane spacing analyzed from the micrographs are shown above. The inset in the figure shows elemental map of Nb of the region superimposed on the image. 59

Fig. 4.11: a) EBSD images showing the grain orientation in SQ Alloy 625. b) Grain size distribution and the average grain size measured from the EBSD map. 61

Fig. 4.12: Grain Average Neighbor Misorientation distribution of SQ Alloy 625 showing ~80% within 0.5^o orientation, while ~99% within 4.5^o orientation. 62

Fig. 4.13: ~63% out of ~67% of CSL boundaries scanned are seen to be Σ3 boundry.62

Fig. 4.14: Changes in CSL Sigma 1, Sigma 3 and the combined Sigma 1 and Sigma 3 fraction due to isothermal holding at 813 K are shown above. 65

Fig. 4.15: Changes in Length, Numerical Fraction and the corresponding ratio of coherent 60^o (111) type boundaries due to isothermal holding at 813 K are shown above. 65

Fig. 4.16: EBSD images of samples after 10 h, 100 h and 1200 h of isothermal holding at 973 K. Color code is based on the pole figure in Fig. 4.11. 66

Fig. 4.17: Variation in area fractions of grain diameter as obtained from Fig. 4.16 (a) – (c). 67

Fig. 4.18: Changes in CSL Sigma 1, Sigma 3 and the combined Sigma 1 and Sigma 3 fraction due to isothermal holding at 973 K are shown above. 67

Fig. 4.19: Changes in Length, Numerical Fraction and the corresponding ratio of coherent 60^o (111) type boundaries due to isothermal holding at 973 K are shown above graphically. 68

Fig. 4.20: EBSD images of samples after 10 h, 100 h and 1200 h of isothermal holding at 1123 K. Color code is based on the pole figure in Fig. 4.11. 69

Fig. 4.21: Variation in area fractions of grain diameters as obtained from Fig. 4.20 (a) – (c). 70

Fig. 4.22: Changes in CSL Sigma 1, Sigma 3 and the combined Sigma 1 and Sigma 3 fraction due to isothermal holding at 1123 K are shown above. 70

Fig. 4.23: Changes in Length, Numerical Fraction and the corresponding ratio of coherent 60^o (111) type boundaries due to isothermal holding at 1123 K are shown above graphically. 71

Fig. 4.24: Variations in the average grain size due to isothermal holding for 10 h, 100 h and 1200 h at 813 K, 973 K and 1123 K. 71

Fig. 5.1: Changes in YS and UTS values due to isothermal holding at 813 K, 973 K and 1123 K, as obtained from Table 5.1 are graphically shown above. 82

Fig. 5.2: Changes in the true strains till uniform elongation and till fracture, as obtained from the tensile tests are depicted above. 82

Fig. 5.3: True stress–strain plot from samples aged at 813 K for 10 h, 100 h and 1200 h along with SQ sample. 83

Fig. 5.4: True stress–strain plot from samples aged at 973 K for 10 h, 100 h and 1200 h along with unaged sample. 84

Fig. 5.5: True stress–strain plot from samples aged at 1123 K for 10 h, 100 h and 1200 h along with unaged sample. 84

Fig. 5.6: (a) – (j) Pictures of broken tensile specimens, which have undergone isothermal treatment as mentioned in Table 3.1 with that of unaged and untested samples have been shown in (a). 86

Fig. 5.7: Low magnification pictures of tensile fracture surfaces of samples having ten different heat-treatment histories are shown in (a) – (h). (a) – (e) and (h) show ductile *cup-and-cone* type fracture, (f) and (i) show deviation from the ductile type fracture, while (g) and (j) show faceted grains and fracture surfaces perpendicular to tensile axes. 88

Fig. 5.8: Fractographs of SQ Alloy 625 sample. Large dimples are shown by the arrows. Downward arrow on the left side is pointing a right-angle-corner particle at the bottom of the dimple.. 90

Fig. 5.9: Pictures in *a, b* and *c* are the fractographs from samples, aged at 813 K for 10 h, 100 h, and 1200 h, respectively. 92

Fig. 5.10: Pictures in *a, b* and *c* are the fractographs from samples, aged at 973 K for 10 h, 100 h, and 1200 h, respectively. Lines in *d* demarcate apparent intersections of prominent facets of fractograph in *c*. 94

Fig. 5.11: Pictures in *a, b* and *c* are the fractographs from samples, aged at 1123 K for 10 h, 100 h, and 1200 h, respectively. Lines in *d* demarcate apparent intersections of prominent facets of fractograph in *c*. 96

Fig. 6.1: (a) – (d) Optical micrographs from the deformed gage length, ~1 mm away from fracture surfaces of SQ, 813 K – 1200 h, 973 K – 1200 h and 1123 K – 1200 h broken tensile specimens showing parallel planes on which extensive slip have occurred. (b) Optical micrograph of deformed 813 K – 1200 h specimen showing twins and planes of extensive dislocation glide that remains contained within the grain. (d) Cutting of δ plates due to dislocation - δ interaction has been shown in the encircled region. 105

Fig. 6.2: Transmission electron micrograph from the deformed gage lengths, ~1 mm away from the tensile fracture surfaces of 813 K – 1200 h specimen showing extensive planar slip. SAD pattern in the inset shows weak intensity from $Ni_2(Cr,Mo)$. 107

Fig. 6.3: (a) Lens shaped γ'', marked “A” and “B” typically, are seen to be oriented along two directions. Except in “B'”, contrast from heavily slipped (111) type parallel

planes is seen on one side of “B” type γ″,. (b) Uniform deformation on both the sides across twin boundaries is observed. 108

Fig. 6.4: Transmission electron micrograph from the deformed gage region, ~1 mm away from the tensile fracture surfaces of 1123 K – 1200 h specimen.. Encirled regions are showing that thick plates of δ laths are sheared due to extensive planar slip....... 109

Fig. 7.1: (a) Normalized work-hardening rate plot of Alloy 625, aged at 813K for 10 h, 100 h and 1200 h along with unaged sample. (b) Normalized σθ vs. σ plot for derived from (a). 116

Fig. 7.2: (a) Normalized work-hardening rate plot of Alloy 625, aged at 973K for 10 h, 100 h and 1200 h along with unaged sample. (b) Normalized σθ vs. σ plot derived from (a). 117

Fig. 7.3: (a) Normalized work-hardening rate plot of Alloy 625, aged at 813K for 10 h, 100 h and 1200 h along with unaged sample. (b) Normalized σθ vs. σ plot derived from (a). 118

Fig. 7.4: Variations of $(\sigma.\theta)_0$ with isothermal holding time have been derived for two different precipitated microstructures of Alloy 625, which have been produced through the isothermal heating at 973 K and 1123 K. 119

Fig. 7.5: Variations of θ_h with isothermal holding time have been derived for two different precipitated microstructures of Alloy 625, which have been produced through the isothermal heating at 973 K and 1123 K. 120

Fig. 8.1: Positions of atoms on the (111) planes of Ni within the supercell when viewed from [111] directions. A’s, B’s and C’s correspond to positions of atoms in A-plane, B-plane and C-plane, respectively. 137

Fig. 8.2: Atoms on the top three (111) type ABC planes within the supercell are shown above. While position 1 is based upon the fully relaxed lattice parameter, relative other five different *z*-dimensions of supercells, which are given in Table 8.1, are indicated at the top using numeric “2” to “6”. 138

Fig. 8.3: Partials in *fcc* are shown on the ball model and on the sketch (right).......... 139

Fig. 8.4: Shockley partials of a perfect ½[1 $\bar{1}$ 0] dislocation in an *fcc* crystal is shown above using (a) ball model and and (b) line sketch. 140

Fig. 8.5: Close packed (1 $\bar{1}$ 2) type parallel planes in DO_{22} structures. Nb is represented by blue sphere and Ni is represented by pink sphere. 142

Fig. 8.6: Positions of Ni and Nb atoms in (1 $\bar{1}$ 2) type A to F planes around [2 $\bar{2}$ 1] axis as depicted in Fig. 8.5. Red color represnts Nb atom green color represents Ni atom. 143

Fig. 8.7: Arrangement of atoms on *ABCDEF…* type planes of Ni_3Nb-DO_{22} (γ''). Four parials in the ordered phases are shown by the bold arrows. Circle represents atoms in *A* & *D* planes, square represents atoms in *B* & *E* planes and triangle represents the atoms in *C* & *F* planes. Positions, *K*, *L*, *M*, *N* etc. are the positions of stacking considered for calculating SFE in the present study.. 145

Fig. 8.8: Shockley partials of a perfect [1 $\bar{1}$ 0] dislocation in Ni_3Nb – DO_{22} (γ'')..... 146

Fig. 8.9: Atoms on 12 Nos. (1 $\bar{1}$ 2) planes of Ni_3Nb-γ'' within the supercell. Nb atom is represented by darker shade. 148

Fig. 8.10: View of the 12 Nos. (1 $\bar{1}$ 2) planes of Ni_3Nb-γ'' supercell, same as Fig. 8.9, but along [1 1 $\bar{1}$] direction. 148

Fig. 8.11: Unit cell of Ni_3Nb – DO_a (δ). Nb is represented by blue sphere and Ni is represented by pink sphere. 149

Fig. 8.12: (a) Positions of Ni and Nb atoms in close packed (010) plane of Ni_3Nb – DO_a (δ). (b) Stack of (010) type *A* and *B* planes. 149

Fig. 8.13: *ABAB*…stacking of Ni_3Nb-DO_a (δ). Four partials in the ordered phases are shown by the bold arrows. Circle represents atoms in *A* plane, square represents atoms in *B* plane. Positions, K_1, L_1, M_1, N_1 etc. are the positions of stacking considered for calculating SFE in the present study.......... 151

Fig. 8.14: BM3 fitting of energies obtained against various volumes to determine fully relaxed lattice parameter of fcc Ni. 154

Fig. 8.15: Forces on atoms due to the formation of SF have been shown by arrows. 155

Fig. 8.16: Cross marks (×) indicating the BM3-fitted minima of the energy vs. volume plots corresponding to bulk and SF. 155

Fig. 8.17: Energy of the SF's at various positions along *K*, *L*, *M*, *N* ... positions as mentioned in Fig. 8.7. 158

Fig. 8.18: Energy of the SF's at various positions along K_1, L_1, M_1, N_1 ... positions as mentioned in Fig. 8.13. 159

Fig. 8.19: 3D surface of (111) plane along [$\bar{1}$ 0 1], [$\bar{2}$ 1 1] and [$\bar{1}$ 1 0], having *z*-vector along [111], due to atoms sitting on (111) plane is shown above. Stacking fault energies of fcc-Ni with (274.07 mJ/m^2) assuming 0.01233 nm additional height in the position of A_2, which is based on the atomistic ball model. 161

Fig. 8.20: Above plot is obtained after combining Fig. 8.17 and Fig. 8.18. It shows stacking fault energies along the partials in the ordered Ni_3Nb-Do_{22} (γ") (as per Fig. 8.7), Ni_3Nb-DO_a (δ) (as per Fig. 8.13) and in *fcc*-Ni. 164

LIST OF TABLES

Table 1.1: Alloying elements in INCONEL® Alloy 625 [27] (a) Nominal (in wt%) and (b) Typical, in both wt% and at%. 3

Table 2.1: Compositions of derivatives of Alloy 625 [5,6]. 16

Table 2.2: Crystal structures and morphologies of major ordered phases 18

Table 3.1: Schedules for isothermal-treatments 35

Table 4.1: Eight elements, obtained using WDX of EPMA in relative atom % and weight % is given below. Nominal composition of Alloy 625 in weight % is given in the last row for comparison. 45

Table 4.2: Fraction of various sigma boundaries and coherent (111) boundaries due to aging at various temperatures are given below. 63

Table 5.1: Tensile parameters of SQ and isothermally treated Alloy 625 samples along with hardness values in Vicker's Hardness No. (VHN). 80

Table 7.1: Parameters for fitting $\{(\sigma.\theta)_0/\mu^2\} \times 10^4$ vs. t using asymptotic function $f(t)= f(t_0) + A\times e^{-t/d}$ 120

Table 7.2: Parameters for fitting $\{\theta_h/\mu\}\times 10^3$ vs. t using asymptotic function $f(t)= f(t_0) + A\times e^{-t/d}$. 121

Table 8.1: Total energies calculated by VASP for the Bulk and the SF for various z-dimensions, as illustrated in Fig. 8.2. 156

Table 8.2: E$_0$, V$_0$ and the values indicating the goodness of fit corresponding to the data in Table 1 is given below. The reduced χ^2 in column 4 is the χ^2 divided by the number of degrees of freedom, while, coefficient of determination in the last column,

indicates the measure of proportion of present data with the variation suggested by the equation of state. 156

CHAPTER 1

1 Introduction

1.1 Background

High performance materials for structural applications in the arena of materials science are those, which retain their strength at high temperatures, maintain ductility at low temperatures and show exceptional corrosion resistance properties in reducing and oxidizing environments. In metallurgy, they are generally referred as "superalloys". These are based upon Ni, Fe, and Co, and essentially include other elements, such as, Cr, W, Mo, Ta, Nb, Ti and Al. Among these three groups, Ni-base superalloys are used in load-bearing structures to the highest homologous temperature, viz. close to 90% of their melting point, of any common alloy system. Face centered cubic (*fcc*) matrix of Ni-base alloys, showing sufficient ductility at low temperature, also make them suitable for cryogenic applications. When alloyed with chromium and molybdenum they exhibit excellent corrosion resistance in various corrosive and oxidizing atmospheres [1,2,3,4].

Among various Ni-base alloys, application of INCONEL® Alloy 625 is widespread over the past fifty years in high performance areas, which require various combinations of high temperature and completely contrasting corrosion resistance properties [5]. While the alloy is chosen for keeping good ductility even in the weldment during cryogenic application, it is one of the very few alloys manufactured today for which the ASME Boiler and Pressure Vessel Code has recommended allowable design stresses for service up to 1255 K (~0.8 T_M). The alloy is resistant to a wide spectrum of corrosive environment, including salt-water, hydrochloric, nitric and high temperature oxidizing atmosphere and, also, to many stress-corrosion atmosphere. This combination of characteristics of Alloy 625, hence, endorses it to be a top-grade superalloy [5,6,7,8].

1.2 Alloy 625

INCONEL® Alloy 625 is a Ni base alloy, in which, a lot of alloying elements, such as, chromium, molybdenum, niobium, iron are added to stiffen its face centered cubic matrix. Although, the alloy has initially been designed to provide high temperature strength due to solid solution strengthening, later it has been found that a large number of ordered phases, common to many Ni base alloys [1,2,9], appear in the alloy during service or on aging at high temperature. Occurrences of these ordered phases, nonetheless, may be inferred from the composition of the alloy and high temperature binary Ni-Nb and ternary Ni-Cr-Mo and Ni-Cr-Fe systems available in the literature [10,11,12,13,14,15,16,17,18]. In other words, there is a solvus-region in this multi-component alloy system and the temperature, below which a typical ordering takes place, is decided by the actual composition rather than the composition range of Alloy 625, given in Table 1.1.

Time-temperature-transformation (TTT) behaviors of the ordered phases in the context of Alloy 625 are available on two widely accepted TTT diagrams [19,20], out of which the most recent one is shown in Fig. 1.1. Earlier works have shown that among all the ordered phases $Ni_3[Nb,Ti]$ type γ'', $Ni_3[Nb,Mo]$ type δ and $Ni_2(Cr,Mo)$ with Pt_2Mo structure make major contribution in the age-hardening process [21,22,23]. Depending upon the service condition various carbides, such as, MC type primary carbide and $M_{23}C_6$ and M_6C type secondary carbides are also seen to form in the alloy matrix and influence the alloy property [19,20,21,22,24,25]. Apart from these, it is also possible to find out topologically-close-packed phases, such as, Laves phase [24], less common γ' (rich in Ni and Nb) [26], and M_2N ('M' rich in Nb, Cr, Mo and Ni) type or some time TiN type nitride [6], depending upon the variation within the broad composition range of the alloy given in Table 1.1.

Table 1.1: Alloying elements in INCONEL® Alloy 625 [27] (a) Nominal (in wt%) and (b) Typical, in both wt% and at%.

(a)

Ni	Cr	Mo	Nb	Fe	Al	Co	Ti	C	Si	Mn	P & S
58.0 min.	**20.0-23.0**	**8.0-10.0**	**3.15-4.15**	**5.0 max.**	**0.40 max.**	**1.0 max.**	**0.40 max.**	**0.10 max.**	**0.5 max.**	**Mn 0.50 max.**	**0.015 max. (Each)**

(b)

	Ni	Cr	Mo	Nb (+Ta)	Fe	Al	Co	Ti	C	Si	Mn	P	S
Wt% (Typical)	60	21.5	9	3.6 (+0.4)	3.5	0.2	0.7	0.3	0.11	0.35	0.35	0.009	0.009
At%	60.7	24.5	5.6	2.3(+0.13)	3.7	0.7	0.44	0.37	0.74	0.38	0.4	0.02	0.02

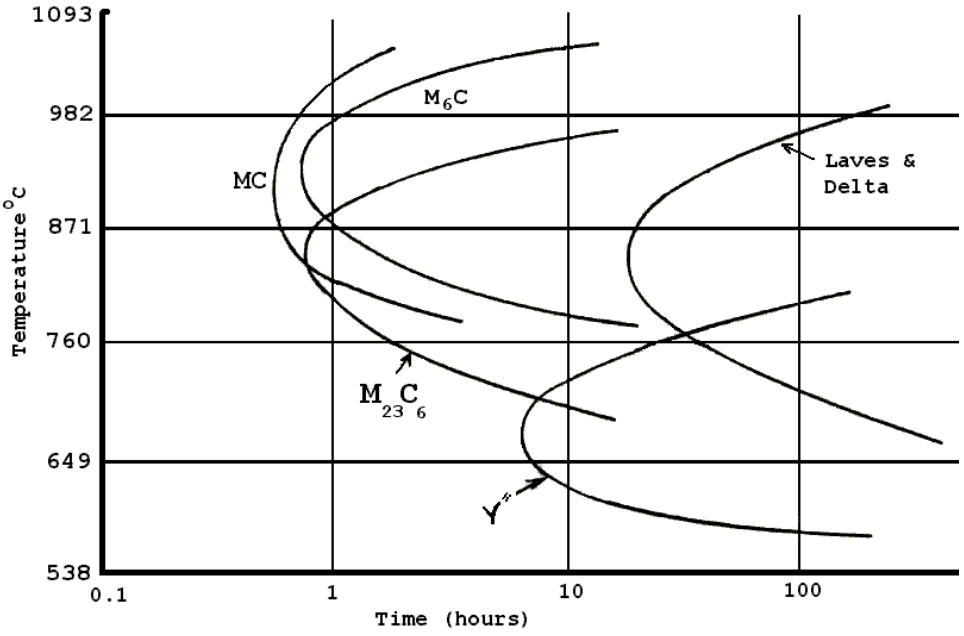

Fig. 1.1: Time-temperature-transformation diagram of Alloy 625 [20].

1.3 Melting Practice

The typical melting practice adopted for producing Alloy 625, on one side, is to achieve desirable composition, in which some are strong oxide-formers and on the other side to keep certain elements and impurities, including C, P, S and N under stringent control. Although, the first commercial heat of Alloy 625, in the year 1962, has been produced in an electric arc furnace subsequently, melting has been done in the electric arc furnace followed by refining in an argon-oxygen decarburization (AOD) vessel. Compared to most Ni-base alloys, Alloy 625 shows a stronger tendency to retain nitrogen because of the relatively high levels of chromium and molybdenum in the alloy. This problem is overcome by vacuum melting of the alloy that brings down the nitrogen level in the alloy. Further improvements in properties and quality have been achieved by remelting in either a vacuum arc remelt (VAR) or electroslag remelt (ESR) furnace. Certain products, such as sheet and plate, are usually vacuum induction melted (VIM) and ESR remelted. Virtually all of the Alloy 625 heats produced currently are remelted in either a VAR or ESR furnaces.

It has been reported in the literature [5,46] that vacuum melting substantially reduces nitrogen content and total residue content of Alloy 625 as compared to air melted material (0.06% for VIM/ESR versus 0.42% for EAF/AOD/ESR). This cleaner microstructure significantly improves the fatigue resistance of Alloy 625LCF products and, thereby increases the service life of the components fabricated from the typical Alloy 625 heat.

1.4 Work-Hardening

Theories of work-hardening (WH) aim to explain and predict stress-strain response of metals and alloys in the plastic range with the help of dislocation concepts. In a simple form, true stress, σ, experienced during mechanical working, may be split into two components, σ_0, and σ_d, respectively, the fixed and the variable one. σ_0 arises from lattice cohesive energy, etc. and σ_d is a function of dislocation density, $f(\rho)$. These are expressed in the following mathematical forms.

$$\sigma = \sigma_0 + \sigma_d \tag{1.1}$$

$$\sigma_d = f(\rho) \tag{1.2}$$

and

$$\rho = g(\varepsilon) \tag{1.3}$$

where, ε being the plastic strain [28,29]. Describing the WH behavior in the above manner using a single dislocation density is also known as 'single parameter' approach and the concept has been found effective in describing the WH behavior of face-centered-cubic single crystal [30,31]. However, modeling WH behavior based on various types of dislocation densities, such as, *dislocations at the grain interior* and *dislocations at the grain boundary*, etc. seems to present more complicated theories, which are difficult to apply into real problems [32,33,34]. In this regard, the 'single parameter' approach, which is based on a uniform dislocation density, is often good enough and simple to explain overall WH phenomena. The single parameter model is modified to take care of dislocation multiplication from a *fixed* mean free path (MFP) concept so as to incorporate the Orowan looping mechanism [31]. This is also referred as the *hybrid* model that combines the effect of a constant dislocation MFP and a variable one, to predict the WH behavior. The hybrid model is represented graphically through $\sigma.\theta$ vs. σ plot in Fig. 1.2 and has following mathematical form.

$$\sigma.\theta = (\sigma.\theta)_0 + \sigma(\theta_h - \theta_r) \quad \textbf{(1.4)}$$

Where, θ is the WH-rate, $\partial\sigma/\partial\varepsilon$. On the right-hand side, $(\sigma.\theta)_0$ is a constant and typical 'hardening' and 'recovery' components of the WH-rate are referred through subscript *h* and *r*, respectively. The above equation may give rise to three situations, typically, when any one of the *constant term*, $(\sigma.\theta)_0$ or the *quotient term*, θ_h, on the right-hand side is equated to zero or all terms are non-zero terms. Phenomenologically these conditions are correlated with the global dislocation activities in the microstructure.

When a face-centered-cubic (*fcc*) solid solution matrix with a low dislocation density starts deforming, dislocation-dislocation interaction begins to raise the dislocation density. In the absence of strong obstacles, which force the moving dislocations to increase the dislocation density, $(\sigma.\theta)_0$ is considered zero and the Eq. (4) can be re-written as in Eq. (5).

$$\sigma.\theta = \sigma(\theta_h - \theta_r) \quad \textbf{(1.5)}$$

This is graphically represented through the "*R*" line in Fig. 1.2. Initially, when dislocation density is quite small and the "recovery term", θ_r, is negligibly small, $\sigma.\theta$ vs. σ goes upward with a slope of θ_h, which is reflected in the initial slope of the "*R*" line in Fig. 1.2. With the rise in the dislocation density, θ_r becomes significant and, hence, locus of the $\sigma.\theta$ goes downward. Inflection point on the "*R*" line apparently balances two competing processes i.e. hardening on the left side and recovery on the right side.

When θ_h is negligibly small but $(\sigma.\theta)_0$ is non-zero, Eq. (4) reduces to Eq. (6). Such situation is intended to incorporate dislocation multiplication through Orowan looping mechanism and is parameterized through a 'fixed mean free path' concept. In such a situation, $\sigma.\theta$ vs. σ goes downward as θ_r term becomes prominent with the progress of deformation and the same may be graphically represented through the "*B*" line in Fig. 1.2. However, when all terms are non-zero terms, the condition may be graphically represented through the "*G*" line in Fig. 1.2.

$$\sigma.\theta = (\sigma.\theta)_0 - \sigma.\theta_r \tag{1.6}$$

As stated above, the WH rate of an *fcc* alloy, θ_h, may be obtained from the initial slope of $\sigma.\theta$ vs. σ plot, typically, when the "true stress" – "true strain" data is obtained from the annealed alloy, thus, ruling out the possibility of any significant recovery term. Hence, when θ_r is negligibly small, Eq. (1) may be rewritten as follows.

$$\sigma.\theta = (\sigma.\theta)_0 + \sigma.\theta_h \tag{1.7}$$

When, the above relation is re-written in terms of dislocation density, ρ, and constant MFP, λ_c, the following expression is obtained, where, b, M and μ are, correspondingly, Burgers vector, Taylor's factor and shear modulus. α and β are the constants relating dislocation density to stress and to mean free path, respectively.

$$\sigma.\theta = \frac{M^3(\alpha\mu)^2 b}{2\lambda_c} + \frac{M^2 \alpha\mu}{2\beta}.\sigma \tag{1.8}$$

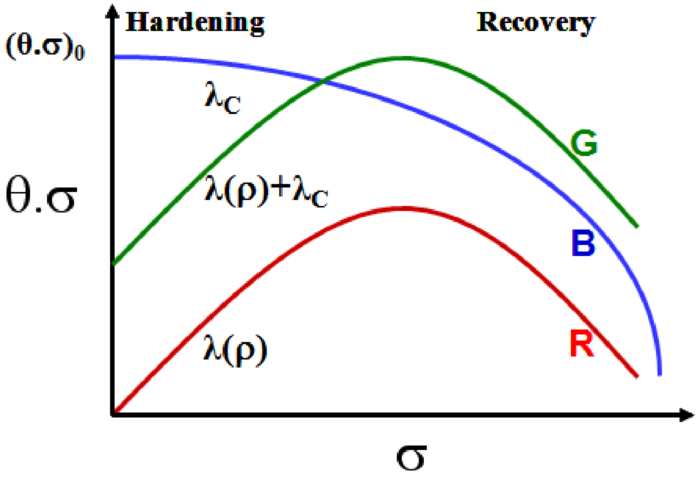

Fig. 1.2: WH behaviors of polycrystalline *fcc* alloy, based upon (a) dislocation – dislocation interaction, (b) fixed mean free path and (c) the combination of these two are schematically shown by *R*, *B* and *G* lines, respectively.

1.5 Ab-initio Modeling of Planar Faults

Mechanical behavior of a crystalline solid is governed by the dislocations in terms of the density, the glissile and sessile types and the gliding process. Glissile dislocations glide on the slip plane to produce plastic deformation, which are typically seen during any low strain rate deformation process, including the tensile or compression testing or metal working processes [35]. In reality, a perfect dislocation is dissociated into partials in order to minimize its cohesive energy. During deformation, the equilibrium separation between the partials dictates the slip process in the solid. The wide separation between partials that occurs when the stacking fault energy (SFE) is low, compels the crystal to obey the planar-slip during the deformation. However, when the SFE is high the tendency to cross-slip rises, which enables the dislocation to jump on to another slip plane.

The first principle based calculations are often used to determine the SFE of a system. Calculations are typically carried out using software that employs a supercell approach. In order to exclude surface energy term, the calculations are typically carried out under the periodic boundary condition. In such a case the stacking fault should be separated from its image by a large enough distance to reduce the interaction between the faults.

1.6 Aim of the Work

As reported in the literature, prolonged use of the alloy at high temperatures results in the appearance of various second phases, which lead to an unacceptably low room temperature ductility and degradation of all possible property-requirements [19,21,55]. Analyses of some of the unserviceworthy Alloy 625 components, reported there, have led to the identification of several microstructural features, responsible for variation in mechanical properties after prolonged service. However, Alloy 625 components, in these reports, have been subjected to high temperature operations for a long duration having imprecise time-temperature-environment histories. Although, the effect of aging on the alloy properties is known to be significant, for the want of data from reliable laboratory experiments a systematic correlation in the structure-property of Alloy 625, delineating the role of various precipitates, at various stages of growth, on mechanical properties and fracture is yet to be established.

In spite of the occurrence of a large number of ordered phases in the alloy matrix, Alloy 625 is continued to being used in the solid solution form. Due to the slow kinetics of formation of major ordered second-phases, use of the alloy in the solution quenched form is considered economical in the industrial time-frame. Nevertheless, as the ordered second-phases in Alloy 625 components grow during high-temperature operation, they strongly influence various properties of the alloy. This study aims to understand the influence of various ordered phases at various stages of their growth on the mechanical behaviors, including tensile, work hardening and fracture behaviors of the alloy and to correlate the same with the dislocation-precipitate interactions.

1.6.1 Scope of the Work

Scope of the present study is as follows.

- To characterize the solution quenched microstructure of the as-received Alloy 625, so as to know the starting condition that would act as a benchmark for comparison with that of isothermally treated conditions.

- To produce various stages of growth of the ordered second phases in the intermediate temperature range through isothermal treatments and to characterize them.
- Deforming the isothermally treated Alloy 625 specimens to understand the influence of the growth of the ordered phases on the tensile properties, stress-strain responses, work-hardening and fracture behavior.
- Studying interactions of dislocations with various types of precipitates in Alloy 625 microstructures in order to correlate them with mechanical properties, work-hardening and fracture behaviors.
- Density functional theory (DFT) based first-principles calculations of stacking fault energy of pure Ni, which is in close approximation to the multi-component Alloy 625 in order to understand the basic slip process that governs the deformation in Alloy 625.
- To explain fundamental causes for various dislocation-precipitate interactions in Alloy 625 through first-principles based calculations.

1.7 Outline of the Thesis

After a short background in *section* 1.1, occurrences of various ordered phases have been described through a description Time-Temperature-Transformation (TTT) diagram in *section* 1.2. Evolution in melting practice that is responsible for the desirable performance is mentioned in 1.3. Following that, work-hardening principles for understanding and analyzing the mechanical properties, which involves dislocation glide in face centered cubic metals and alloys, have been mentioned in *section* 1.4. The role of SFE to correlate the deformation in the crystal lattice through the motion of dislocation are given in brief in *section* 1.5. Towards the end *section* 1.6 describes the aims and the objectives of the present work.

INCONEL® Alloy 625, continues with the composition that is known at present, due to its exceptional performance in demanding applications. This is elaborated in *section* 2.1 of literature survey in chapter 2. It is necessity to know the *derivatives of Alloy 625*, which inherits the structure-properties of Alloy 625 to a great extent and the same is described in *section* 2.2. Major ordered phases, which changes the properties of the alloy significantly, are mentioned in *section* 2.3. Other ordered phases, such as carbides and other less significant topologically close packed phases in the context of Alloy 625 are described in 2.4. *Microstructural changes and the procedure for recovery* in *section* 2.6 narrate the rejuvenation procedure for Alloy 625 that has suffered in-service degradation. Since, thermal exposure in Alloy 625 causes formation of intermetallic compounds in its *fcc* matrix, studies on the deformation behavior of the ordered phases, pertinent to Alloy 625 have been mentioned in *section* 2.5 with special emphasis upon the slip systems and the stacking fault energy. At the end, various applications of the alloy in high performance areas are summarized in *section* 2.7.

Chapter 3 starts with the sampling of as-received solution-quenched Alloy 625 block followed by the fabrication of tensile specimens in 3.1. Choice of three isothermal temperatures for effectively producing three types of ordered intermetallic compounds in this alloy have been mentioned in 3.2. After describing the tensile testing and data analysis in *section* 3.3, various microstructural characterizations using scanning electron microscopy, transmission electron microscopy and orientation imaging microscopy techniques have been described in *sections* 3.5, 3.6 and 3.7, respectively. Next, method of first principles based atomistic modeling of the ordered phases in Alloy 625 has been described in *section* 3.8.

Major categorical findings have been described in the next five chapters (chapter 4 – 8). Microstructural investigation of Alloy 625, without and with various degrees of growth of $Ni_2(Cr,Mo)$, γ'' and δ, using various electron microscopy techniques have been summarized in chapter 4. Mechanical response of aged Alloy 625 that includes mechanical properties, true stress – true strain behavior and fracture behaviors, as obtained from the tensile testing, have been summarized in chapter 5. This, on one side, reflects the impact of the microstructure on the properties and, on the other side, creates the basis for work-hardening analysis in chapter 7. In chapter 6, study of deformed microstructures resolves the way of interactions of dislocations with various ordered phases in Alloy 625. This is essential to establish the correlation (a) between its microstructure and fracture and, also, (b) between the dislocation-precipitate interaction and the typical work-hardening behavior that has been analyzed in chapter 7. Motivation for the investigation on the disparity in the interaction of dislocation with γ'' and δ ordered phases that has been revealed by the study of deformed microstructures in chapter 6 has led to the study of the stacking fault energies through first-principles based calculation of the ordered phases and Alloy 625 matrix in chapter 8. Role of fault energies of *fcc*-Ni, γ''-Ni_3Nb (DO_{22}) and δ-Ni_3Nb (DO_a) ordered phases in the dislocation dissociation and the deformation micro-mechanism, per se, has also been discussed there. Finally, conclusions of the thesis, followed by the future direction that is apparent from the present work are presented in chapter 9.

CHAPTER 2

2 Literature Survey

2.1 Evolution of Alloy 625

Strive for a solid solution strengthened alloy, suitable for application in the area of high temperature and corrosive environments, has been the cause for invention of Ni-base Alloy 625. Its classification as "625" is apparently due to its development on the base of Alloy 600. However, it has been realized during the developmental stage that formation of several ordered phases, although cannot be formed economically in the industrial time-frame, are inevitable in this alloy system. While, such findings have slowed down its launch and gave birth to other precipitation-hardened alloy, such as, Alloy 718, the alloy was finally launched in the solid solution form. The reason for this is its simple heat-treatment procedure, i.e. simple air-cooling from the solution annealing temperature, to retain the single phase, and an unmatched combination of properties discussed earlier. Even after fifty years of existence, this has kept Alloy 625 on high demand in several high-performance areas.

Alloy 625 has been invented in the 1950s and has been first sold commercially in 1962. On December 8, 1964, Herbert L. Eiselstein and John Gadbut of the Huntington Alloys Products Division of the International Nickel Company in Huntington, West Virginia, USA has officially launched, what is widely known as Alloy 625 today, with the issue of United States Patent Number 3,160,500 INCONEL® Alloy 625 (UNS N06625) [6].

Experimental work on ternary phase diagram of Ni-Cr-Mo, way back in 1925, has been the pioneer work for the development of Ni-Cr-Mo base superalloys [12]. By

1950s, significant amount of work on the strengthening effects of various amounts of the common major alloying elements, i.e., Cr, Mo, Nb, Al, and Ti in an INCONEL alloy 600 base has been done and the performance of INCONEL alloy X-750, which is strengthened by Ti and Al had already been known [6]. It had been noticed that the strengthening effects of these elements one at a time have not been impressive. So it has been decided to use molybdenum and Nb in combination with varying amounts of Ni. Little change in properties had been noticed with Nb additions up to 2%. Mo increased the strength of the matrix and may alone or through some interaction with niobium increase the age-hardening response and decrease the impact strength after exposure. While higher levels of Nb allows rise in strength levels after an aging cycle, the penalty of decreased room-temperature ductility levels after prolonged service exposure is not worth the small advantage that the capability of intentional aging provides. Increasing Cr content from 16%, as in Alloy 600 to 22% in Alloy 625 caused an increase in the strength of the alloy matrix but did not appear to have any effect on the age-hardening response at these levels of Cr. Mo, Cr and Nb impart creep strength to the alloy. In order to improve the intermediate-temperature low-cycle fatigue (LCF) properties of Alloy 625, modifications have been made to the C, Si and Ni levels. By limiting the C level to 0.03% max, the Si level to 0.15% max. and the N content to 0.02% max. and by modifying the melting method and annealing practice, a considerable improvement in LCF strength has been realized. An added advantage to a low level of AI+Ti in Alloy 625 is intended to improve weldability and brazeability. Nickel plating, which has been almost a necessity when brazing alloys with higher levels of AI+Ti, bas been unnecessary. Controlling these elements within solubility is also responsible for the elimination ordered γ' in Alloy 625.

2.2 *Various Derivatives of Alloy 625*

Aforementioned understandings have also poured in numerous variations of the alloy, as shown in Fig. 2.1. Compositions of these derivatives have been described in Table 2.1. This is to say that the derived alloys inherit the property the parent Alloy 625. Hence, microstructural studies of these derived alloys are, in a sense, complementary to that of Alloy 625.

Alloy 718 has lower solubility for niobium, and consequently shows higher annealed and aged strength, due to lower Ni and higher Al and Ti content. A further modification of Alloy 718 has led to the development of Alloy 706, an age-hardenable alloy being used for large turbine wheels because of its high strength, good machinability and capability of maintaining ductility at the notch in large cross-sections. Addition of Co in Alloy 625 base by gas turbine manufacturers has resulted into the alloys, such as, Rene 220 from GE, and PWA 1472 from Pratt & Whitney, which have extended the upper service temperature capability of alloy 718.

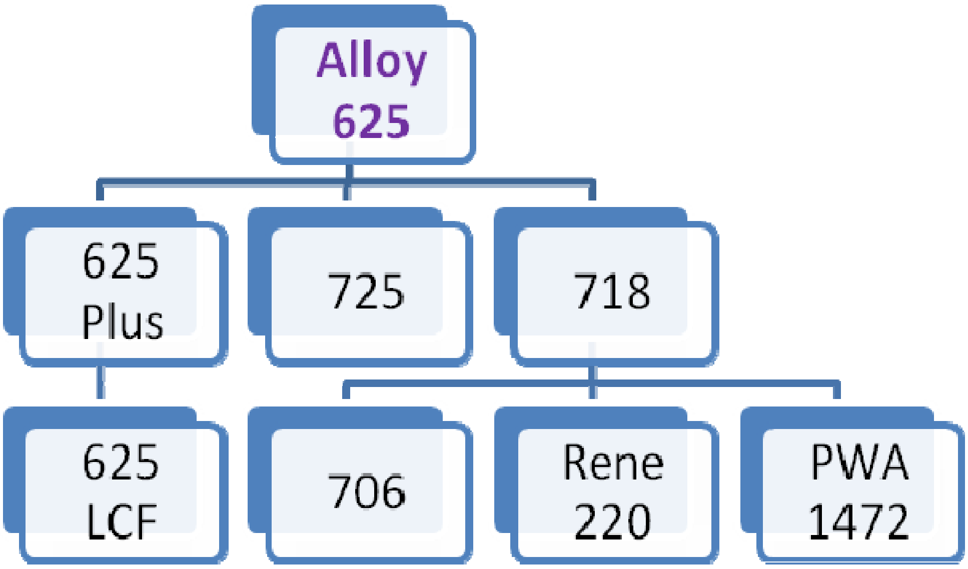

Fig. 2.1: Tree of descendants of Alloy 625 [5,6].

Table 2.1: Compositions of derivatives of Alloy 625 [5,6].

Alloy	**Ni**	**Cr**	**Mo**	**Nb**	**Al**	**Ti**	**C**	**Si**	**Fe**	**Other**
600	72.0	15.5	-	-	-	-	0.15	0.5	8.0	Mn 1.0, Cu 0.5
625	61.0	21.5	9.0	3.6	0.2	0.2	0.06	0.25	2.5	
625 LCF®	61.0	21.5	9.0	3.6	0.2	0.2	0.03M	0.15M	2.5	N 0.02M
718	52.5	19.0	3.0	5.1	0.5	0.9	0.04	0.18	18.5	B 0.002
706	41.5	16.0	-	2.9	0.2	1.75	0.03	0.18	40	
625PLUS®	61.0	21.0	8.0	3.4	0.2	1.3	0.01	0.12	2.5	
725	57.0	21.0	8.0	3.5	0.25	1.5	0.01	0.15	9.0	
Rene® 220	52.5	19.0	3.3	5.1	0.5	1.0	0.04	<0.1	Bal	B 0.005 Co 12.0
PWA1472®	58.0	12.0	3.0	6.0	0.6	2.0	0.04	0.15M	18.0	B0.002

The age hardening response of Alloy 625 was further improved by the addition of titanium to produce a new alloy designated INCONEL® alloy 725 (UNS N07725). This has been done by the lnco Research and Development Center in Suffern, NY, during their investigation of age-hardenable Ni-base alloys for sour gas use through appropriate autoclave technology. The alloy possessed an attractive combination of strength and sour gas corrosion resistance. Alloy 725 exhibits essentially the same chemical composition (Table 1) as Alloy 625 except that the titanium content is increased to about 1.5% to enhance precipitation hardening. Thus, it exhibits the excellent corrosion resistance of Alloy 625. In essence, alloy 725 offers the excellent strength properties of alloy 718 with the proven corrosion resistance of Alloy 625.

However, topologically close-packed phases, such as, η (eta) and σ (sigma) are formed during high temperature operation. Excess titanium also causes formation of γ'. Separately, the effort from Cartech on developing a similar alloy has produced Custom Age 625 PLUS.

2.3 Major Ordered Phases in Alloy 625

Ordered phases, $Ni_2(Cr,Mo)$, γ" and δ, comprising major alloying elements, such as, Ni, Cr, Mo and Nb, fall in this category. Availability of these elements in excess to their solubility limit in the *fcc*-Ni matrix is responsible for the formation of these phases. Details of crystal structure of these phases are given in Table 2.2 and the arrangements of atoms in the lattices are given in "Modeling" *section*. All of these ordered phases have one thing common in them; i.e. they are derived from the *fcc* structure and arrangements of atoms in their close-packed plane is similar to that of their parent *fcc* lattice.

Like other precipitates in any alloy system, shape, size and distribution of these three ordered phases in Alloy 625 too depends upon the time and temperature of exposure. Since, formation of an useful combination of shape – size – distribution of these ordered phases is uneconomical in the industrial-frame of time and cost, in spite of their significant contribution in the mechanical properties, Alloy 625 components for structural application are manufactured in the solution annealed condition, ever since its inception. Details of these ordered phases in the context of Alloy 625 are discussed below.

Table 2.2: Crystal structures and morphologies of major ordered phases [2,11,36,37,38]

Ordered Phase	Pearson Symbol/ Space Group/ Strukturbericht designation/ Prototype	Lattice Parameter (pm)	Morphology/ Number of variants
$Ni_2(Cr)$ (approximated to $Ni_2(Cr,Mo)$)	oI6 / *Immm* / D_{2h}^{25} / $MoPt_2$	a = 251.4 b = 754.1 c = 355.5	Snowflake/ six
Ni_3Nb (tetragonal)	tI8 / I4/mmm / DO_{22} Al_3Ti	a = 362.4 c = 740.6	Lens shaped/ three
Ni_3Nb (orthorhombic)	oP8 / Pmmn / DO_a / β-$TiCu_3$	a = 503.0 – 511.0 b = 425.4 c = 457.3	Plate – shaped/ twelve

2.3.1 $Ni_2(Cr,Mo)$ – D_{2h}^{25} Phase

Discovery of ordered orthorhombic $Ni_2(Cr,Mo)$ phase took place in an Alloy 625 component, which has been subjected to a long service exposure below 873 K. This phase has maximum influence on the mechanical properties at this intermediate temperature range and is comparatively a new finding in the alloy [21,22]. The ordered phase is having a $Ni_2(Cr_{0.75},Mo_{0.25})$ stoichiometry and a D_{2h}^{25} - *Immm* structure. The orthorhombic ordered phase exhibits a snowflake morphology and can have six variants in Alloy 625 matrix, details of which, including composition and the orientation relationship with the parent *fcc*-lattice (a = 358.7 pm) is given by Sundararaman et. al. [22].

$Ni_2(Cr,Mo)$ phase is presumably the most important phase in Alloy 625, when exposure of the alloy in the intermediate service temperature range is considered [18]. However, "*C*"-curve corresponding to TTT of $Ni_2(Cr,Mo)$ phase in Alloy 625 has not been shown on the TTT diagrams [19,20], depicting transformation below 813 K up to 2000 h. The absence gives an impression that the $Ni_2(Cr,Mo)$ precipitates form after a long aging time (> 2000 h) at temperatures below 823 K. However, occurrence of the phase is quite natural in Ni-Cr-Mo base Alloy 625, since, Cr and Mo is available in this alloy beyond their solubility limit, which is supposed to have been maintained in the composition range of Alloy 600, as shown in Table 2.1. It has been observed that metastable $Ni_2(Cr,Mo)$ is likely to dissolve above 923 K and precipitate below 898 K [11].

Existence of $Ni_2(Cr,Mo)$ phase in Alloy 625 is first noticed in a feed-stock super-heater of a petrochemical plant, which has been in service for about 50,000 h at around 773 K [21]. The <001> Selected area diffraction (SAD) patterns, obtained from the aged material, revealed extra reflections in addition to γ'' and parent γ. These extra reflections were correlated with $Ni_2(Nb,Mo)$ phase having Pt_2Mo structure by Bajaj et. al. [39], who irradiated the alloy to a fluence of 2.3 x 10^{20} neutrons/cm^2 at 633 K. Later, it has been reported that a precipitate with Pt_2Mo structure, having $Ni_2(Cr,Mo)$ composition, formed in Alloy 625, when exposed to near 873K temperature for about 28,000 h and 70,000 h [22].

Formation of the second phase with the Pt_2Mo structure in Alloy 625 has been observed in the components subjected to a wide range of service exposures at temperatures around 873 K [23] and, also, in a laboratory experiment after 100 h of isothermal holding at 813 K [40]. It has also been noticed that, reflections corresponding to $Ni_2(Cr,Mo)$, in the SAD patterns from Alloy 625 have always been associated with that of γ'' [21,22,40]. Compared to γ'', which is having three variants of ellipsoidal morphology, $Ni_2(Cr,Mo)$ is seen to have six variants of snowflake morphology. Precipitation of ellipsoidal $Ni_2(Cr,Mo)$ (Pt_2Mo structure) has already been known in some other Cr and Mo bearing Ni-base alloys such as, Hastelloys [41,42] and in Haynes Alloy 242 [43], and in the latter alloy it has been seen on aging at temperatures up to 1023 K. However, $Ni_2(Cr,Mo)$ in Alloy 625 undergoes complete dissolution on heating for a short duration above 923 K [21] or 873 K, as reported in a later report [44], leaving γ'' and other precipitates in the matrix. Theoretical calculation using CALPHAD has shown that the kinetics of ordering is quite slow below 773 K [45]. This indicates that depending upon the actual Cr and Mo concentration, Alloy 625 crosses the solvus-surface of $Ni_2(Cr,Mo)$ in the Ni-Cr-Mo ternary somewhere around 873 K and 923 K and remains as a supersaturated solid solution due to remarkably slow kinetics at the room-temperature [45]. This ordered phase makes significant impact on the mechanical properties of Alloy 625 in the intermediate operating temperature up to 873 K, since, selective dissolution of the phase reduces the strength and increases the ductility.

2.3.2 γ'' – DO_{22} Phase

The formation of γ'' ordered phase in Alloy 625 is one of the most important phenomena, since, it has been noticed in all Alloy 625 components, which are exposed to high temperature and is known to alter its ductility and strength significantly. γ'' in Alloy 625 group of alloys [46], including in Alloy 718, maintains a stoichiometry close to Ni_3Nb. The ordered phase exhibits lens shaped morphology having a maximum 30 nm diameter in an aged component [44]. The nose of the "*C*" curve in the TTT digram is located at 973 K and it is possible to get the ordered phase even at 813 K after 100 h. γ" being the strengthening precipitate in Alloy 718, details of the deformation behavior of the γ" strengthened matrix is studied in that context [47,48].

The body-centered tetragonal DO_{22} superstructure of γ" is having a *c*/*a* ratio of 2.06. The ordered phase can have three variants, which grow along the three principle axes of the alloy matrix. This phase is considered metastable since, it transforms into stable δ at little higher temperature. γ" phase being common to many Ni base alloys, including the precipitation hardened Alloy 718, information about its crystal structure, shape, size, morphology and orientation relationship with the parent lattice, which is presumably valid for Alloy 625, has been widely studied by several workers [49,50] using electron microscopy.

It has been reported that room temperature deformation of γ" strengthened Alloy 718 is associated with profuse formations of twins and stacking faults in the ordered phases. These twins are seen to be perfect twins where ordered atomic arrangements are not disturbed [51]. Deformation of precipitated Alloy 718 is seen to raise the density of the stacking faults in γ" and the faults are seen to spread out uniformly in the ordered phase. In all the cases, stacking fault in γ" are seen to be geometric in nature that has not caused the first nearest neighbor violation. The same has also been elaborated in a high resolution TEM observation of the phase [52]. Atomic arrangements on the close packed planes of γ" being similar to that of δ, stacking fault in the former is presumed to cause nucleation of the later phase [51].

2.3.3 δ – DO_a phase

As stated above, ordered δ is having the orthorhombic DO_a symmetry, which is a stable structure at high temperature [53,54]. The stoichiometry and the arrangements of atoms on the close packed (010) plane of δ – DO_a closely matches with close packed plane of γ''. Although, δ phase is almost always seen to be associated with the γ'' in the microstructure, it is possible to grow this phase in the alloy matrix by isothermally holding the alloy above γ'' – solvus [54]. The nose of the "*C*" curve of δ in TTT – diagram is at ~ 1123 K and the phase can be completely dissolved into Alloy 625 matrix by heating above 1373 K.

Orthorhombic δ can grow homogenously and heterogeneously in plate shaped and globular shaped morphologies, respectively. In can have twelve variants in the parent alloy matrix and the details of the orientation relationship is given in the literature [50,53]. Recent high resolution TEM study has confirmed that this ordered phase remains coherent on its (010) close-packed plane with the equivalent (111) plane of parent *fcc* γ [54]. Details of atomic arrangements on its lattice and close packed plane would be discussed in the "Modeling" *section*.

2.4 Other Ordered Phases in Alloy 625

2.4.1 Carbides

Occurrence of carbides in any structural alloy is known to be detrimental to its fracture [55] and fatigue behavior [56] and, hence, a lot of studies have been carried out to characterize the carbides in Alloy 625. Depending upon their origin, carbides in Alloy 625 may be divided into two types, i.e. primary and secondary. Primary carbide is MC ('M' rich in Nb) type NbC, while secondary carbides are mostly $M_{23}C_6$, ('M' rich in Cr), and M_6C ('M' rich in Ni, Nb and Mo) [57,58]. As discussed in the literature, [58] formation of the primary carbide in this alloy is sensitive to Nb:C ratio, in a way, that when the ratio is not high, topologically close packed Laves phase appears, while for low ratio primary carbide forms in this alloy. For the ratio lying in-between the two extreme conditions, which is not so well defined, a mixture of primary carbide and Laves phase can be found in this alloy.

Primary carbide is formed during solidification and is blocky in nature. This carbide does not show any preference for grain boundary, thereby appearing everywhere in the matrix. In this respect, secondary carbides form on aging the alloy during service at high temperature and are seen several times on the grain boundaries. They get dissolved on solution annealing above 1373 K [19,44,59].

2.4.2 Topologically Close Packed and Other Ordered Phases

As discussed above that presence of both, primary carbide and laves phase, are possible in this group of alloys [57,58]. Presence of Laves phase becomes prominent when the concentration of carbon becomes very low [58]. It has also been reported in the literature that higher Si and Fe increase the formation of Laves, especially, as the former element segregate into the topologically closed packed phase to stabilize the same [20]. This dictates the necessity of keeping Si and Fe in low concentration in the alloy.

Apart from the Laves and primary carbide, γ' having ordered *fcc* structure is also quite rare and has not been reported in most of the detailed characterization study of the alloy. However, recent investigation, using Extended X-ray Absorption Fine Structure (EXAFS), which is capable of determining the minute presence has confirmed the presence of the phase in this alloy [26]. It is to be noted that the presence of Al beyond the solubility limit in Alloy 625 matrix is responsible for the formation of the phase. Hence, small amount of γ' is apparently possible when the Al is on the higher side within the composition range of Alloy 625.

Influence of γ' precipitates on the fracture-surface morphologies of various Ni-base IN738LC and CMSX-4 alloys has been reported earlier [60,61]. It has been observed that the variations in distribution and morphology of this second-phase may result in a wide range of fracture surfaces, such as, dimple-ductile, quasi-cleavage and cleavage types. Characteristics of the fracture surfaces and the crystallographic planes of the facets are seen to depend upon the size of the precipitates and the type of the loading. It has been reported that IN738LC microstructure with fine γ′ (70 nm) and with the mixture of fine and medium sizes, of 70 nm and 450 nm, respectively, produce transgranular quasi-cleavage type fracture. The fractographs obtained from the samples tested at room temperature are reported to have facets parallel to {100} type crystallographic planes [60]. However, the samples tested at high temperature are reported to also produce {111} type facets [60]. Inability of the fine precipitates to initiate voids has been reported to be responsible for such faceted cleavage type fracture. Microstructure with γ′ precipitates of medium size and of coarse size, 450 nm and 700 nm, respectively, are reported to be responsible for void nucleation, which resulted in the dimple type fracture surface. Such dimple-ductile fracture is also seen with coarser carbide precipitates, of 1 – 2 μ, at the grain boundary which resulted in the micro-crack in the region. However, during room-temperature fatigue, cracks are reported to cut through γ′ precipitates and propagate along {111} planes, resulting in {111} plane type faceted fracture surface in Ni-base CMSX-4 alloy [61].

2.5 *Deformation of Ordered Phases*

A perfect dislocation splits into the partials, which glide in the lattice to cause plastic deformations. In the case of an *fcc* system deformation takes place on the well known <110>{111} slip systems, where a perfect $\frac{1}{2}\overrightarrow{[110]}$ dislocation moves by splitting into $\frac{1}{6}\overrightarrow{[211]}$ and $\frac{1}{6}\overrightarrow{[12\bar{1}]}$ partials. However, when an ordered phase forms in the matrix, e.g. the formation of γ" and δ in Alloy 625, it requires fulfillment of additional criteria for unhindered movement of the dislocation across the parent lattice and the ordered phase.

Since, a dislocation moves on the close packed planes and on the close packed directions, it is necessary to look into the slip systems in γ" and δ ordered phases those are equivalent to <110>{111} of Alloy 625. In the case of γ", [110] is the close packed direction, while $(1\ \bar{1}\ 2)$ is the close packed plane that has been shown using the ball model in Fig. 8.5. Equivalently, the close packed direction in δ ordered phase is [100] and (010) is the close packed plane that is comparable to [110] and (111) of the parent *fcc*, respectively.

As postulated by Yamaguchi and Umakoshi [62], the perfect dislocations in these ordered phases need to split into four partials in order to restore the lattice. Hence, in order to cause deformation through the motion of dislocation, it is also necessary to look into the orientation relationship between the parent *fcc* Alloy 625 matrix and γ" and δ ordered phases. In the case of γ" and δ in Alloy 625, orientation relationships are as follows.

For the 3 variants of γ" [50]

Variant A: $(100)_{\gamma''} //(010)_{\gamma}$; $[001]_{\gamma''} //[100]_{\gamma}$

Variant B: $(100)_{\gamma''}$ //$(001)_{\gamma}$; $[001]_{\gamma''}$ //$[010]_{\gamma}$

Variant C: $(100)_{\gamma''}$ //$(100)_{\gamma}$; $[001]_{\gamma''}$ //$[001]_{\gamma}$

And for the 12 variants of δ [50]

Variant 1: $(010)_{\delta}$ //$(111)_{\gamma}$; $[100]_{\delta}$ //$[110]_{\gamma}$

Variant 2: $(010)_{\delta}$ //$(111)_{\gamma}$; $[100]_{\delta}$ //$[101]_{\gamma}$

Variant 3: $(010)_{\delta}$ //$(111)_{\gamma}$; $[100]_{\delta}$ //$[011]_{\gamma}$

Variant 4: $(010)_{\delta}$ //$(111)_{\gamma}$; $[100]_{\delta}$ //$[110]_{\gamma}$

Variant 5: $(010)_{\delta}$ //$(111)_{\gamma}$; $[100]_{\delta}$ //$[101]_{\gamma}$

Variant 6: $(010)_{\delta}$ //$(111)_{\gamma}$; $[100]_{\delta}$ //$[011]_{\gamma}$

Variant 7: $(010)_{\delta}$ //$(111)_{\gamma}$; $[100]_{\delta}$ //$[110]_{\gamma}$

Variant 8: $(010)_{\delta}$ //$(111)_{\gamma}$; $[100]_{\delta}$ //$[101]_{\gamma}$

Variant 9: $(010)_{\delta}$ //$(111)_{\gamma}$; $[100]_{\delta}$ //$[011]_{\gamma}$

Variant 10: $(010)_{\delta}$ //$(111)_{\gamma}$; $[100]_{\delta}$ //$[110]_{\gamma}$

Variant 11: $(010)_{\delta}$ //$(111)_{\gamma}$; $[100]_{\delta}$ //$[101]_{\gamma}$

Variant 12: $(010)_{\delta}$ //$(111)_{\gamma}$; $[100]_{\delta}$ //$[011]_{\gamma}$

As discussed in the literature, stacking fault energy governs the dissociation and movement of the partials [62,63]. Hence, it is also necessary to look into the stacking fault energy of parent Alloy 625 and of relevant ordered phases, which form due to high temperature exposure.

To apprehend the deformation process of the parent matrix with the ordered phases, it is important to look into the coherence strain that comes from the lattice mismatch between the parent and the second phase and grow with the growth of the ordered phases. Hence, apart from the aforementioned three necessary conditions of deformation in this sub-*section*, it is also necessary to look into the lattice parameters of the parent Alloy 625 and γ" and δ ordered phases in order to estimate the coherency strain.

2.6 In- Service Changes and the Procedure for Recovery

During service Alloy 625 group of alloys undergo microstructural changes, which include formation of a large number of ordered phases, as discussed earlier, causing degradation of their mechanical properties [19,21,22,23,64]. The service-exposed components made of these alloys showing unacceptably low mechanical properties are usually recovered through rejuvenation heat treatments. The rejuvenation treatment essentially comprises holding the alloy isothermally at solutionizing temperature between 1373 K and 1423 K to dissolve all the ordered phases except primary carbides. Once solutionized, these alloys also recover their mechanical properties akin to the virgin ones.

However, it has been noticed in the context of Alloy 718 that grain refinement occurred during the rejuvenation heat treatments. The transformation is not seen to be influenced by any phase transformation but has rather occurred "statically" [64]. Thereby, it has been shown with the help of orientation imaging microscopy that the grain-refinement and recrystallization have been an inhomogeneous process. The conclusion of the work has been that the as-received material in this case retained some small grains since the time of hot deformation that involved dynamic recrystallization. During high temperature exposure, intragranular δ phase precipitation hinders the recrystallization of the small deformed areas in the material. However, upon dissolution of this pinning δ phase the material is postulated to have undergone grain refinement owing to the stored energy in the small deformed grains, which are retained in the as received Alloy 718 component. In contrary to intragranular δ, it has been noticed that bar shaped δ did not stop recrystallization process. It has been further noticed that Σ3 boundaries have been quite mobile and dominated in the recrystallization process.

2.7 Application of Alloy 625

Alloy 625 has been developed as a Ni-Cr alloy solid solution strengthened by its content of molybdenum and niobium. It has been established soon enough that Alloy 625 is suitable in two main areas of application i.e., resistance to aqueous corrosion at ambient to slightly elevated temperatures and for high strength and resistance to creep, rupture, and corrosion at high temperatures. This has resulted in the definition of two grades of the alloy that ASTM designated as grades 1 and 2. Grade 1 material is described as "annealed" and is intended for service up to 866 K (1100 °F/ 593 °C). These products are normally annealed in the range of 1144 K to 1255 K (1600 to 1800 °F / 871 to 982 °C) and exhibit a fine grain structure. Grade 2 products are described as "solution annealed" and are intended for service at temperatures over 866 K (1100 °F/ 593 °C) when resistance to creep and rupture is needed. While ASTM specifications require a minimum annealing temperature of 1366 K (2000 °F/ 1093 °C), products are normally annealed between 1394 K and 1450 K (2050 and 2150 °F/ 1211 and 1177 °C), hence, exhibiting a coarse grain structure. This enhances the alloy's resistance to creep and rupture at high operating temperatures.

Alloy 625 also offers properties, which make the alloy attractive for service at elevated temperatures. Chromium is the key element in giving a Ni-base alloy its resistance to corrosive attack at elevated temperatures (e.g, oxidation, carburization, and sulfidation). Molybdenum and niobium are especially effective in their role of strengthening an alloy at elevated temperatures. Thus, Alloy 625 (grade 2) offers a desirable combination of strength and creep and rupture resistance along with resistance to corrosive attack at service temperatures up to about 2100 °F (1140 °C).

Alloy 625 is one of the few alloys manufactured today for which the ASME Boiler and Pressure Vessel Code has defined allowable design stresses for service up to 1255 K (1800°F/ 982°C).

It is known that chromium imparts resistance to attack from oxidizing acids (e.g, nitric acid) and salts (e.g, ferric and cupric chloride) to Ni-base alloys. It is also known that molybdenum and niobium (and to a lesser extent, chromium) help define an alloy's resistance to attack by reducing acids (e.g, sulfuric and hydrochloric acids). With 22% chromium, 9% molybdenum and 3.5% niobium, Alloy 625 offers excellent resistance to reducing, oxidizing, and mixed media. It also provides particularly good resistance to marine corrosion. Hence, Alloy 625 (grade 1) is widely used for fabrication of shipboard components and associated support hardware.

Welding of austenitic and super-austenitic stainless steels containing Ni-Cr-Mo and Fe-Ni-Cr-Mo experience elemental segregation upon solidification. This results in simultaneous enrichment and depletion of some alloying elements in different parts of the weld structure, which is undesirable from the corrosion point of view. For this reason, welding of these alloys with matching composition welding electrodes are recommended. Alloy 625 welding products are well suited for joining the molybdenum-bearing austenitic stainless steels (e.g, 316, 317, and 904L), the 6% molybdenum, nitrogen-enhanced super-austenitic stainless steels (alloy 25-6MO, AL6XN, 254SMO, etc.), and even the G-alloys. Also, Alloy 625 welding products are used for joining alloys for high temperature service. They obviously are the choice for joining Alloy 625 products for high temperature operation. They have also been widely used for joining other high temperature alloys such as alloys 800H and 800HT, 802, 330, 601, and others similar materials. Alloy 625 welding products are widely used for overlay of alloy steel tubes in coal-fired power boilers and municipal waste incineration waste-to-energy boiler. Alloy 625 welding products are often used for in-situ overlay of boiler tubes. Also, boiler tubes are overlaid with Alloy 625 prior to installation to increase their service life several times that of the unprotected steel tubes subjected to aggressive halide environment.

Alloy 625 welding products are classified by the American Welding Society as ENiCrMo-3 and ERNiCrMo-3. The flux covered welding electrodes are used for shielded metal-arc welding (SMAW) while the bare filler metal can be used for gas metal-arc welding (GMAW), gas tungsten-arc welding (GTAW), and submerged arc welding (SAW). As with the base metal, Alloy 625 welding products are used for applications at cryogenic, ambient, and elevated temperatures. The products' strength and toughness at cryogenic temperatures make the product popular for welding nickel steels (e.g, 3 ½% and 9% nickel grades) for service at sub-zero temperatures.

High tensile, creep, and rupture strength; outstanding fatigue and thermal-fatigue strength; oxidation resistance; and excellent weldability and brazeability are the properties of Alloy 625, which make the alloy a suitable structural material in the aerospace field. It is being used in this area as aircraft ducting systems, engine exhaust systems, thrust-reverser systems, resistance-welded honeycomb structures for housing engine controls, fuel and hydraulic line tubing, spray bars, bellows, turbine shroud rings, and heat-exchanger tubing in environmental control systems. It is also suitable for combustion system transition liners, turbine seals, compressor vanes, and thrust-chamber tubing for rocket motors.

Alloy 625 is an excellent choice for sea-water applications due to freedom from pitting and crevice corrosion, high corrosion-fatigue strength, high tensile strength, and resistance to chloride-ion stress-corrosion cracking. It is used as wire rope for mooring cables, propeller blades for motor patrol gunboats, submarine auxiliary propulsion motors, submarine quick-disconnect fittings, exhaust ducts for Navy utility boats, sheathing for undersea communication cables, submarine transducer controls, and steam-line bellows. Potential applications based on the above mentioned properties include springs, seals, bellows for submerged controls, electrical cable connectors, fasteners, flexure devices, and oceanographic instrument components.

In the nuclear water reactors, Alloy 625 may be used for reactor-core and control-rod components because of its high strength, excellent resistance to uniform corrosion, resistance to stress corrosion cracking and excellent pitting resistance in 533 K to 589 K (500 – 600 °F/ 260 – 316 °C) salt water. Alloy 625 is also being considered in advanced reactor concepts because of its high allowable design strength at elevated temperatures, especially between 922 K to 1033 K (1200 – 1400 °F/ 649 – 760 °C).

Other applications of Alloy 625 in the nuclear field include its use as wrought and centrifugally cast tube forms in the cracker units of ammonia based Heavy Water Plants [19]. Alloy 625 has been found suitable for pot-material for melting borosilicate glass, which is a potential repository material for high level waste [65]. The alloy is also being considered as canister material for the dumping of high-level nuclear waste. Excellent corrosion resistance properties in contrasting corrosive environments in combination with matching microstructural stability up to 573 K are the properties, which make the alloy suitable for the repository application [18,45].

CHAPTER 3

3 Experimental Methodology

In order to establish *structure-property correlation* in Alloy 625 with different precipitated microstructure, a solution quenched (SQ) block of Alloy 625, having 150 mm ×150 mm × 30 mm dimensions was used for fabricating specimens in the present study. Following experimental methodologies were adopted to realize the aforementioned set of objectives.

After machining out the blanks for the tensile specimens, the left-out portions was divided into ten pieces, which were subjected to microstructural study and composition-analysis in order to characterize SQ Alloy 625. Microstructural study was carried out using optical microscope, orientation imaging microscopy (OIM) and electron probe micro-analyzer (EPMA), while composition-analysis was carried out using EPMA. Apart from these, as-received material was subjected to tensile testing and investigation of the fracture surface using scanning electron microscope (SEM).

3.1 Fabrication of Tensile Samples

Threaded tensile specimens, having 28 mm gauge length and 6 mm diameter were machined out from the blanks, as per the dimensional details given in Fig. 3.1. The gauge lengths of the specimens were oriented along the direction of maximum flow in the wrought working operation.

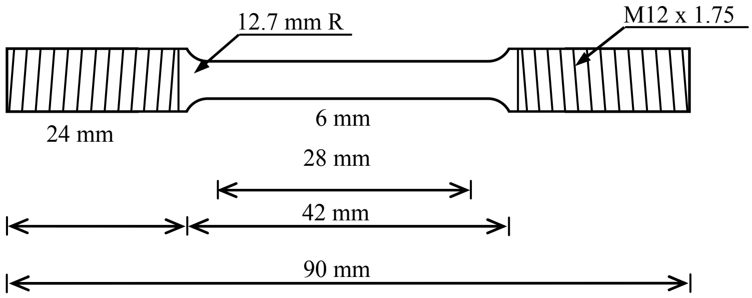

Fig. 3.1: Sketch of a tensile sample showing various dimensions.

3.2 Isothermal Treatment at Three Temperatures for Three Durations

The isothermal treatments on Alloy 625 specimens were decided keeping in mind the kinetics of precipitation of the major ordered phases as was apparent from the time-temperature-transformation (TTT) diagram shown in Fig. 1.1. It could be seen that "*C*" – curves of γ" and δ were having their respective noses at 973 K and 1123 K. Hence, Alloy 625 specimens were isothermally held at 973 K and 1123 K, respectively, for studying the growths of γ" and δ ordered phases.

In the absence of any TTT "*C*" – curve corresponding to $Ni_2(Cr,Mo)$, isothermal treatment at 813 K was based upon the providence of wisdom. As discussed earlier, the composition line of Alloy 625 could be expected to cross the solvus of $Ni_2(Cr,Mo)$ anywhere around 923 K. Although, heating the composition close to the solvus was desirable from the kinetics point of view, the precipitation was expected to be less in quantity. Hence, isothermal holding temperature, 813 K was thought to balance the prominence of $Ni_2(Cr,Mo)$ with that of the kinetics of formation.

Fabricated tensile specimens and specimens for microstructural investigation were isothermally held inside three resistance-heating furnaces at 813 K, 973 K and 1123 K. Aged samples were taken out of the respective furnaces at the intervals of 10 h, 100 h and 1200 h and subsequently quenched. Temperatures of the furnaces were controlled within ± 3 K using proportional-integral-derivative (PID) type loop feedback mechanism controller. Hence, including the as-received *SQ material* and nine other isothermally treated specimens, as shown in Table 3.1, a total of ten varieties of samples were produced for the investigations.

Table 3.1: Schedules for isothermal-treatments

	813 K	**973 K**	**1123 K**
10 h	✓ 813 K – 10 h	✓ 973 K – 10 h	✓ 1123 K – 10 h
100 h	✓ 813 K – 100 h	✓ 973 K – 100 h	✓ 1123 K – 100 h
1200 h	✓ 813 K – 1200 h	✓ 973 K – 1200 h	✓ 1123 K – 1200 h

3.3 Tensile Testing with Data Analysis and Hardness measurement

SQ and isothermally treated tensile specimens were tested until fracture using a screw driven INSTRON universal testing machine at a crosshead speed of 0.5 mm/minute, giving a nominal strain rate of 3.0×10^{-4} s^{-1}. Load vs. displacement data were recorded in an attached computer, and the output was processed for various flow properties of the material, such as, true stress (σ), true strain (ε) and work-hardening rate ($\partial\sigma/\partial\varepsilon$) using Origin Pro 8 SR4 software. The hardness measurements were carried out in an automatic microhardness tester using 50 g load and 30 s dwell time.

3.4 Optical Microscopy

Microstructures of SQ and isothermally treated Alloy 625 sample have been investigated at various length scales. Optical microscopy on all the samples have been carried out using Leica make REICHERT MeF3A and DMI5000M Optical microscope following the grinding, polishing and electro-etching, using saturated oxalic acid solution .

3.5 Scanning Electron Microscopy of Fracture Surface

As depicted in Fig. 5.6 (a), the fractured surfaces of all the broken tensile specimens were separated out from the gauge region using slow speed cutter for studying under SEM. Fracture surfaces from that of a particular isothermal holding temperature but with different holding times were expected to bring out the effect of growth of the ordered phases on the fracture. Viz. study of tensile fracture surfaces of 973 K – 10 h, 973 K – 100 h and 973 K – 1200 h were meant for understanding the effect of the growth of γ'' on the fracture process. Investigation of fracture surfaces were carried out in the Philips Phillips XL30 scanning electron microscope using 25 kV accelerating voltage.

3.6 Transmission Electron Microscopy

In order to view the sample inside the transmission electron microscope, all samples were sectioned using slow speed diamond wheel cutting machine. These cut-samples were less than 1 mm in thickness, which were further thinned down using fine emery paper under the flow of water. The secondary thinning was done in a dual-jet electro-polisher under optimized voltage and current density using 20 % perchloric acid in ethanol, which was maintained within 233 K – 238 K.

Transmission electron microscopy in the present study was intended to deal with two distinct aspects. First aspect was aimed at studying the shape, size and distribution of the ordered phases due to the holding at three different isothermal temperatures. Purpose of the second aspect was to understand the interactions of dislocations with the ordered phases through the study of the deformed tensile-gauge region, as depicted in Fig. 5.6 (a). These studies were carried out using two TEMs, JEOL 200 kV and FEI TITAN 300kV.

3.7 Orientation Imaging Microscopy

Electron back scattered diffraction (EBSD) studies of the electropolished samples were carried out in an orientation imaging microscope, FEI Quanta 200 HV instrument. Electron beam scanning speed was maintained at 0.5 μs^{-1}. Grain size, grain orientation spread (GOS) and grain average misorientation (GAM) were calculated from the EBSD data.

3.8 First-principles Based Modeling

Ab-initio modeling approach was used in order to understand the slip pattern, governing the dislocation precipitate interactions. Spin-polarized, plane-wave based first principles calculations were employed in the frame work of density functional theory within the generalized-gradient-approximation (GGA), parameterized by Perdew-Burke-Ernzerhof (PBE) [66,67] scheme, as implemented in the Vienna ab initio simulation package (VASP 5.2) program [68,69,70]. The spin-polarized, ion-electron interaction was incorporated using projector-augmented-wave (PAW) potentials [71,72] as supplied in the VASP database.

In order to achieve a precision better than 10^{-7} eV per atom in the calculation of total energy, the optimized cutoff for plane wave and kinetic energy were taken to be 1050 eV and 540 eV, respectively, in order to accurately calculate the *small energy differences*. These optimized cutoffs were about 1.5 times the default values in the corresponding PAW potential.

3.8.1 Computational Facility

Computational work in the present study has been carried out in the *Anupam-Adhya* clusters, located in Supercomputing Facility building inside Bhabha Atomic Research

Centre, Mumbai, India. The cluster consists of 576 nodes, which are interconnected using Infiniband and Gigabit Ethernet networks. There are two Quad Core Xeon @ 3.0 GHz processor and 32GB 800MHz DDR2 FBDIMM memory in each node. Anupam Adhya has Infiniband as its primary network to connect all 576 nodes of the system.

Each first principles based calculation job has been posted in the dedicated 8 nodes of the *Adhya* cluster, thereby, distributing the job in 64 cores.

3.9 Instruments for Characterization

Optical microscopes

Leica make REICHERT MeF3A and DMI5000 M

Transmission electron microscope (TEM)

JEOL 200 kV and FEI TITAN 300kV with monochromator and capable of with electron energy loss spectroscopy (EELS), energy dispersive x-ray spectroscopy (EDX) and high angle annular dark-field (HAADF) imaging

Electron probe micro-analyzer (EPMA)

CAMECA SX100, 30 kV

Scanning electron microscope (SEM)

PhillipsXL30, 30 kV

Universal testing machine (UTM)

Screw driven 50 kN INSTRON

Microhardness tester

Future-Tech automatic microhardness tester having load range, 10 g – 1000 g

Orientation imaging microscope (OIM)

FEI Quanta 200 HV instrument

3.9.1 Computational Hardware

Anupam-Adhya supercomputing clusters having Infiniband connected 576 nodes, where each node comprises 2 Nos. Quad Core Xeon @ 3.0 GHz processor and 32GB 800MHz DDR2 FBDIMM memory

3.9.2 Software for Calculations and Data Processing

Origin Pro 8 SR 4

Vienna ab-initio simulation package version 5.2

CHAPTER 4

4 Microstructural Characterization of Alloy 625

4.1 Introduction

It can be seen in the literature that the ductile matrix of solid-solution Alloy 625 produces quasi-brittle fracture at room-temperature after typical high-temperatures exposures [19,21]. Although, occurrences of the ordered phases are known from the TTT diagrams and from a few microstructural studies [20,49], understanding the evolution of microstructures, including that of the coincidence site lattice boundaries and the growth of the ordered phases at high temperature, needs to be substantiated experimentally. Hence, SQ and isothermally treated samples are subjected to microstructural characterization to comprehend the formation and growth of the ordered phases and to understand the changes in the boundary and grain structure, which influence the properties of the alloy. Microstructural study of Alloy 625 would also enable the correlation of the same with its mechanical behavior in the later chapters.

In order to investigate the microstructures at various length scales, SQ and isothermally treated Alloy 625 samples have been subjected to optical microscopy, transmission electron microscopy (TEM) and orientation imaging microscopy (OIM). These are expected to reveal the size, shape and orientation of the ordered phases and the growth of the intermetallics, thereby. Electron probe micro-analyzer (EPMA) has also been used to see the distribution of major alloying elements in the microstructure and to analyze the composition of SQ Alloy 625.

4.2 Results

4.2.1 Characterization of as-received SQ Alloy 625 using EPMA

Back scattered electron (BSE – Z) image, for obtaining 'height' contrast along Z-direction from SQ, is shown in Fig. 4.1. Although, the overall microstructure is clean and consists of annealed austenite grains, occasionally some primary-carbide particles with sharp edges and corners, as seen in Fig. 4.1, are observed there. A thousand-point x-ray line scan of a carbide particle as indicated on Fig. 4.1, has been carried out along the AB-line (from 'A' to 'B') to detect the carbide formers.

Fig. 4.1: X-ray line scan from 'A' to 'B' on Primary carbide particles in Alloy 625 as observed under EPMA using back scattered electron, especially to give surface topology (hence giving clarity in Z-dimension).

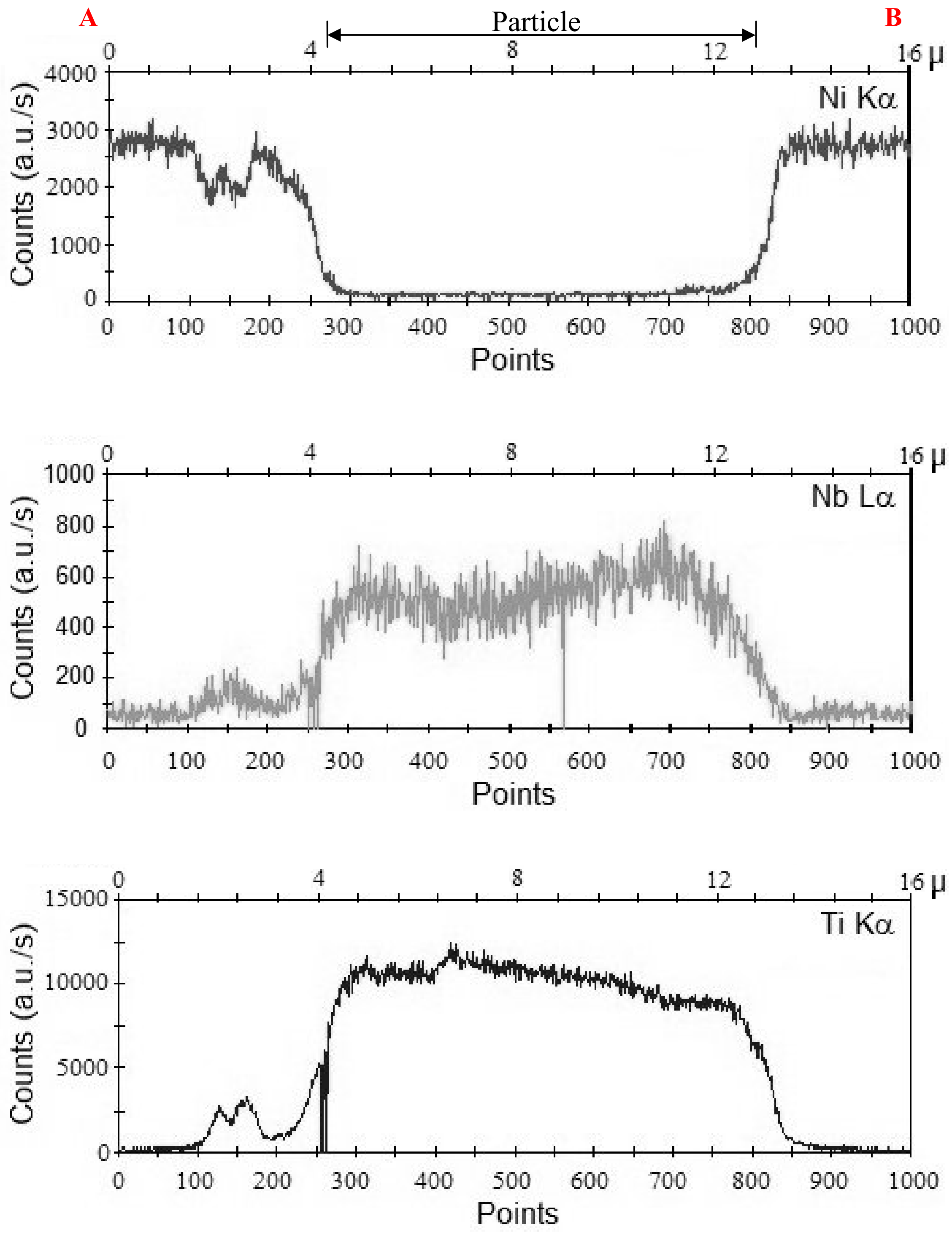

Fig. 4.2: Ni Kα, Ti Kα and Nb Lα x-ray intensities in counts per second across scanned AB line, as shown on Fig. 4.1.

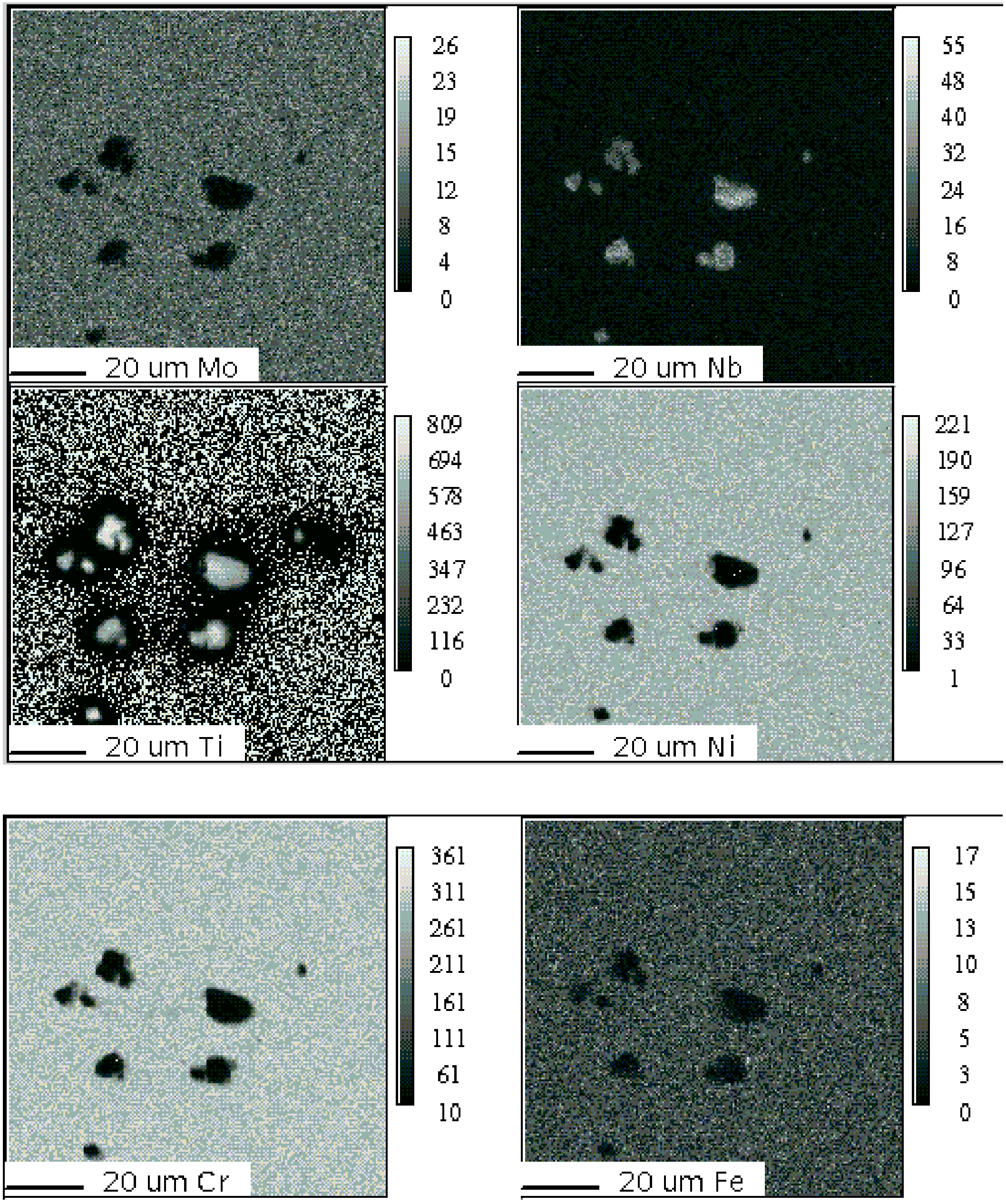

Fig. 4.3: Presence of Mo, Nb, Ti, Ni, Cr and Fe within and around the primary carbide is shown using x-ray mapping under EPMA.

Ni-Kα, Nb-Lα and Ti-Kα x-ray intensity line-profiles, obtained along the line AB across the carbide have been given in Fig. 4.2. These profiles clearly show that the carbide is rich in Nb, Ti and devoid of Ni. The gradual change in the x-ray line intensity over a length of ~ 1 µm is likely to be due to the probe-size of the EPMA, which is 1 µm in CAMECA SX 100. However, wider slopes of the line profiles corresponding to Nb and Ti in Fig. 4.2 indicate diffusion of these elements across the interface, which is apparently very less in this case.

X-ray elemental mapping in Fig. 4.3 shows elemental distributions of major alloying elements, viz. Ni, Cr, Mo, Nb, Ti and Fe, in different areas on the region shown in Fig. 4.1. As can be expected, x-ray area mapping of Nb and Ti also confirms the enrichment of these elements in the carbides. Apart from this, absence of Cr, Mo and Fe, which are usually found in secondary carbides, are also confirmed through the area profiles. It has been noticed that the regions, just outside the primary carbides, are to some extent depleted in Ti.

Table 4.1: Eight elements, obtained using WDX of EPMA in relative atom % and weight % is given below. Nominal composition of Alloy 625 in weight % is given in the last row for comparison.

	Ni	**Cr**	**Mo**	**Nb**	**Fe**	**Co**	**Ti**	**Si**
At% (EPMA)	**63.45**	**25.87**	**5.9**	**2.95**	**1.4**	**0.65**	**0.1**	**0.3**
Corresponding Wt%	**61.67**	**22.28**	**9.37**	**4.54**	**1.29**	**0.63**	**0.08**	**0.14**
Wt% (nominal)	~62	20-23	8-10	3.15-5.15	5.0	1.0	0.4	0.5

Eight elements, comprising more than 99 (wt)% of total elements present in Alloy 625 have been analyzed using wavelength dispersive x-ray spectrometer (WDS) fitted in the EPMA and are given in Table 4.1. When converted to "weight %" they conform to nominal composition of Alloy 625.

4.2.2 Microstructures of solution-quenched and Isothermally Treated Alloy 625

Optical and transmission electron micrographs from SQ and isothermally treated Alloy 625 specimens are given in this *section*. Among that of aforementioned ten varieties of isothermal history, in most of the cases, most representative micrographs have been presented below. In a few cases, more than one micrographs have been presented to support the observation.

4.2.2.1 Optical Microscopy

SQ sample in Fig. 4.4 (a) shows 125 – 150 μ equiaxed grains having annealing twins. No significant changes in the optical microstructures, as can be seen in Fig. 4.4 (b) – (d) are seen as a result of isothermal holding at 813 K. Micrographs in Fig. 4.4 (e) – (g) show changes in the grain structure with the increase in the duration of isothermal holding. Evolution of δ-Ni$_3$Nb with the duration of holding is shown in micrographs Fig. 4.4 (h) – (j).

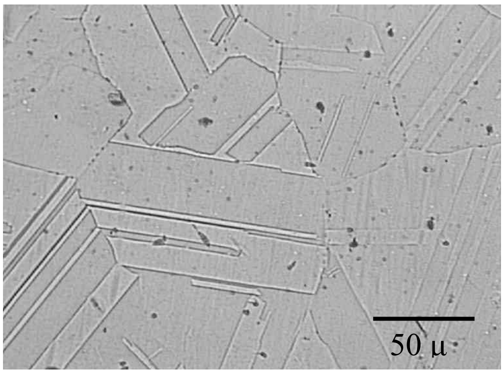

a) As received Alloy 625

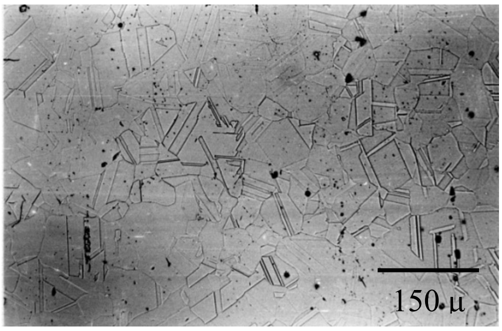

b) 813 K 10 h

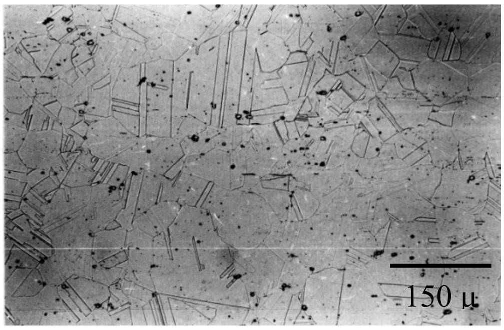

c) 813 K 100 h

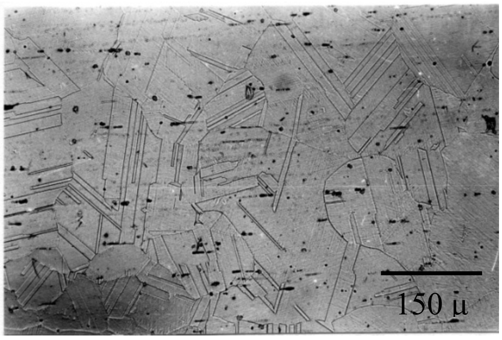

d) 813 K 1200 h

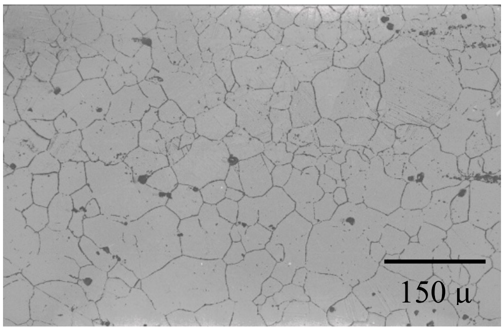

e) 973 K 10 h

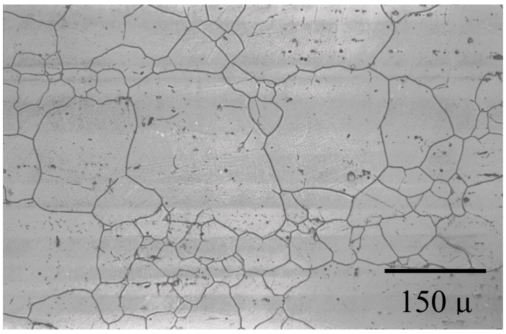

f) 973 K 100 h

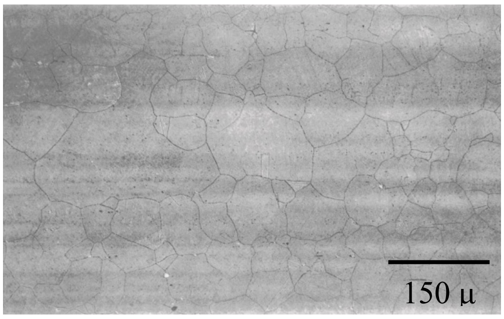

g) **973 K 1200 h**

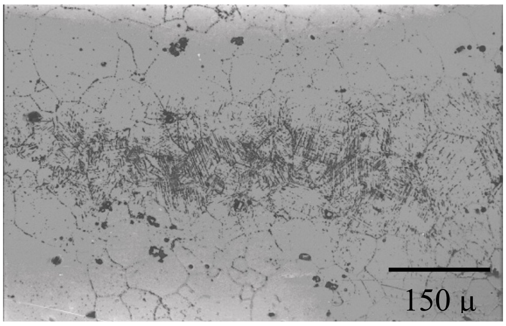

h) **1123 K 10 h**

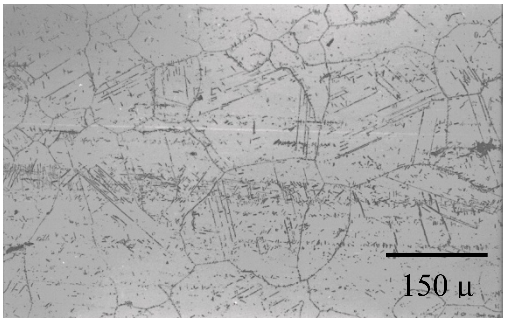

i) **1123 K 100 h**

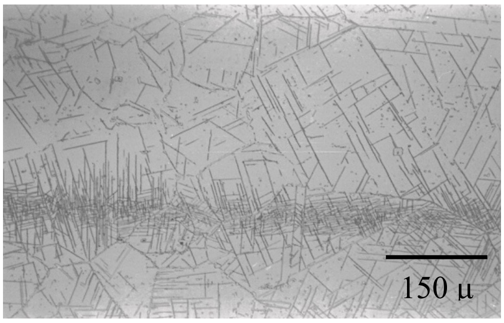

j) **1123 K 1200 h**

Fig. 4.4: Optical microstructures of Alloy 625: solution-quenched and isothermally treated samples.

4.2.2.2 Transmission Electron Microscopy

Transmission electron micrographs provided in the following subsections are based on isothermal holding temperatures. The micrographs have brought out the effect of duration of holding on the growth of the ordered phases and the change in the microstructure, such as, evolution of geometrically necessary dislocation.

Isothermally Treated at 813 K

Transmission electron micrograph recorded from 813 K – 100 h sample is shown in Fig. 4.5 (a). Micrographs from 813 K – 1200 h sample are shown in Fig. 4.5 (c) & (d). Selected area diffraction (SAD) patterns recorded from the regions of Fig. 4.5 (a) and Fig. 4.5 (c) are presented in Fig. 4.5 (b) and (e), respectively. In Fig. 4.5 (b), diffused intensities can be observed near transmitted beam and are schematically shown in the inset by dots and circle. The crystallographic d-spacing of the eight diffused spots are about 3.25Å, which correspond to (½ 1 0) of γ''. The d-spacing for the diffused intensities shown by the circle is 2.45Å, which correspond to (⅔ $^4/_3$ 0) of Ni_2(Cr,Mo). It appears that the very low intensity diffracted beams, resulting from <⅔ ⅔ 0> of Ni_2(Cr,Mo) cannot be deciphered in the [001] SAD pattern of Fig. 4.5 (a) due to their proximity to transmitted beam. Indexing of spots belonging to parent γ, ordered γ'' and Ni_2(Cr,Mo) in the [001] SAD patterns of Fig. 4.5 (b) are represented by "X", "o" and "■", respectively, in the Fig. 4.5 (f). Apart from these, following the precipitation of the ordered phases, dislocations and microtwins are seen in 813 K – 1200 h.

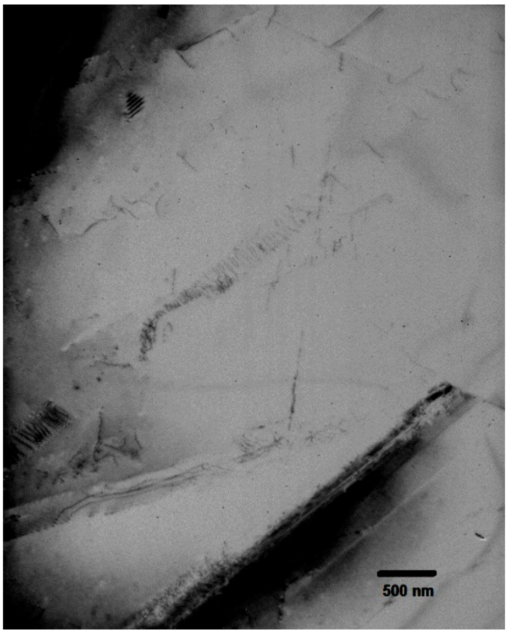

a) 813 K – 100 h

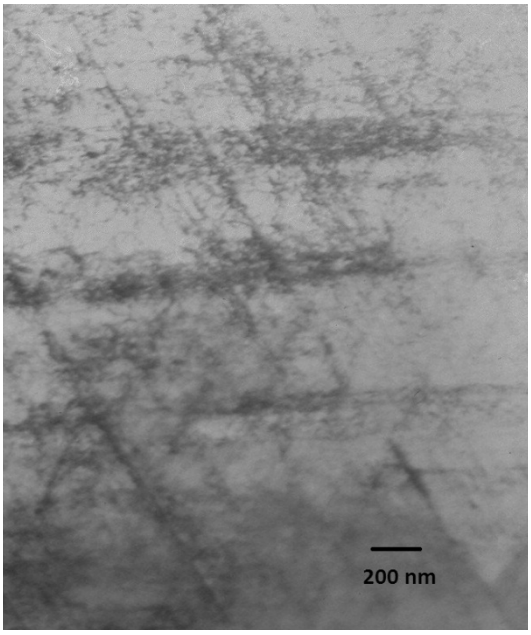

c) 813 K – 1200 h

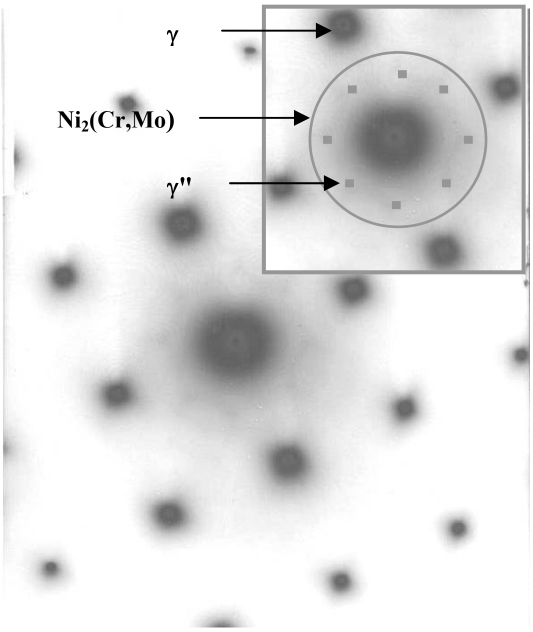

b) 813 K – 100 h

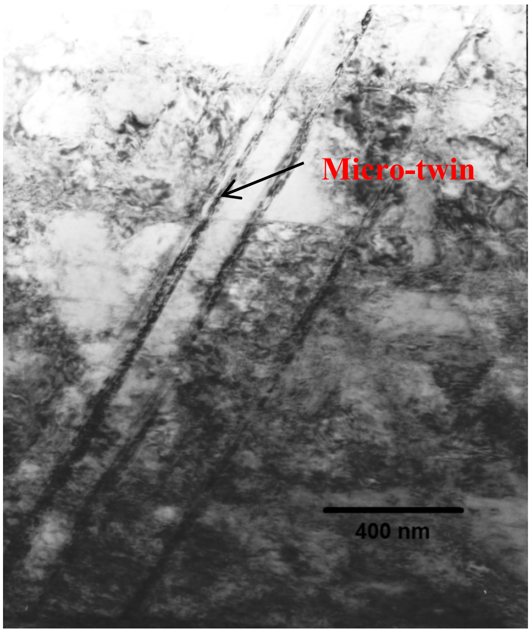

d) 813 K – 1200 h

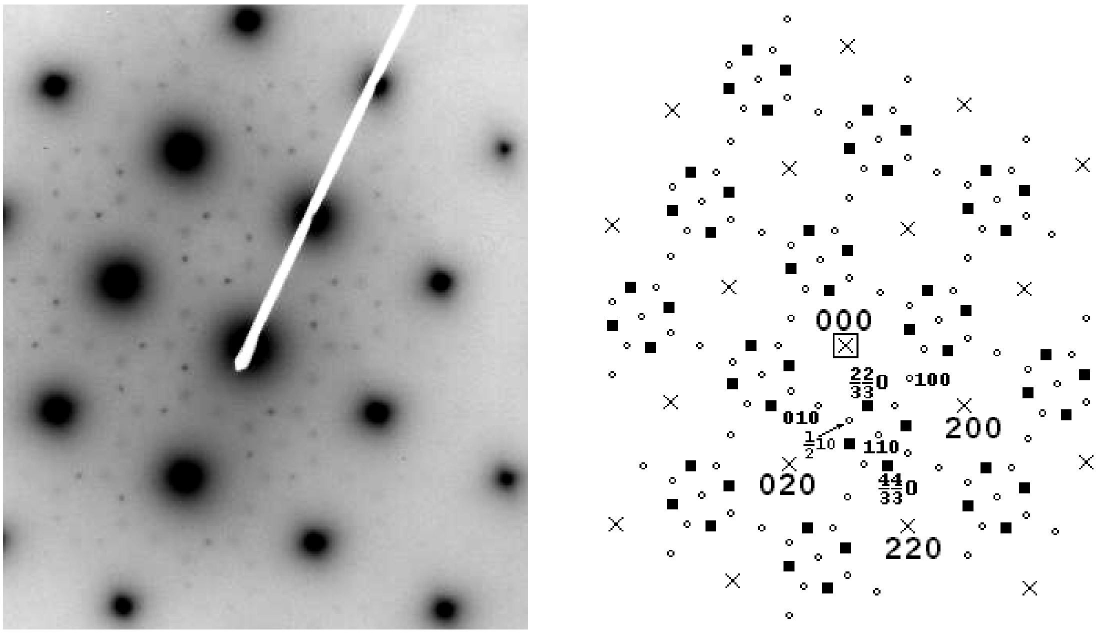

e) 813 K – 1200 h
f) 813 K – 1200 h

Fig. 4.5: (a) – (f) show transmission electron micrographs from 813 K – 100 h and 1200 h samples. (a) Planar array of dislocations are seen after 100 h of aging at 813 K. (b) [0 0 1] SAD pattern from 813 K – 100 h shows diffused intensities from Ni_2(Cr,Mo), which has been highlighted in the inset. (c) Precipitated region showing high dislocation densities on {111} planes. (d) Thin twinned regions in 813 K – 1200 h. (e) [001] SAD pattern from the region of (c); (f) γ, γ″ and Ni_2(Cr,Mo) are represented by "×", "o" and "■", respectively.

Isothermally Treated at 973 K

Fine precipitates of γ″ have been observed in the encircled region of the micrograph in Fig. 4.6 (a), which is taken from 973 K – 10 h sample. Fig. 4.6 (b) shows the geometrically necessary dislocations (GND's), which are associated with the precipitation of γ″. Micrographs in Fig. 4.6 (c) and (d) not only have brought out the growth of γ″ after 100 h of holding in 973 K but it has also revealed its typical orientation, array and shape.

Information on different variants of γ'' ordered phase and also on shape and size of the phase has been obtained from 973 K – 1200 h sample. Fig. 4.6 (e) shows the bright field image of a region, where existence of three variants of γ'', having orientation along [100], [010] and [001] lattice axes has been shown in the dark field images of Fig. 4.6 (f), (g) and (h), respectively. Three perpendicular views confirm that the second phase is lens shaped. Particularly, the view along [001] indicates the encircled γ'' lens is of elliptical geometry, which has, approximately, 120 nm short-axis and 150 nm long-axis.

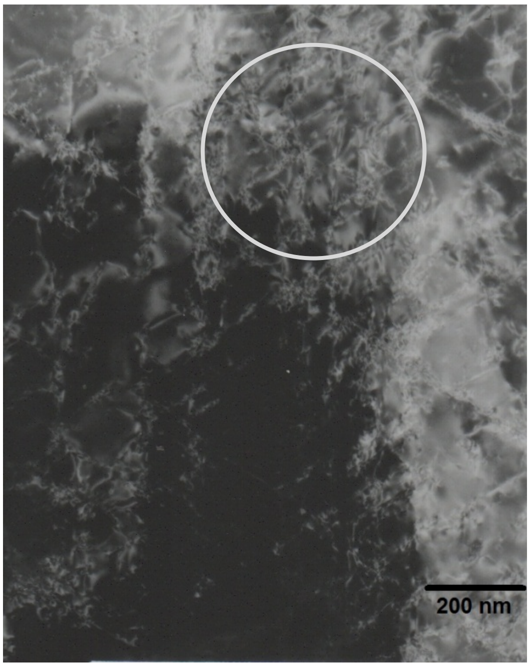

a) 973 K – 10 h

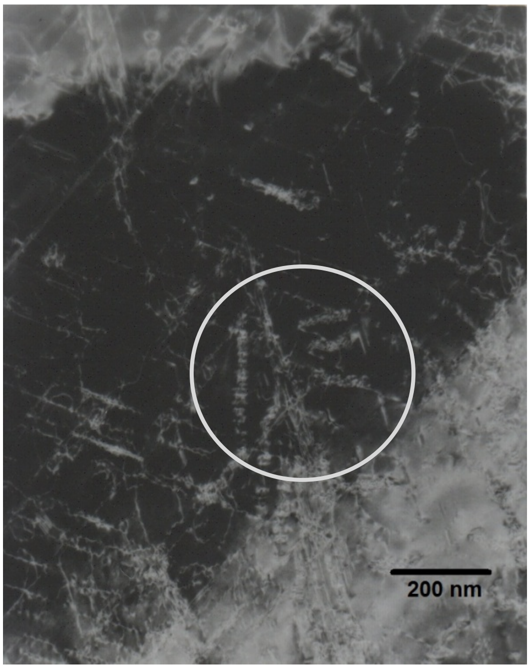

c) 973 K – 100 h

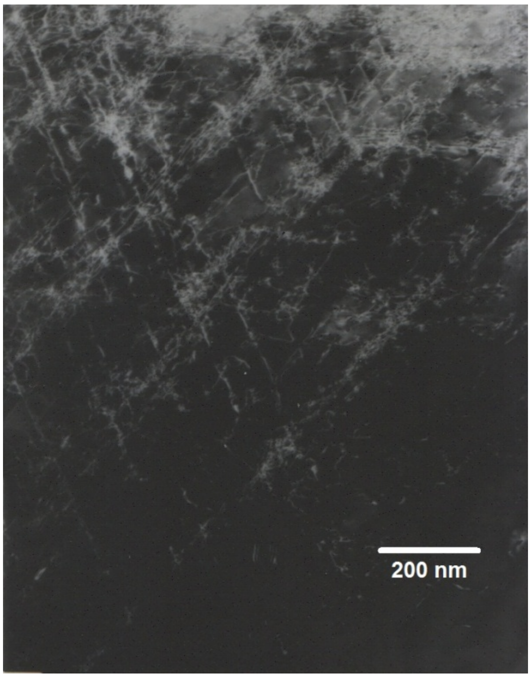

b) 973 K – 10 h

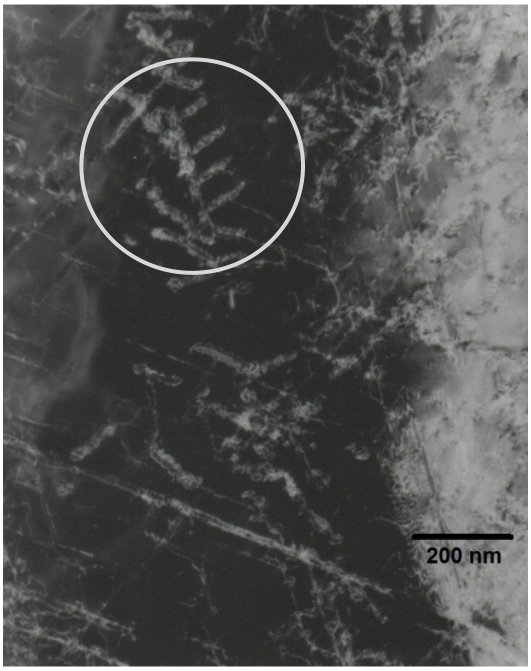

d) 973 K – 100 h

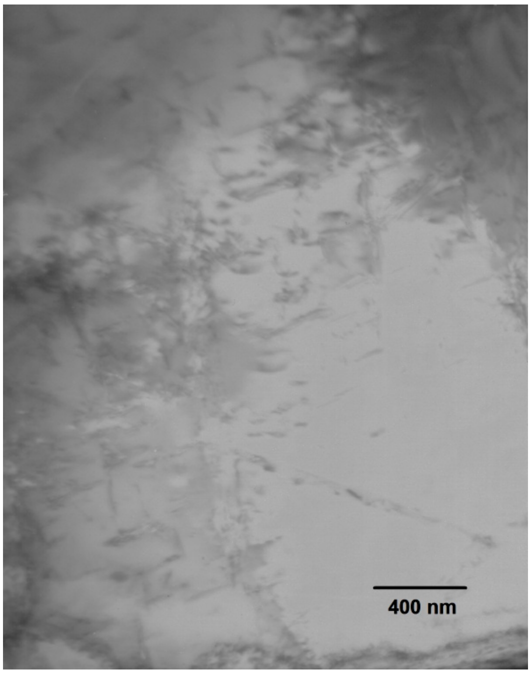

e) 973 K – 1200 h

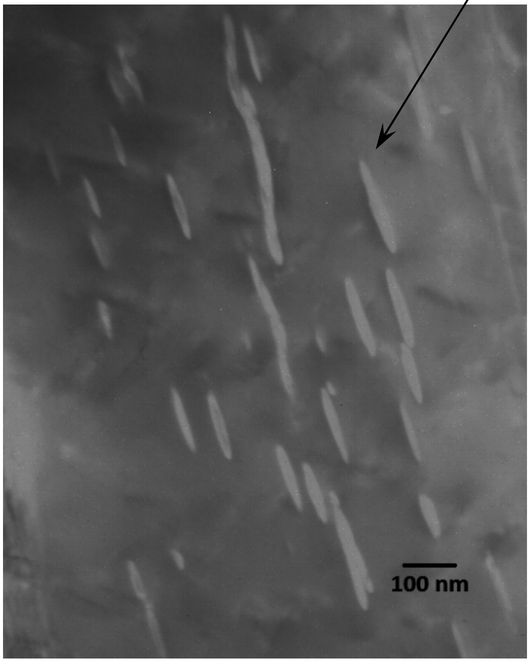

f) 973 K – 1200 h

γ″-Ni_3Nb

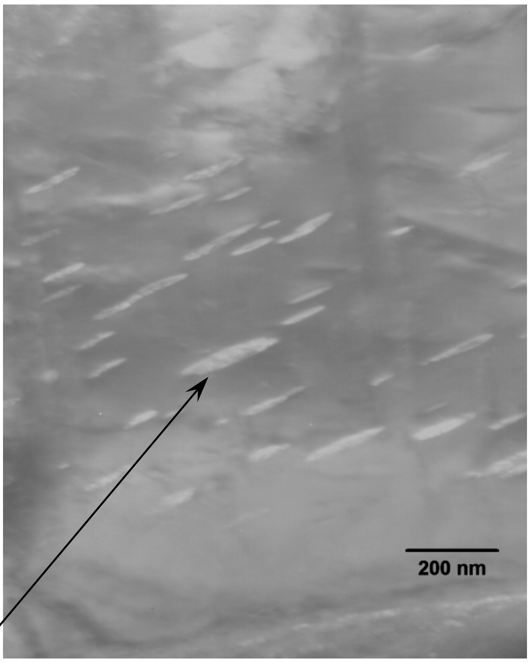

g) 973 K – 1200 h

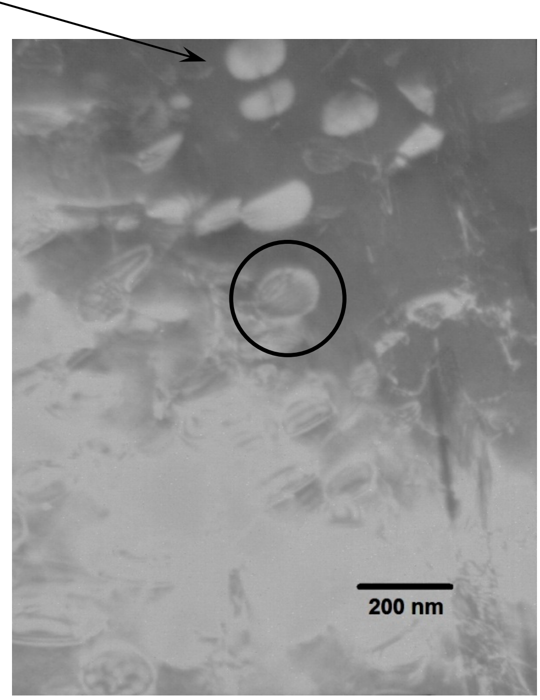

h) 973 K – 1200 h

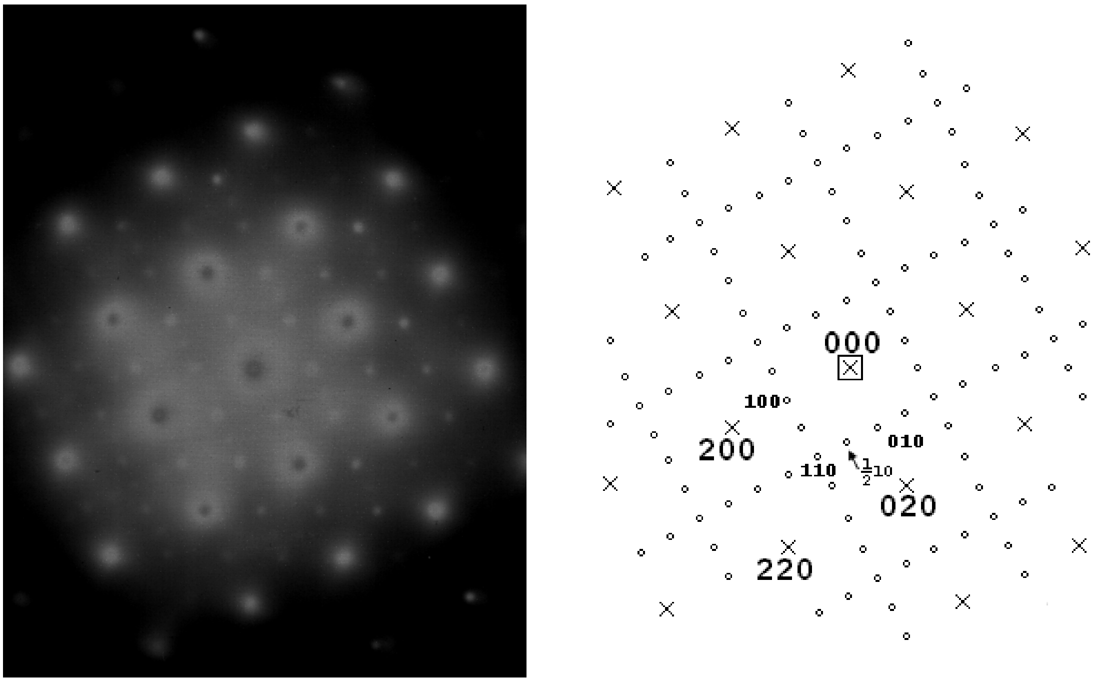

i) 973 K – 1200 h j) 973 K – 1200 h

Fig. 4.6: (a) – (j) show transmission electron micrographs from samples aged at 973 K for 10h, 100 h and 1200 h. (a) and (b) Planar arrays of dislocations are seen after 10 h of aging. (c) and (d) Array of precipitations with surrounded dislocations are seen after 100 h. (e) – (h) Dark field images showing different variants of γ'' in 973 K – 1200 h sample. Circled region in (h) clearly shows the shape and size of the ordered phase. (i) [0 0 1] SAD pattern from the region of (f) is shown in (i), and the indexing of the same is shown in (j). γ and γ'' are represented by "×" and "o" respectively.

Isothermally Treated at 1123 K

High-angle annular dark-field (HAADF) image of straight laths of δ phases, oriented in nine different directions has been recorded from 1123 K – 1200 h sample and shown in Fig. 4.7 (a). As shown in Fig. 4.7 (b), typical thickness values of laths are seen to be in the range of 100 ~ 200 nm. Analysis of energy dispersive X-ray spectrums (EDX) across the Ni_3Nb-δ phase in Fig. 4.7 (b) is given in Fig. 4.8. Dotted-lines are drawn across Fig. 4.8 (a) and (b) to show Full-Width at Half-Maxima (FWHM). While FWHM of Nb-Lα line-profile matches with the thickness of Ni_3Nb-δ phase in Fig. 4.7 (b), FWHM of Ni-Kα line-profile is seen to be little higher than that. In the case of Ni-Kα line, width of the peak has been observed due to the presence of Ni in both the phases (Ni_3Nb-δ phase and matrix phase) in high concentration. Stoichiometry of Ni and Nb in the ordered phase has been analyzed to be in the ratio of 3:1.

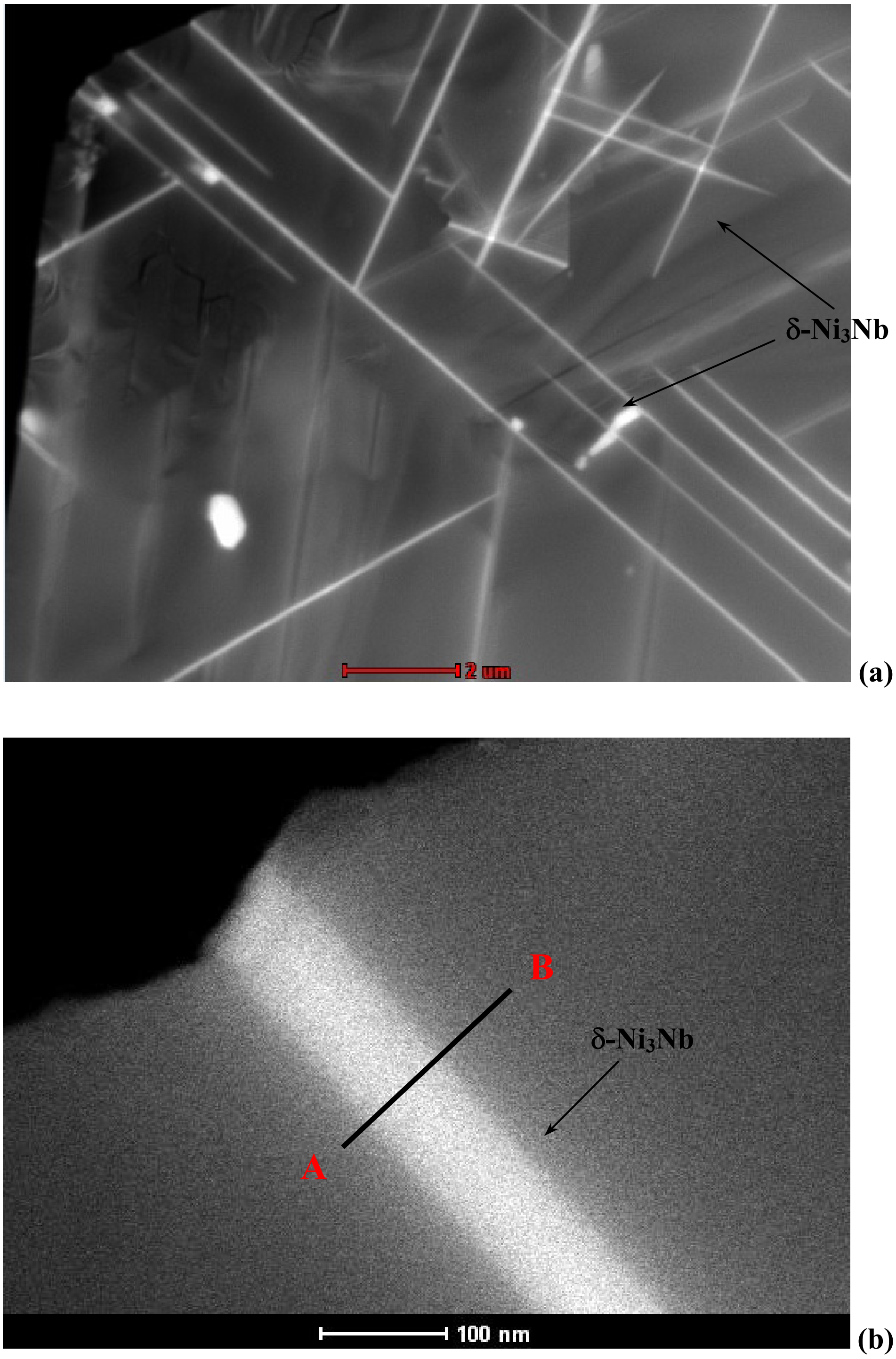

Fig. 4.7: HAADF – Scanning Transmission Electron micrographs at different magnifications from samples aged at 1123 K for 1200 h have been shown in (a) and (b). EDX scan along AB path is given in Fig. 4.8.

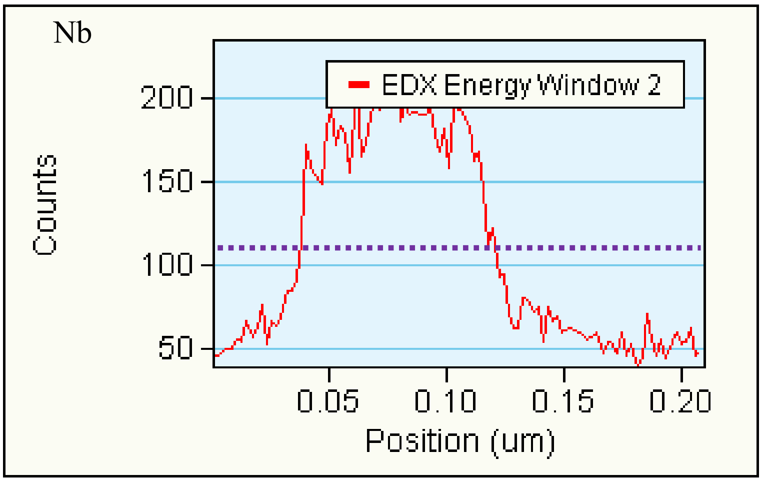

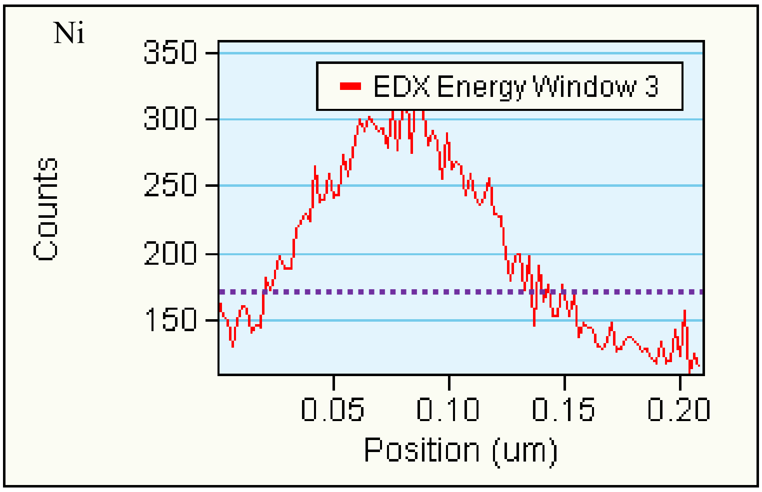

Fig. 4.8: Energy dispersive X-ray spectrums across the Ni_3Nb-δ phase showing distribution of Ni (Ni-K) and Nb (Nb-L).

High resolution transmission electron micrograph from 1123 K – 1200 h sample is shown in Fig. 4.9. The plane spacing and elemental mapping analyzed from the micrograph in Fig. 4.9 are shown in Fig. 4.10. Analysis of intensity spectrums at two places reveals two plane spacing, 0.245 nm and 0.278 nm. In order to understand the reason for the variation in lattice parameters, same region has been re-examined under STEM-HAADF mode. The inset in the Fig. 4.10 shows elemental map of Nb (in blue dot) of the region superimposed on the image. As has been noticed from the inset of

Fig. 4.10, there are regions where Nb atoms appear to get segregated in the matrix phase.

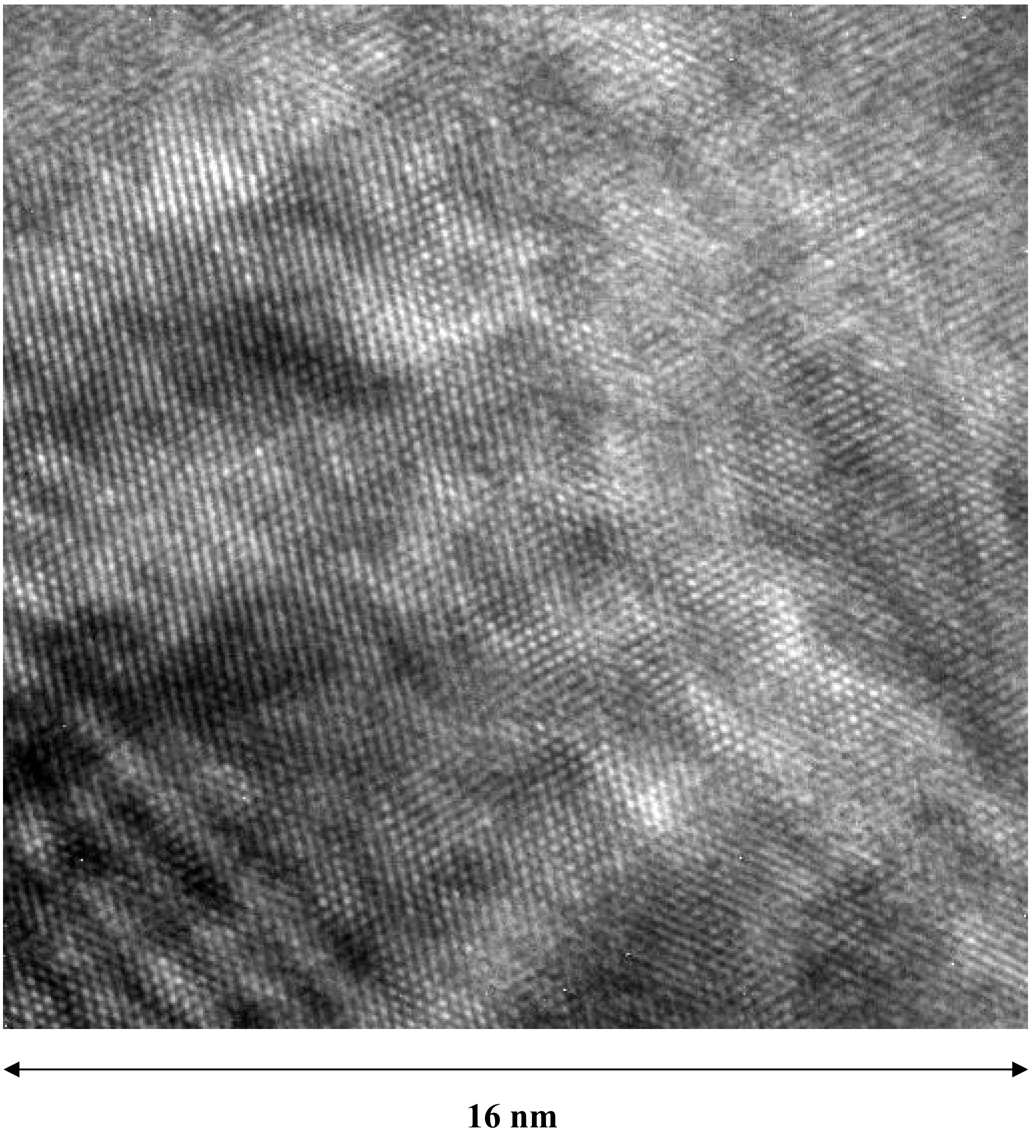

Fig. 4.9: High resolution transmission electron micrograph from 1123 K – 1200 h sample.

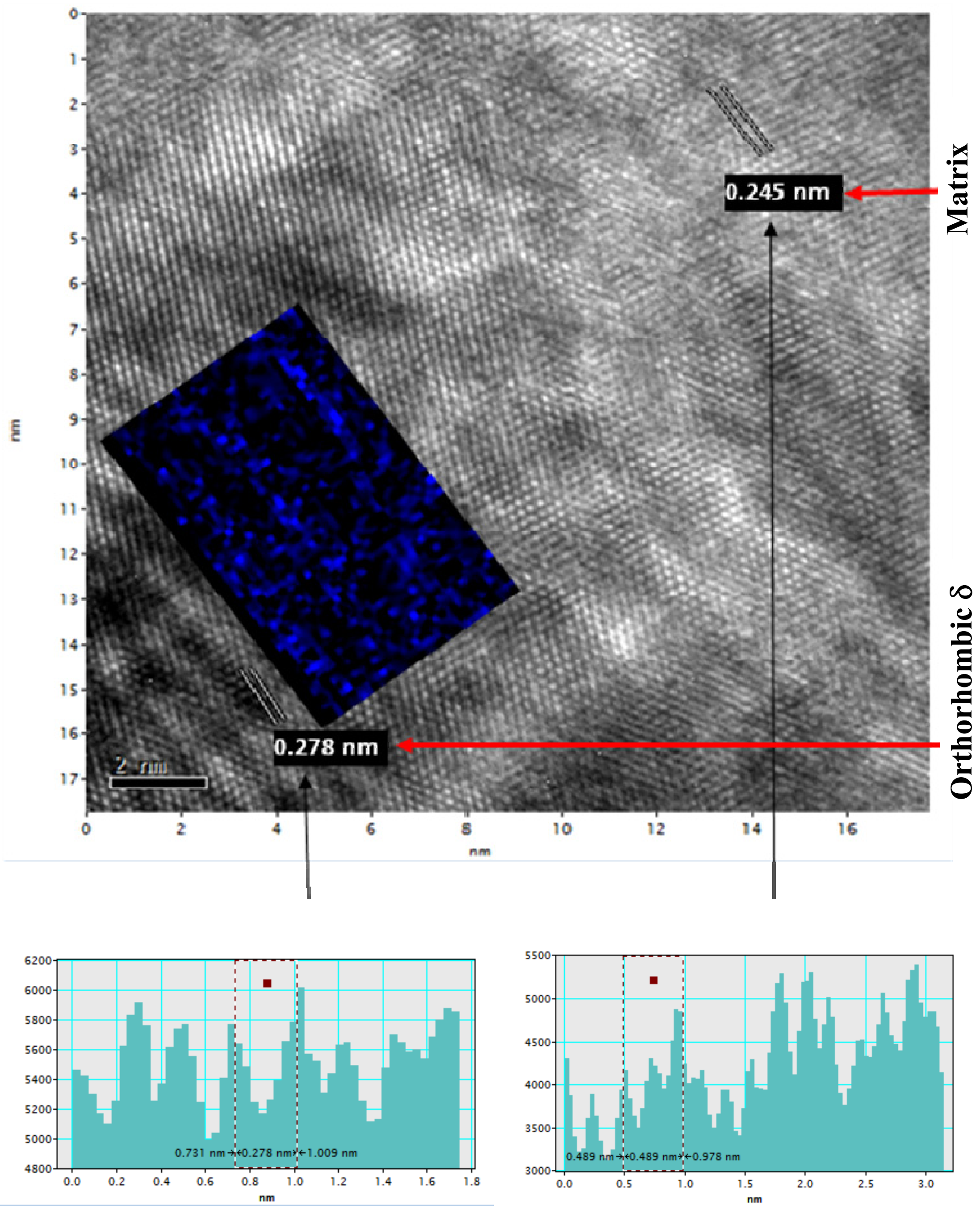

Fig. 4.10: High resolution transmission electron micrograph from 1123 K – 1200 h sample and the plane spacing analyzed from the micrographs are shown above. The inset in the figure shows elemental map of Nb of the region superimposed on the image.

4.2.2.3 Orientation Imaging Microscopy

Solution-quenched Alloy 625

Based on electron backscatter diffraction (EBSD) map, orientation of grains in SQ Alloy 625 is given in Fig. 4.11 (a). Grain size distribution from this has been given in Fig. 4.11 (b) and the average EBSD grain size measured is found to be ~50 μm. Grain Average Neighbor Misorientation (GANM) distribution of SQ Alloy 625 is shown in Fig. 4.12. Calculation has revealed that ~80% of the neighbors remain within 0.5^{o} misorientation, while ~99% remain within 4.5^{o} orientation.

Fig. 4.13 shows that SQ Alloy 625 contains about 63% sigma (Σ) 3 coincident site lattice (CSL) boundaries. However, scanning of CSL boundaries of SQ Alloy 625 from $\Sigma3$ to $\Sigma13$ up to 8.5^{o} of deviation shows that number fraction of $\Sigma1$ boundary is 0.298 – 0.25 and the same for $\Sigma3$ boundary is 0.477 – 0.53. Apart from these, average length and number fraction of coherent 60^{o} (111) boundary have been measured to be 0.16 and 0.095, respectively. Fraction of various sigma boundaries and coherent (111) boundaries due to isothermal holding of SQ Alloy 625 at various temperatures are given in Table 4.2 with the aforementioned results from SQ material.

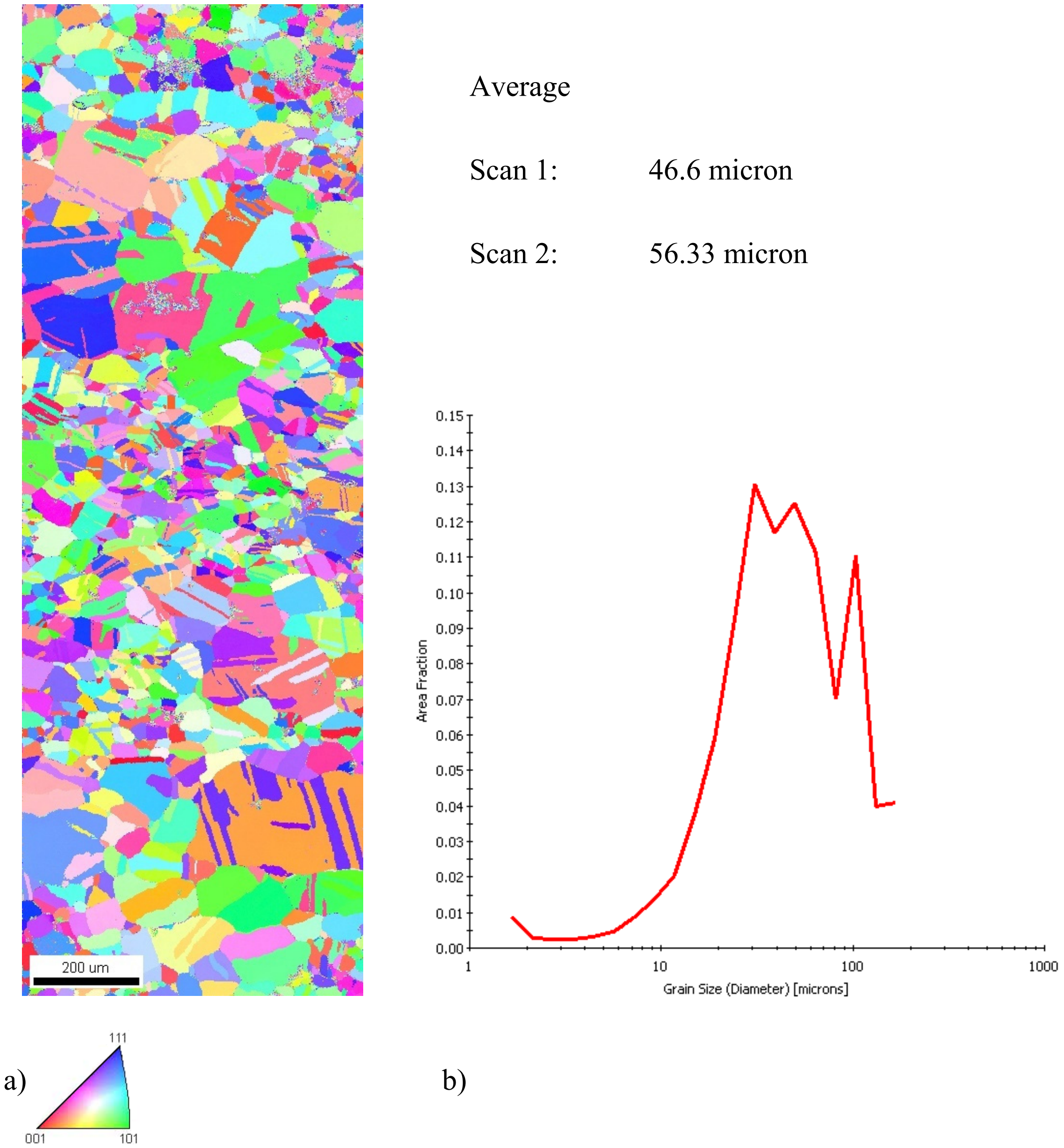

Average

Scan 1: 46.6 micron

Scan 2: 56.33 micron

a)

b)

Fig. 4.11: a) EBSD images showing the grain orientation in SQ Alloy 625. b) Grain size distribution and the average grain size measured from the EBSD map.

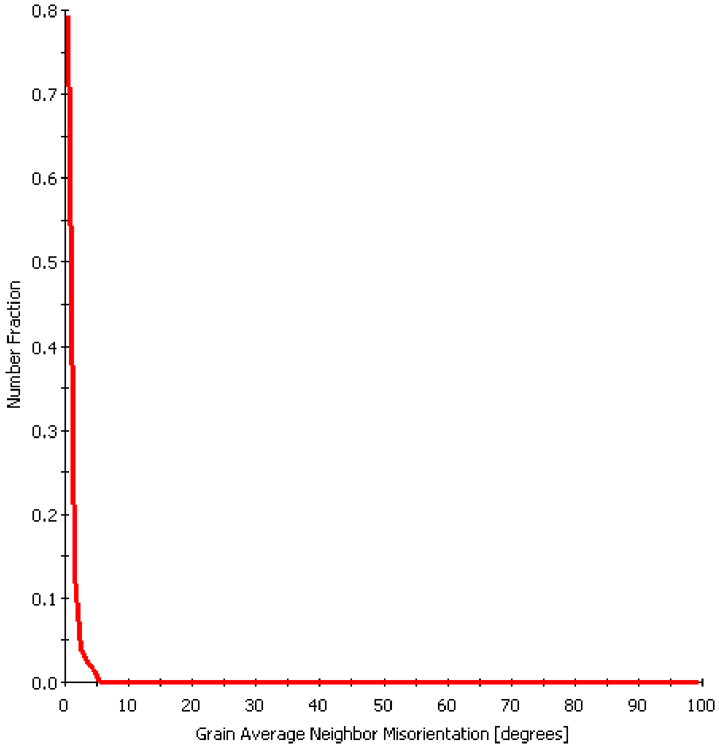

Fig. 4.12: Grain Average Neighbor Misorientation distribution of SQ Alloy 625 showing ~80% within 0.5^o orientation, while ~99% within 4.5^o orientation.

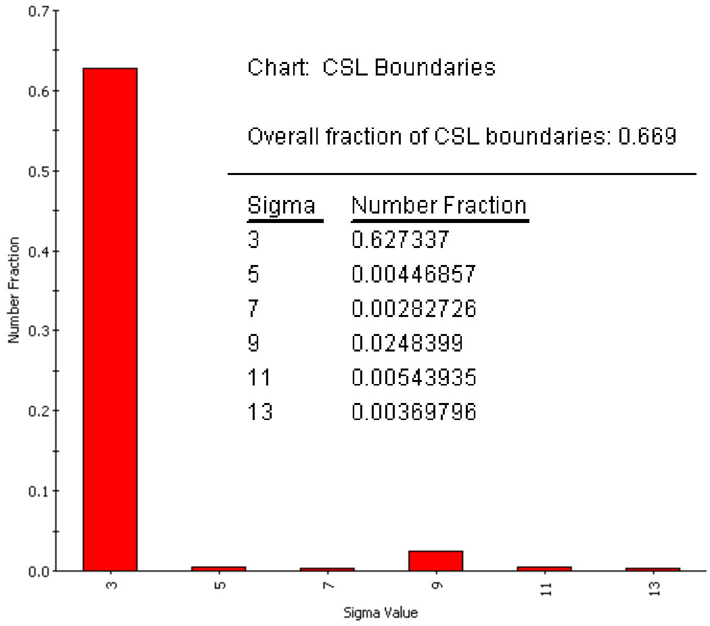
Chart: CSL Boundaries

Overall fraction of CSL boundaries: 0.669

Sigma	Number Fraction
3	0.627337
5	0.00446857
7	0.00282726
9	0.0248399
11	0.00543935
13	0.00369796

Fig. 4.13: ~63% out of ~67% of CSL boundaries scanned are seen to be Σ3 boundry.

Table 4.2: Fraction of various sigma boundaries and coherent (111) boundaries due to aging at various temperatures are given below.

	Duration of isothermal holding		
Temperature	10 h	100 h	1200 h
Sigma 1 boundary (fraction) – SQ: 0.25 – 0.30			
813 K	0.32	0.14	0.48
973 K	0.39	0.51	0.70
1123 K	0.64	0.05	0.08
Sigma 3 boundary (fraction) – SQ: 0.48 – 0.53			
813 K	0.29	0.56	0.28
973 K	0.35	0.29	0.18
1123 K	0.20	0.34	0.52
Sigma 1 + Sigma 3 – SQ = 0.78			
813 K	0.61	0.70	0.76
973 K	0.74	0.80	0.88
1123 K	0.84	0.39	0.60
Grain size (fraction) – SQ: ~50 μ			
813 K	24.91 μ	50.23 μ	41.16 μ
973 K	46.28 μ	51.93 μ	70.63 μ

1123 K	68.27 μ	42.97 μ	67.2 μ
Coherent 60° (111) (fraction) – SQ: Avg. Length Fraction – 0.160 :Numerical Fraction – 0.095 = 1.68			
813 K	0.104:0.061= 1.70	0.138:0.075= 1.84	0.147:0.082= 1.80
973 K	0.140:0.080= 1.75	0.179:0.098= 1.82	0.510:0.230= 2.21
1123 K	0.317:0.154= 2.06	0.336:0.157= 2.14	0.450:0.190= 2.37

Isothermally Treated at 813 K

Microstructures of Alloy 625, which have been treated at 813 K are similar to that of SQ Alloy 625 and, hence, not shown here. However, analysis of various CSL boundaries have been included in Table 4.2, which would be compared with that of other isothermally treated Alloy 625 samples. In order to compare the effect of isothermal holding temperature on the CSL boundaries graphically, relevant data of Table 4.2 have been plotted for each temperature. Trends in the evolutions of CSL $\Sigma1$, $\Sigma3$ and $\Sigma1 + \Sigma3$ during isothermal holding at 813 K are shown in Fig. 4.14. Change in the Length fraction, Numerical fraction and their ratios, which are seen in the same set of samples, are shown in Fig. 4.15. Variations in the average grain size due to isothermal holding for all temperatures, as given at the end of Table 4.2, are graphically shown in Fig. 4.24.

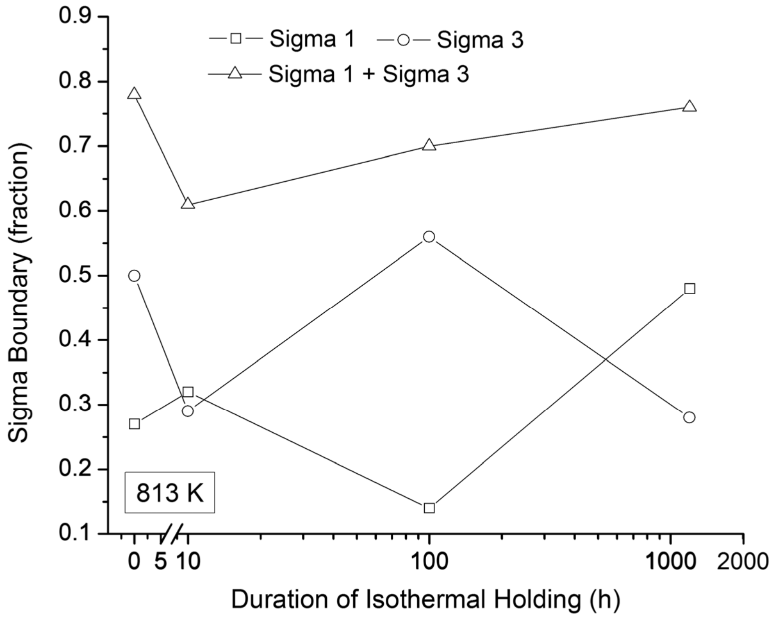

Fig. 4.14: Changes in CSL Sigma 1, Sigma 3 and the combined Sigma 1 and Sigma 3 fraction due to isothermal holding at 813 K are shown above.

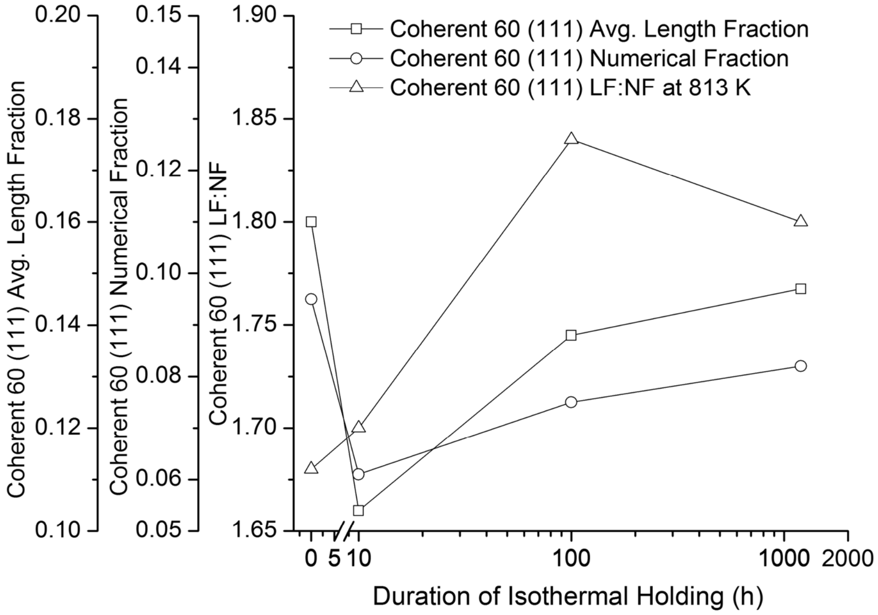

Fig. 4.15: Changes in Length, Numerical Fraction and the corresponding ratio of coherent 60^o (111) type boundaries due to isothermal holding at 813 K are shown above.

Isothermally Treated at 973 K

EBSD images obtained using OIM from the Alloy 625 specimens, which have been held isothermally for 10 h, 100 h and 1200 h have been given in Fig. 4.16. Analysis of these images in terms of Σ1, Σ3 and coherent 60° (111) boundaries have been given in Table 4.2. It can be seen in Table 4.2 that fraction Σ1 increases and Σ3 decreases with the increase in the duration of holding. In aggregate, total Σ1 + Σ3 is seen to rise, while the fraction of coherent 60° (111) boundary is measured to be > 0.5. This has been the maximum compared to that of all isothermally treated specimens. The grain size is also seen to go up with the increase in holding time. Area fraction of the same is given in Fig. 4.17.

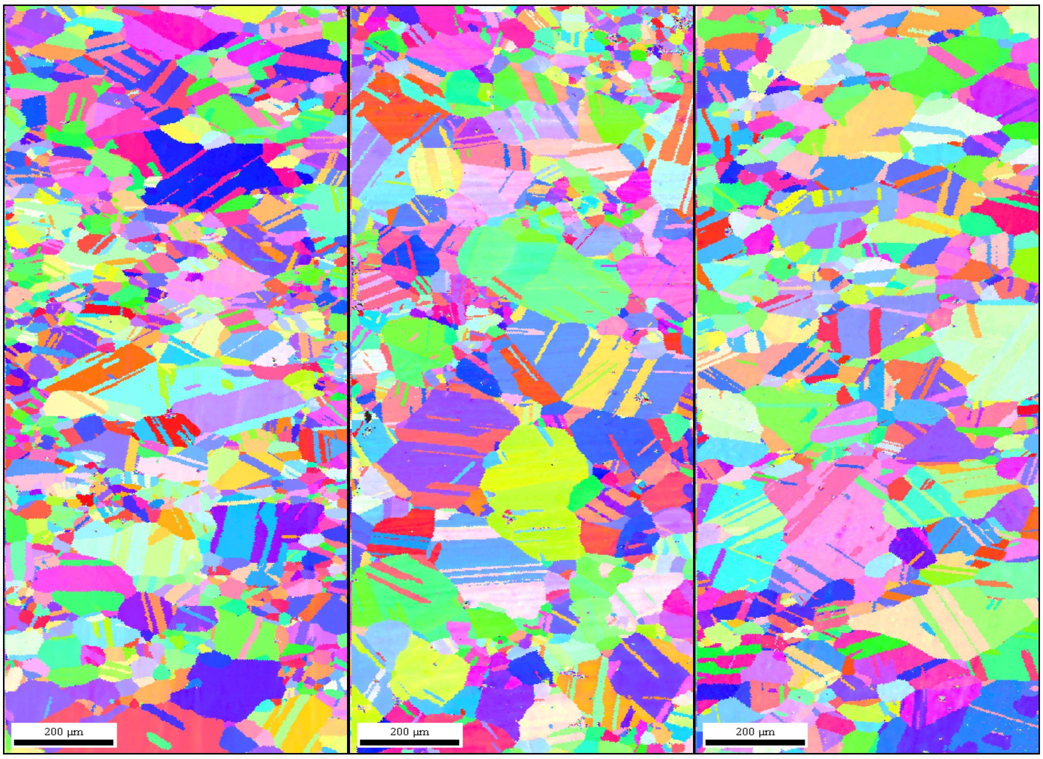

a) 973 K – 10 h b) 973 K – 100 h c) 973 K – 1200 h

Fig. 4.16: EBSD images of samples after 10 h, 100 h and 1200 h of isothermal holding at 973 K. Color code is based on the pole figure in Fig. 4.11.

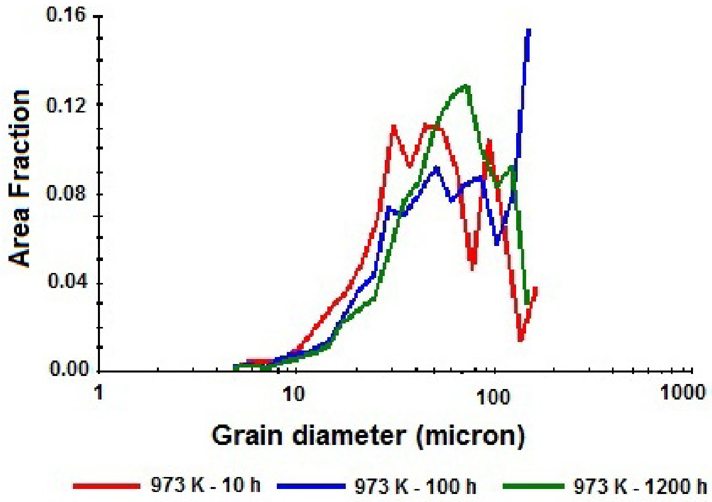

Fig. 4.17: Variation in area fractions of grain diameter as obtained from Fig. 4.16 (a) – (c).

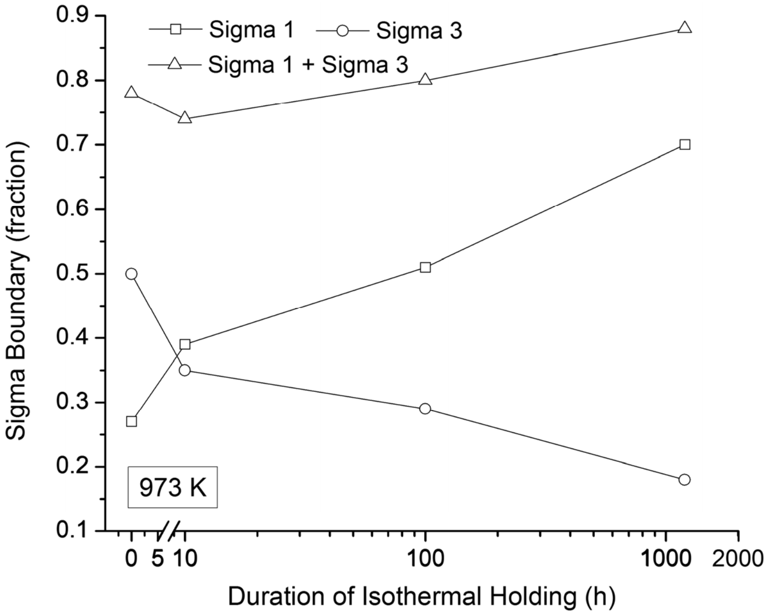

Fig. 4.18: Changes in CSL Sigma 1, Sigma 3 and the combined Sigma 1 and Sigma 3 fraction due to isothermal holding at 973 K are shown above.

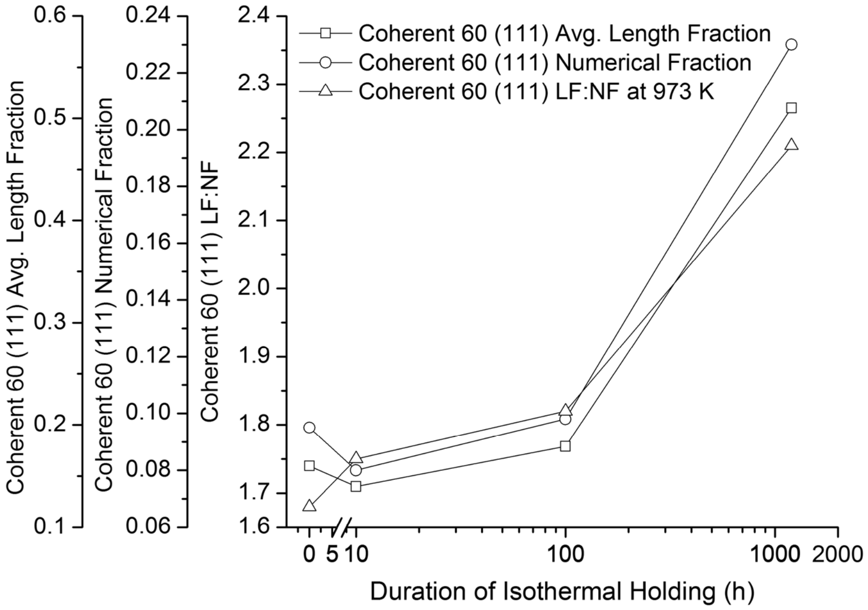

Fig. 4.19: Changes in Length, Numerical Fraction and the corresponding ratio of coherent 60^o (111) type boundaries due to isothermal holding at 973 K are shown above graphically.

Isothermally Treated at 1123 K

EBSD images obtained from the Alloy 625 specimens, which have been held isothermally at 1123 K for 10 h, 100 h and 1200 h are given in Fig. 4.20. Analysis of these images in terms of Σ1, Σ3 and coherent 60^o (111) boundaries have been given in Table 4.2.

As can be seen in Table 4.2, with the increase in the duration of isothermal holding, fraction of Σ1 decreases drastically to < 0.1, the lowest among all, while Σ3 increases to 0.52, the maximum among all. The fraction of coherent 60^o (111) boundary is measured to be > 0.45. When this is multiplied with the Σ3 fraction, the overall fraction of Σ3 boundaries after 1200 h of holding at 1123 K is seen to be the maximum. The grain size is seen to go down after 100 h of holding but later is seen to go up with the increase in holding time. Plot of area fraction against grain size diameter for all the specimens aged at 1123 K is given in Fig. 4.21.

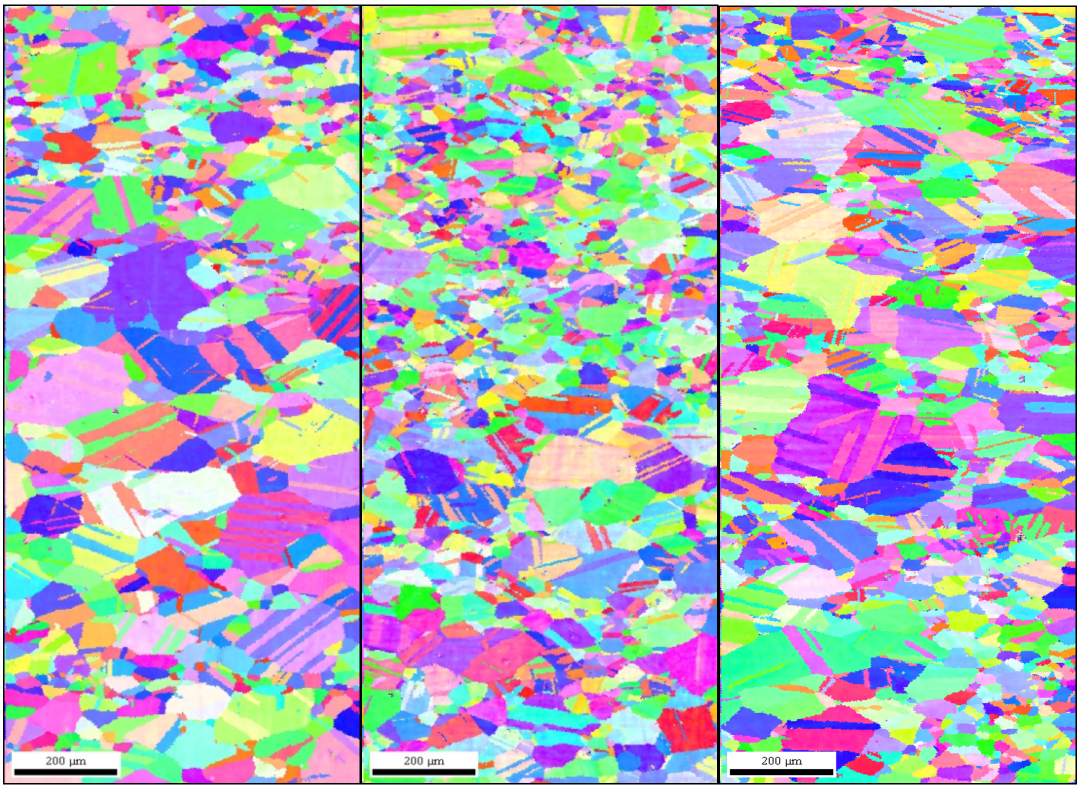

a) 1123 K – 10 h b) 1123 K – 100 h c) 973 K – 1200 h

Fig. 4.20: EBSD images of samples after 10 h, 100 h and 1200 h of isothermal holding at 1123 K. Color code is based on the pole figure in Fig. 4.11.

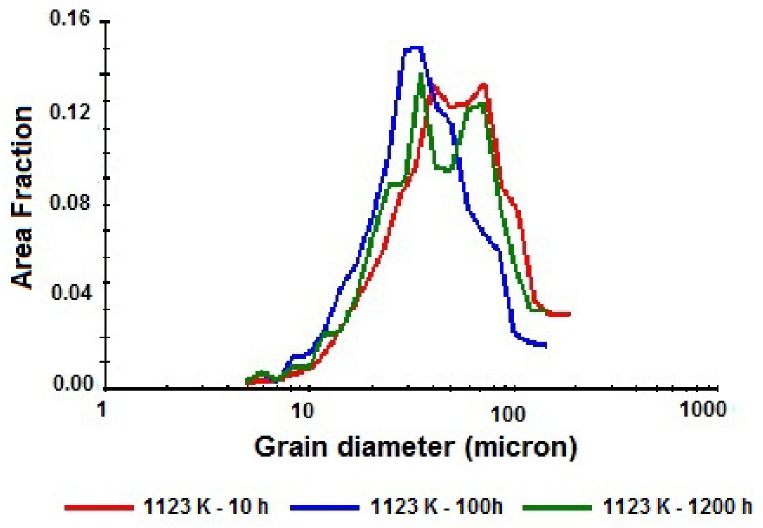

Fig. 4.21: Variation in area fractions of grain diameters as obtained from Fig. 4.20 (a) – (c).

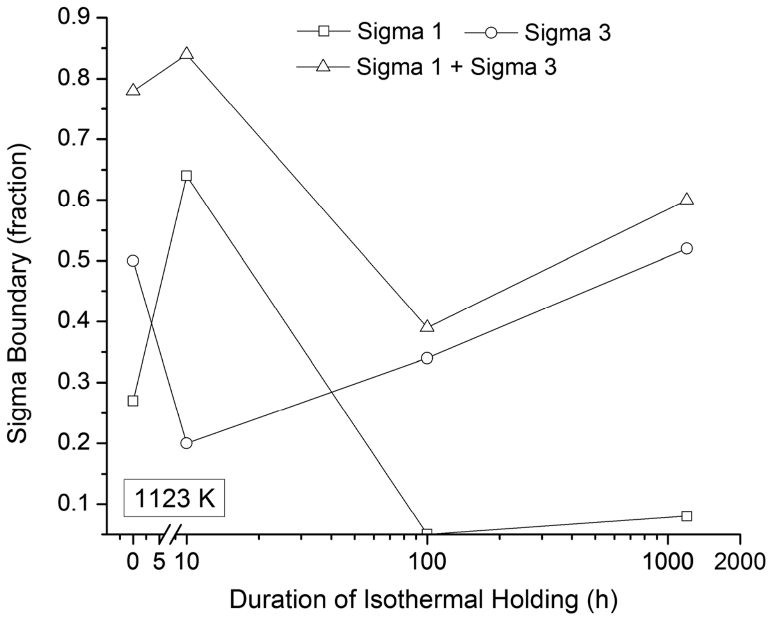

Fig. 4.22: Changes in CSL Sigma 1, Sigma 3 and the combined Sigma 1 and Sigma 3 fraction due to isothermal holding at 1123 K are shown above.

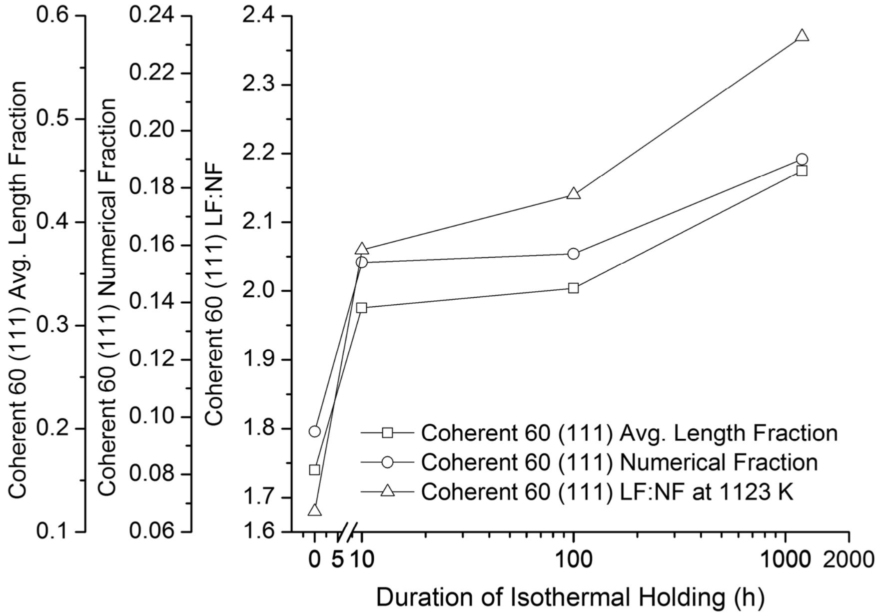

Fig. 4.23: Changes in Length, Numerical Fraction and the corresponding ratio of coherent 60^o (111) type boundaries due to isothermal holding at 1123 K are shown above graphically.

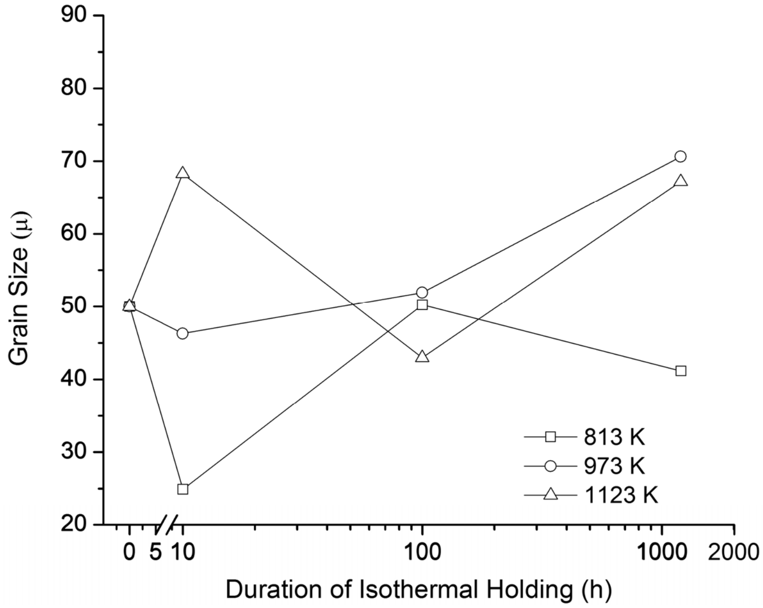

Fig. 4.24: Variations in the average grain size due to isothermal holding for 10 h, 100 h and 1200 h at 813 K, 973 K and 1123 K.

4.3 Discussion

Solution-quenched Alloy 625

EPMA result, as given in Table 4.1, endorses that the starting material conforms to standard Alloy 625 composition. Fig. 4.1 and Fig. 4.2 confirm that (Nb,Ti)C type primary carbides are present in the starting material. Since, the probe-diameter of the EPMA is ~1 μm, broadenings of X-ray line profiles in the case of Ni and Ti by ~1 μm can be attributed to the probe-geometry and not to the diffusion of these elements across the interface to smoothen those concentration profiles in Fig. 4.2.

In the case of Nb, broadening is seen to be wider than the probe diameter. However, looking into the smaller counts, compared to that of Ti, and the discontinuous appearance of the carbide on the "A" side in Fig. 4.1, the broadening does not appear to be due to the diffusion of Nb from the carbide to the matrix. X-ray mapping in Fig. 4.3 confirms that major elements in SQ Alloy 625 is uniformly distributed. It also reveals that regions around the primary carbides is depleted in Ti. This is likely to indicate the diffusion of Ti in the primary carbides from the matrix at high temperature.

Big, twinned, equiaxed grains in Alloy 625, as evidenced through microstructures from EPMA, optical microscope and OIM (correspondingly in Fig. 4.1, Fig. 4.4 (a) and Fig. 4.11 (a)) reflects the solution annealed state of Alloy 625. This is further supported by the normal distribution of grain size in Fig. 4.11 (b) and data from grain average neighbor misorientation in Fig. 4.12, where ~80 % within 0.5^o orientation and ~99% within 4.5^o orientation, which reflect a strain-free grain structure in SQ Alloy 625. Quantitatively, twinned microstructure of Alloy 625 is measured to have ~ 63 % Σ3 boundaries.

Isothermally Treated at 813 K

Optical micrographs in Fig. 4.4 (b), (c) and (d) show that there is no obvious change in the grain structure due to the isothermal holding up to 1200 h at 813 K. OIM results in Fig. 4.18 show that the fraction of low angle grain boundary initially goes down from 0.32 (813 K – 10 h) to 0.139 (813 K – 100 h) but increases to 0.48 (1200 h). Rise in the fraction of Σ3 in 813 K – 100 h does not seem to reflect a real but a relative one, which have been due to the annihilation of Σ1 boundaries.

Since, the melting point of the alloy is about 1548 K, the isothermal holding temperature 813 K, at which ordering of $Ni_2(Cr,Mo)$ and γ" is studied, is higher than 0.5 T_M. Hence, until 100 h of aging, when the ordered phase is coherent and is in the initial stage of formation, annihilation of small angle boundaries brings down the Σ1 boundary fraction. Formation of dense network of geometrically necessary dislocations due to the growth of $Ni_2(Cr,Mo)$ and γ", which have been confirmed through transmission electron micrograph in Fig. 4.5, appears to have raised the fraction Σ1 boundaries in 813 K – 1200h. However, locking of dislocations by the ordered phases in addition to the lack of activation energy for cross-slip at 813 K apparently prevented the annihilation of the GND's in 813 K – 1200 h sample.

Isothermally Treated at 973 K

Optical micrographs in Fig. 4.4 (e), (f) and (g) shows restructuring and grain growth in Alloy 625 due to the isothermal holding at 973 K. The OIM results, however, indicate a grain refinement at the intermediate stage in 973 K – 100 h sample.

As shown in Fig. 4.6, formation of γ" due to the holding at 973 K is associated with the formation of GND's. The steady increase in the Σ1 boundaries with the duration of holding, hence, similar to that of 813 K – 1200 h sample is due to the GND's. Three orthogonal views of γ'', as shown in Fig. 4.6 (e) – (g) shows that the ordered phase is elliptical-lens shaped and the maximum diameter is measured to be ~150 nm, which is much larger than the maximum size, ~28 nm, reported in the case of service-exposed components. Uniform distribution and larger size of the ordered phases in the present study is due to the holding of the alloy isothermally at the nose of the "*C*" curve of γ'', depicted in the TTT diagram (Fig. 1.1).

As per the OIM results in Table 4.2, CSL Σ1 boundaries at 973 K rises and are not annihilated at this temperature, although, grain restructuring can be confirmed through Fig. 6.1 and Table 4.2. Pinning of Σ1 boundaries by γ'' and inadequate thermal activation for the dislocation to cross-slip have, apparently, acted as deterrents in triggering the annihilation process. Rise in Σ1 boundaries and grain restructuring appears to have led to the fall in Σ3 boundary fraction. However, rise in the coherent 60^o (111) boundary seems to affirm the stability of the same in Alloy 625. All other boundaries seems to get annihilated due to the isothermal holding at 973 K, as the summation of Σ1 and Σ3 boundaries becomes almost 90 % of the total boundaries.

Isothermally Treated at 1123 K

Formation and growth of ordered δ phase at 1123 K is clearly seen in the optical micrographs of Fig. 4.4 (h), (i) and (j). Presence of nine varieties of δ phases, which are of Ni_3Nb stoichiometry have been confirmed through HAADF micrographs and EDS scan in Fig. 4.7 and Fig. 4.8, respectively.

Analysis of high-resolution micrograph in Fig. 4.10 shows two regions within the matrix phase, although, at low magnification the region shows the presence of a single phase. As evidenced from Fig. 4.10, at high resolution mode the matrix showed systematic variation in the lattice parameters. While, 0.245 nm can be ascribed to (110) plane spacing of the matrix, 0.278 nm appears to be close to the (200) type plane of Ni_3Nb-DO_a, which is actually reported to be ~ 0.256 nm [2]. In order to understand the reason for the variation in lattice parameters, nearby region has been re-examined under STEM-HAADF mode. The inset in Fig. 4.10 shows elemental map of Nb of the region superimposed on the image. It is noticed from Fig. 4.10 that Nb atoms get segregated in the matrix phase. Considering 0.292 nm diameter of Nb atom, possibility of measuring the higher plane spacing at Nb-rich region seems to be plausible. Separation between two successive shoulder peaks by ~10 nm, in the Nb and the Ni line profiles in Fig. 4.8, hence, appears to be due to the similar manifestation of segregation of Nb. Such segregation of Nb atoms apparently indicates the early stage of Ni_3Nb-DO_a formation.

OIM results in Table 4.2 ascertain that, CSL Σ1 boundaries are not stable at 1123 K and reduces to 0.08 (1123 K – 100 h) fraction from 0.64 (1123 K – 10 h) and are maintained at that level. This annihilation of Σ1 boundaries may be attributed to the cross-slip mechanism owing to the availability of high thermal activation energy at 1123 K. In this case, Σ3 boundaries are seen to be stable and dominating, which is one of the reason for the uniform corrosion behavior of Alloy 625. The grain refinement after 100 h of holding at 1123 K seems to be similar to that of 973 K trend. Reduction in the grain boundaries having high energy as has been postulated in the case of Alloy 718 [64] seems to have influenced such grain restructuring in Alloy 625. As compared to that of 973 K, the grain growth at 1123 K, in spite of higher temperature has been hindered due to the uniform spreading of δ in the matrix.

General Observations on the Effect of Isothermal Holding of Alloy 625

For all temperatures, microstructural evolutions during isothermal holding seems to have increased the stability of coherent {111} type boundaries, since both numerical fraction (NF) and length fraction (LF) are seen to rise with the duration of aging. E.g. LFs are seen to rise from 0.1 (813 K-10 h) to 0.147 (813 K-1200 h), 0.14 (973 K-10 h) to 0.51 (973 K-1200 h) and 0.32 (1123 K-10 h) to 0.45 (1123 K-1200 h). While, increase in the NF of the coherent {111} type boundaries indicate the growth of the same at the expense of other type of {111} boundaries, increase in the ratio of LF to NF is likely to indicate the growth of the {111} type boundary with the duration of isothermal holding.

4.4 Summary

Microstructural study of isothermally treated Alloy 625 has not only revealed the size, shape and growth of various ordered phases but also brought out the stability of various important CSL boundaries due to the isothermal treatment at high temperatures. Following salient observations can be made from this *section*.

1. The starting SQ Alloy 625 comprises strain-free equiaxed twinned-grains and is having uniform elemental distribution of major alloying elements.
2. (Nb,Ti)C type primary carbides, having no preference for occurrence may occasionally be discovered in the solution-annealed grains. A narrow Ti depleted zone around the carbides is likely to indicate the diffusion of the element inside the carbide during solutionizing treatment.

3. The growth of $Ni_2(Cr,Mo)$ and γ" at 813 K and the growth of γ" at 973 K is associated with the formation geometrically necessary dislocations, which is directly reflected in the rise of coincidence site lattice boundaries.
4. γ" is elliptical-lens shaped and can grow more than ~150 nm.
5. Geometrically necessary dislocations, which are produced as a result of the formation of γ" are not annihilated at 973 K due to the pinning by γ" and inadequate activation energy for cross-slipping at 973 K.
6. Exposures of solution quenched Alloy 625 at 973 K and at 1123 K causes refinement of the grains. Necessary driving force apparently comes from the high-energy boundaries.
7. Plate shaped δ of Ni_3Nb stoichiometry can become more than 200 nm thick.
8. High temperature exposure of Alloy 625 causes increase in the coherent (60^o) (111) type boundaries. Excellent uniform corrosion behavior of the alloy apparently comes from this inherent quality.

Effect of the changes in the microstructure on the mechanical behavior of the alloy is discussed in the forthcoming chapters.

CHAPTER 5

5 Mechanical Response of Precipitated Alloy 625

5.1 Introduction

As in the case of any alloy system, mechanical properties of Alloy 625 depends upon its microstructures. Some reports on the aged and failed Alloy 625 components have shown that the ordered phases can drastically change the mechanical behavior of the alloy [19,21,23,25]. However, understanding of the effect of different ordered phases and, particularly, the effect of growth of the major ordered phases on the mechanical behavior of the alloy has remained limited from these studies. In the present study, tensile testing of SQ Alloy 625 and all the isothermally treated Alloy 625 samples, which are having different degrees of growth of $Ni_2(Cr,Mo)$, γ'' and δ are intended to reveal the effect of different microstructures on the mechanical properties of the alloy.

Metals and alloys fracture in two distinct modes, viz. ductile tearing and brittle cleavage types [35,73]. Ductile fracture is a result of void nucleation and growth, while brittle cleavage fracture is the separation of two planes when dislocation movement becomes difficult in the crystal lattice. Often, in between these two extreme fracture modes, most of the metals and alloys exhibit mixed mode fractures. Hence, it is important to study the influence of the microstructures of metals and alloys on the fracture surfaces and vice versa.

Various combinations of ductile and cleavage surfaces may occur in the same alloy system due to precipitation of second phases [74,75]. As discussed in Chapter 4, isothermal treatments of Alloy 625 at 813 K, 973 K and 1123 K produces different second phases, growths of which are controlled by the duration of holding. Study of the tensile fracture surfaces, extracted from all the ten varieties (Table 3.1) of specimens has been presented below in order to establish correlation between different microstructures discussed earlier with the fracture behavior of Alloy 625.

5.2 Results

5.2.1 Mechanical Properties

5.2.1.1 Tensile Parameters

Various tensile parameters obtained from SQ and aged samples are summarized in Table 5.1. Salient observations in the trends of tensile properties are pictorially shown in , given in the table are as follows:

1. For all the three aging temperatures, strength and ductility values of the alloy samples are seen to vary with the duration of aging, albeit, with different trends. The SQ samples show maximum ductility and near lowest yield strength (YS). Other two specimens, aged at 973 K for 10 h and aged at 1123 K for 10 h, have recorded the second lowest and the lowest YS values, respectively.

Table 5.1: Tensile parameters of SQ and isothermally treated Alloy 625 samples along with hardness values in Vicker's Hardness No. (VHN).

Condition	**YS (MPa)**	**UTS (MPa)**	**Uniform Strain**	**Fracture Strain**	**Hardness (VHN)**
SQ	373 ± 29	838 ± 26	0.54 ± 0.08	0.71 ± 0.04	220 ± 4
813 K – 10h	385 ± 33	853 ± 22	0.54 ± 0.067	0.68 ± 0.045	255 ± 6
813 K – 100h	422 ± 42	958 ± 47	0.40 ± 0.06	0.50 ± 0.065	285 ± 6
813 K - 1200h	557 ± 49	1045 ± 56	0.46 ± 0.04	0.61 ± 0.045	390 ± 10

973 K – 10h	372 ± 24.5	815 ± 29	0.466 ± 0.045	0.54 ± 0.06	289 ± 6
973 K – 100h	493 ± 40.5	906 ± 45	0.38 ± 0.035	0.46 ± 0.027	265 ± 6
973 K - 1200h	577 ± 49.5	961 ± 29	0.235 ± 0.022	0.31 ± 0.022	370 ± 9
1123 K- 10h	353 ± 22	836 ± 36.5	0.465 ± 0.031	0.55 ± 0.026	260 ± 6
1123 K - 100h	380 ± 42.5	803 ± 47	0.31 ± 0.027	0.38 ± 0.031	233 ± 4 (precipitate depleted region) 350 ± 9 (precipitate rich region)
1123 K - 1200h	484 ± 42.5	856 ± 46.5	0.23 ± 0.024	0.29 ± 0.027	368± 9

2. YS of specimens with 10 h of isothermal holding shows decreasing trend with the increase in holding temperature.
3. Upon comparing with respect to that of SQ sample rising trends in YS and UTS with the duration of aging are seen for 813 K and 973 K but not for 1123 K aging temperature. In the case of latter temperature, rise in the YS is seen to be slow and UTS is seen to fall, till 100 h of holding.

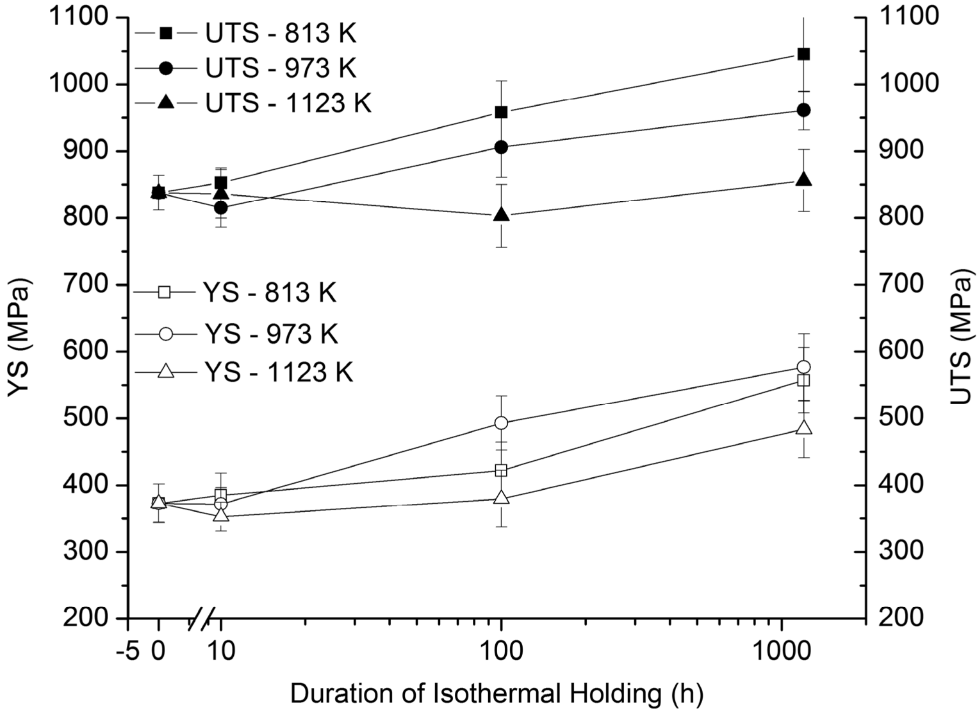

Fig. 5.1: Changes in YS and UTS values due to isothermal holding at 813 K, 973 K and 1123 K, as obtained from Table 5.1 are graphically shown above.

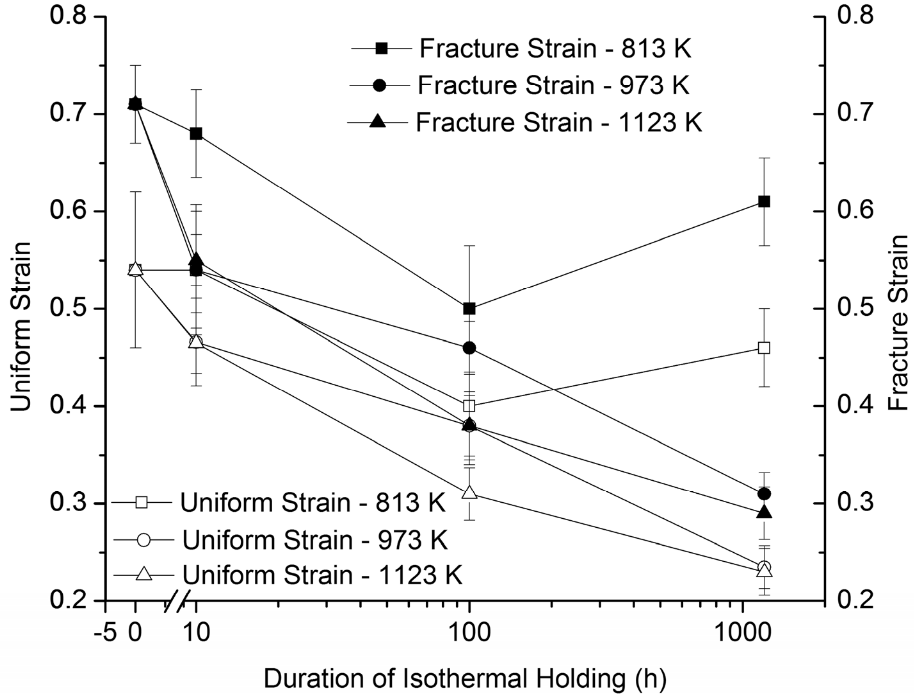

Fig. 5.2: Changes in the true strains till uniform elongation and till fracture, as obtained from the tensile tests are depicted above.

4. Trends in the variation in ductility are seen to be different from those of strengths. Ductility is seen to fall with the duration of holding for all isothermal temperatures except for 813 K, where ductility is seen to rise after 100 h, albeit, maintaining the overall trend in ductility falling.

5.2.1.2 True-Stress – True-Strain Behavior

True stress (σ) – true strain (ε) behaviors of SQ and aged Alloy 625 samples in the plastic region are shown in Fig. 5.3, Fig. 5.4 and Fig. 5.5, respectively. These have been processed further in terms of $\partial\sigma/\partial\varepsilon$ vs. σ plot to understand the strain hardening behavior of the isothermally aged Alloy 625 having various precipitates in the matrix in Chapter 7.

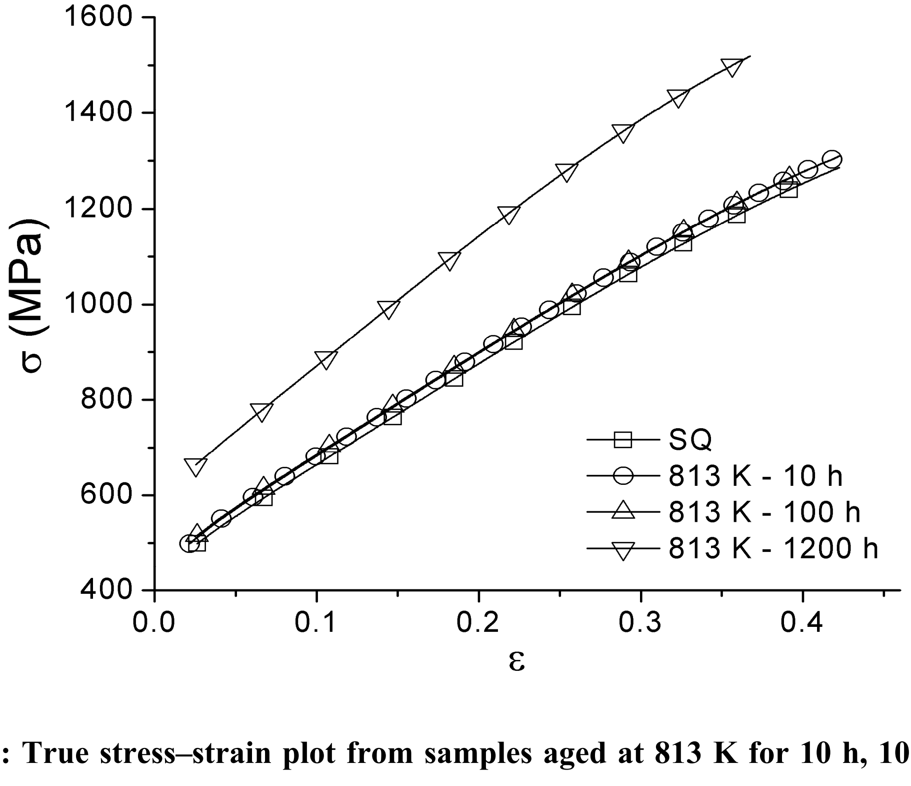

Fig. 5.3: True stress–strain plot from samples aged at 813 K for 10 h, 100 h and 1200 h along with SQ sample.

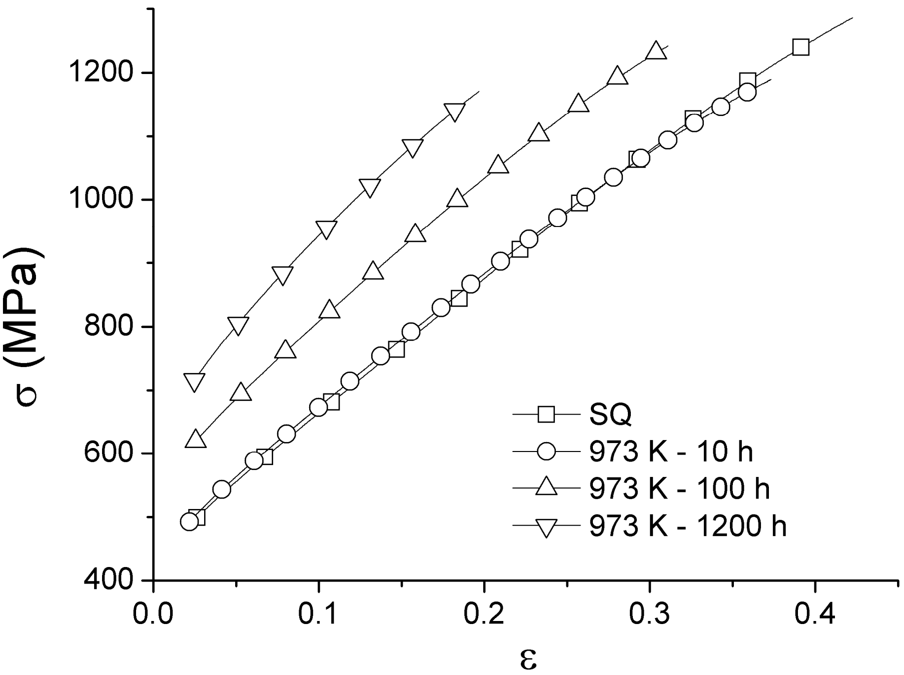

Fig. 5.4: True stress–strain plot from samples aged at 973 K for 10 h, 100 h and 1200 h along with unaged sample.

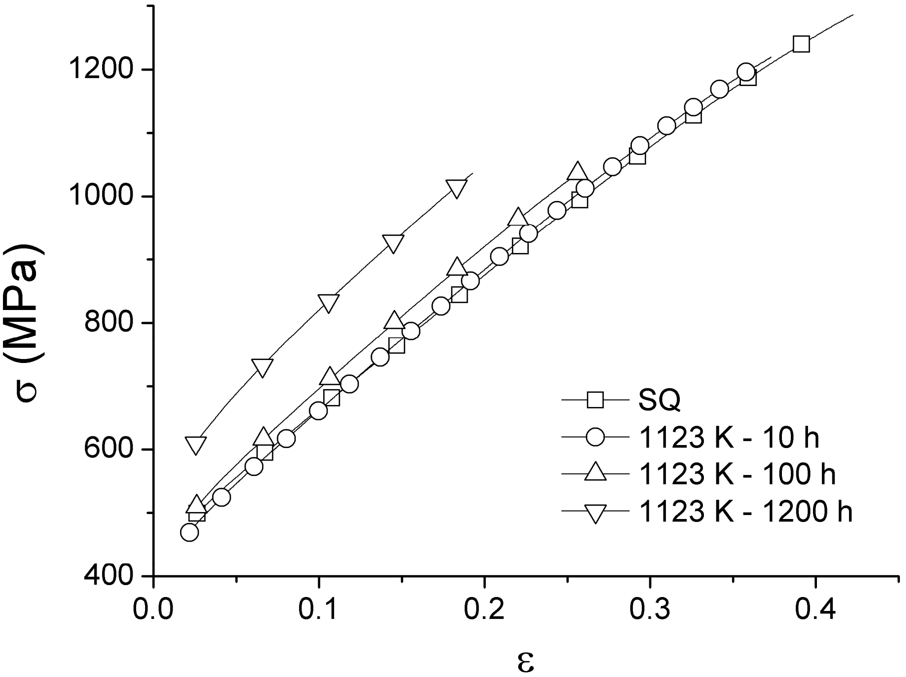

Fig. 5.5: True stress–strain plot from samples aged at 1123 K for 10 h, 100 h and 1200 h along with unaged sample.

5.2.2 Fracture Behavior

Observation of the fracture surfaces at various magnifications are important two gain macro and micro information. In the next sub-*section* visual observations of two halves of fracture tensile surfaces are given in Fig. 5.6, while scanning electron microscopic observations at different magnifications are presented in Fig. 5.7 and Fig. 5.8.

5.2.2.1 Visual Observations of Fractured specimens

Visual observation of broken tensile-fractured samples are presented in Fig. 5.6. These shows that there is a gradual shift from the usual "cup & cone" type fracture to cleavage type fracture (which is perpendicular to the tensile axis), as a result of isothermal holding at different elevated temperatures.

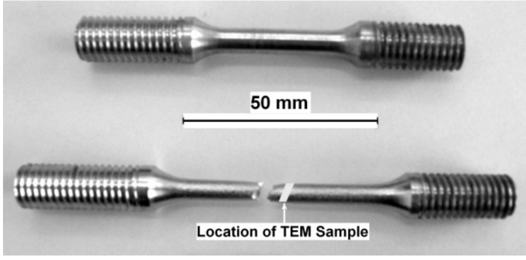

a) SQ specimen

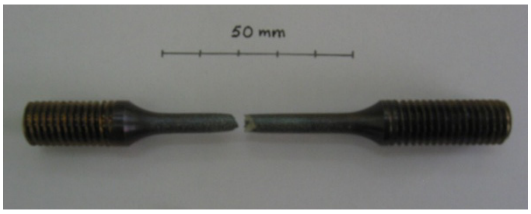

b) 813 K – 10 h

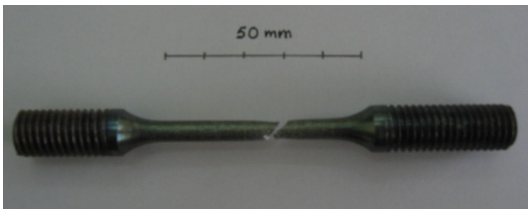

c) 813 K - 100 h

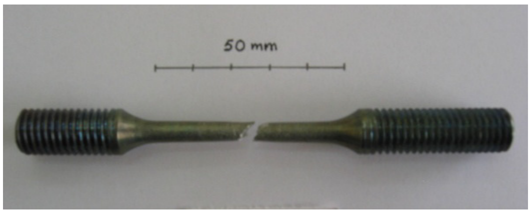

d) 813 K - 1200 h

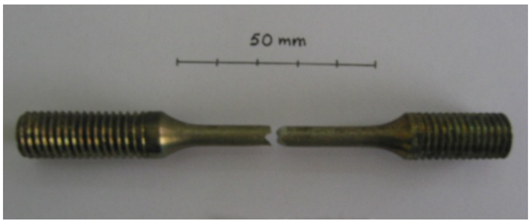

e) 973 K – 10 h

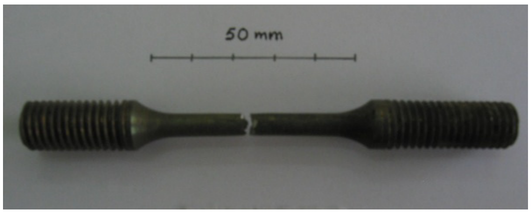

f) 973 K – 100 h

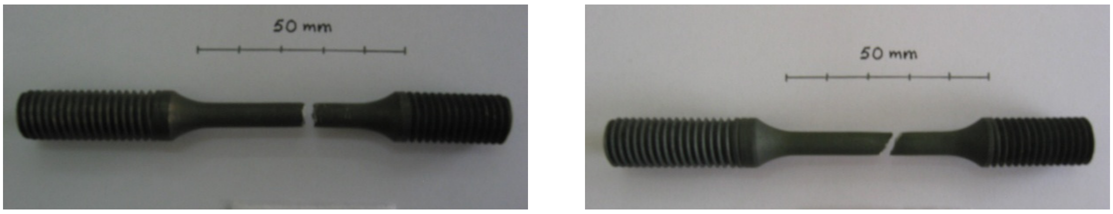

g) 973 K – 1200 h

i) 1123 K – 100 h

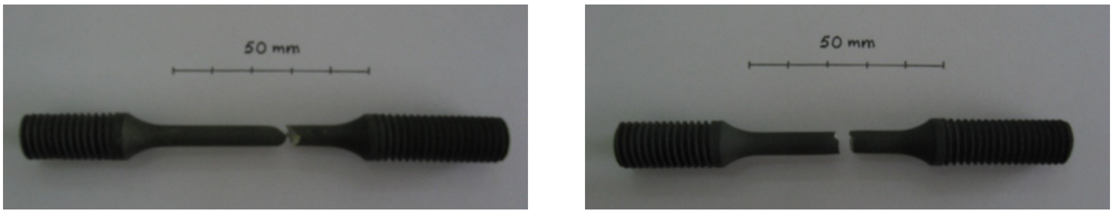

h) 1123 K – 10 h

j) 1123 K - 1200 h

Fig. 5.6: (a) – (j) Pictures of broken tensile specimens, which have undergone isothermal treatment as mentioned in Table 3.1 with that of unaged and untested samples have been shown in (a).

5.2.2.2 Low Resolution Fractographs

The fractographs in Fig. 5.7 (a) – (h) are of low magnifications and are presented here to strengthen the visual observations presented in *section* 5.2.2.1. Fig. 5.7 (a) – (e) and (h) show ductile "cup-and-cone" type fracture, (f) and (i) show deviation from the ductile type fracture, while (g) and (j) show faceted grains, where fracture surfaces are perpendicular to tensile axes.

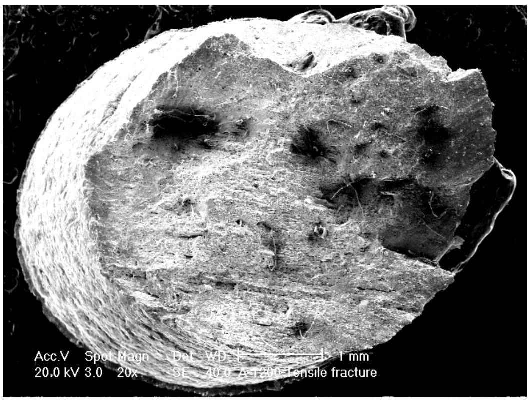

a) Unaged

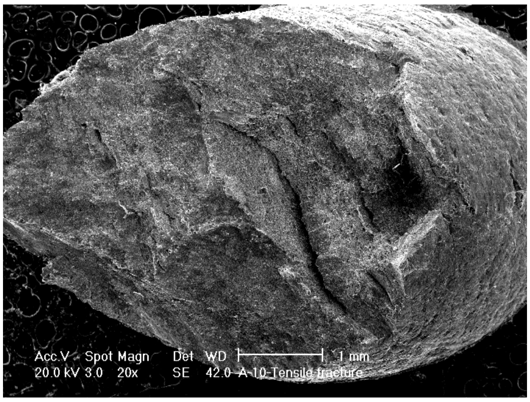

b) 813 K – 10 h

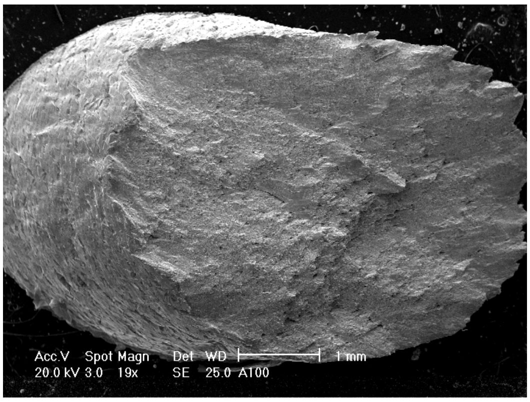

c) 813 K – 100 h

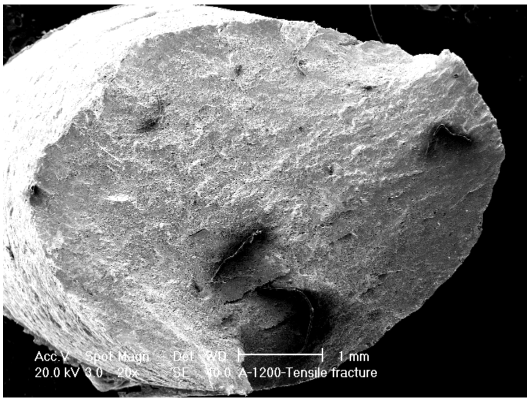

d) 813 K – 1200 h

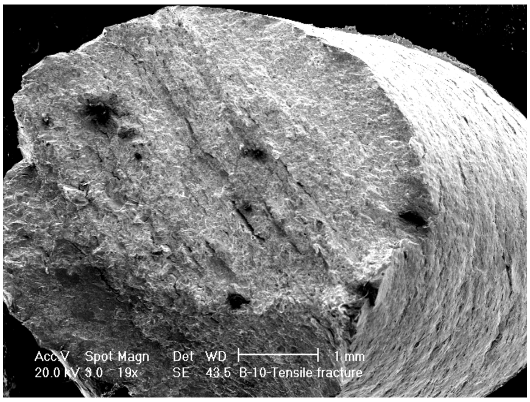

e) 973 K – 10 h

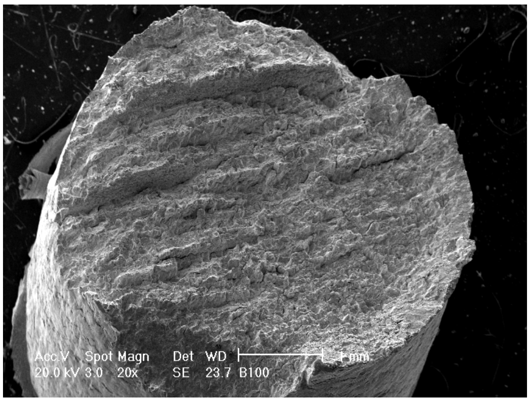

f) 973 K – 100 h

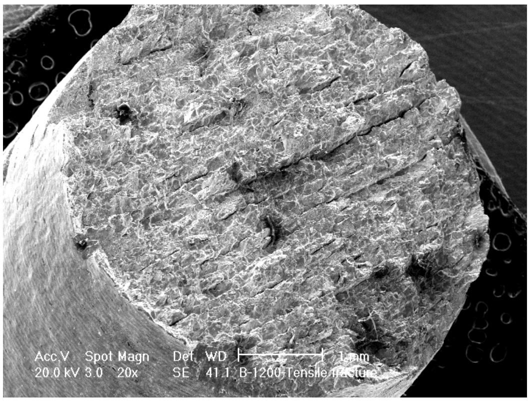

g) 973 K – 1200 h

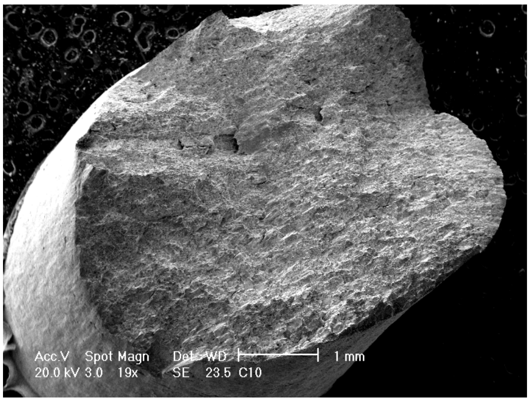

h) 1123 K – 10 h

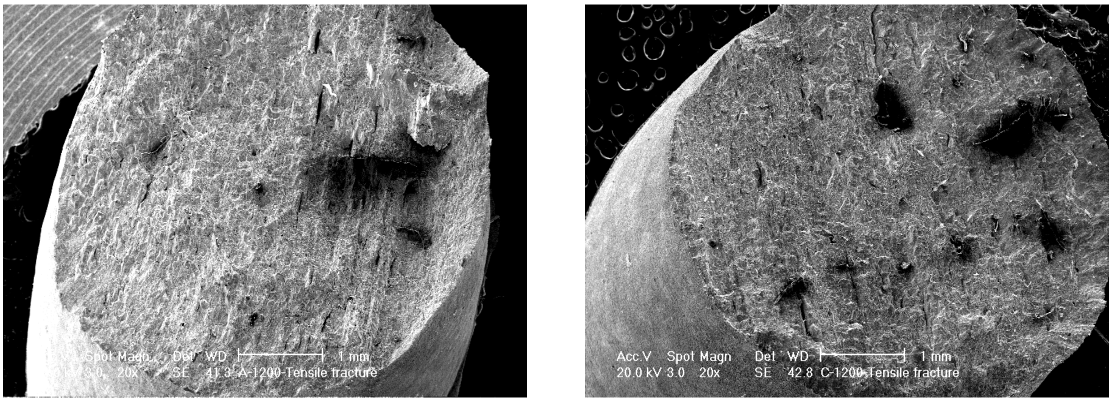

i) 1123 K – 100 h j) 1123 K – 1200 h

Fig. 5.7: Low magnification pictures of tensile fracture surfaces of samples having ten different heat-treatment histories are shown in (a) – (h). (a) – (e) and (h) show ductile *cup-and-cone* type fracture, (f) and (i) show deviation from the ductile type fracture, while (g) and (j) show faceted grains and fracture surfaces perpendicular to tensile axes.

5.2.2.3 High Resolution Fractographs

Fractographs of all the broken tensile specimens, as observed inside SEM at high magnification, are given in Fig. 5.8, Fig. 5.9, Fig. 5.10 and Fig. 5.11. The fractograph in Fig. 5.8 is from SQ sample that shows large dimples (marked with the arrows). Particles responsible for the creation of voids are seen at the bottom of dimples. For example a particle with sharp edges, located at the bottom of the dimple is marked with a down-arrow on the left side of Fig. 5.8.

Fractographs obtained from the samples, which were aged at 813 K for 10 h, 100 h and 1200 h are shown in Fig. 5.9 (a), (b) and (c), respectively. The type of ductile tearing seen in 813 K – 10 h sample in Fig. 5.11 (a) is similar to that of the SQ sample in Fig. 5.8 and the only difference between these fractographs appears to be the lower depth of dimples in the former. Region-I from Fig. 5.9 (b), which is obtained from 813 K – 100 h sample, shows the region of crack initiation. As evidenced from region-II, dimples are of various sizes and are associated with the sheared regions (region-III). In contrast to the fractograph of 100 h sample, the size and the distribution of dimples, as seen in region-I of Fig. 5.9 (c), obtained from 813 K – 1200 h of aging is more uniform. Region-II of the surface shows signs of shear and is similar to that of 813 K – 100 h sample.

In comparison to that of sample aged at 813 K, Alloy 625 after 10 h of aging at 973K, shows fewer dimples on the fracture surface, as shown in Fig. 5.10 (a). Region of crack initiation with river pattern is encircled in Fig. 5.10 (a). The arrows on the left side of Fig. 5.10 (a) also indicate the region of crack initiation. The fractographs of 973 K – 100 h sample in Fig. 5.10 (b) shows that the majority of the fracture surface is faceted leaving aside a small fraction of fibrous regions. The arrow in the extreme right indicates void formation within the grain, although many regions indicated by other arrows show crack initiation from boundaries and triple junctions. The fracture surface after 1200 h of aging at 973 K, as can be seen in Fig. 5.10 (b), comprises faceted regions. In this regard, Fig. 5.10 (d) depicts the lines demarcating the facets. The arrow in the upper right corner of Fig. 5.11 (g) apparently indicates the initiation of crack at the boundary. The arrow in the left points to a lens shaped crack that has apparently formed within the grain and branched out at right angle.

Two distinguished features in the fractograph from 1123 K – 10 h sample are encircled in region-I and II, as shown in Fig. 5.11 (a). Region-I is quite flat, having some point-like obstacles to the crack propagation. Region-II has fibrous appearance, consisting of tiny voids, which are much finer than those of all the fractographs shown earlier. The linear feature, which is marked with an arrow in Fig. 5.11 (a), appears to be the grain boundary and, also, to be the crack initiation point. Appearance of river pattern in region-I, and a fibrous surface, as seen in region-II, are the characteristics of the fractograph in Fig. 5.11 (b). After, 1200 h of aging at 1123 K the fracture surface, as shown in Fig. 5.11 (c), appears to consist of several facets, demarcation of which are depicted in Fig. 5.11 (d). The facets appear to meet each other at $\sim 70^{o}$ angles, as shown by the red lines in Fig. 5.11 (c) and (d). Surfaces of the facets are full of uniform and fine dimples. These tiny dimples are similar to what are seen in region II's of Fig. 5.11 (a) and Fig. 5.11 (b).

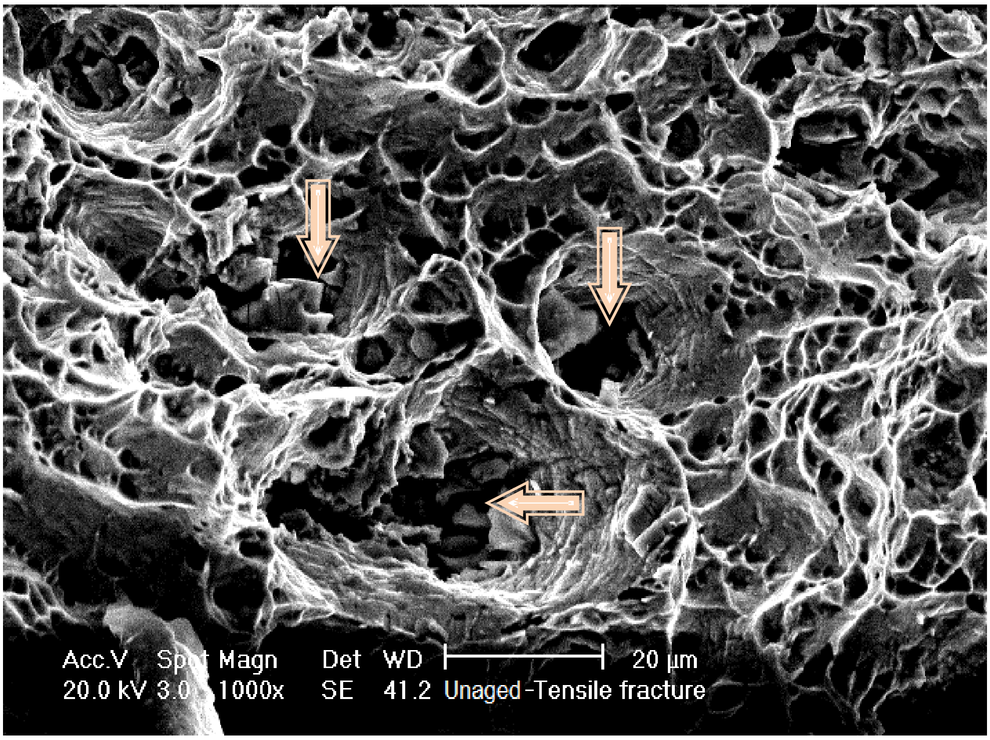

Fig. 5.8: Fractographs of SQ Alloy 625 sample. Large dimples are shown by the arrows. Downward arrow on the left side is pointing a right-angle-corner particle at the bottom of the dimple.

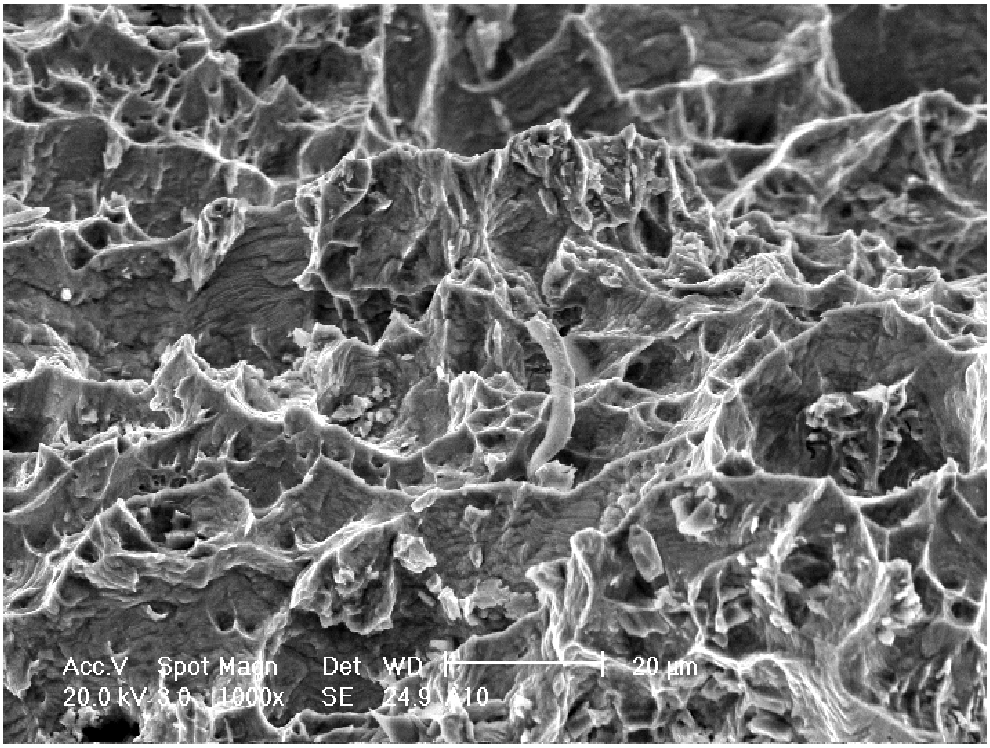

a) 813 K – 10 h

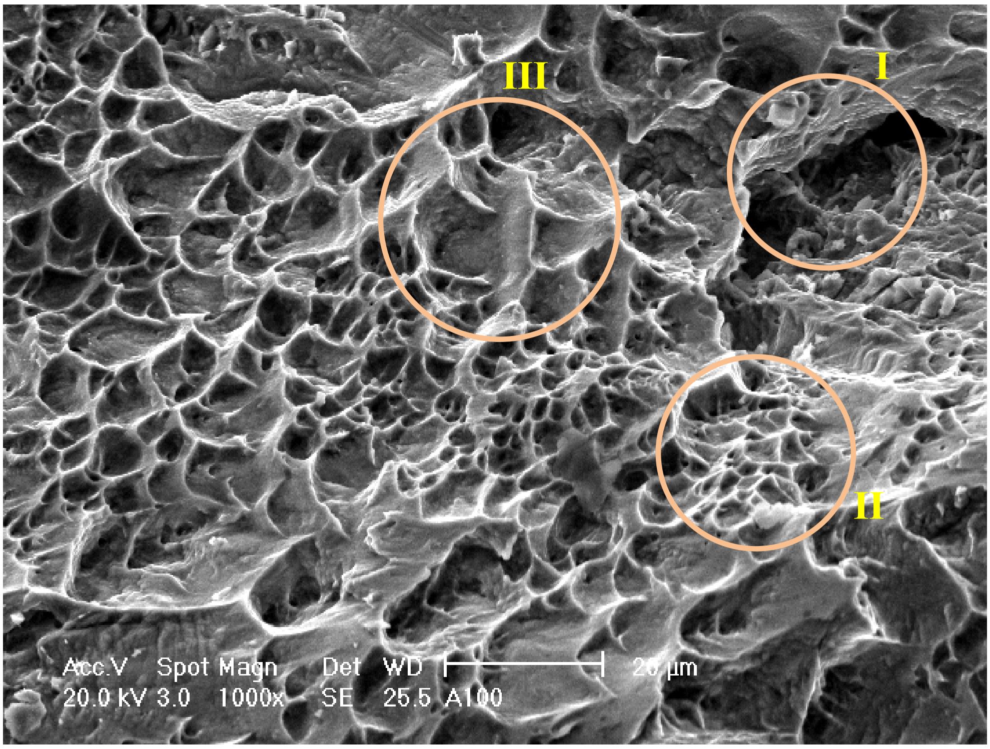

b) 813 K – 100 h

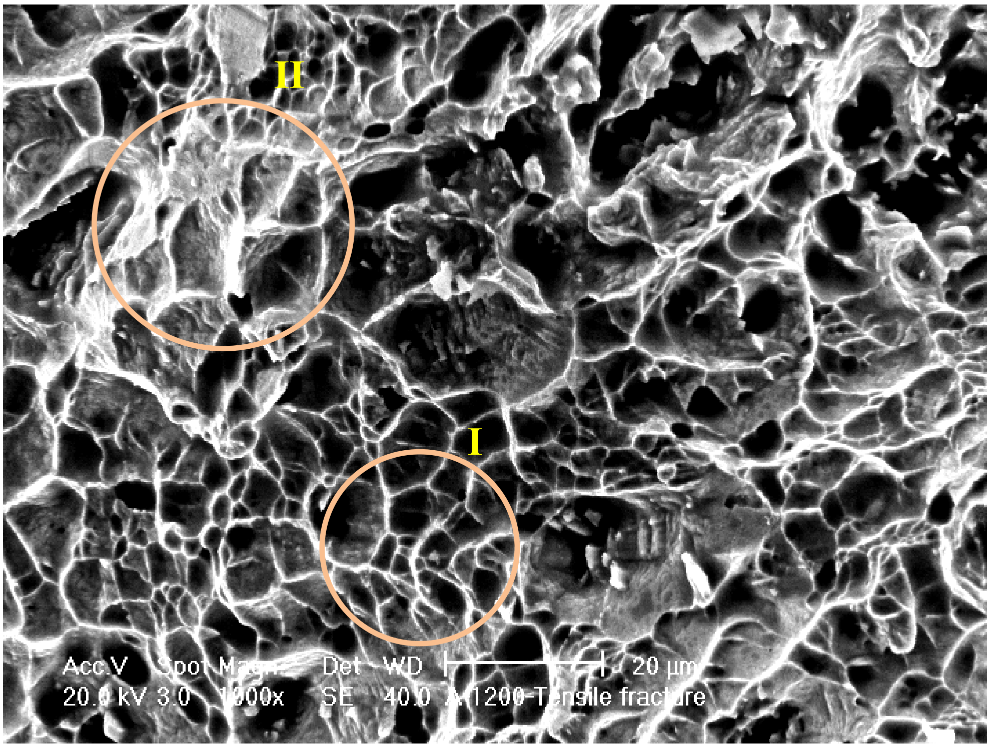

c) 813 K – 1200 h

Fig. 5.9: Pictures in *a, b* and *c* are the fractographs from samples, aged at 813 K for 10 h, 100 h, and 1200 h, respectively.

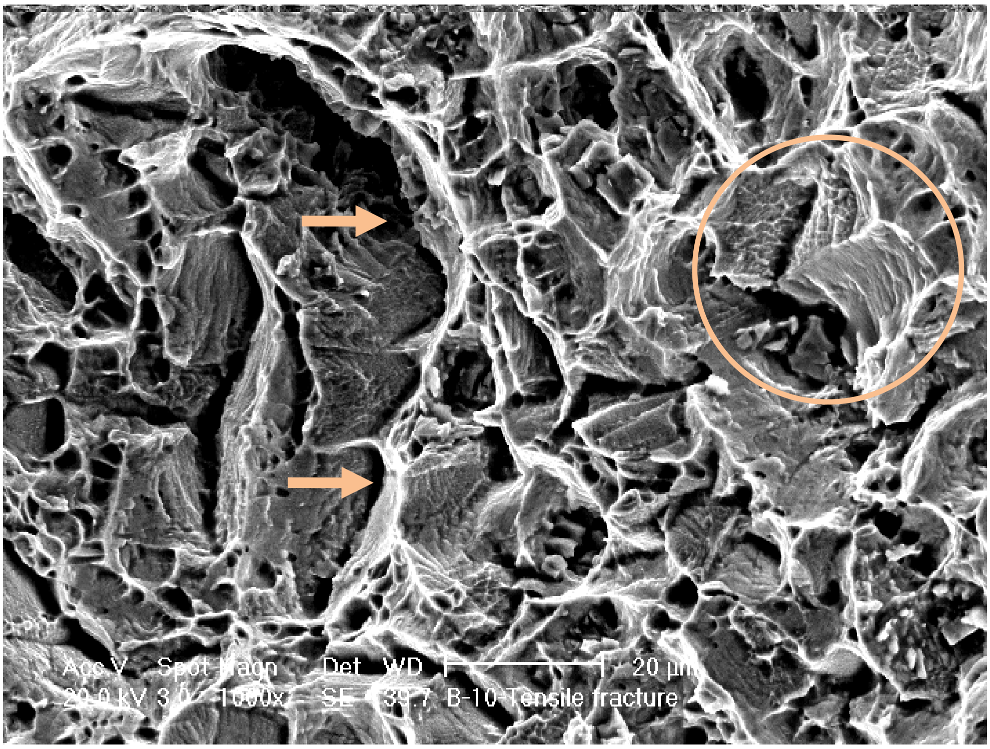

a) 973 K – 10 h

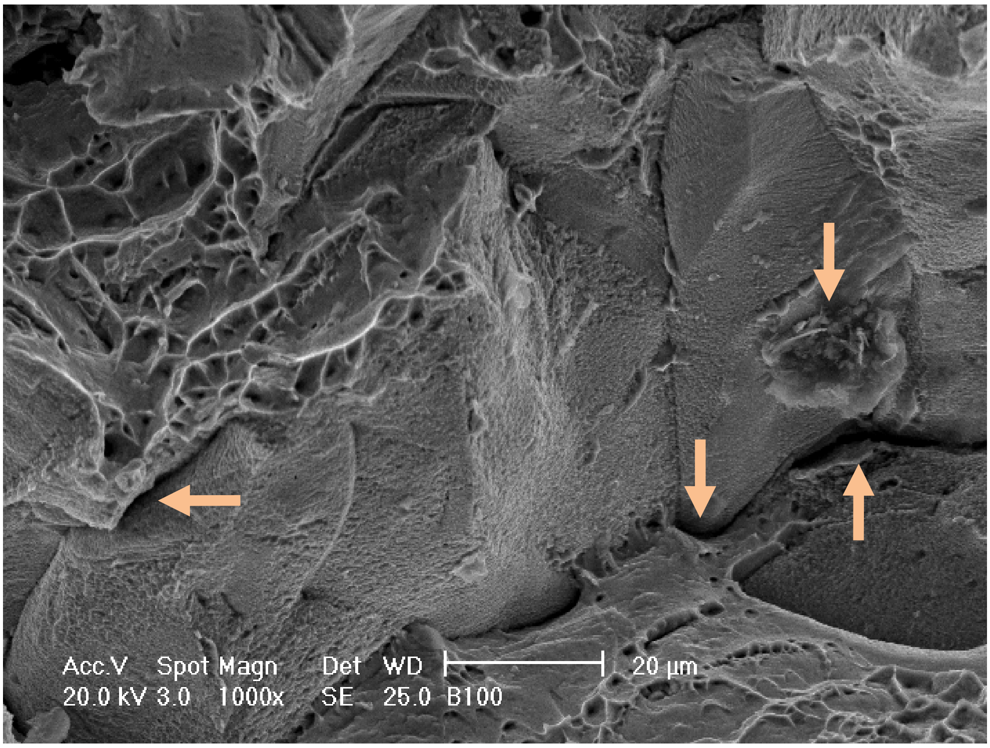

b) 973 K – 100 h

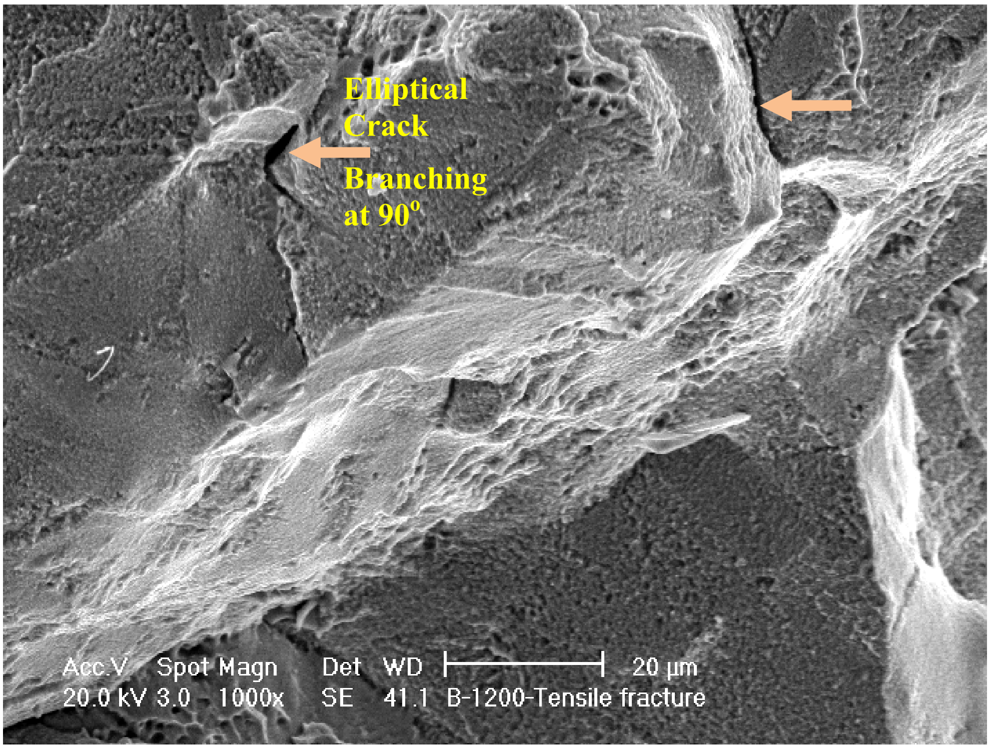

c) 973 K – 1200 h

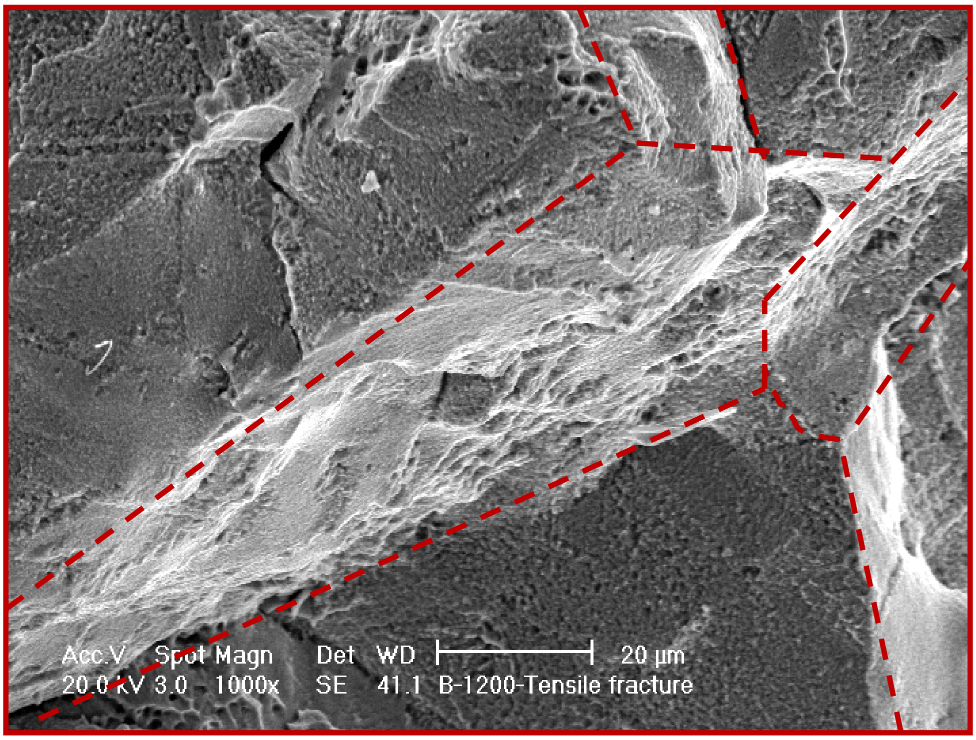

d)

Fig. 5.10: Pictures in *a, b* and *c* are the fractographs from samples, aged at 973 K for 10 h, 100 h, and 1200 h, respectively. Lines in *d* demarcate apparent intersections of prominent facets of fractograph in *c*.

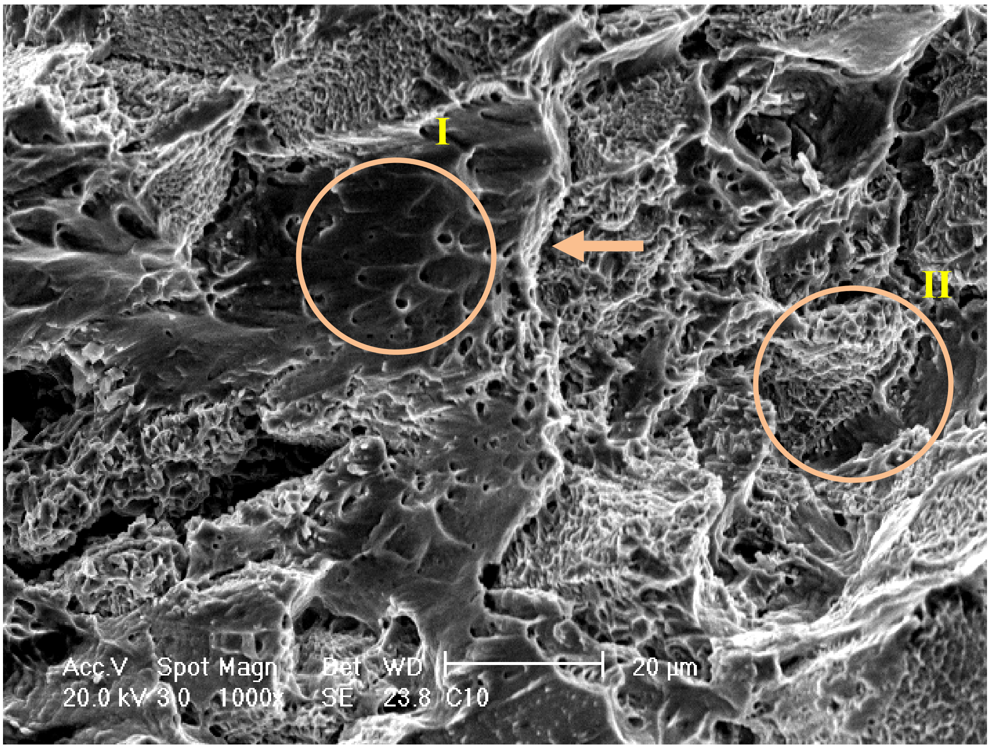

a) 1123 K – 10 h

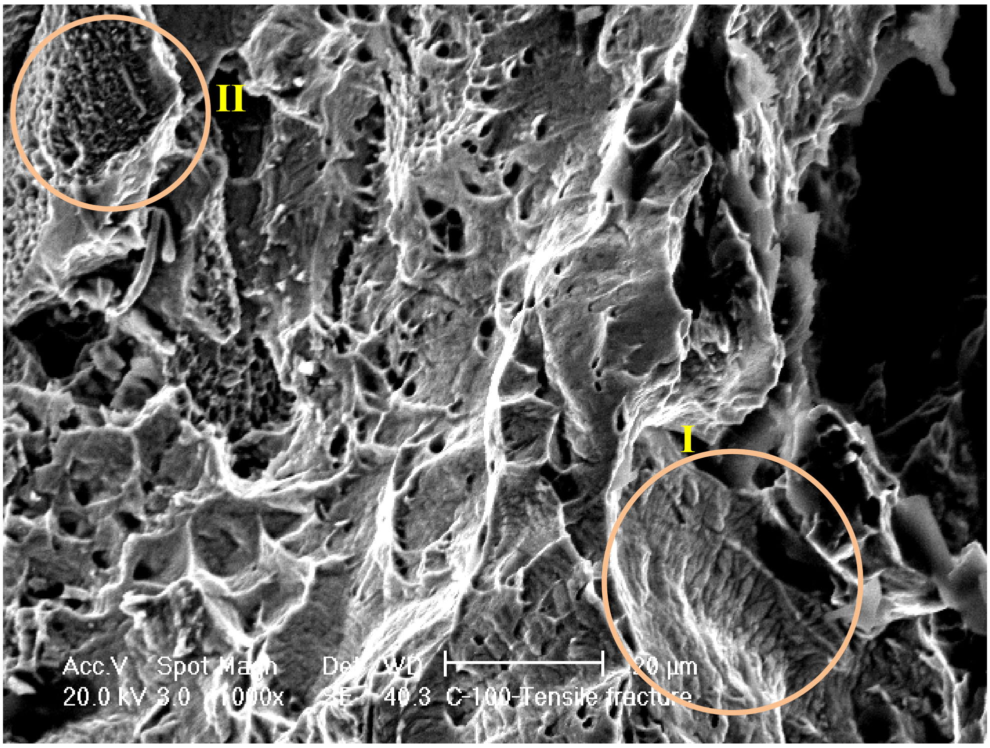

b) 1123 K – 100 h

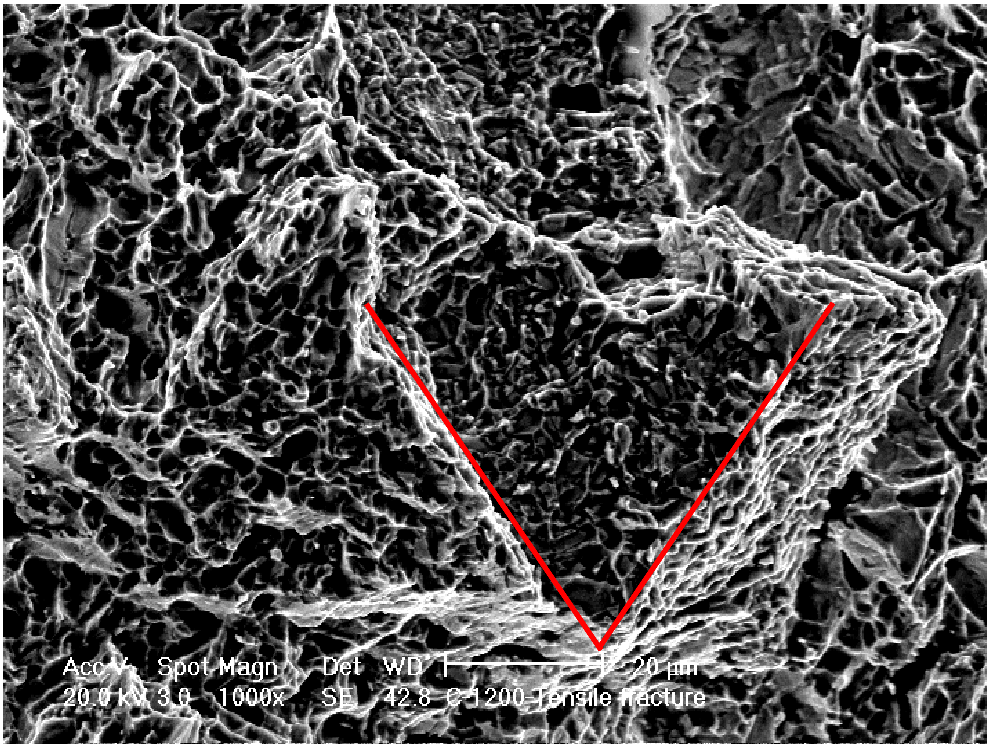

c) 1123 K - 1200 h

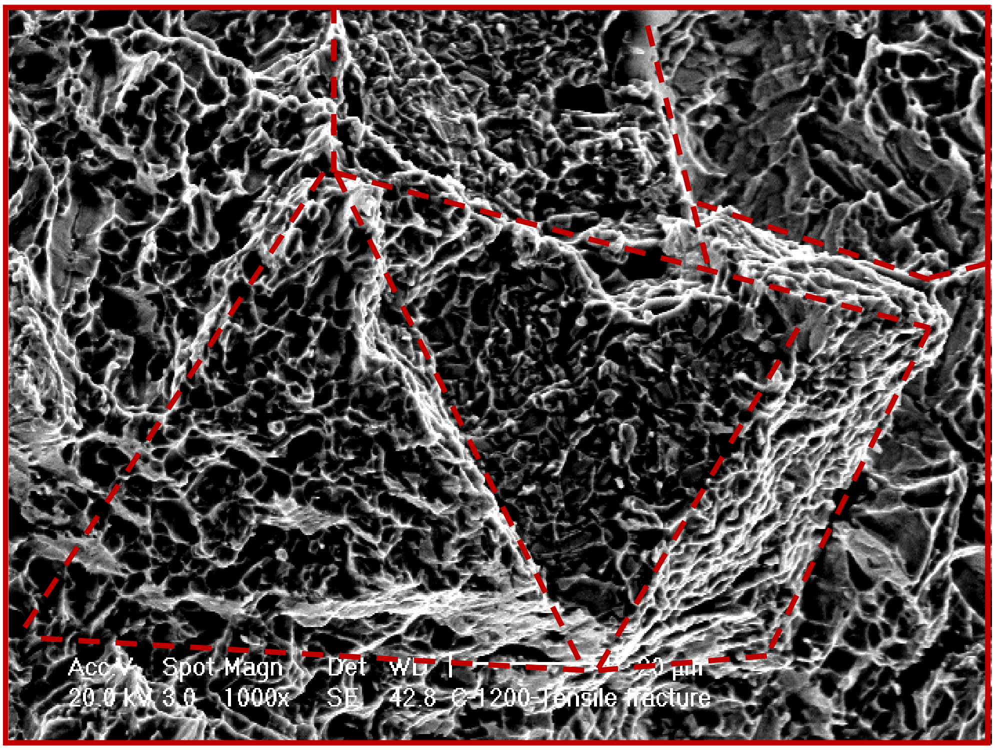

d)

Fig. 5.11: Pictures in *a, b* and *c* are the fractographs from samples, aged at 1123 K for 10 h, 100 h, and 1200 h, respectively. Lines in *d* demarcate apparent intersections of prominent facets of fractograph in *c*.

5.3 Discussion

In the present study, isothermal aging treatments of Alloy 625 samples at 813 K, 973 K and 1123 K have revealed the effect of various precipitations on the room temperature mechanical properties of the alloy. While, $Ni_2(Cr,Mo)$ and γ'' are formed on aging at 873 K, aging at 973 K and 1123 K have rendered emphasis on the formation of γ'' and δ phases, respectively. In this *section*, effect of these ordered phases, on the tensile properties and fracture behavior of Alloy 625 has been discussed and correlated with the corresponding microstructures.

5.3.1.1 Solution Quenched

As discussed in 4.3, SQ Alloy 625 microstructure comprises single matrix phase that of a typical solution annealed face-centered-cubic alloy, thereby showing good ductility as given in Table 5.1. Appearance of large dimples in the fractographs of SQ sample in Fig. 5.8 indicates that solid-solution matrix of Alloy 625 undergoes a void nucleation and growth process that culminates into the fracture. Blocky primary-carbide particles, as has been analyzed in Fig. 4.1 and Fig. 4.2 and is shown by the down-arrow in Fig. 5.8, act as nucleation sites for the large voids. Changes in the fractographs as a result of isothermal holding at three other temperatures, is discussed in the following sub-*section*s and would be compared with that of SQ Alloy 625 to ascertain the differences.

5.3.1.2 Isothermally Treated at 813 K

Formation of $Ni_2(Cr,Mo)$ and γ'' in Alloy 625 due to isothermal holding at 813 K, has produced GND's. As reported earlier [40], these second phases are coherent or semi-coherent in nature and are sheared by dislocation during deformation. Hence, while ordered phases, blocking the dislocation gliding, causes rise in the YS, dislocation cutting past the ordered phases leads to the weakening of the precipitate, that promote planar slip. Compared to all other aging temperatures, isothermal treatment at 813 K, producing $Ni_2(Cr,Mo)$ and γ'', has maximum influence on the YS and UTS of the alloy. The maximum YS of the service exposed alloy, as reported in the literature [21], due to γ'' and $Ni_2(Cr,Mo)$, is 1083 MPa that is much higher than that of the sample aged for 1200 h at 813 K, which is 557 MPa. This suggests that the precipitation after 1200 h at 813 K is far from the completion. Although, strengthening at this temperature is due to the formation of both the ordered phases, formation of $Ni_2(Cr,Mo)$ at 813 K appears to have major contribution on the strengthening, since, dissolution of $Ni_2(Cr,Mo)$ above 873 K is known to cause significant reduction in strength and increase in ductility [21,22].

In general, the effect of aging at 813 K on the fracture process may be summarized in terms of the evolution of shear facets and the reduction in the overall depth and size of dimples. In particular, fractographs from 813 K - 10 h sample are almost similar to that of the SQ sample, except, in the size and depth of its dimples. Hence, the reduction in ductility after 10 h of aging is supposedly caused by the initiation of precipitation process rather than a statistical variation. Upon aging beyond 10 h, escalation in the short-range rearrangement of solute atoms is expected to enhance the planar slip. After 1200 h at 813 K, when γ'' and $Ni_2(Cr,Mo)$ is more prominent in Alloy 625 matrix but is still in the coherent or semi-coherent state, gliding dislocations weaken them by shearing. This causes extensive planar slip and localization of the plastic flow. Shallow dimples and micro-cracks observed in. Fig. 5.9 (b) are due to the high density of flow-localization. However, upon long duration of aging, $Ni_2(Cr,Mo)$ becomes semi-coherent making availability of a large number of GND's in 813 K – 1200 h sample [76]. These GNDs possibly make provision for large amount of cumulative slips avoiding formation of micro-cracks, and, as a result of this, the ductility of this sample is higher than nearly all the aged samples.

5.3.1.3 Isothermally Treated at 973 K

Holding Alloy 625 isothermally at this temperature results in the growth of γ'', which is associated with the formation of GND's as has been evidenced through TEM and OIM results in Fig. 4.6 and Table 4.2, respectively. Result in Table 5.1 suggests that the locking of the GND's and blocking of the gliding dislocation during deformation, which is intensified with the duration of aging, cause steady rise in the tensile strength and reduction in ductility of the alloy. Change in the $\sigma - \varepsilon$ behavior of 973 K – 100 h sample (Fig. 5.4) from that of SQ sample is seen to be significantly higher than that of all other 100 h sample. This may be attributed to the rise in CSL Σ1 boundaries, which have come from the GND's.

The fractographs presented in Fig. 5.10 (a) – (c) show that the fracture mode gradually shifts from ductile to intragranular cleavage fracture as the holding time at 973 K is increased. Fracture process in 973 K – 10 h specimen is predominantly through microcracks, as shown by the arrows in Fig. 5.10 (a). On the path of planar dislocation motion, accumulation of dislocation at the obstacles is likely to be the mechanism behind such microcrack formation. Apart from this, fracture of 973 K – 10 h sample also show river like pattern (shown in the encircled region of Fig. 5.10 (a)). With further growth of γ", as in the case of 973 K – 100 h sample, fracture surface becomes prominently faceted with some less prominent dimple-regions.

Such faceted fracture due to the presence of γ' precipitates is also noticed in many other precipitated Ni-base alloys, reported in the literature [60,61], where, both {111} type and {100} type facets are observed. In the case of Alloy 625, elliptical cracks are seen to be branching-out at right-angle (Fig. 5.10 (c)) which is attributed to the orthogonal orientation of elliptical γ" in 973 K – 1200 h matrix. Hence, as some of the facets in Fig. 5.10 (c) are visually seen to be perpendicular to each other, they are along the plane of γ" precipitates and, therefore, to be along {100} plane [77], which is in agreement with a similar phenomenon, identified in an earlier work reported in the case of IN738LC alloy with γ' precipitates [61].

Increase in the faceted region and decreases in the dimple content of the fracture surface are attributed to growth of γ" and the associated changes in the CSL boundaries in Alloy 625. Although, the intragranular facets of the fracture surface in Fig. 5.10 (c), apparently, indicate much lesser ductility, the Superalloy with γ" actually shows a uniform strain above 23 %. Hence, when the alloy is deformed with considerable amount of γ" phase in the matrix, it fractures into cleavage manner only after considerable amount of dislocation motion followed by looping and its accumulation around γ" phase.

5.3.2 Isothermally Treated at 1123 K

Since, 1123 K is the nose temperature of the "*C*" curve corresponding to δ phase of Alloy 625 (Fig. 1.1), the ordered phase is present in all the samples, including in 1123 K – 10 h. This is confirmed through Fig. 4.4 (h).

At 1123 K, thermal activation is supposed to be high enough for the dislocation to cross-slip across the glide planes. Hence, initial reduction in YS of 1123 K – 10 h sample, as mentioned in Table 5.1, is possibly due to the combined effect of softening of the Alloy 625 matrix due to annihilation of the defect at 1123 K, as explained in *section* 4.3, and inability of fine δ-phase to offer significant resistance to dislocation motion. It is also evidenced from Table 5.1 that the growth of δ as a result of longer isothermal holding at 1123 K causes rise in strength and fall in ductility. When compared to 973 K samples with γ" in the matrix, it may be observed that 1123 K samples with δ laths in the matrix offer lesser strength and ductility. This may be attributed to the absence of contribution from GND's, as can be confirmed through the annihilation of $\Sigma 1$ in Table 4.2, which is in opposition to the case of 973 K samples, where $\Sigma 1$ boundary fraction keeps rising with the growth of γ''.

The fractographs from samples, aged at 1123 K, are characterized with fine dimple surface, as confirmed through Fig. 5.11 (a), (b) and (c). Reason for such appearance may be attributed to micro-void nucleation as a result of dislocation motion in the matrix with fine δ phases. The fracture surface of 1123 K – 1200 h sample appears to comprise planar regions, the outline of which is shown in Fig. 5.11 (d). These planar regions are containing uniform micro-dimples, as opposed to the facets in 973 K -1200 h sample (Fig. 5.10 (c)). Since, 70.5^{o} angle is observed among $\{111\}$ planes, appearance of similar angles between two planes, as marked by two red lines on Fig. 5.11 (c) and (d), indicates the facets to be of $\{111\}$ plane type [77]. This is in agreement with the postulation that the pinning of dislocation by the lath type δ in 1123 K – 1200 h sample is ineffective that indicates some shearing of the precipitates during dislocation glide are inevitable. Similar $\{111\}$ type facets are also observed by earlier workers in γ' containing Ni-base alloy, typically when the precipitates are cut by the fatigue crack [61].

5.4 Summary

5.4.1 Mechanical Properties

Changes in the mechanical properties due to the changes in the microstructure of Alloy 625 are summarized below.

1. Growths of ordered phases raise strength and lower ductility of Alloy 625.
2. Growths of $Ni_2(Cr,Mo)$ and γ'' at 813 K in comparison to that of other ordered phases are seen to have maximum effect on the UTS.

3. Compared to that of 973 K – 1200 h sample, near about 20% smaller YS of 1123 K – 1200 h sample indicate that the plate shaped δ in the latter is less effective in pinning the dislocation than that of γ'' in the former. However, values of uniform strain in both of them are comparable.
4. Work-hardening analysis of the *true stress – true strain* curves should be carried out in order to correlate the changes in slopes of those plots, albeit, deformation micro-mechanisms with the microstructures.

5.4.2 Fracture Behavior

Different types and sizes of ordered phases have influenced the deformation process of Alloy 625 matrix to produce various types of fracture surfaces.

1. Primary carbides act as void nucleation sites in solution quenched Alloy 625 during tensile deformation.
2. Growth of $Ni_2(Cr,Mo)$ and γ'' and associated restructuring of coincidence site lattice boundaries at 813 K lead to the reduction in dimple size and the possible rise in the facets in tensile-fracture surface.
3. Connection of crack along (100) lens plane, which is the direction of orientation of γ'' causes the faceted cleavage type fracture after significant amount of uniform strain.
4. Interaction of dislocation with lath type δ is not only limited to impenetrable interactions but also extended to some shearable interactions, which causes fine dimple-fracture surface along (111) plane. These warrant the investigation of deformed structure in further detail.

CHAPTER 6

6 Study of Deformed Microstructures of Alloy 625

6.1 Introduction

Study of deformed microstructure is useful in revealing the micromechanism of deformation in test specimen [47,78]. Such posterior study is possible from the imprint of interaction of dislocations with various constituents of the microstructure. In the previous chapters, it has been observed that various degrees of growth of different types of precipitate has influenced the mechanical properties and fracture behavior of Alloy 625. This has acted as motivation for studying the deformed microstructures of Alloy 625 that is expected to give details of the dislocation-precipitation interaction in the alloy.

6.2 Results

6.2.1 Study of Deformed Tensile-Gauge Regions

As depicted in Fig. 5.6 (a), thin sections from the deformed gage regions near tensile-fracture surface have been observed under TEM and the adjacent surfaces have been observed under optical microscope. While optical micrographs, in general, show planar slip pattern for all the deformed samples, TEM micrographs give details of interaction of dislocations with the ordered phases.

6.2.1.1 Optical Micrographs

Optical micrographs in Fig. 6.1 are from the deformed gauge length, ~1 mm away from fracture surfaces of SQ, 813 K – 1200 h, 973 K – 1200 h and 1123 K – 1200 h broken tensile specimens, respectively.

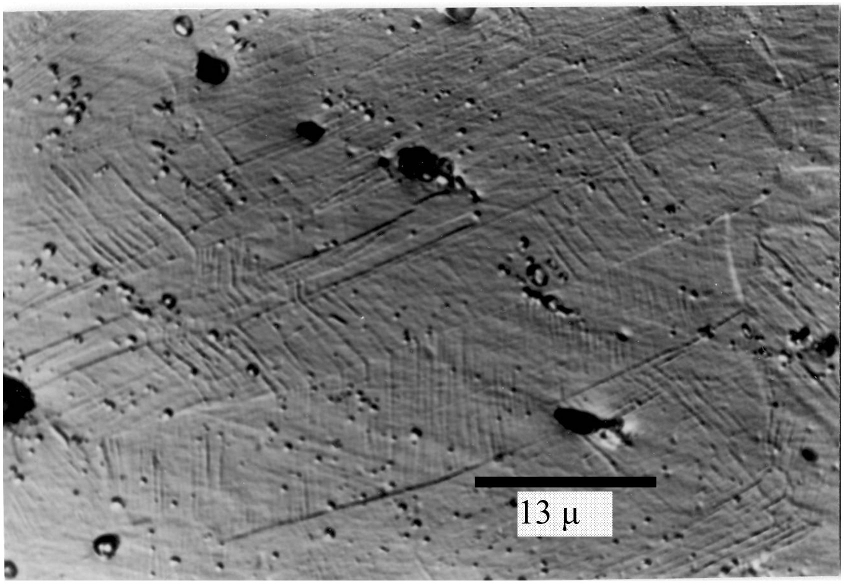

a) SQ

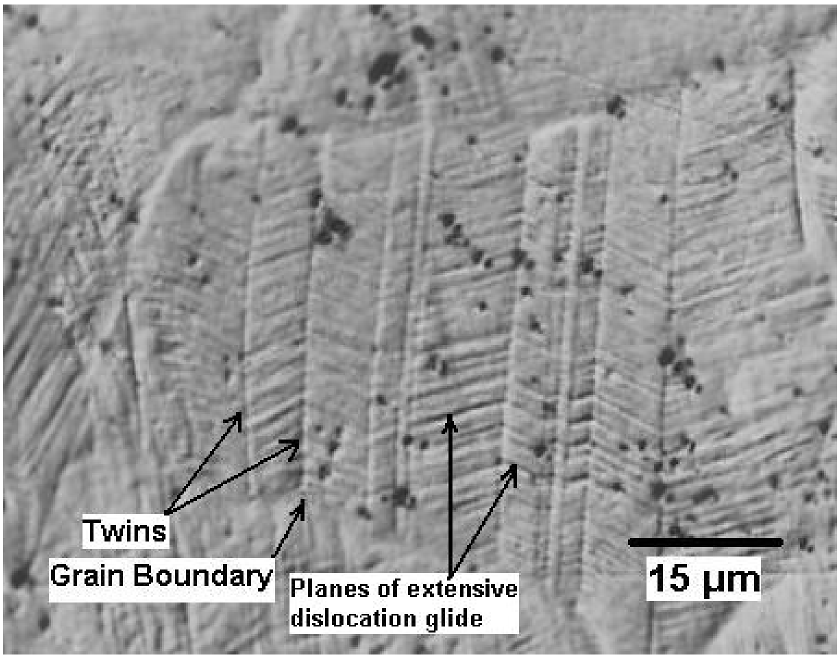

b) 813 K – 1200 h

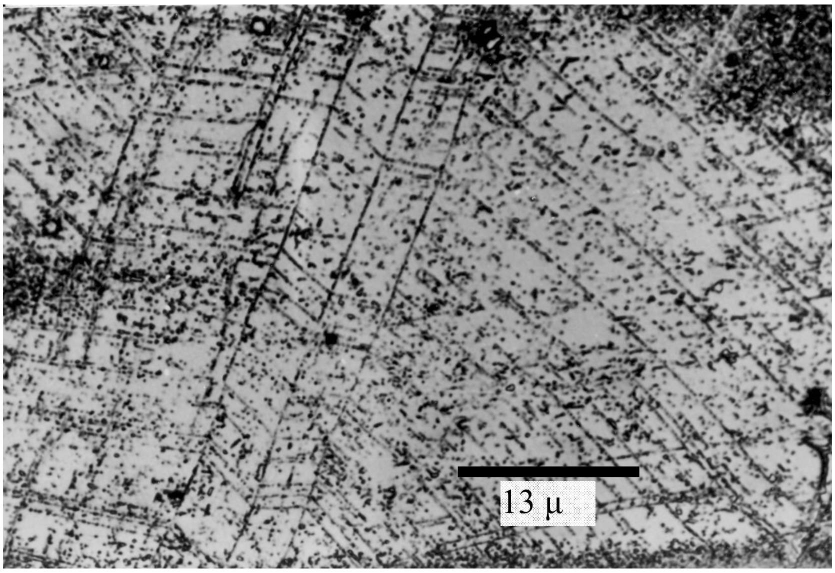

c) 973 K – 1200 h

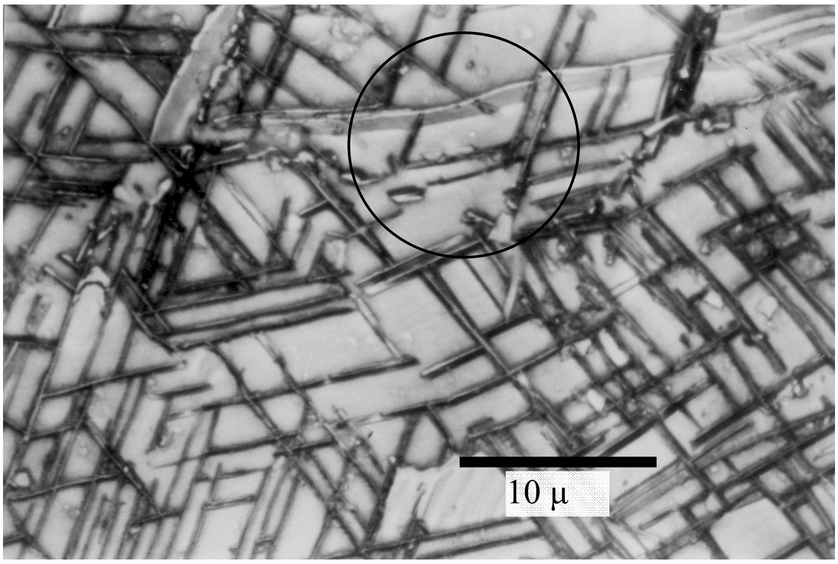

d) 1123 K – 1200 h

Fig. 6.1: (a) – (d) Optical micrographs from the deformed gage length, ~1 mm away from fracture surfaces of SQ, 813 K – 1200 h, 973 K – 1200 h and 1123 K – 1200 h broken tensile specimens showing parallel planes on which extensive slip have occurred. (b) Optical micrograph of deformed 813 K – 1200 h specimen showing twins and planes of extensive dislocation glide that remains contained

within the grain. (d) Cutting of δ plates due to dislocation - δ interaction has been shown in the encircled region.

Parallel slip lines are seen on all the micrographs, as a result extensive dislocation glide. Although, it is quite common in all varieties of samples, slip lines are seen to spread across the twin boundaries but to remain within grain boundary, as shown by labeling in Fig. 6.1 (b), which is from 813 K – 1200 h specimen. Cutting of δ plates due to dislocation - δ interaction has been shown in the encircled region Fig. 6.1 (d).

6.2.1.2 Transmission Electron Micrographs

Transmission electron micrograph and the selected area diffraction pattern in Fig. 6.2 are from the deformed region of tensile-fractured 813 K – 1200 h specimen, which shows the region of planar slip with high dislocation density. SAD pattern from the deformed region, at the most, shows only weak intensity from $Ni_2(Cr,Mo)$ and no indication of γ''.

TEM micrographs from the near-fracture surface of broken tensile specimen, which underwent isothermal treatments for 1200 h at 973 K and 1123 K, respectively, prior to deformation, are shown in Fig. 6.3 and Fig. 6.4. The micrograph in Fig. 6.3 (a) shows uniformly distributed γ″ with the mark of deformation in the matrix, across the twin boundaries. Further magnification of the area shows that lens shaped γ″, marked “A” and “B” typically, are oriented along two directions. However, contrast from heavily slipped (111) type parallel planes is seen only on one side of “B” type γ″, except in a few cases, such as “B'”. There has been hardly any instance during the TEM investigation of the deformed sample, where γ″ in 973 K – 1200 h is seen to be sheared as a result of the dislocation pile-up at the matrix side of matrix-γ″ interface.

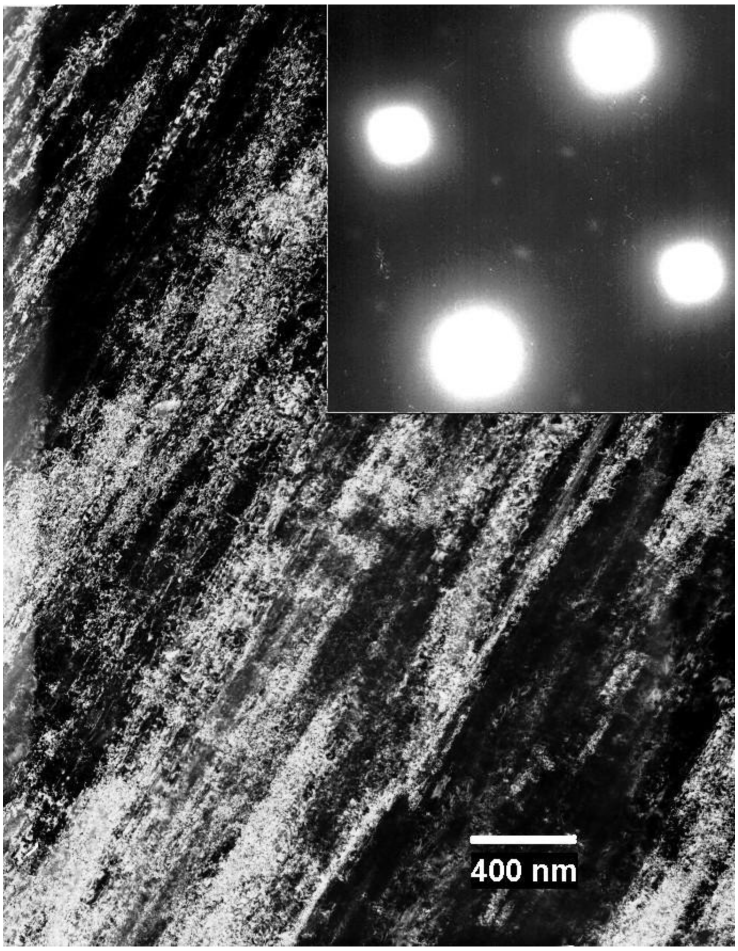

Fig. 6.2: Transmission electron micrograph from the deformed gage lengths, ~1 mm away from the tensile fracture surfaces of 813 K – 1200 h specimen showing extensive planar slip. SAD pattern in the inset shows weak intensity from $Ni_2(Cr,Mo)$.

Similar to that of Fig. 6.3, contrast in Fig. 6.4 has also been produced by viewing along (111) plane of the *fcc* matrix of Alloy 625. At least on three instances, which are encircled on the micrograph in Fig. 6.4, thick plates of δ laths are clearly seen to be sheared by the dislocations. Shear-step measured from the encircled region-I, near centre of the micrograph shows the length of the step is approximately 29 nm long. This may be correlated with the passage of about 120 dislocations, having the burger's vector of 0.249 nm in magnitude.

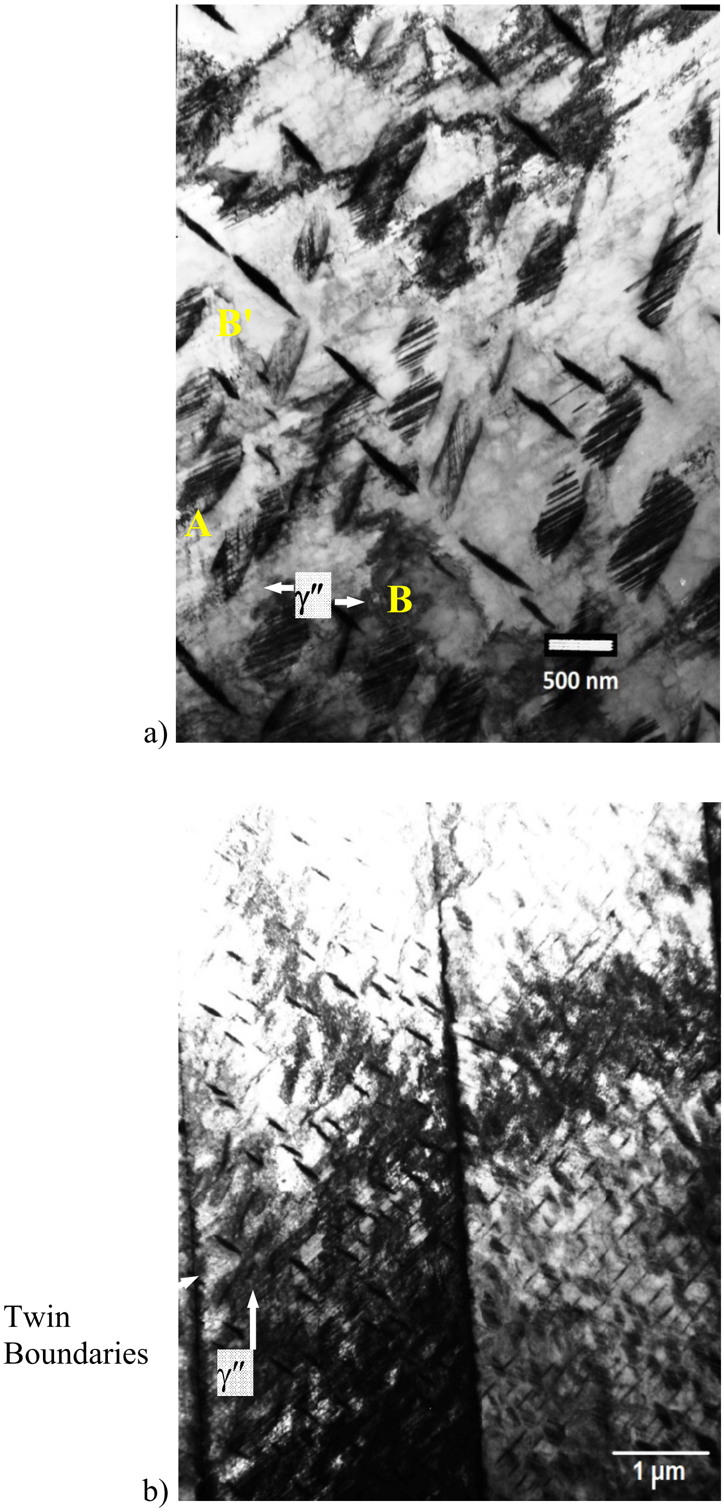

Fig. 6.3: (a) Lens shaped γ″, marked "A" and "B" typically, are seen to be oriented along two directions. Except in "B'", contrast from heavily slipped (111) type parallel planes is seen on one side of "B" type γ″,. (b) Uniform deformation on both the sides across twin boundaries is observed.

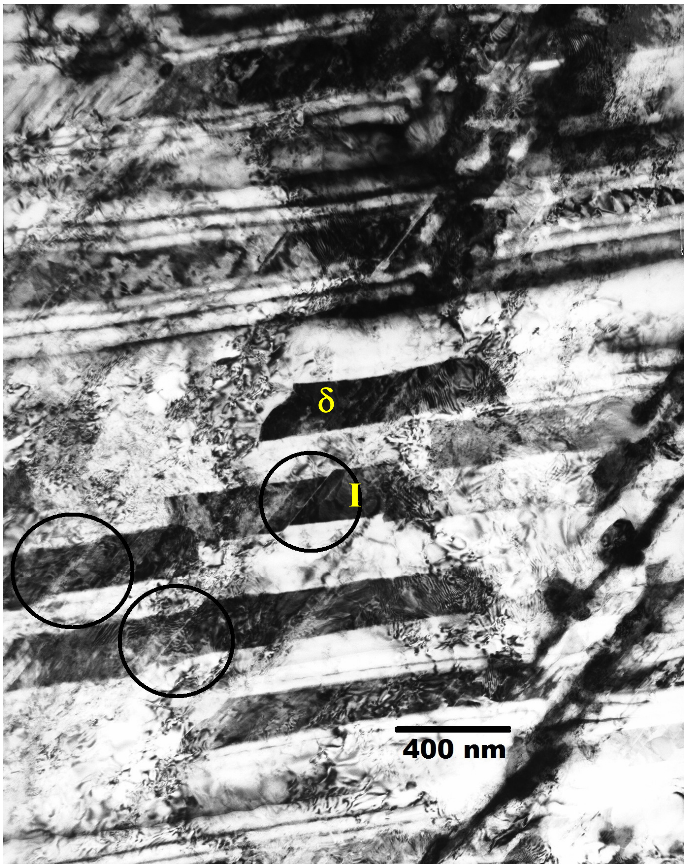

Fig. 6.4: Transmission electron micrograph from the deformed gage region, ~1 mm away from the tensile fracture surfaces of 1123 K – 1200 h specimen.. Encirled regions are showing that thick plates of δ laths are sheared due to extensive planar slip.

6.3 Discussion

6.3.1 Dislocation Interaction in $Ni_2(Cr,Mo)$ and γ" Precipitated Alloy 625

Among various modes of interaction of moving dislocations in the precipitated alloy system, *shearing* of particles dominates for particles having size less than 10 nm [79]. In the case of isothermal exposure at 813 K, even after 100 h, early stages of ordering is seen in Ni_2(Cr,Mo) and γ", which is confirmed through the diffused intensities in the SAD pattern in Fig. 4.5 (b).

Optical and TEM micrographs (in Fig. 6.1 (b) and Fig. 6.2, respectively) from the heavily deformed regions, having Ni_2(Cr,Mo) and γ" in the matrix, clearly indicate that the planar-slip is the predominant mode of dislocation motion during room temperature deformation, in-spite of wide difference in the nature of the precipitates. This is in contrast to the deformation of Al-alloys, where gliding-dislocations, due to high SFE (about 200 $mJ.m^{-2}$) cross-slips to overcome the precipitate and other obstacles. Hence, low SFE of Alloy 625, which is ~130 $mJ.m^{-2}$ [80], and the lack of activation energy for cross-slip at room temperature appear to be the reasons for the deformation to be strictly governed by the planar-slip, in which plastic strain is produced by the cutting and looping around the precipitates.

Since, change in the grain structure is not significant, as revealed through OIM study reported in Table 4.2, increase in the YS in 813 K – 1200 h appears to be due to the pinning of dislocations by precipitates and partly due to the increased dislocation density. No diffracted intensities from γ″ and weak diffracted intensities from Ni_2(Cr,Mo) in deformed 1200 h aged sample, as shown in Fig. 6.2, indicate that during the process of deformation, γ″ has been *dissolved* while, the size of Ni_2(Cr,Mo) has been reduced due to repeated shearing by dislocations. A similar phenomenon has already been reported by Sundararaman *et. al.* in their work on the low cycle fatigue behavior of aged NIMONIC PE16 alloy [81]. Analysis of the results of that study has also indicates that γ″ is likely to be in the coherent state, while, Ni_2(Cr,Mo) is in the semi-coherent state.

6.3.2 Dislocation Interaction in γ" Precipitated Alloy 625

TEM micrograph in Fig. 6.3 clearly shows that γ″ precipitates are not shearable after 1200 h of growth at 973 K. Parallel dark fringes on one side of one variant of γ″ are the heavily dislocated parallel (111) planes, which are visible when offset from the incident electron beam by a fraction of a degree. Orientation of *B*' exactly along the transmitted e^- beam supports this observation. This heavily deformed region has resulted either from the pile-up at the precipitate or from the looping of dislocation around the precipitates. With the progress of deformation, such deformed regions are expanded, which reduces the gliding length of dislocation. It appears that when the gliding of dislocations is completely hindered due to the expansion of deformed regions, voids followed by decohesion of γ″- matrix interface takes place. This causes connections of micro-cracks along the planes of the precipitates, i.e., along the principal axes of the Alloy 625 matrix. Because of this, Alloy 625 has faceted and orthogonal fracture surfaces, seen in Fig. 5.10 (c) and discussed in 5.3.1.3.

As discussed in earlier [40,76], ordered γ″ is expected to be less impenetrable during the initial stages of formation and growth. Reconciliation of these facts indicates that interaction of dislocation with γ″ gradually changes from cutting to looping with the growth of the precipitate. This has resulted in the increase in the facets with the growth of the precipitates (Fig. 5.10).

6.3.3 Dislocation Interaction in δ Precipitated Alloy 625

Three instances in the TEM micrograph, as marked by the circles on Fig. 6.4, clearly show that δ slabs in 1123 K – 1200 h, which is much thicker than γ″ in 973 K – 1200 h precipitates are sheared by the gliding dislocations. Obviously, such shearing is along

(111) plane of the matrix and the compact (010) plane of the precipitate. This supports the separation of planes, at fracture, along (111) plane with micro-dimples, which is reflected in the fractographs depicted in Fig. 5.11 (c). While this helps to accept the shearability of the thick δ slabs, dislocation – δ interaction in 1123 K – 1200 h is likely to have a large number of non-shearable interactions too.

Shearability of δ in 1123 K – 1200 h indicates easy shearability of the ordered phases during the deformations of 1123 K – 10 h and 1123 K – 100 h samples. Hence, the fractographs in Fig. 5.11 (a) and (b) are devoid of the typical faceted look, as can be seen in Fig. 5.11 (c).

6.4 Summary

Following salient points are summarized from the microscopic study of deformation in Alloy 625 with different precipitated microstructures.

1. Planar slip governs the room-temperature deformation of Alloy 625 under all precipitation conditions.
2. Domination of planar slip during room-temperature deformation restricts the interactions of dislocation in the precipitated Alloy 625 matrix within the domain of cutting and looping of $Ni_2(Cr,Mo)$, γ'' and δ ordered phases.
3. Looping and dislocation pile-up at γ'' lead to decohesion of the ordered phase followed by the linking along the planes ({100}) of the γ''-lenses, which in turn causes faceted fracture.
4. Shearing interactions of closely-spaced thick δ slabs along {111} plane causes faceted fracture surface with micro-dimples.

CHAPTER 7

7 Evaluating Work-Hardening Behavior of Alloy 625 with different precipitated-microstructures

7.1 Introduction

Modeling of work-hardening behavior aims to understand the physical phenomena behind the stress-strain response of metals and alloys. As discussed earlier, work-hardening model developed by KME explains the stress-strain behavior in terms of the *density* and the *mean free-path* of dislocation (*see* section 1.4). Physically, when a moving dislocation interacts with another dislocation or loops around an obstacle, it raises the density of dislocation in the matrix and as a result of this metals and alloys work-harden. Rise in the dislocation density is linked to the *mean free-path* of the dislocation only when the gliding dislocation adheres to a particular slip plane, since, cross-slip of dislocation does not raise dislocation density through looping. Hence, underlying principles of KME model of work-hardening analysis is that dislocation motion should adhere to the planar slip. Microstructural study of deformed samples in the previous chapter has established that dislocation precipitation interactions in the precipitated and unprecipitated Alloy 625 matrix is governed by the planar slip. work-hardening analysis of the stress-strain responses discussed in 4 is carried out here with an aim to correlate the same with the interaction of dislocation with various stages of growth of $Ni_2(Cr,Mo)$, γ'' and δ ordered phases.

In this context, it is emphasized that as long as precipitates are shearable, dislocation-dislocation interactions become responsible for the rise of its density. With the growth of precipitates, precipitates become more impenetrable to the gliding dislocation and, hence, looping of dislocation around the precipitates takes over. When the precipitates become completely impenetrable, a situation may arise, where dislocation looping becomes the predominant mode of interation for raising the dislocation density in the alloy matrix, as the chance for interacting with another dislocation between two successive looping-interaction comes down.

7.2 Work-hardening Analysis of Tensile Data

7.2.1 Work-hardening Behavior of Alloy 625 with Intermetallic Compounds

Normalized work-hardening-rate (θ/μ) vs. $(\sigma-\sigma_{YS})/\mu$ and $\sigma.\theta/\mu^2$ vs. σ/μ plots derived from Fig. 5.3, Fig. 5.4 and Fig. 5.5 are given in Fig. 7.1, Fig. 7.2 and Fig. 7.3, respectively. The region, where θ is quite independent of the flow stress is marked as stage-II in Fig. 7.1 (a). While, the work-hardening rate of 813 K – 1200 h is higher than that of other samples (Fig. 7.1 (a)), it is noticed that the initial drop in θ, prior to the stage-II is less in 813 K – 1200 h compared to that of other samples. A gradual rise in θ is clearly visible in 813 K – 1200 h when the work-hardening data is plotted in terms of $\sigma.\theta/\mu^2$ vs. σ/μ (Eq 8). Further, it may be noticed that $(\sigma.\theta)_0/\mu^2$ values for SQ and all samples held at 813 K, as shown in Fig. 7.1 (b) are close to 0.2×10^{-4}.

Similarly, normalized work-hardening-rate (θ/μ) vs. $(\sigma-\sigma_{YS})/\mu$ plots for Alloy 625, which have been held isothermally at 973 K and 1123 K, are given in Fig. 7.2 (a) and Fig. 7.3 (a), respectively. Both the plots are characterized with gradual change in strain-hardening behavior as a result of isothermal holding Equations corresponding to the straight lines, where $F(x)$ stands for $\sigma.\theta/\mu^2 \times 10^4$ and x stands for $\sigma/\mu \times 10^3$, are fitted and depicted on the respective plots. Re-writing Eq. (4) in Eq. (11), $(\theta_h/\mu) \times 10$

and $(\sigma.\theta)_0/\mu^2 \times 10^4$ values are equated with the slopes and the constants of the straight lines depicted on Fig. 7.1 (b), Fig. 7.2 (b) and Fig. 7.3 (b).

$$\frac{\sigma.\theta}{\mu^2}\times 10^4 = \frac{(\sigma.\theta)_0}{\mu^2}\times 10^4 + \frac{\theta_h}{\mu}\times 10\left(\frac{\sigma}{\mu}\times 10^3\right) \qquad \textbf{(7.1)}$$

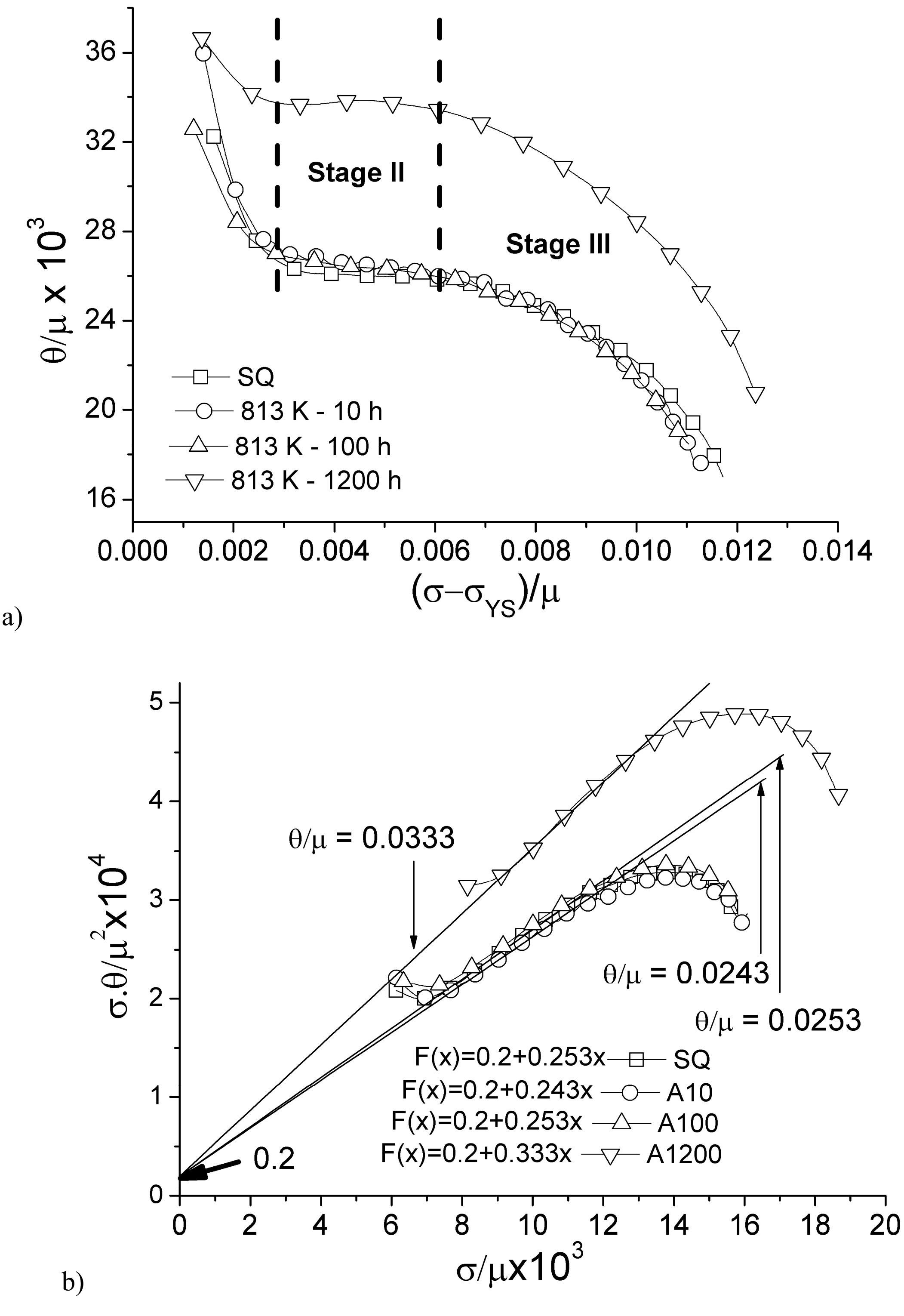

Fig. 7.1: (a) Normalized work-hardening rate plot of Alloy 625, aged at 813K for 10 h, 100 h and 1200 h along with unaged sample. (b) Normalized σθ vs. σ plot for derived from (a).

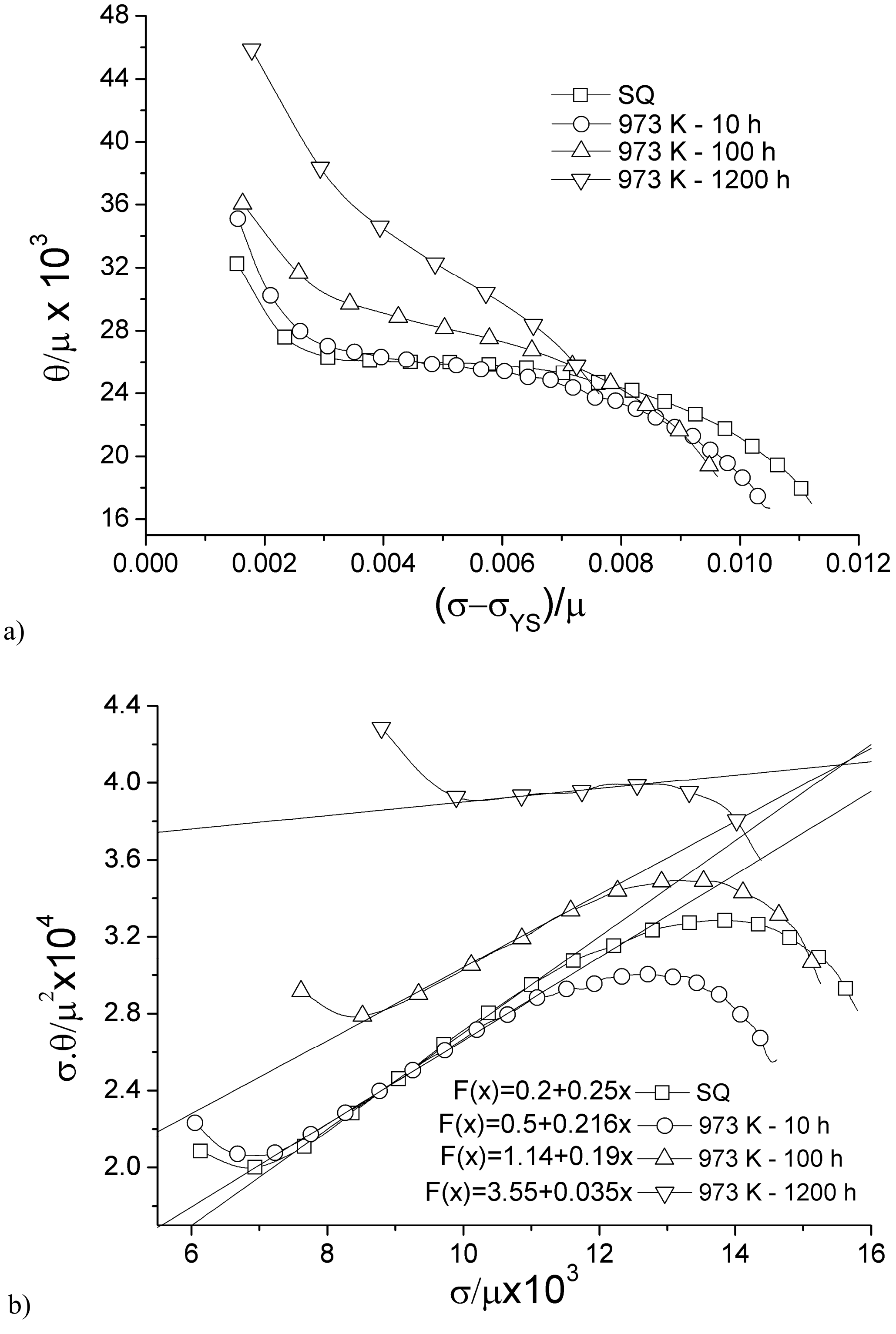

Fig. 7.2: (a) Normalized work-hardening rate plot of Alloy 625, aged at 973K for 10 h, 100 h and 1200 h along with unaged sample. (b) Normalized σθ vs. σ plot derived from (a).

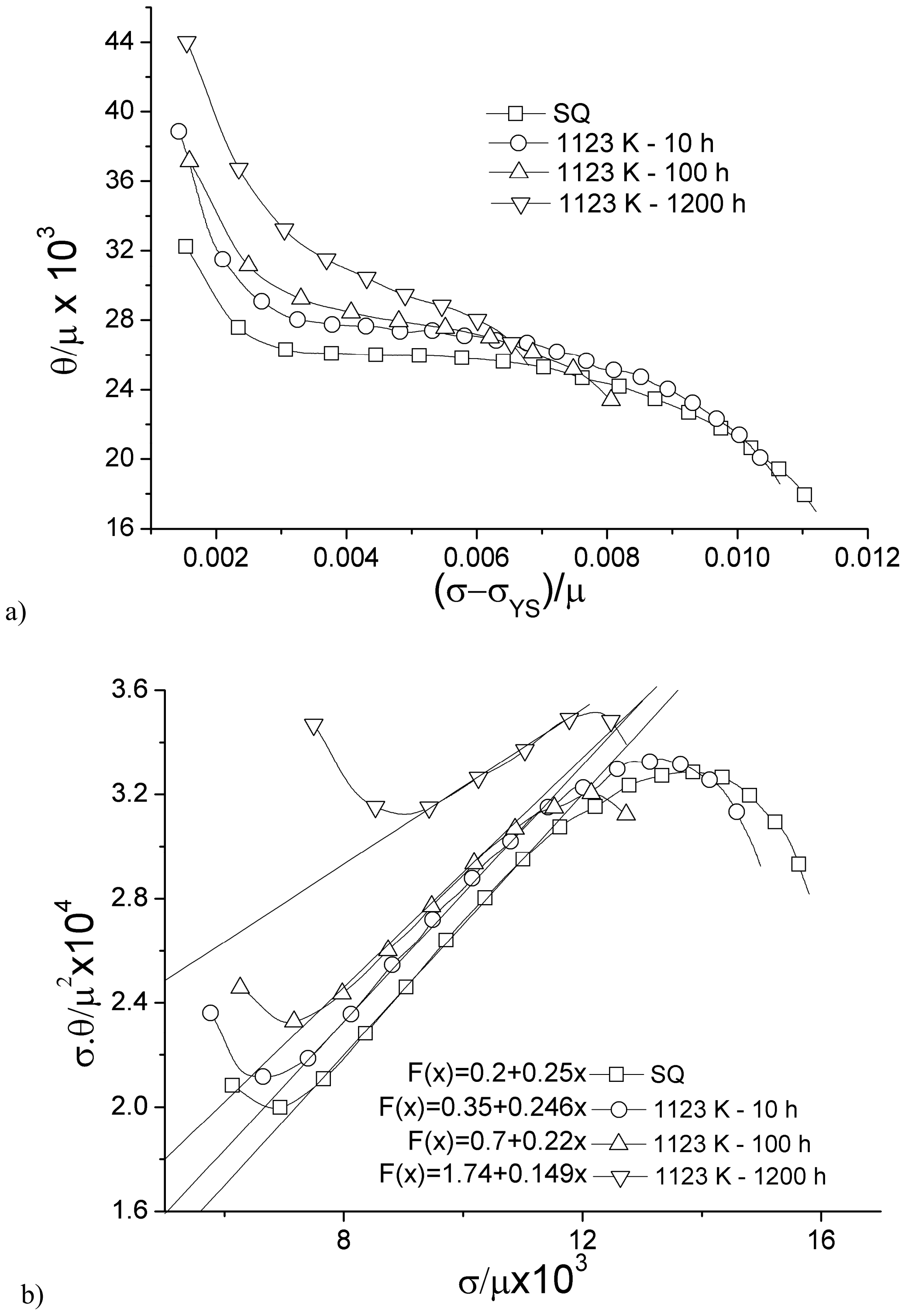

Fig. 7.3: (a) Normalized work-hardening rate plot of Alloy 625, aged at 813K for 10 h, 100 h and 1200 h along with unaged sample. (b) Normalized σθ vs. σ plot derived from (a).

7.2.2 Work-hardening Trend of Alloy 625 with Intermetallic Compounds

To obtain the trend in variations of $(\sigma.\theta)_0/\mu^2 \times 10^4$, and $(\theta_h/\mu) \times 10$ with the isothermal holding time, *t*, for both 973 K and 1123 K treated specimens, corresponding values are plotted in Fig. 7.4 and Fig. 7.5, respectively, and fitted with the exponential decay function, $f(t)= f(t_0) + A.e^{-(t/d)}$. Various constants of the fittings, such as, offset, $f(t_0)$, amplitude, *A* and decay constant, *d*, along with the χ^2 and goodness of fit, R^2, are given in Table 7.1 and Table 7.2, respectively, for 973 K and 1123 K isothermal holding cases.

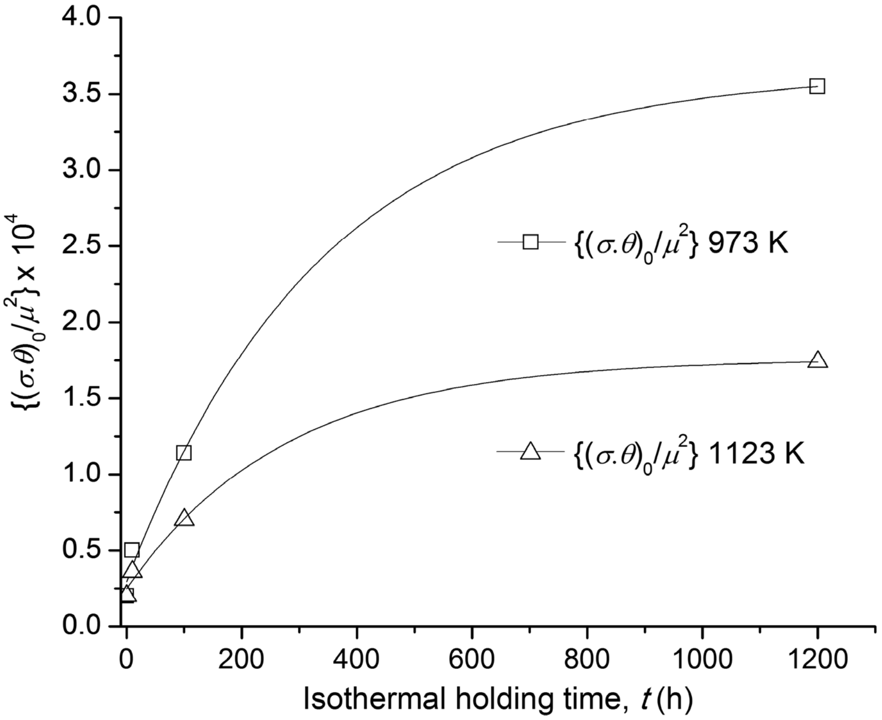

Fig. 7.4: Variations of $(\sigma.\theta)_0$ with isothermal holding time have been derived for two different precipitated microstructures of Alloy 625, which have been produced through the isothermal heating at 973 K and 1123 K.

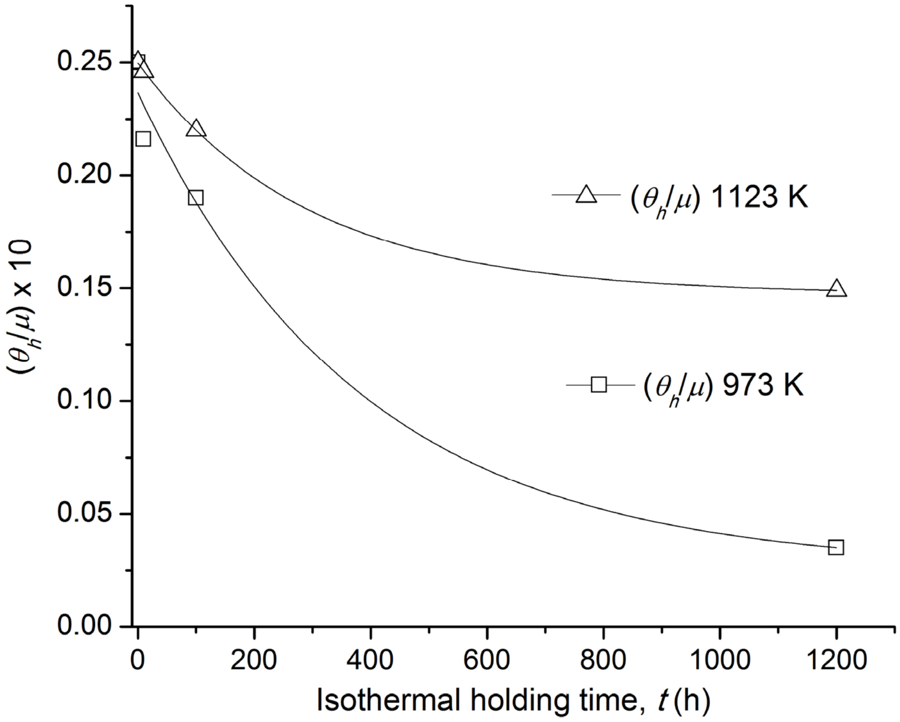

Fig. 7.5: Variations of θ_h with isothermal holding time have been derived for two different precipitated microstructures of Alloy 625, which have been produced through the isothermal heating at 973 K and 1123 K.

Table 7.1: Parameters for fitting $\{(\sigma.\theta)_0/\mu^2\} \times 10^4$ vs. t using asymptotic function $f(t) = f(t_0) + A \times e^{-t/d}$.

Isothermal holding Temperature	$f(t_0)$	A	d	χ^2	R^2
973 K	3.6447±0.1910	3.3506±0.1952	337.0316±90.4618	2.071×10^{-2}	0.997
1123 K	1.7592±0.0852	1.5098±0.0964	276.2073± 71.2645	5.744×10^{-3}	0.996

Table 7.2: Parameters for fitting $\{\theta_h/\mu\}\times10^3$ vs. t using asymptotic function $f(t) = f(t_0) + A\times e^{-t/d}$.

Isothermal holding Temperature	$f(t_0)$	A	d	χ^2	R^2
973 K	0.0261±0.0321	-0.2106±0.0307	$0.9974\pm1.81\times10^{-3}$	4.13×10^{-4}	0.985
1123 K	$0.1473\pm4.46\times10^{-4}$	$-0.1024\pm4.93\times10^{-4}$	$0.9966\pm6.93\times10^{-5}$	1.48×10^{-7}	0.999

7.3 Discussion

Deformations of Alloy 625 specimens, which have been isothermally treated at three temperatures for three different durations, have essentially led to the interactions of dislocation with three stages of growth of three different precipitates. Hence, deformation phenomena in Alloy 625 specimens, which have been isothermally treated at 813 K, is a result of the interactions of dislocations with different stages of growth of γ" and $Ni_2(Cr,Mo)$ ordered phases and associated changes in CSL boundaries. Similarly, tensile behavior of Alloy 625 specimens, which have been isothermally treated at 973 K and 1123 K, should be explained through the interactions of dislocations with different stages of γ" and δ, respectively. While, deformation of SQ is presumably by the planar slip mechanisms, as can be seen in Fig. 6.1 (a), micrographs from the deformed precipitated regions are correlated with the work-hardening analyses in the following subsections.

7.3.1 Work-hardening Behavior of Alloy 625 having $Ni_2(Cr,Mo)$ and γ'' phases in the Microstructure

As seen in Fig. 7.1 (a), work-hardening behavior of Alloy 625 in the unaged and aged condition is characterized with the initial sharp fall in θ, followed by a plateau and then a further gradual fall, which may be denoted as pre-stage II, stage II and stage III work-hardening, respectively.

Pre-stage II work-hardening

In compared to the deformation in the single crystal, there is no stage I region in the deformation of polycrystalline aggregate. However, a region prior to stage II is generally observed in the σ-θ plot of polycrystalline material. This region is characterized with the drop in θ that is sharper than that of stage II. In the literature, the reason for such behavior is attributed to gradual elasto-plastic transition of the [7,15].

However, the plausible phenomenological explanation of the elasto-plastic transition region, which has emerged from the present study, is as follows. Since, the starting material is solution annealed and the temperature of aging is greater than recrystallization temperature of the alloy, dislocation density remains low, as can be confirmed through the TEM micrographs in Fig. 4.5 (a) and Σ1 fraction in 813 K – 100 h, shown in Table 4.2. However, as the ordered phases develop incoherency, resulting in the formation of GND's, which is confirmed through TEM micrographs in Fig. 4.5 (c) and Σ1 fraction in 813 K – 1200 h, shown in Table 4.2.

During deformation, gliding of dislocation in large numbers are necessary to cause plastic strain in the material. Study indicates that in the stage II region, the density of mobile dislocation remains a constant, which is in the order of 10^8 cm/cm^3 [28,82]. However, the density of mobile dislocation and possibly the overall dislocation density in SQ and 813 K – 100 h, are presumably much lower than the density of dislocation required for the deformation in the stage II. Since, θ indicates the rate of dislocation storage, in absence of dislocation annihilation, θ equals to the rate of dislocation generation necessary for the deformation in stage II. In the present study, deformation of all samples starts with high θ followed by a large drop in θ, for all samples, except for 813 K – 1200 h sample. As confirmed through the TEM micrograph and Σ1 fraction in Table 4.2, compared to other samples, higher starting dislocation density in 813 K – 1200 h sample appears to be the reason behind the lesser drop in θ therein. This indicates that, in the pre-stage II work-hardening, which is also known as elasto-plastic transition region, *rate of dislocation generation gradually falls until it meets the necessary mobile dislocation density on the slip plane to carry out the deformation in stage II*. The drop in θ in the pre-stage II due to the availability GND's in 813 K – 1200 h sample supports this fact [76].

Stage II work-hardening

Significant part of the deformation of all categories of samples is characterized with an almost constant θ, which is, therefore, called stage II region. This indicates that the deformation mode is governed by the planar slip that is in agreement with the microstructural observations in Fig. 6.1 (a) and Fig. 6.2. Hence, a special case θ_h herein may also be called θ_{II}. Similar work-hardening trend may be noticed in the work of Del Valle *et. al.* in INCONEL X-750 alloy with an average precipitate size of 7 nm [83]. This phenomenon is quite different from that of precipitation hardened aluminium alloys, where drop in θ_h in the unaged sample is intensified further after precipitation [84,85] indicating early beginning of the recovery processes.

The athermal storage rate, θ_h/μ for SQ sample is 0.0253. This may be attributed to the *dislocation generation through dislocation-dislocation interaction* [31] that is the characteristic of SQ Alloy 625. Such value for 813 K – 10 h sample is lower by 0.001. Although the drop is minute, this may be correlated with the annihilation of dislocation, since, physically total (Σ1 + Σ3) boundary fraction as is actually seen to go down quantitatively from 0.775 (SQ) to 0.61 (813 K – 10 h). The characteristic apparently changes with the duration of aging, since, as seen in Fig. 7.1 (b), θ_h/μ increases by 0.008 in 813 K – 1200 h specimen. Such increase in θ_h/μ from 0.0253 to 0.0333 may be attributed to the formation of GNDs, which is reflected in the rise of Σ1 boundary fraction in Table 4.2 and in the TEM micrographs (Fig. 4.5 (d)).

As discussed in section 1.4, in the domain of *single parameter approach* θ_h is expressed as follows:

$$\theta_{II} = \theta_h = \frac{M^2 \alpha\mu}{2\beta} \qquad \textbf{Eq. 7.2}$$

It is possible for athermal storage rate to be high only when α is high or β is low since, M and μ is considered constant for the given alloy and testing condition. Hence, modeling of stage-II work-hardening behavior of Alloy 625 in the presence of GNDs, which is produced during precipitation is beyond the scope of the 'single parameter approach' or the modified 'hybrid model', which does not allow change in α and β and warrants a multiple dislocation density approach with an emphasis upon different types of mobile and sessile dislocations. Hence, as indicated by the TEM micrographs and OIM results, *formation of GNDs, appears to be responsible for the increase in* θ_h/μ.

As described by Kocks-Mecking-Estrin (KME), nature of $\sigma.\theta/\mu^2$ vs. σ/μ plot indicates whether the deformation is governed by the changing mean free path due to dislocation-dislocation interaction alone or by the impenetrable obstacle providing a fixed mean free path [30,31]. Analysis of $\sigma.\theta/\mu^2$ vs. σ/μ plot in Fig. 7.1 (b) results in a finite value of $(\sigma.\theta)_0/\mu^2$, 0.2×10^{-4}, and a positive starting slope, 0.0253. As described by KME, a positive θ_h occurs due to the continuous reduction in mean free path during dislocation-dislocation interaction. Same $(\sigma.\theta)_0$ value for all types of samples indicates absence of impenetrable obstacles i.e. precipitates are shearable even after 1200 h of aging. It appears from Fig. 6.1 (b) that the movement of dislocations is restricted within the grain boundary. This *largest value of gliding distance of dislocation, controlled chiefly by the grain size, appears to have reflected in the small value of* $(\sigma.\theta)_0$.

However, present understanding largely differs from that of Del Valle *et al* [83] where, low value of $(\sigma.\theta)_0$ was argued from two angles. First, the density of GNDs actually present in the sample has been thought to be less than what is obtained from the precipitate size and volume fraction. Second, stress contribution of the GNDs was thought to be less than what is arising from forest dislocations.

Present investigation, based on the determination of CSL boundaries and the study of deformed micrographs from optical and TEM, leads to the following understanding. GNDs increases the work-hardening rate, θ_h and dislocation annihilation causes lowering of θ_h/μ,. The constant term, $(\sigma.\theta)_0$, of $\sigma.\theta/\mu^2$ vs. σ/μ plot is not affected by the shearable precipitate in the matrix. Shearable precipitate gives maximum resistance during yielding and once sheared, they facilitate planar slip.

Stage III work-hardening

The drop in the slope of 813 K – 1200 h sample of Fig. 7.1 (b) occurs early and is more intense than that of rest of the samples, held isothermally at 813 K. This indicates faster recovery rate of 813 K – 1200 h sample compared to others. This may be attributed to higher dislocation density in 813 K – 1200 h sample that facilitate an early annihilation of process, vis-à-vis, faster recovery in the work-hardening.

7.3.2 Work-hardening Behavior of Alloy 625 having γ" phase in the Microstructure

Various work-hardening responses in Fig. 7.2 are ascribed to the changes in the interactions of dislocations with various degrees of growth of γ″ during the tensile deformation of Alloy 625. Hence, the gradual change in the interaction of dislocation-γ″ from cutting to looping is responsible for the rise in $(\sigma.\theta)_0$ and fall in θ_h values, as revealed in the work-hardening plot in Fig. 7.2 (b).

With the increase in the duration of isothermal holding, γ″ becomes fully impenetrable. As discussed in 6.3.1, dislocation cutting through the precipitate is responsible for the rise in the YS of the alloy. Since, the MFP of dislocation is not affected by the cutting process, contribution in θ_h continues to come from the dislocation multiplication process, which is similar to that of the unprecipitated-SQ Alloy 625 matrix. However, when the precipitates grow to become impenetrable, gliding dislocations undergo looping type interaction, making the fixed MFP, λ_c, term prominent, which is otherwise provided by the grain boundaries in the case of SQ

Alloy 625 (section 7.3.1). Apart from this, lowering in θ_h values with the growth of both types of precipitates, as seen in Fig. 7.2 (a) appear to come from a less intense dislocation multiplication process as compared to the SQ Alloy 625. This also may be attributed to the lowering of average travel length of gliding dislocations, vis-à-vis decrease in MFP, since, the planar-slip governs the dislocation glide process.

Various work-hardening behaviors obtained from the tensile deformation of SQ and precipitated Alloy 625 may be correlated with the KME model in the following manner. The SQ Alloy 625 represents the case of largest starting fixed-MFP, where the effect of variable MFP, based upon the dislocation density, becomes significant and, hence, the work-hardening may be closely approximated by Eq. (5). With the rise in the impenetrable interactions of dislocation, as it becomes maximum with γ'' after 1200 h of isothermal holding at 973 K, θ_h continues to fall to become negligibly small and the work-hardening of the precipitated alloy may be appropriately represented by Eq. (6). Rests of the work-hardening responses are seen to be describable by Eq. (4), which represents the combined effect of fixed and variable MFP. Hence, the *hybrid model* of KME [30,31] is found suitable to describe the work-hardening behavior of γ'' precipitated Alloy 625, as the deformation with various degrees of growth of γ'' remains adherent to planar-slip.

$(\sigma.\theta)_0$ and θ_h values, associated with the growth of γ'' ordered phase, as obtained from the expressions in Fig. 7.2 (b), are seen to vary systematically. When fitted with exponential decay functions in Fig. 7.4 and Fig. 7.5, χ^2 and goodness of fit R^2 values show excellent fit except for the one representing the variation in θ_h due to isothermal holding at 973 K. As may be seen from Fig. 7.5, the goodness of fit is affected by the lack of parity in the fall of θ_h after 10 h at 973 K. The fall appears to have resulted from dislocation interaction in the precipitated matrix associated with rapid initial growth of γ″ phase.

7.3.3 Work-hardening Behavior of Alloy 625 having δ phase in the Microstructure

The gradual change in the interaction of dislocation with δ from cutting to looping is responsible for the rise in $(\sigma.\theta)_0$ and fall in θ_h values, as revealed in the work-hardening plot in Fig. 7.3 (b). However, compared to that of γ″, increase in $(\sigma.\theta)_0$ and drop in θ_h to a lesser degree are ascribed to the smoother change in dislocation- δ interactions, which remains partially shearable even after the growth of δ for 1200 h at 1123 K. Annihilation of Σ1 boundary due to the holding at 1123 K also ensures smooth gliding of dislocation and a larger effective MFP of dislocation thereby.

$(\sigma.\theta)_0$ and θ_h values, associated with the growth of δ, as obtained from the expressions in Fig. 7.3 (b) are seen to vary systematically. When fitted with exponential decay functions in Fig. 7.4 and Fig. 7.5, χ^2 and goodness of fit R^2 values show excellent fit.

7.3.4 Comparison between the interaction of dislocations with γ″ and δ

Interactions of dislocations with two types of precipitates, γ″ and δ, having various degrees of growth in Alloy 625 matrix and the corresponding work-hardening responses have been discussed above. With the increase in the duration of isothermal holding, γ″ becomes fully impenetrable, while δ remains partially penetrable to the gliding dislocations. As discussed earlier, dislocation cutting through the precipitate is responsible for the rise in the YS of the alloy. As long as gliding dislocations cut through the precipitates, contribution in θ_h continues to come from a dislocation multiplication process vis-à-vis from a variable MFP, which is similar to that of solution-quenched Alloy 625. However, when the precipitates grow to become impenetrable, it causes looping type interaction with the gliding dislocation and brings down the fixed MFP, λ_c. Apart from this, lowering in θ_h values with the growth of both types of precipitates, as seen in Fig. 7.2 and Fig. 7.3, appear to come from a less intense dislocation multiplication process as compared to that of SQ Alloy 625. This is also attributed to the lowering of average travel length of gliding dislocations, vis-à-vis decrease in MFP, since, the planar-slip governs the dislocation glide process. Hence, compared to that of 973 K – 1200 h sample, higher value of θ_h in the case of 1123 K – 1200 h sample may be attributed to more intense dislocation-dislocation interaction in the latter. This has been possible through the cutting of δ and annihilation of Σ1 boundaries in 1123 K – 1200 h in contrast to 973 K – 1200 h, where Σ1 boundary fractions are seen to go up.

It may be noticed that the peak $\sigma.\theta$ value, 3.52 (Fig. 7.3 (a)), due to the dislocation interaction with δ in 1123 K – 1200 h sample, is also close to the maximum $(\sigma.\theta)_0$, 3.55, for γ'' in 973 K - 1200 h, in which the work-hardening behavior is described by Eq. (6). This indicates that maximum $(\sigma.\theta)_0$ in Alloy 625 is possibly bound the limit 3.6447 ± 0.1910, which is obtained from the asymptotic relation with infinite isothermal holding time at 973 K (Table 7.1). Hence, the parameters in Table 7.1 and Table 7.2 not only *provide the relation to predict the work-hardening behaviors of Alloy 625* against the duration of isothermal holding at 973 K and 1123 K but also *predict the ranges of* $(\sigma.\theta)_0$ *and* θ_h *values for different degrees of growth of* γ'' *and* δ in Alloy 625.

Various work-hardening behaviors, noticed during the deformation of SQ and precipitated Alloy 625 are correlated with the KME model as follows. The SQ Alloy 625 and, also, Alloy 625 samples with shearable $Ni_2(Cr,Mo)$ and γ represents the case of largest starting fixed-MFP. Here, variable MFP is based upon the dislocation density and, hence, the work-hardening is closely approximated by Eq. (5). With the rise in the impenetrable interactions of dislocation, as it becomes maximum with γ'' after 1200 h at 973 K, θ_h continues to fall to become negligibly small ($\theta_h/\mu = 0.0035$) and the work-hardening of the precipitated alloy may be appropriately represented by Eq. (6). Rests of the work-hardening responses can be described by Eq. (4), which represents the combined effect of fixed and variable MFP.

As elaborated earlier, in the *hybrid model* of KME, variable MFP and fixed MFP concepts parameterizes two physical phenomena of work-hardening, i.e. dislocation multiplication through dislocation – dislocation interaction and through looping of impenetrable precipitates, respectively. Hence, in any system deformation mechanism adhering to these two dislocation-multiplication processes is a prerequisite to interpret the work-hardening behavior of the system satisfactorily in terms of KME model. It essentially means that the gliding of dislocation during deformation should obey the *planar-slip*. In the present study, it has been possible to described work-hardening behavior of Alloy 625 satisfactorily through the KME model as it has remained adherent to planar-slip under all precipitation conditions.

7.4 Summary

Work-hardening (WH) behaviors of precipitated and SQ specimens have been analyzed in terms of $\sigma.(d\sigma/d\varepsilon)$ vs. σ from the corresponding room-temperature tensile true-stress (σ) – true-strain (ε) plots.

1. It has been revealed that the *work-hardening quotient term*s (θ_h), which is a function of the variable mean-free-path (MFP) of dislocation and the *constant term*s, ($(\sigma.\theta)_0$), which is a function of the fixed MFP, remains unchanged when the gliding dislocation completely shear the precipitates.
2. It has also been observed that the GND's as a result of precipitation can raise the work-hardening rate and can trigger the dislocation-annihilation process early. However, the *quotient term* and the *constant term* vary systematically with the growth of the precipitates.
3. Under all precipitation condition the deformation process in Alloy 625 remains adherent to the planar slip, which has been facilitated by the low stacking fault energy of the alloy.
4. The study is able to ascertain that γ" after 1200 h of growth at 973 K became impenetrable, whereas, δ after 1200 h of growth at 973 K, in spite of its massive size, remained penetrable to the gliding dislocation.
5. Present work concludes that the work-hardening behaviors of Alloy 625 has been controlled by the fixed MFP when gliding dislocation is not able to shear the impenetrable γ" hence, either loops around it or is blocked by γ". When gliding dislocation shears δ, the fixed MFP remains quite large and the work-hardening of the alloy is controlled by the variable MFP similar to that of unprecipitated SQ Alloy 625.
6. *Work-hardening quotient term*s and *constant term*s are seen to obey asymptotic relationship against isothermal holding time. The ranges of these *term*s are seen to be the characteristic of the system and are keys to

model and predict the work-hardening behavior of Alloy 625 at the aforementioned isothermal holding temperatures.

CHAPTER 8

8 First-Principles Based Studies on Planar Faults and Dislocations Dissociation

8.1 Introduction

A few major observations have come out from the study of fracture behavior, deformed microstructure and work-hardening analysis, in the previous chapters. These are as follows.

1. Planar slip is the predominant mode of deformation in Alloy 625 at room-temperature.
2. With the growth, the γ" ordered phase becomes quickly *impenetrable* to the gliding dislocation.
3. In spite of large size, the δ ordered phase remains *penetrable* to the gliding dislocation.

It is known that in a typical *fcc* matrix, a perfect dislocation splits into the partials to reduce its energy. When the energy of the stacking fault is low the partials are widely separated. In such a situation, cross slip by the dislocation is difficult. Hence, n the present work, it is essential to calculate the SFE of the matrix and the two ordered phases in order to explain above observations.

The calculations of SFE of pure Ni and generalized SFE have been carried using the first-principles density functional theory (DFT) based method as implemented in the VASP package (*section* 3.8) [66-72]. Since, SFE of any alloy system is usually lower than that of its base, SFE of Alloy 625 is presumably lower than that of pure Ni. Hence, calculation of SFE of pure Ni is carried out, in the present study, not only to represents a conservative value, but also to reduce the difficulty of calculating the SFE of a multi-component alloy system. Generalized SFE of γ''and δ ordered phases are carried out to explain the differential mode of interaction of dislocations with the above two ordered phases.

8.2 Lattice Parameter Optimization (LPO)

During the calculations of SFE's, it is necessary to ensure the precision at every step of calculations, as the value of SFE's are usually quite small, in the range of ~ 100 mJ/m^{-2}. Hence, in the present study, lattice parameter of Ni, γ''and δ ordered phases are carried out through spin polarized calculations and high energy cut-off to ensure an accurate value of the SFE's, up to 1st decimal place in mJ/m^{-2}.

8.2.1 LPO of Pure Ni

Optimized lattice parameters of pure Ni and the ordered phases were calculated as a prerequisite to determine the precise SFE of pure Ni and the ordered phases. This process for *fcc*-Ni was relatively easy, compared to that of the ordered phases. For Ni, unit cells with nine different lattice parameters around the tentative optimum value were created and static energy calculations on these structures were carried out using VASP. Brillouin zone integration was done using corrected tetrahedron method [86] with Γ-centered *k*-meshes of 23×23×23. Equation of state, as suggested by Murnaghan [87] and Birch [88], henceforth called *BM3*, was used to obtain minimum values of energy (E_0) and volume (V_0). The *BM3*-fitted V_0, so obtained, was used as an initial value for further optimization over volume in order to achieve true minimum in the energy. This optimized lattice parameter was used for constructing the supercells, which were used for calculating the total energies of the bulk and of the stacking fault (SF).

8.2.2 LPO of Tetragonal γ"

Compared to that of *fcc*-Ni, lattice parameter optimization of tetragonal γ" and orthorhombic δ involved a larger number of calculations to ensure the accuracy in *b*/*a* and *c*/*a* ratios. In the case of tetragonal γ", six variations in *a* and *c* lattice parameters for the DO_{22} lattice, around the tentative optimum values of *a* and *c*, respectively, comprising a total eight Ni and Nb atoms were created. Static energy calculations on thr 36 unit cells were carried out using VASP. The tetragonal γ" unit cell showing the lowest energy, which also closely conformed to the *c*/*a* ratio of the experimentally measured γ" [44,48] was taken up for next stage of lattice parameter optimization process. In this step, it underwent ionic relaxation and volume relaxation in a loop keeping the *c*/*a* ratio fixed. Brillouin zone integrations in the above calculations were done using corrected tetrahedron method with Γ-centered 19×19×9 *k*-meshes.

8.2.3 LPO of Orthorhombic δ

Similarly, in the case of orthorhombic δ, five variations in *a*, *b* and *c* lattice parameters around their tentative optimum values, comprising a total four Ni and Nb atoms were created and static energy calculations on 125 unit cells were carried out using VASP. The orthorhombic δ unit cell showing the lowest energy, which also conformed closely to the *c*/*a* and *c*/*b* ratios of the experimentally measured δ [53] was taken up for next stage of lattice parameter optimization process. In this step, it underwent ionic relaxation and volume relaxation in a loop keeping the *c*/*a* and *c*/*b* ratios fixed.

Brillouin zone integrations in the above calculations were done using the corrected tetrahedron method with Γ-centered 19×23×21 *k*-meshes.

8.3 Calculations of SFE

8.3.1 Methodology for Calculating the Precise SFE of *fcc*-Ni

For calculating the SFE of pure Ni, input structure comprising 24 atoms, as shown in Fig. 8.1, was created by stacking 12 (111)-planes having three orthogonal vectors in directions, $[1\ \bar{1}\ 0]$, $[11\ \bar{2}]$ and [111]. Brillouin zone integration was done using the corrected tetrahedron method with Γ-centered *k*-meshes having 23 divisions in $[1\ \bar{1}\ 0]$ direction, 13 divisions in $[11\ \bar{2}]$ direction 3 divisions in [111] direction. When viewed from a <111> direction, atomic arrangements on the (111)-type *ABC* planes of Ni appear like the arrangement depicted in Fig. 8.1, which was illustrated using XCRYSDEN [89]. Hence, based on the optimized lattice parameter, the dimensions of the supercell are set to be one (110)-plane spacing in the *x*-direction ($[1\ \bar{1}\ 0]$), $d_{(110)}$, three (112)-plane spacing in the *y*-direction ($[11\ \bar{2}]$), $3d_{(112)}$, and twelve (111)-plane spacing in the *z*-direction ([111]), $12d_{(111)}$. This 24-atom supercell was chosen as the basis for calculating the energies of both the bulk and the structure containing the SF. The latter structure was achieved by tilting *z*-vector, as suggested in the literature [90,91]. Hence, when the structure is repeated as per the *periodic boundary condition*, the (111) type *A*-plane (1st plane at the bottom of the supercell) no longer sits on its position on top of the *C*-plane (12th plane at the top of the supercell) but shift laterally to create a fault.

Apart from calculating cohesive energies of the bulk and the *SF containing structure*s, static energy calculations were also carried out on five different structures, having variation only in *z*-dimension, as depicted in Fig. 8.2. Here the *z*-dimension corresponding to “position 1” for both, bulk and SF, equals to 12 times (111) plane spacing of the optimized Ni-lattice. These steps were intended to provide precise SFE of pure Ni.

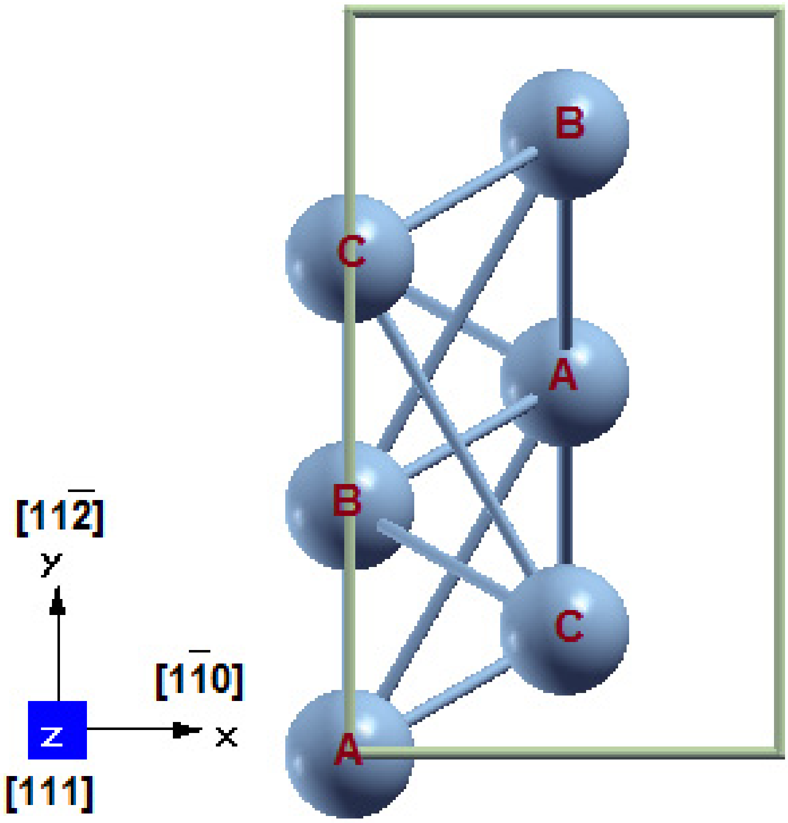

Fig. 8.1: Positions of atoms on the (111) planes of Ni within the supercell when viewed from [111] directions. A’s, B’s and C’s correspond to positions of atoms in A-plane, B-plane and C-plane, respectively.

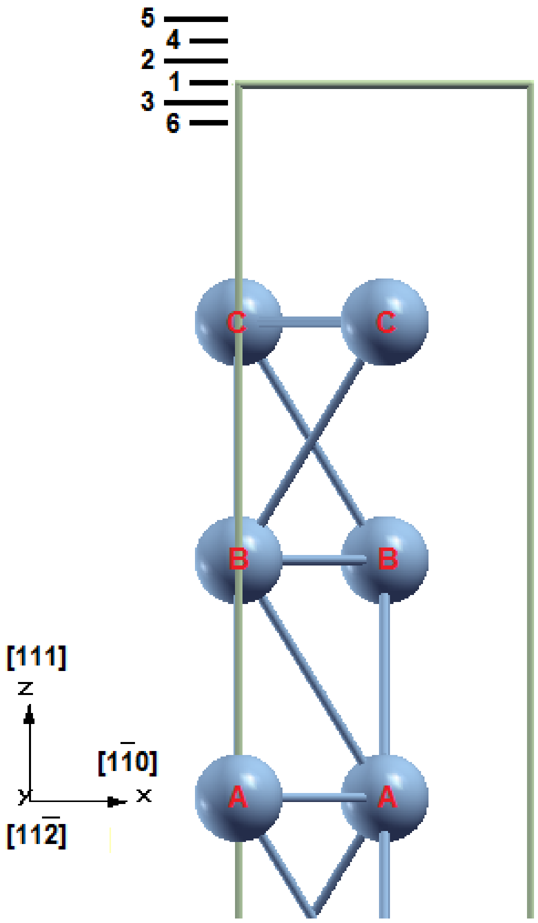

Fig. 8.2: Atoms on the top three (111) type ABC planes within the supercell are shown above. While position 1 is based upon the fully relaxed lattice parameter, relative other five different *z*-dimensions of supercells, which are given in Table 8.1, are indicated at the top using numeric "2" to "6".

Generalized stacking fault energy along the partials, as illustrated in Fig. 8.3, was calculated in order to understand, quantitatively, the resistance experienced by a dislocation in pure Ni. Fig. 8.3 depicts an *fcc* crystal as a stacking of (111) type *ABC* planes, where a dislocation, $\overrightarrow{A_1A_5}$, splits into $\overrightarrow{A_1A_3}$ and $\overrightarrow{A_3A_5}$. In the form of a equation,

$$\overrightarrow{A_1A_5} = \overrightarrow{A_1A_3} + \overrightarrow{A_3A_5} \qquad \textbf{(8.1)}$$

or

$$\frac{1}{2}\overrightarrow{[1\,1\,0]} = \frac{1}{6}\overrightarrow{[2\,1\,1]} + \frac{1}{6}\overrightarrow{[1\,2\,\bar{1}]} \qquad \textbf{(8.2)}$$

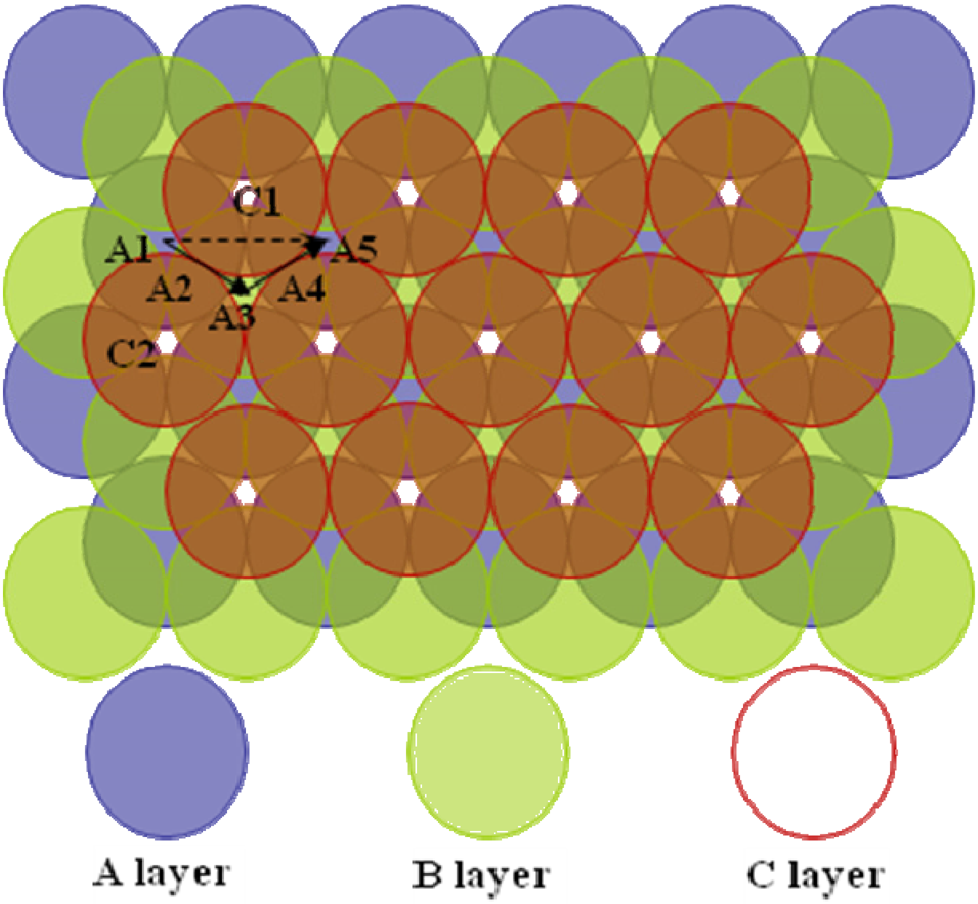

Fig. 8.3: Partials in *fcc* are shown on the ball model.

This is illustrated through Fig. 8.4. The vertical yellow lines indicate the dislocation partials as stated in Eq. 8.1. Conventionally the above equation is also represented in the form of a line sketch, which is shown in Fig. 8.4b.

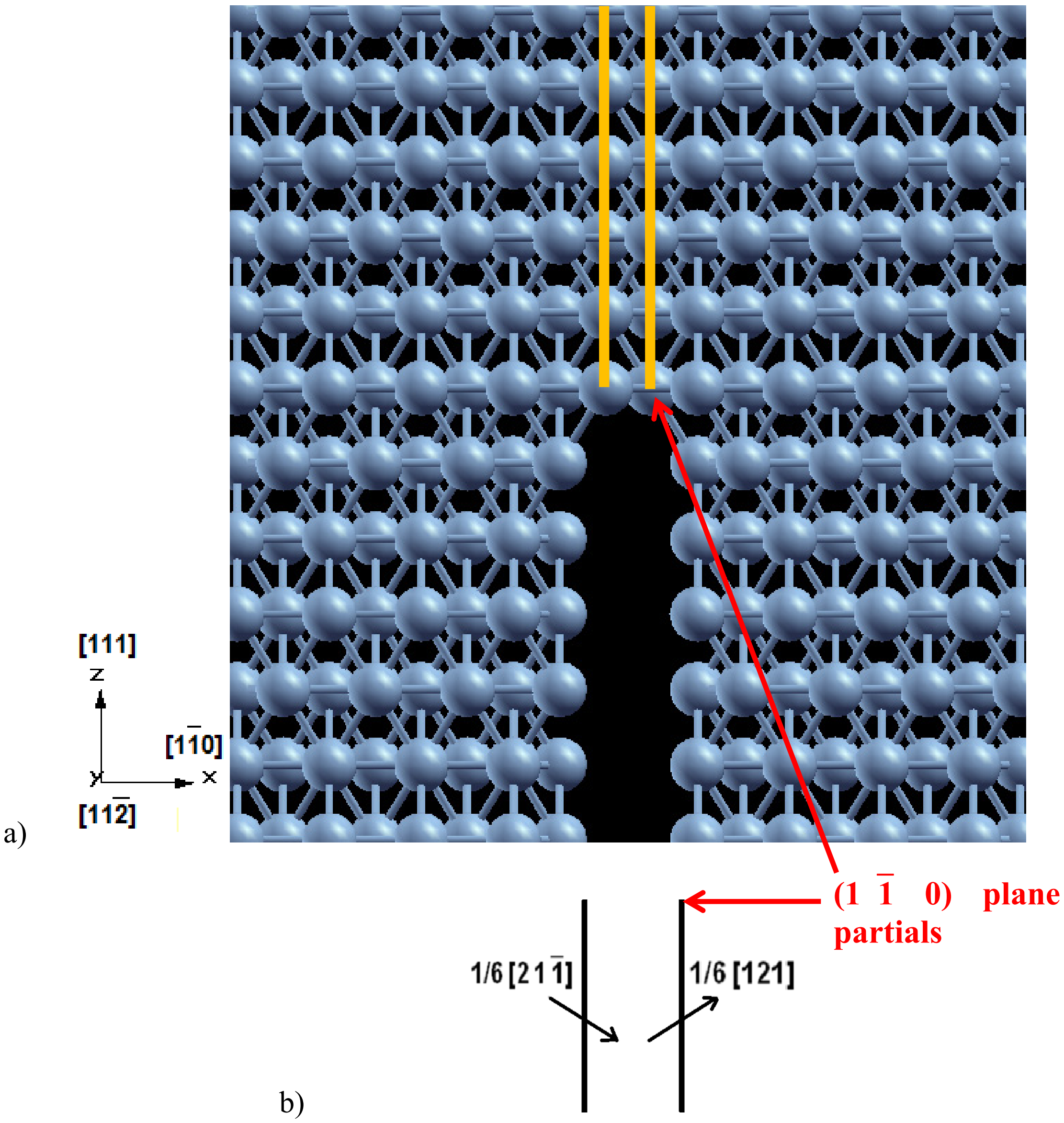

Fig. 8.4: Shockley partials of a perfect ½[1 $\bar{1}$ 0] dislocation in an *fcc* crystal is shown above using (a) ball model and and (b) line sketch.

During the stacking of the close-packed (111) plane, perfect stacking was maintained only when the A layer sits in the $\overrightarrow{A_1}$ or the equivalent positions above C layer. For placing the A layer anywhere except those positions resulted in the stacking fault. However, measuring the SFE by stacking above A_2, which is the middle point of $\overrightarrow{A_1A_3}$, gives the idea of the resistance experienced by a moving partial. In the present study, SFE of pure Ni was also calculated in A_2 position (middle of $\frac{1}{6}\overrightarrow{[211]}$), after taking into account the correction in height, as apparent from the atomistic ball-model.

8.3.2 Methodology for Calculating the SFE of Ni_3Nb – DO_{22} (γ")

Stack of 2×2×2 unit cells of Ni_3Nb – DO_{22} is depicted in Fig. 8.5 to show the *ABCDEF* type stacking of $(1\ \bar{1}\ 2)$ type, close-packed parallel planes in DO_{22} structure that is equivalent to the close packed {111} plane in *fcc*. $[2\ \bar{2}\ 1]$ direction, which, in turn, is equivalent to <111> of *fcc* and the relative positions of Ni and Nb atoms around this axis in *ABCDEF* planes are shown in Fig. 8.6. In this ordered phase, a perfect stacking is maintained only when the close packed (112) plane sits in the *K* and *S* positions. For rest of the positions SF's are produced.

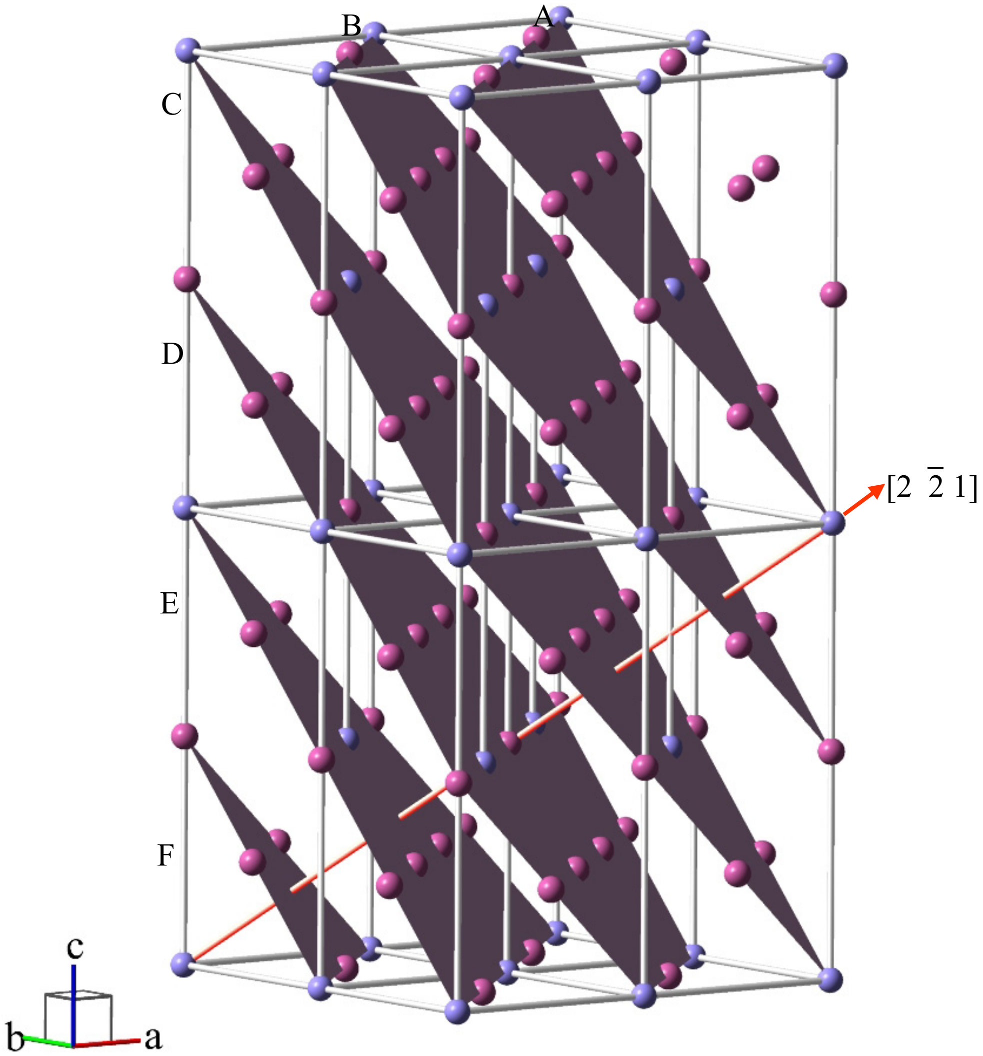

Fig. 8.5: Close packed (1 $\bar{1}$ 2) type parallel planes in DO_{22} structures. Nb is represented by blue sphere and Ni is represented by pink sphere.

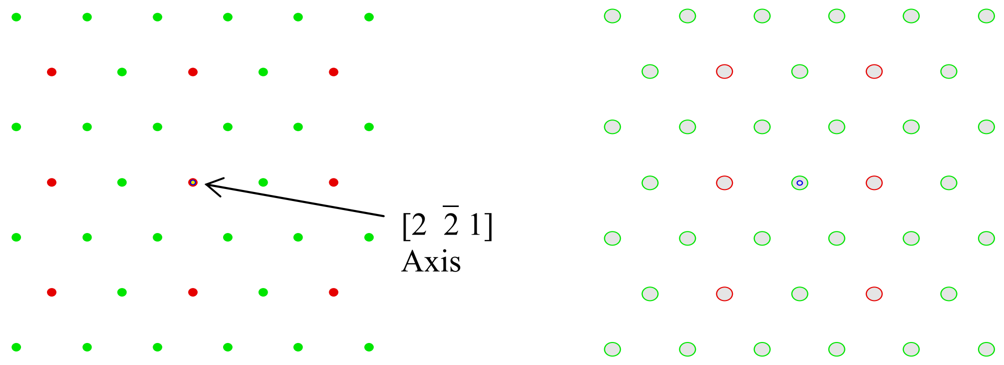

A Layer of γ'' (Ni$_3$Nb)

D Layer of γ'' (Ni$_3$Nb)

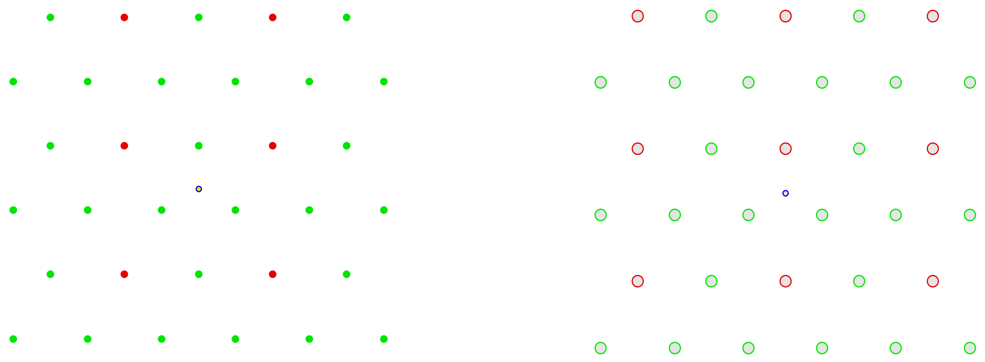

B Layer of γ'' (Ni$_3$Nb)

E Layer of γ'' (Ni$_3$Nb)

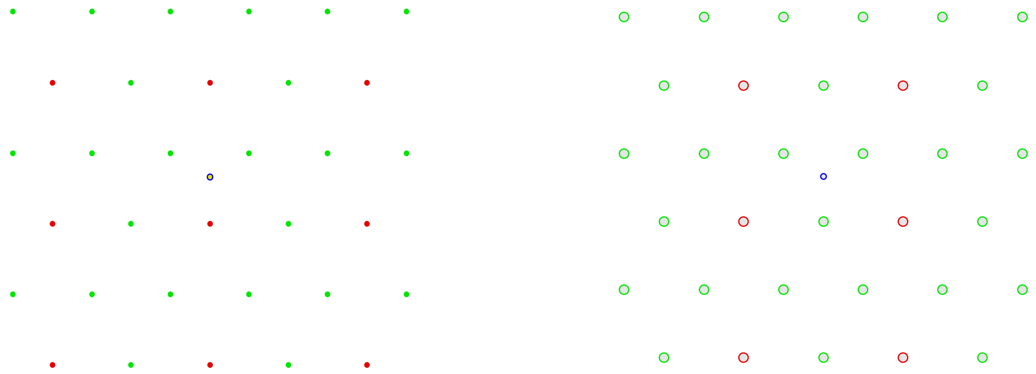

C Layer of γ'' (Ni$_3$Nb)

F Layer of γ'' (Ni$_3$Nb)

Fig. 8.6: Positions of Ni and Nb atoms in $(1\ \bar{1}\ 2)$ type A to F planes around $[2\ \bar{2}\ 1]$ axis as depicted in Fig. 8.5. Red color represnts Nb atom green color represents Ni atom.

Determining the generalized SFE's along the path of *K*, *L*, *M*, *N*, *O*, *P*, *Q*, *R* & *S*, as marked on Fig. 8.8 is significant, since geometrically, this is the path on which partials of a perfect dislocation with Burger's vector [1 $\bar{1}$ 0] should split into the four partials, as given in Eq. (14).

$$\overrightarrow{[1\,1\,0]} = \underbrace{\frac{1}{12}\overrightarrow{[4\,2\,1]}}_{\overrightarrow{KM}} + \underbrace{\frac{1}{12}\overrightarrow{[2\,4\,\bar{1}]}}_{\overrightarrow{MO}} + \underbrace{\frac{1}{12}\overrightarrow{[4\,2\,1]}}_{\overrightarrow{OQ}} + \underbrace{\frac{1}{12}\overrightarrow{[2\,4\,\bar{1}]}}_{\overrightarrow{QS}} \qquad \textbf{Eq. 8.3}$$

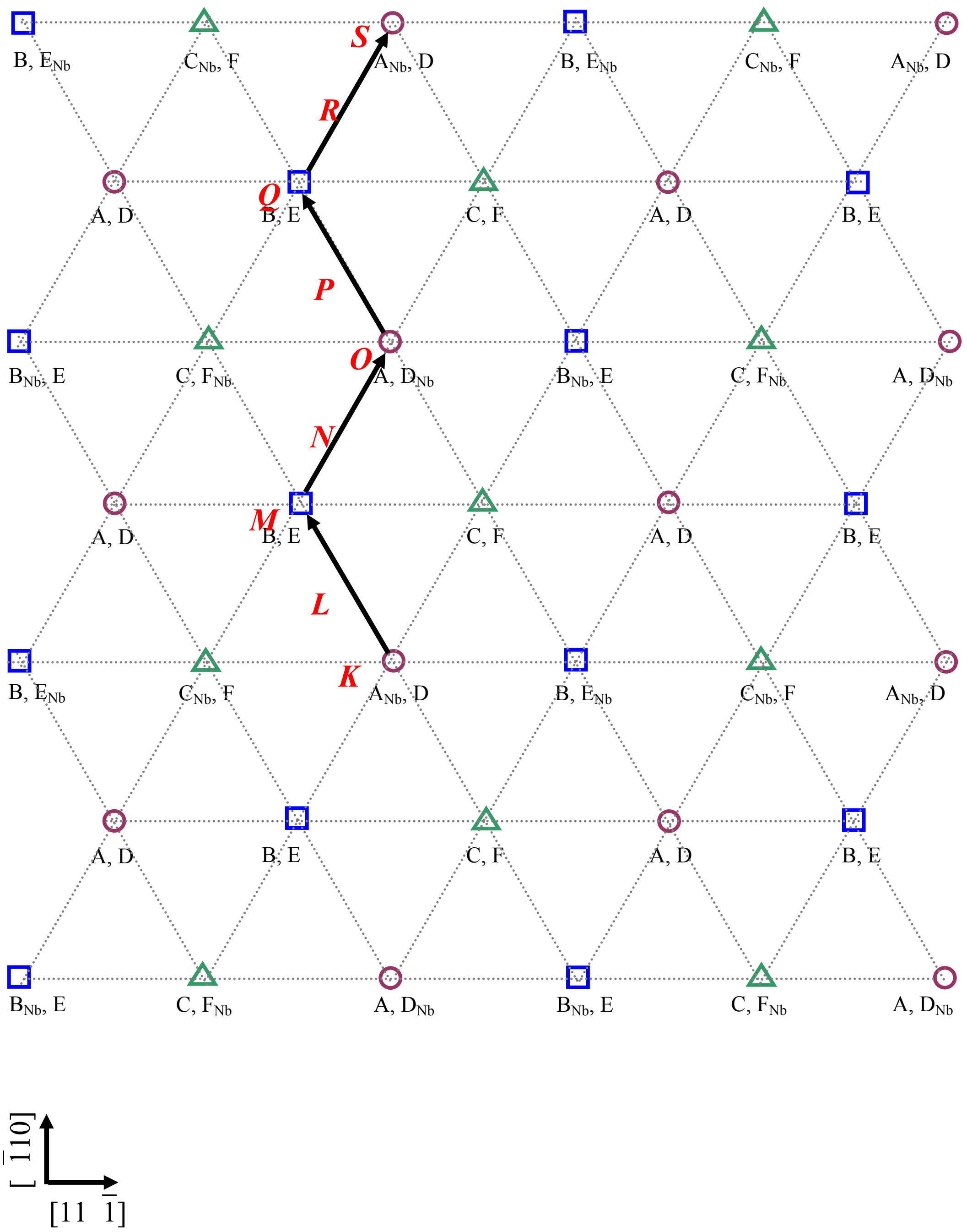

Fig. 8.7: Arrangement of atoms on *ABCDEF…* type planes of Ni$_3$Nb-DO$_{22}$ (γ''). Four parials in the ordered phases are shown by the bold arrows. Circle represents atoms in *A* & *D* planes, square represents atoms in *B* & *E* planes and

triangle represents the atoms in *C* & *F* planes. Positions, *K*, *L*, *M*, *N* etc. are the positions of stacking considered for calculating SFE in the present study.

Similar to that of the line sketch of partials in Fig. 8.4(b), four partials of perfect $[1\bar{1}0]$ dislocation in Ni_3Nb – DO_{22} (γ'') as per Eq. (13) can be illustrated as follows.

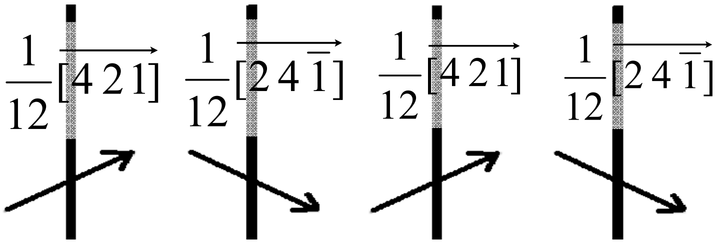

Fig. 8.8: Shockley partials of a perfect $[1\bar{1}0]$ dislocation in Ni_3Nb – DO_{22} (γ'').

For calculating the SFE of Ni_3Nb – DO_{22}, the input structure comprising 48 atoms was created by stacking 12 (112)-planes having three vectors in directions, $[1\bar{1}0]$, $[11\bar{1}]$ and [221]. Based on the optimized lattice parameter, the dimensions of the supercell were set to two (110)-plane spacing, $2d_{(110)}$, in the $[1\bar{1}0]$-direction, three (114)-plane spacing, $3d_{(114)}$, in the $[11\bar{1}]$-direction and twelve (112)-plane spacing, $12d_{(112)}$ in the [221]-direction. Brillouin zone integration was done using corrected tetrahedron method with Γ-centered *k*-meshes having 9 divisions in $[1\bar{1}0]$ direction, 10 divisions in $[11\bar{1}]$ direction 2 divisions in [221] direction. When viewed along the normal of the plane, comprising $[1\bar{1}0]$ and $[11\bar{1}]$ vectors, atomic arrangements on the (112)-type planes of Ni_3Nb – γ'' appear like the arrangement as depicted in Fig. 8.7.

Fig. 8.9 is the view of the same supercell along $[1\ \bar{1}\ 0]$ direction. This 48-atom supercell was the basis of calculating the energies of both the bulk and the SF-structures. The latter structure was obtained under periodic boundary condition, by tilting the z-vector appropriately, to produce stacking fault in L, M, N, O, P, Q, R & S positions, as elaborated earlier in section 8.3.1.

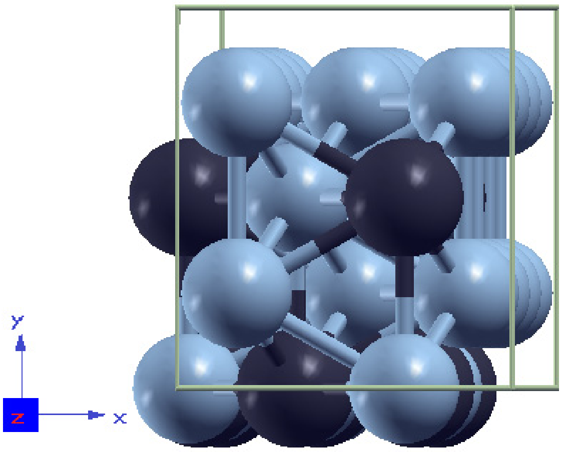

Fig. 8.9: Atoms on 12 Nos. (1 $\bar{1}$ 2) planes of Ni_3Nb-γ" within the supercell. Nb atom is represented by darker shade.

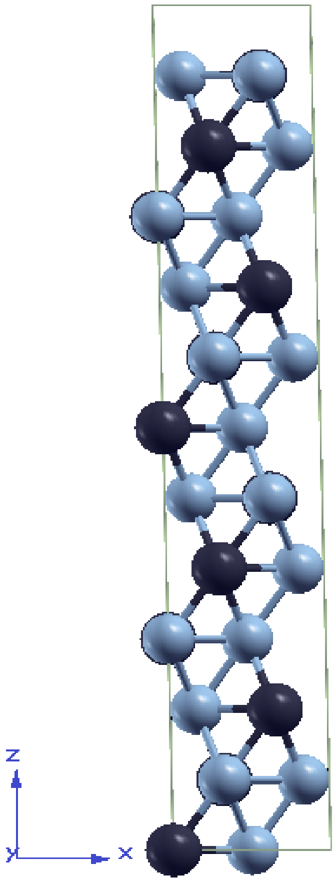

Fig. 8.10: View of the 12 Nos. (1 $\bar{1}$ 2) planes of Ni_3Nb-γ" supercell, same as Fig. 8.9, but along [1 1 $\bar{1}$] direction.

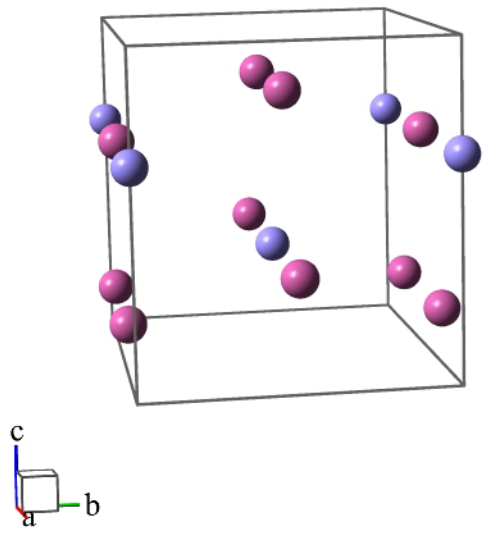

Fig. 8.11: Unit cell of Ni_3Nb – DO_a (δ). Nb is represented by blue sphere and Ni is represented by pink sphere.

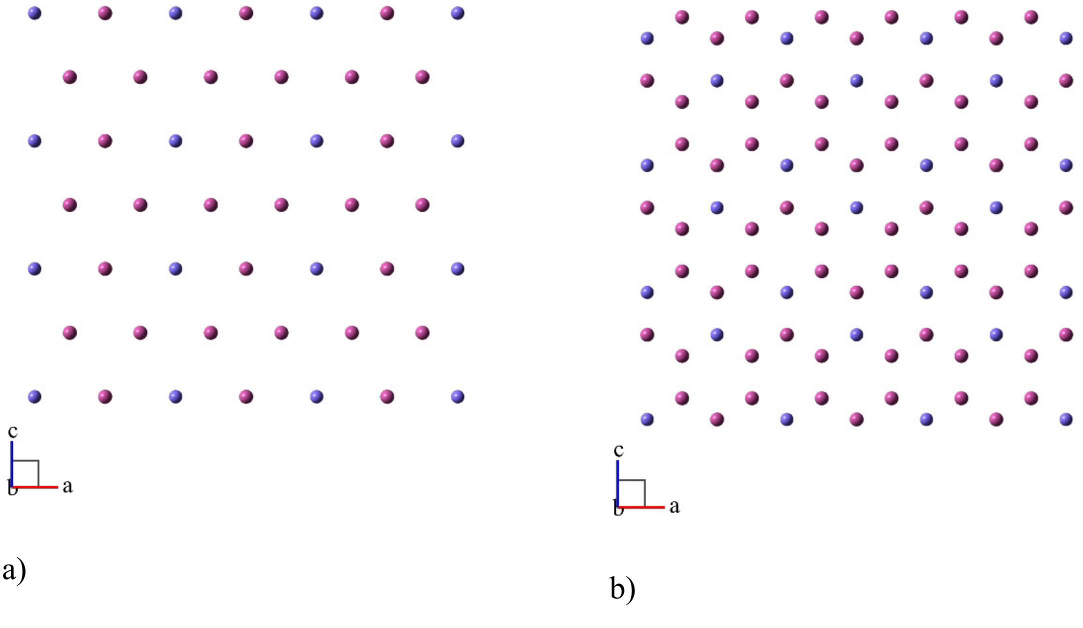

a)

b)

Fig. 8.12: (a) Positions of Ni and Nb atoms in close packed (010) plane of Ni_3Nb – DO_a (δ). (b) Stack of (010) type *A* and *B* planes.

8.3.3 Methodology for Calculating the SFE of Ni_3Nb – DO_a (δ)

Atomic arrangements in the unit cell of Ni_3Nb – DO_a is shown in Fig. 8.11 Arrangement of Nb and Ni atoms on the close packed (010) plane of Ni_3Nb – DO_a is similar to that of (112) plane in Ni_3Nb – DO_{22}. The *ABAB*… stacking of Ni_3Nb – DO_a is depicted in Fig. 8.12(b) and in Fig. 8.13.

For calculating the SFE of Ni_3Nb – DO_a, the input structure comprising 48 atoms was created by stacking 12 (010)-planes having three orthogonal vectors in directions, [1 0 0], [010] and $[0\ 0\ \bar{1}]$. Brillouin zone integration was done using corrected tetrahedron method with Γ-centered *k*-meshes having 9 divisions in [100] direction, 10 divisions in [001] direction 2 divisions in [010] direction. When viewed along the [010] vector, atomic arrangements on the (010)-type planes of Ni_3Nb – δ is shown in Fig. 8.12(b) and Fig. 8.13. Hence, based on the optimized lattice parameter, the dimensions of the supercell are set to be one (100)-plane spacing, $d_{(100)}$, in the [100]-direction, one (001)-plane spacing, $d_{(001)}$, in the [001]-direction and twelve (010)-plane spacing, $12d_{(010)}$, in the [010]-direction. This 48-atom supercell was the basis of calculating the energies of both the bulk and the SF-structure. The latter structure was obtained under periodic boundary condition, by tilting the *z*-vector appropriately, as suggested in the literature [90,91].

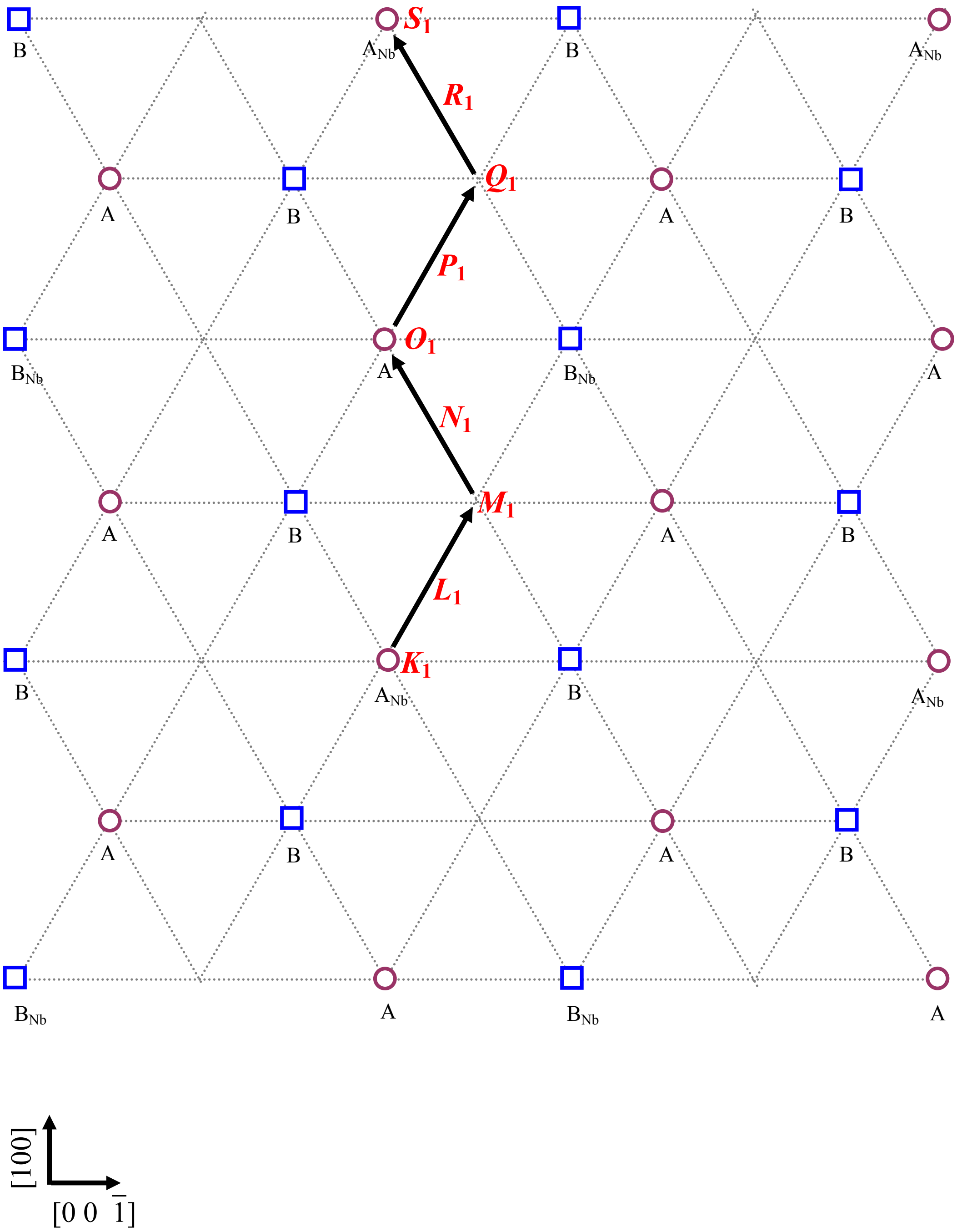

Fig. 8.13: *ABAB*…stacking of Ni_3Nb-DO_a (δ). Four partials in the ordered phases are shown by the bold arrows. Circle represents atoms in *A* plane, square represents atoms in *B* plane. Positions, K_1, L_1, M_1, N_1 etc. are the positions of stacking considered for calculating SFE in the present study.

In Ni_3Nb – DO_a, a perfect stacking is maintained only when the close packed (010) plane sits in the K_1 and S_1 positions. SF's were produced when any other stacking is considered. However, as discussed in 8.3.2 in the context of Eq. (13) and Fig. 8.8, SF's along the path of K_1, L_1, M_1, N_1, O_1, P_1, Q_1, R_1 & S_1, as marked on Fig. 8.13, are significant. This is due to the fact that moving of a perfect dislocation with Burger's vector [1 0 0], would require splitting into following four partials.

$$\overrightarrow{[1\,0\,0]} = \underbrace{\frac{1}{12}\overrightarrow{[3\,0\,\bar{2}]}}_{\overrightarrow{K_1M_1}} + \underbrace{\frac{1}{12}\overrightarrow{[3\,0\,2]}}_{\overrightarrow{M_1O_1}} + \underbrace{\frac{1}{12}\overrightarrow{[3\,0\,\bar{2}]}}_{\overrightarrow{O_1Q_1}} + \underbrace{\frac{1}{12}\overrightarrow{[3\,0\,2]}}_{\overrightarrow{Q_1S_1}} \qquad \textbf{Eq. 8.4}$$

In this study, calculations of bulk energies were carried out on a supercell that was stacked in the perfect manner and that of SFE's were carried out on a 48-atom supercell that was tilted under periodic boundary condition to produce stacking fault in L_1, M_1, N_1, O_1, P_1, Q_1 & R_1 positions.

8.4 SFE's of Ni, γ" and δ

8.4.1 SFE of Ni

For various lattice parameters, energies of *fcc*-Ni unit cells, each comprising 4 atoms have been plotted against their volumes in Fig. 8.14. Based on the *BM3*-fitted volume corresponding to the minimum energy, optimized lattice parameter of *fcc*-Ni has been calculated to be 352.26124×10^{-3} nm. Cohesive energies of Bulk and SF supercell for various *z*-dimensions (viz. position 1 to 6), as illustrated in Fig. 8.2, which are abbreviated as, TE_B and TE_{SF}, respectively, have been given in Table 8.1. Forces on the atoms in the 24-atom supercell due to the formation of SF, which is based upon bulk planar spacing (i.e. corresponding to "position 1") have been shown by arrows in

Fig. 8.15. Fittings of these energies against their respective volumes using *BM3*, as illustrated in Fig. 8.16, have given the minimum energies, E_0's, corresponding to the volumes, V_0's, which are listed in Table 8.2 along with the corresponding goodness of fit data. Fittings of Bulk and SF data in Fig. 8.16 show that unlike the energy-well of *bulk structure*s, the minimum of the energy-well of *SF-containing structure*s is significantly away from "position 1". Value of the *z*-dimension corresponding to the minimum of *SF-containing structure*, Z_{SF}, is obtained as follows.

Z_{SF} (in nm) $= \{V_0$ corresponding to energy-well of SF$\}/\{$Area of the (111) plane$\}$

$= \{V_0$ corresponding to energy-well of SF$\}/\{d_{(110)} \times 2d_{(112)}\}$

$= \{262.50312\times10^{-3}\ \mathrm{nm}^3\}/\{(249.08631\times10^{-3}\ \mathrm{nm})\times(431.43015\times10^{-3}\ \mathrm{nm})\}$

$= 2442.72242\times10^{-3}\ \mathrm{nm}$

The cohesive energy computed by VASP on the 24-atom supercell of SF with above Z_{SF} value is -138.55606 eV. This is further lower than the previously calculated cohesive energy of SF and, henceforth, referred as TE_{SFR}. Based on this total-energy of SF, the stacking-fault energy (SFE) of *fcc*-Ni is calculated from the following formula. If the total bulk energy of 24 Ni-atoms, based on fully relaxed *fcc*-Ni lattice parameter, i.e. TE_{B} corresponding to "position 1", is referred as TE_{B1}, then SFE is calculated as follows.

SFE $= \{(TE_{\mathrm{SFR}}) - (TE_{\mathrm{B1}})\}/(\text{Area of the (111) plane})$

$= (-138.55606 + 138.647748)/\{(249.08631\times10^{-3})\times(431.43015\times10^{-3})\}\ \mathrm{eV/nm^2}$

$= 136.683\ \mathrm{mJ/m^2}$

Similarly, without the consideration of relaxation, the SFE of *fcc*-Ni, based upon TE_B and TE_{SF} values is calculated to be 138.66 mJ/m^2, which is about 2 mJ/m^2 higher than that of the SFE value calculated with relaxed supercell. The lattice dilation in percentage, as a result of SF, LD_{SFE}, which is equivalent to the decrease in the bulk density, is determined from the following expression.

$$LD_{SFE} = 100 \times \{Z_{SF} - (12d_{\{111\}} \text{ of Ni})\} / (12d_{\{111\}} \text{ of Ni})$$

$$= 0.0895$$

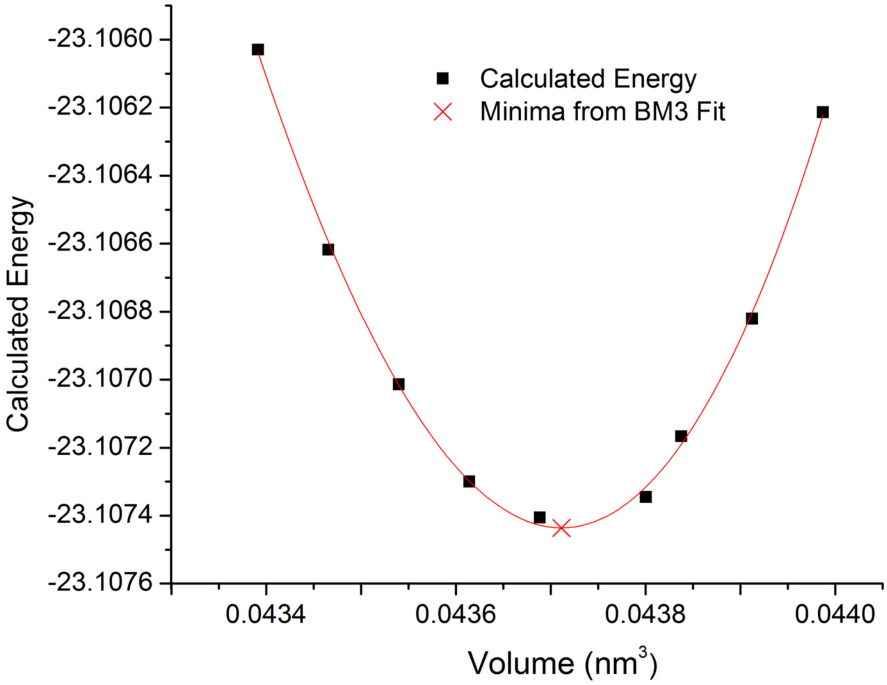

Fig. 8.14: BM3 fitting of energies obtained against various volumes to determine fully relaxed lattice parameter of fcc Ni.

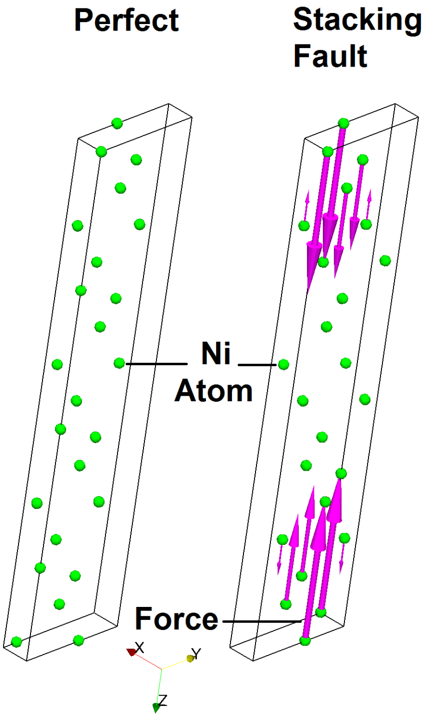

Fig. 8.15: Forces on atoms due to the formation of SF have been shown by arrows.

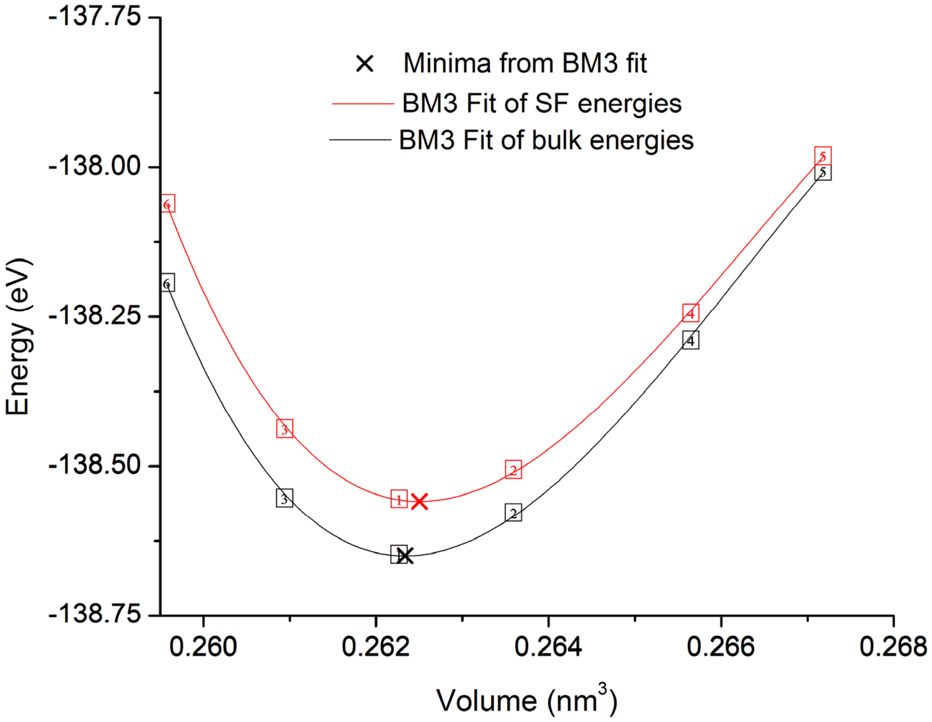

Fig. 8.16: Cross marks (×) indicating the BM3-fitted minima of the energy vs. volume plots corresponding to bulk and SF.

Table 8.1: Total energies calculated by VASP for the Bulk and the SF for various *z*-dimensions, as illustrated in Fig. 8.2.

Positions	**1** (12$d_{\{111\}}$ of Ni)	**2**	**3**	**4**	**5**	**6**
Z-dimension (in $\times 10^{-3}$ nm)	2440.53746	2452.87442	2428.20052	2472.00017	2486.24566	2415.47285
TE_{B} (in eV)	-138.647748	-138.577489	-138.553248	-138.289086	-138.006464	-138.19248
TE_{SF} (in eV)	-138.554734	-138.505894	-138.437939	-138.243833	-137.981133	-138.06086

Table 8.2: E$_0$, V$_0$ and the values indicating the goodness of fit corresponding to the data in Table 1 is given below. The reduced χ^2 in column 4 is the χ^2 divided by the number of degrees of freedom, while, coefficient of determination in the last column, indicates the measure of proportion of present data with the variation suggested by the equation of state.

Structure	E_0 **(eV)**	V_0 **(nm^3)**	**Reduced χ^2**	**R^2**
24 atoms supercell - Bulk	-138.65023 ± 0.00564	$0.26234 \pm 3.04593 \times 10^{-5}$	7.35544×10^{-5}	0.99886
24 atoms supercell – SF (under PBC)	-138.55898 ± 0.00424	$0.26250 \pm 2.51296 \times 10^{-5}$	4.17889×10^{-5}	0.99928

Fundamentally, the “cohesive energy” of a crystal reaches minimum when a particular type of atomic planes are stacked in a certain order. Breaking the order of stacking results in the stacking fault, which essentially increases the “cohesive energy” of the crystal. In the case of *fcc* lattice, {111} planes in the typical *ABCABC…* order are separated by $d_{\{111\}}$ to have minimum “total energy” configuration. Conventionally, separation of $d_{\{111\}}$ is not considered variable even if the stacking of {111} planes in the positions of *A*, *B* and *C* are shuffled to produce SF. This appears to have been taken for granted as much as that the change in the plane-spacing due to a faulty stacking has not assumed much significance.

In the present study, it has been measured that the {111}-type stacking fault energy of *fcc*-Ni, based upon the twelve {111}-plane spacing of the bulk ($12d_{\{111\}}$), 138.66 mJ/m^2, is higher by ~ 2 mJ/m^2 than the energy of the SF corresponding to a supercell, having dilation along its plane-normal. Occurrence of stacking fault in *fcc*-Ni at a distance of $2440.53746 \times 10^{-3}$ nm, which is equivalent to the SF density of 4.09746×10^5 mm^2/mm^3 due to PBC, is seen to be capable of decreasing the bulk density of *fcc*-Ni by 0.0895 %. It appears that the magnitude of the dilation and the reduction of SFE thereby are appropriately small due to the overall small magnitude of SFE. The measured value of SFE of *fcc*-Ni, 136.683 mJ/m^2 is within 10 % that of the experimental value, 125 mJ/m^2, mentioned in the literature [15]. Influence of a certain SF density, observed in the present study, on the local dimensional change of the crystal may be conceptually extended to calculate more accurate generalized SFE and to measure distortion in the lattice due to various other defect densities.

8.4.2 SFE of $\gamma'' - Ni_3Nb$

Lattice parameters *a* (=*b*) and *c* of tetragonal γ'' is calculated to be 0.364786 nm and 0.747929 nm, respectively. Energies of the SF's at *K*, *L*, *M*, *N* etc. positions are given in Fig. 8.17. It can be seen that energies of the SF's keep on rising and become highest at *N* or *P* positions. However, at *O* position the SFE falls down, even than that of *M* or *Q* positions.

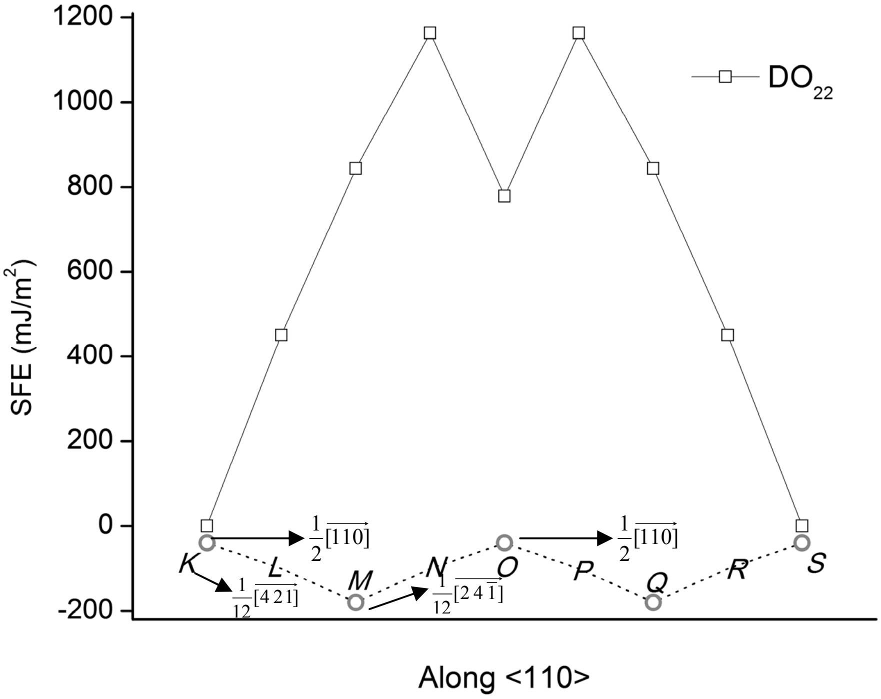

Fig. 8.17: Energy of the SF's at various positions along *K*, *L*, *M*, *N* ... positions as mentioned in Fig. 8.7.

8.4.3 SFE of $\delta - Ni_3Nb$

Lattice parameters *a*, *b* and *c* of orthorhombic δ is calculated to be 0.514374 nm, 0.427345 and 0.453552 nm, respectively. Energies of the SF's at K_1, L_1, M_1, N_1, etc. positions are given in Fig. 8.18. It can be seen that similar to that of $\gamma'' - Ni_3Nb$, energies of the SF's keep on rising and become highest at N_1 or P_1 positions. However, at O_1 position the SFE, unlike that of O position in Fig. 8.17, remains higher than that of M_1 or Q_1 positions.

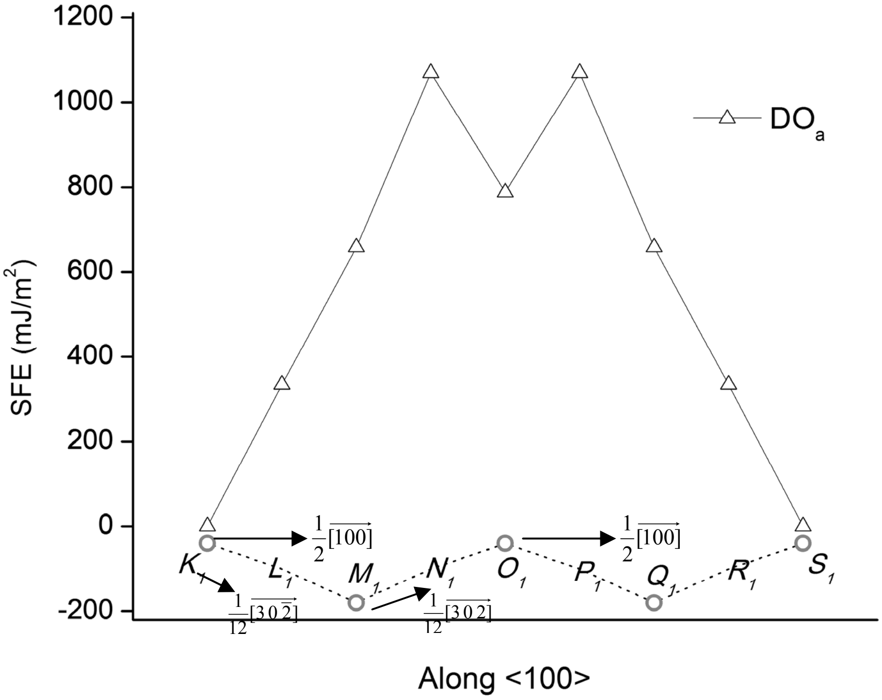

Fig. 8.18: Energy of the SF's at various positions along K_1, L_1, M_1, N_1 ... positions as mentioned in Fig. 8.13.

8.5 Discussion

The aim of the present work to comprehend the evolution of *structure* in Alloy 625 due to thermal exposure and its effect on the mechanical *properties* has been tackled using experimental and modeling techniques. First of all, starting SQ Alloy 625 has been analyzed to know the initial conditions, such as annealed state, elemental distribution, grain structure and CSL boundaries. Subsequent changes in the microstructure due to isothermal treatment have been analyzed for growths of relevant ordered phases and for changes in CSL boundaries etc. to ascertain their effect on the strength and ductility of the alloy. However, for deeper understanding of *structure*-

property relationship, in terms for dislocation-precipitate interactions, deformed regions of isothermally treated and tensile-fractured Alloy 625 specimens have been microstructurally investigated and stress-strain responses have been analyzed to correlate the same with their work-hardening behavior. Furthermore, to ascertain the fundamental mechanisms of deformation involving interaction of dislocation in Alloy 625 with γ'' and δ ordered phases, gliding of dislocations in *fcc*-matrix and in the ordered phases by the means of Shockley partials have been critically evaluated through the calculations of SFE's. Discussions in the following sub-sections are the comprehensive analyses of the results, which are carried out to establish the subtle *structure-property* correlation in precipitated Alloy 625.

8.6 Deformation Micro-Mechanism in Alloy 625

8.6.1 Role of Stacking Fault in Planar Slip

Microscopic study of deformed precipitated-Alloy 625 structure has confirmed that the planar-slip dominates the deformation process. Absence of cross-slip and the domination of planar-slip occurs when the dislocation-partials are widely separated and there is a lack of activation energy for cross-slip. Low SFE of Alloy 625, presumably lower than that of the SFE of pure Ni, viz. ~136 mJ/m^2, and lack of activation energy for cross-slip appears to have ensured the domination of planar-slip during room-temperature deformation of Alloy 625. Apart from this, present study has revealed that ~274 mJ/m^2 of SFE in position of A_2 (as depicted on Fig. 8.3) provide metastability to the $\frac{1}{6}\overrightarrow{[211]}$ type Shockley partials. This is illustrated on the 3D surface contour of the atoms, sitting on the (111) plane, as shown in Fig. 8.19.

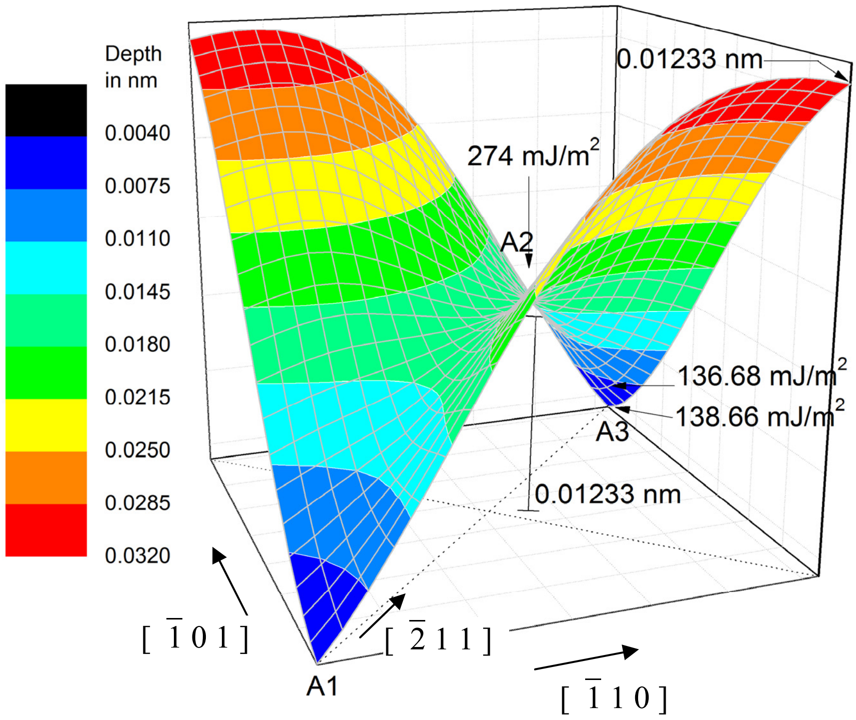

Fig. 8.19: 3D surface of (111) plane along [$\bar{1}$ 0 1], [$\bar{2}$ 1 1] and [$\bar{1}$ 1 0], having *z*-vector along [111], due to atoms sitting on (111) plane is shown above. Stacking fault energies of fcc-Ni with (274.07 mJ/m^2) assuming 0.01233 nm additional height in the position of A_2, which is based on the atomistic ball model.

Calculations have revealed that atoms close to stacking fault of face-centered-cubic (*fcc*) Ni experience compressive force (Fig. 8.15). Relaxation of the system with stacking fault (SF) leads to the dilation of plane spacing. Calculations based upon a 12 (111)-plane supercell have shown that the SF energy (SFE) in the case of "conventional" stacking is higher by ~2 mJ/m^2 than 136.7 mJ/m^2, which is based upon the supercell having suitable dilation along the fault-plane normal. This study has also shown that SF in *fcc*-Ni lowers its bulk density, at least, by 0.0895 %. This quantitatively establishes the old postulation that the crystal defect lowers the theoretical density of a system, which is accepted since the discovery of crystal structure and is referred in 1930's [92]. The methodology of relaxation of a structure with stacking faults, used in the present study, is likely to render more accurate generalized stacking fault energy surface in all systems.

8.6.2 SFE's Governing Interactions of Dislocations with γ''-DO_{22} and δ-DO_a Ordered Phases

Ordered atomic arrangements on $(1\ \bar{1}\ 2)$ plane of DO_{22} is same as (010) of DO_a, in terms of close-packing, which is similar to (111) plane of an *fcc* system. From the similitude of movement of dislocations in an *fcc* system, as it is through $\frac{1}{6}\overrightarrow{[211]}$ type Shockley partials (Eq. (12)), dislocations in ordered γ''-DO_{22} and δ-DO_a need to move through the four types of partials depicted in Fig. 8.17 and Fig. 8.18, respectively.

Two plots in Fig. 8.17 and Fig. 8.18, respectively, are combined in Fig. 8.20 in order to reveal the difference in SFE's along the equivalent [112] type partials in an *fcc* system and, hence, to ascertain the reasons behind the shearing of δ-DO_a and looping of γ''-DO_{22} during the deformation. Fig. 8.20 clearly shows that splitting of a *perfect* [110] type dislocation in γ''-DO_{22} into four geometric partials as per Eq. (16) cannot be energetically feasible and should merge together to become two partials of ½ $[1\ \bar{1}\ 0]$ type as per Eq. (17). This is in complete agreement with the experimental findings on the high-resolution TEM investigation of γ''-DO_{22}, reported in the literature, where no $\frac{1}{12}\overrightarrow{[421]}$ type partials but only $\frac{1}{2}\overrightarrow{[110]}$ type partials are seen to be existing [52].

(In the case of DO_{22})

$$\overrightarrow{[1\,1\,0]} = \underbrace{\frac{1}{12}\overrightarrow{[4\,2\,1]} + \frac{1}{12}\overrightarrow{[2\,4\,\bar{1}]}}_{\frac{1}{2}\overrightarrow{[110]}} + \underbrace{\frac{1}{12}\overrightarrow{[4\,2\,1]} + \frac{1}{12}\overrightarrow{[2\,4\,\bar{1}]}}_{\frac{1}{2}\overrightarrow{[110]}} \qquad \textbf{Eq. 8.5}$$

In the case of δ-DO$_a$ structure, SFE calculations reveal that the splitting of a *perfect* $\overrightarrow{[1\,0\,0]}$ type dislocation into $\frac{1}{12}\overrightarrow{[3\,0\,\bar{2}]}$ type partials as per Eq. (18) is not energetically feasible and needs to combine into $\frac{1}{2}\overrightarrow{[1\,0\,0]}$ type metastable partials as per Eq. (19).

i.e $\overrightarrow{[1\,1\,0]} = \frac{1}{2}\overrightarrow{[110]} + \frac{1}{2}\overrightarrow{[110]}$ **Eq. 8.6**

(In the case of DO$_a$)

$$\overrightarrow{[1\,0\,0]} = \underbrace{\frac{1}{12}\overrightarrow{[3\,0\,\bar{2}]} + \frac{1}{12}\overrightarrow{[3\,0\,2]}}_{\frac{1}{2}\overrightarrow{[100]}} + \underbrace{\frac{1}{12}\overrightarrow{[3\,0\,\bar{2}]} + \frac{1}{12}\overrightarrow{[3\,0\,2]}}_{\frac{1}{2}\overrightarrow{[100]}} \qquad \textbf{Eq. 8.7}$$

i.e. $\overrightarrow{[1\,0\,0]} = \frac{1}{2}\overrightarrow{[1\,0\,0]} + \frac{1}{2}\overrightarrow{[1\,0\,0]}$ **Eq. 8.8**

Although, generalized SFE's along the Burger's vectors of Shockley partials are quite similar in γ''-DO$_{22}$ and δ-DO$_a$, some significant differences can be noticed between them, which may play crucial role during the splitting of the *perfect* dislocations into the respective partials. First of all, the SFE of γ''-DO$_{22}$ at *O* position is less than the SFE of δ-DO$_a$ at *O*$_1$ position. Also, the generalized SFE line along the partials in δ-DO$_a$ is more flat than that of γ''-DO$_{22}$, since, the difference in the energies between *N* and *O* positions of γ''-DO$_{22}$ is more than the difference in energies between *N*$_1$ and *O*$_1$ positions of δ-DO$_a$. Apart from these, it can be seen that the SFE of γ''-DO$_{22}$

at *O* position is lower than that of the *M* position. However, SFE of δ-DO_a at O_1 position is seen to be significantly higher than that of the M_1 position. This, in certain cases, may help to explain differences in the interaction of dislocations with these ordered phases.

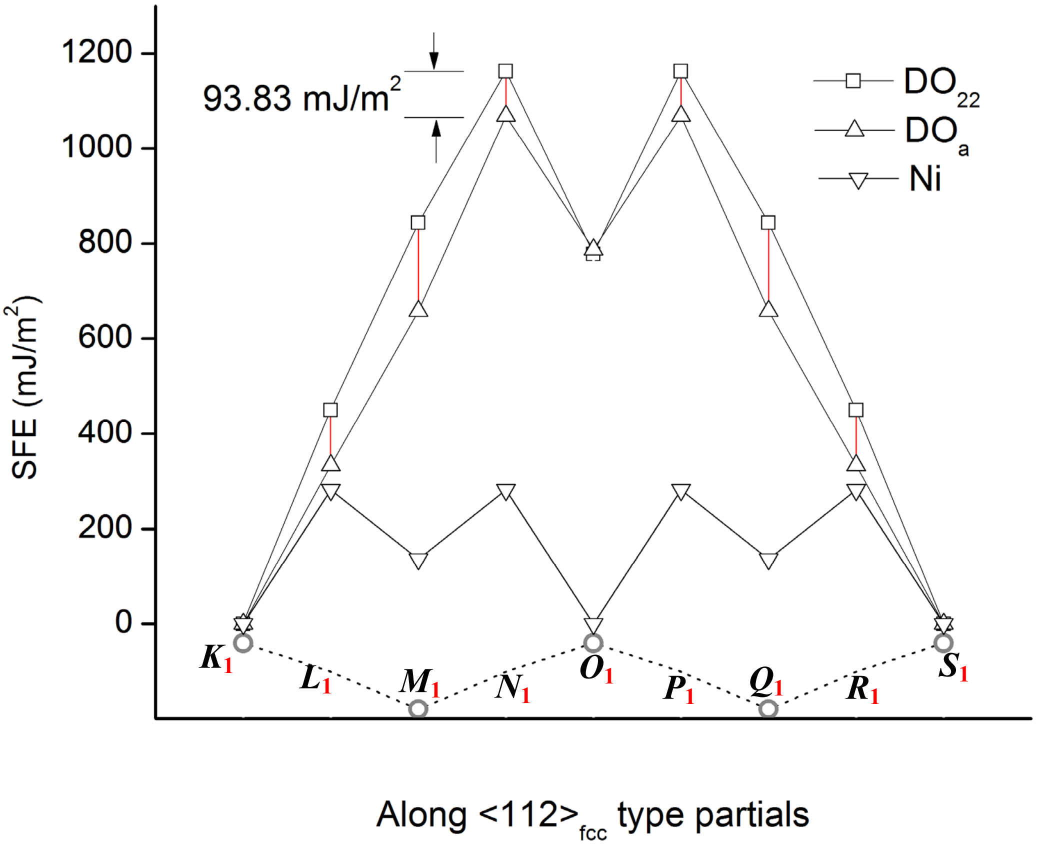

Fig. 8.20: Above plot is obtained after combining Fig. 8.17 and Fig. 8.18. It shows stacking fault energies along the partials in the ordered Ni_3Nb-Do_{22} (γ") (as per Fig. 8.7), Ni_3Nb-DO_a (δ) (as per Fig. 8.13) and in *fcc*-Ni.

Fig. 8.20 also reveals that the energy required to move dislocations in the ordered δ-DO_a is lower by ~94 mJ/m^2 than that of the γ"-DO_{22}. Hence, compared to the plate shaped massive δ phase in 1123 K – 1200 h sample, much smaller size of lens shaped γ" in 973 K – 1200 h sample and higher energy required to form and move partials in γ'' forces the gliding dislocations in Alloy 625 to loop around the latter phase. However, massive width of δ-DO_a in 1123 K – 1200 h sample and favorably lower energy required to form and move partials in this ordered phase, instead of looping, forces the gliding dislocation to cut through the ordered phase.

8.6.2.1 Other Factors Governing Interactions of Dislocation with the Ordered Phases

While, determining generalized SFE's along the path of the partials reveals one of the important considerations for non-shearing interactions of dislocations with γ''-DO_{22}, other two factors, viz. orientations and size of these two ordered phases appear to, with the first factor, have governed the interactions of dislocation with these two ordered phases. Slip systems between Alloy 625 matrix and γ''-DO_{22} being non-parallel (*see* section 2.5), planar slip in Alloy 625 during deformation is hindered by DO_{22} due to higher *critical resolved shear stress* in the ordered phase. In the case of δ-DO_a ordered phase, slip systems are parallel with that of the Alloy 625 matrix, where coherency strain on some slip plane can be negligibly small. In such a case, only barrier experienced by the gliding dislocation is SFE, as can be seen in Fig. 8.20. Apart from these, compared to δ-DO_a ordered phases, much smaller size of γ''-DO_{22} appears to have helped the dislocation in looping the latter.

8.7 Summary

Following points are summarized from the first-principles based calculations.

1. Stacking fault energy of pure Ni, which is in close approximation to the SFE of Alloy 625 is calculated to be 136.7 mJ/m^2. The low fault energy in synergism with inadequate thermal activation energy for cross-slip at room

temperature lead to the domination of planar slip during the deformation process.

2. First-principles based precise calculations of {111} type SFE of *fcc*-Ni with an SF density of 4.09746×10^5 mm^2/mm^3 is seen to be capable of lowering the bulk density of *fcc*-Ni by 0.0895 %.
3. Ab-initio calculations clearly shows that splitting of a *perfect* [110] type dislocation in γ''-DO_{22} into four partials of $\frac{1}{12}\overrightarrow{[4\,2\,1]}$ type and the splitting of a *perfect* $\overrightarrow{[1\,0\,0]}$ type dislocation into four $\frac{1}{12}\overrightarrow{[3\,0\,\bar{2}]}$ type partials are not feasible. These partials are, respectively, shown to recombine into two $\frac{1}{2}\overrightarrow{[1\,1\,0]}$ type metastable partials in γ''-DO_{22} and into two $\frac{1}{2}\overrightarrow{[1\,0\,0]}$ metastable partials in δ-DO_a.
4. Present work has revealed that there is a parity in splitting the partials in both γ''-DO_{22} and δ-DO_a ordered phases, where energy barriers resist the motion of dislocation. However, barrier to the formation of partial, albeit to the motion of dislocation in DO_{22} is higher by ~94 mJ/m^2 than that of DO_a.

CHAPTER 9

9 Conclusion

High temperature exposure of Alloy 625 results in the formation and growth of $Ni_2(Cr,Mo)$, γ'' and δ ordered phases and restructuring of coincidence site lattice boundaries with attendant changes in the mechanical behaviors of the alloy. Studies of microstructures of the solution quenched and isothermally treated Alloy 625, the analysis of tensile behavior and the first-principles based calculations have established the *structure-property* correlation in this alloy and are given below.

9.1 Microstructure

1. The growth of $Ni_2(Cr,Mo)$ and γ'' at 813 K and the growth of γ'' at 973 K is associated with the formation of geometrically necessary dislocations, which is directly reflected in the rise of coincidence site lattice boundaries.

2. Geometrically necessary dislocations, which are produced as a result of the formation of γ'' are not annihilated at 973 K due to the pinning by γ'' and inadequate activation energy for cross-slipping at 973 K.

3. Exposures of solution quenched Alloy 625 at 973 K and at 1123 K causes refinement of the grains. Necessary driving force apparently comes from the high-energy boundaries.

4. Elliptical-lens shaped γ'' with Ni_3Nb stoichiometry can grow more than ~150 nm in dia, while plate shaped δ of same stoichiometry can become more than 200 nm thick.

5. High temperature exposure of Alloy 625 causes increase in the coherent (60^o) (111) type boundaries. Excellent uniform corrosion behavior of the alloy apparently comes from this inherent quality.

9.2 Tensile and Fracture Behavior

6. Growths of $Ni_2(Cr,Mo)$ and γ'' at 813 K in comparison to that of other ordered phases are seen to have maximum effect on the UTS, although, all the ordered phases are seen to raise strength and lower ductility of Alloy 625.
7. Compared to that of 973 K – 1200 h sample, near about 20% smaller YS of 1123 K – 1200 h sample indicate that the plate shaped δ in the latter is less effective in pinning the dislocation than that of γ'' in the former. However, values of uniform strains in both of them are comparable.
8. (Nb,Ti)C type primary carbides, having no preference towards the grain boundary, act as void nucleation sites in solution quenched Alloy 625 during tensile deformation.
9. Growth of $Ni_2(Cr,Mo)$ and γ'' and associated restructuring of coincidence site lattice boundaries at 813 K lead to the reduction in dimple size and the possible rise in the facets in tensile-fracture surface.
10. Domination of planar slip during room-temperature deformation restricts the interactions of dislocation in the precipitated Alloy 625 matrix within the domain of cutting and looping of $Ni_2(Cr,Mo)$, γ'' and δ ordered phases.

11. Looping and dislocation pile-up at γ" lead to the decohesion of the ordered phase followed by the linking along the {100} planes of the Alloy 625 matrix, which in turn causes faceted fracture.

12. Interaction of dislocation with lath type δ is not only limited to impenetrable interactions but also extended to some shearable interactions, which causes fine dimple-fracture surface along (111) plane.

9.3 Work-Hardening Analysis

13. It has been revealed that the *work-hardening quotient term* (θ_h), which is a function of the variable mean-free-path (MFP) of dislocation and the *constant term*, ($(\sigma.\theta)_0$), which is a function of the fixed MFP, remain unchanged when the gliding dislocations completely shear the precipitates.

14. It has also been observed that the GND's as a result of precipitation can raise the work-hardening rate and can trigger the dislocation-annihilation process early. The work-hardening *quotient term* and the *constant term* vary systematically with the growth of the precipitates.

15. Under all precipitation condition the deformation process in Alloy 625 remains adherent to the planar slip, which has been facilitated by the low stacking fault energy of the alloy.

16. The work-hardening analysis is able to ascertain that γ" after 1200 h of growth at 973 K becomes unshearable, whereas, δ after 1200 h of growth at 973 K, in spite of its massive size, remains penetrable to the gliding dislocation.

17. Present work establishes that the work-hardening behaviors of Alloy 625 has been controlled by the fixed MFP when gliding dislocation is not able to shear the

impenetrable γ'' hence, either loops around it or is blocked by γ''. When gliding dislocation shears δ, the fixed MFP remains quite large and the work-hardening of the alloy is controlled by the variable MFP similar to that of SQ Alloy 625.

18. Work-hardening *quotient term*s and *constant term*s are seen to obey asymptotic relationship against isothermal holding time. The ranges of these *term*s are seen to be the characteristic of the system and are keys to model and predict the WH behavior of Alloy 625 at the aforementioned isothermal holding temperatures.

9.4 First principle based calculations

19. Stacking fault energy of pure Ni, which is in close approximation to the SFE of Alloy 625 is calculated to be 136.7 mJ/m^2. The low fault energy in synergism with inadequate thermal activation energy for cross-slip at room temperature lead to the domination of planar slip during the deformation process.
20. First-principles based precise calculations of {111} type SFE of *fcc*-Ni with an SF density of 4.09746×10^5 mm^2/mm^3 is seen to be capable of lowering the bulk density of *fcc*-Ni by 0.0895 %.
21. Ab-initio calculations clearly shows that splitting of a *perfect* [110] type dislocation in γ''-DO$_{22}$ into four partials of $\frac{1}{12}\overrightarrow{[4\,2\,1]}$ type and the splitting of a *perfect* $\overrightarrow{[1\,0\,0]}$ type dislocation in δ-DO$_a$ into four $\frac{1}{12}\overrightarrow{[3\,0\,\bar{2}]}$ type partials are not feasible. These partials are, respectively, shown to recombine into two $\frac{1}{2}\overrightarrow{[1\,1\,0]}$ type metastable partials in γ''-DO$_{22}$ and into two $\frac{1}{2}\overrightarrow{[1\,0\,0]}$ metastable partials in δ-DO$_a$.

22. Present work has revealed that there is a parity in splitting the partials in both γ"-DO$_{22}$ and δ-DO$_a$ ordered phases, where energy barriers resist the motion of dislocation. However, barrier to the formation of partial, albeit to the motion of dislocation in Ni$_3$Nb – DO$_{22}$ is higher by ~94 mJ/m^2 than that of Ni$_3$Nb – DO$_a$.

9.5 Future Direction

It has been revealed through the present and earlier studies that Ni$_2$(Cr,Mo), which forms in Alloy 625 during the exposure below ~873 K, immensely affect its mechanical properties. Hence, from the successful rendition of the first-principles based calculations in revealing the stability of partials in ordered γ" and δ phases, it is expected that an exercise of first-principles approach in this case too is likely to uncover the dislocation-partial reactions in this ordered phase. This is necessary to appreciate the interaction of dislocation with Ni$_2$(Cr,Mo) in terms of cutting and looping. Such understanding, from the similitude of deformation micro-mechanisms in Alloy 625 with γ" and δ phases, is likely to through the light on the cause of high strength of Alloy 625 due to Ni$_2$(Cr,Mo).

REFERENCES

---

1. B. Geddes, H. Leon and X. Huang, "Superalloys: Alloying and Performance", ASM International, 2010.

2. M. J. Donachie and S. J. Donachie, "Superalloys: A Technical Guide", 2nd ed., ASM International 2002.

3. R. C. Reed, "The Superalloys: Fundamentals and Applications", Cambridge University Press, 2006.

4. J. C. Williams and E. A. Starke, "Progress in Structural Materials for Aerospace Systems", Acta Materialia, 51 (2003), 5775 – 5799.

5. G. D. Smith, D. J. Tillack and S. J. Patel, “Alloy 625 – Impressive Past/ Significant Presence/ Awesome Future” Superalloys 718, 625,706 and Various Derivatives, ed. E. A. Loria, (TMS, Warrendale, PA, 1997), 35-46.

6. D. J. Tillack and H. L. Eiselstein, “The Invention and Definition of Alloy 625”, Superalloys 718, 625 and Various Derivatives, ed. E. A. Loria, (TMS, Warrendale, PA, 1991), 1-14.

7. J. F. Grubb, “Fatigue Resistance of Alloy 625 Sheet”, Superalloys 718, 625, 706 and Various Derivatives, ed. E. A. Loria, (TMS, Warrendale, PA, 1991), 629-638.

8. P. Ganesan, C. M. Renteria and J. R. Crum, “Versatile Corrosion Resistance of Inconel Alloy 625 in Various Aqueous and Chemical Processing Environments”, Superalloys 718, 625, 706 and Various Derivatives, ed. E. A. Loria, (TMS, Warrendale, PA, 1991), 629-638.

---

9. L. Ferrer, B. Pieraggi and J. F. Uginet, "Microstructural Evolution During Thermomechanical. Processing of Alloy 625", Superalloys 718, 625 and Various Derivatives, ed. E. A. Loria, (TMS, Warrendale, PA, 1991), 217 – 228.

10. J. R. Davis, "Nickel, Cobalt and Their Alloys", ASM Speciality Handbook, ASM International, 2000.

11. Materials Science International Team, MSIT ®, and Lukas, Hans Leo: "Chromium – Molybdenum – Nickel", ed. G. Effenberg, S. Ilyenko, SpringerMaterials – The Landolt-Börnstein Database (http://www.springermaterials.com) Springer-Verlag Berlin Heidelberg,. DOI: 10.1007/978-3-642-00771-2_13 (2010) 170 – 181.

12. E. Siedschlag, "The Ternary System Cr-Ni-Mo (in German)", Z. Metallkd., 17(2) (1925) 53 – 56.

13. S. P. Rideout, W. D. Manly, E. L. Kamen, B.S. Lement, P. A. Beck, "Intermediate Phases in Ternary Alloy Systems of Transition Elements", Trans. AIME, 191 (1951) 872-876.

14. D. S. Bloom, N. J. Grant, "An Investigation of the Systems formed by Chromium, Molybdenum and Nickel", Met. Trans. (J. Metals AIME), 2 (1954) 261-268.

15. A. K. Jena, S. B. Rajendraprasad, K. P. Gupta, "Cr-Mo-Ni (Chromium - Molybdenum -Nickel) System", J. Alloy Phase Diagrams, 5(3) (1989) 164-177.

16. P. Nash, "The Chromium-Nickel System", Bull. Alloy Phase Diagrams, 7(5), (1986) 466-476.

17. M. Raghavan, R. R. Mueller, G. A. Vaughn, S. Floreen, "Determination of Isothermal Sections of Nickel Rich Portion of Ni-Cr-Mo System by Analytical Electron Microscopy", Metal. Trans. A, 15(5) (1984) 783 – 792.

18. P. E. A. Turchi, L. Kaufman, Z. -K. Liu, “Modeling of Ni-Cr-Mo Based Alloys: Part I Phase Stability”, Calphad, 30(1) (2006) 70 – 87.

19. G. E. Prasad, M.K. Asundi, “Failure Analysis of Inconel Reactor Tubes During Hydrogen Service” Trans. of the Indian Institute of Metals 42 (1989) 291 – 298.

20. S. Floreen, G. E. Fuchs and W. J. Yang, “The Metallurgy of Alloy 625” Superalloys 718, 625,706 and Various Derivatives, ed. E. A. Loria, (TMS, Warrendale, PA, 1994), 13-38.

21. C. Thomas, P. Tait, “The Performance of Alloy 625 in Long-Term Intermediate Temperature Applications” Int. J. Pressure Vessel and Piping 59 (1994) 41 – 49.

22. M. Sundararaman, L. Kumar, G. E. Prasad, P. Mukhopadhyay and S. Banerjee, “Precipitation of an Intermetallic Phase with Pt2Mo-Type Structure in Alloy 625” Met. and Mat. Trans. A 30A, (1999) 41-52.

23. V. Shankar, M. Valsan, K. Bhanu Sankara Rao, S. L. Mannan, "Room Temperature Tensile Behavior of Service Exposed and Thermally Aged Service Exposed Alloy 625", Scripta Mater. 44 (2001) 2703 – 2711.

24. M. J. Cieslak, T. J. Headley, T. Kollie and A. D. Romig, Jr., “A Melting and Solidification Study of Alloy 625” Metall Trans. A 19A (1988) 2319 – 2331.

25. M. G. Burke, W. J. Mills and R. Bajaj, “Microstructures and Properties of Direct-Aged Alloy 625”, Superalloys 718, 625, 706 and Various Derivatives, ed. E. A. Loria, (TMS, Warrendale, PA, 2001), 389-398.

26. N. Binsted, A. B. Edwards, "EXAFS studies of nickel superalloys", Journal of Physics: Conference Series: 14th International Conference on X-Ray Absorption Fine Structure (XAFS14), 190 (2009) 1 – 4.

27. Technical Bulletin (pdf) http://www.specialmetals.com/products/inconelalloy625.php.

28. Y. Bergström, "A Dislocation Model for the Stress-Strain Behaviour of Polycrystalline α-Fe with Special Emphasison the Variation of the Densities of Mobile and Immobile Dislocations" Mat Sci and Engg. 5 (1969/70) 193 – 200.

29. U. F. Kocks, "Laws for Work-Hardening and Low-Temperature Creep" J. Eng. Mater. Tech. (1976) 76 – 85.

30. Y. Estrin, H. Mecking, "A Unified Phenomenological Description of Work Hardening and Creep Based on One-Parameter Models" Acta Metall. 32 (1984) 57 – 70.

31. U.F. Kocks, H. Mecking, "Physics and Phenomenology of Strain Hardening: the FCC Case" Prog. Mater. Sci. 48 (2003) 171 – 273.

32. E. Nes, "Modelling of Work Hardening and Stress Saturation in FCC Metals", Prog in Mat Sci 41 (1998) 129 – 193.

33. F. Roters, D. Raabe and G. Gottstein Acta Mater 48 (2000) 4181 - .

34. G. V. S. S. Prasad, M. Goerdeler and G. Gottstein, "Work Hardening Model Based on Multiple Dislocation Densities" Mat Sci Engg. A 400-401 (2005) 231 – 233.

35. G. Dieter, "Mechanical Metallurgy", McGraw-Hill, New York, ISBN 978-0-07-016893-0 1986.

36. L. Karmazin, "Lattice Parameter Studies of Structure Changes of Ni-Cr Alloys in the Region of Ni2Cr", Mater. Sci. Engg., 54 (1982) 247-256.

37. L. Karmazin, J. Krejci, J. Zeman, "Phase and Ni2Cr-Type Long-Range Order in Ni-rich Ni-Cr-Mo Alloys", Mater. Sci. Engg. A, 183 (1-2) (1994) 103-109.

---

38. A. Arya, G. K. Dey, V. K. Vasudevan, S. Banerjee, “Effect of Chromium Addition on the Ordering Behaviour of Ni-Mo Alloy: Experimental Results vs. Electronic Structure Calculations”, Acta Mater., 50, (2002) 3301-3315.

39. R. Bajaj, W. J. Mills, M. R. Lebo, B. Z. Hyatt, M. G. Burke, “Irradiation Assisted Stress Corrosion Cracking of HTH Alloy-750 and Alloy 625”, Proceedings of the Seventh International Symposium on Environmental Degradation of Materials in Nuclear Power System – Water Reactors, eds. G. Airey et al. NACE International, Houston, TX, USA, 1995, 1093-1107.

40. J. Mittra, J. S. Dubey, S. Banerjee, “Acoustic Emission Technique Used for Detecting Early Stages of Precipitation During Aging of Inconel 625”, Scripta Mater. 49 (2003) 1209-1214.

41. H. W. Tawancy, R. B. Herchenrocder and A. J. Asphanani, “High Performance Ni-Cr-Mo-W Alloy” J. Metals. 35(6) (1983) 37-43.

42. H. W. Tawancy, “Order Strengthening in a Nickel Base Superalloy (Hastelloy Alloy S)”, Metall. Trans. A, 11A (1980) 1764 – 1765.

43. M. Kumar, V. K. Vasudevan, “Ordering Reactions in a Ni-25Mo-8Cr Alloy”, Acta Metall. et Mater. 44 (1996) 1591 – 1600.

44. M. Sundararaman, P. Mukhopadhyay and S. Banerjee, “Influence of Intermetallic Phase Precipitation During Prolonged Service in Alloy 625” Superalloys 718, 625,706 and Various Derivatives, ed. E. A. Loria, TMS, Warrendale, PA (2001) 367-378.

45. P. E. A. Turchi, L. Kaufman, Z. -K. Liu, “Modeling of Ni-Cr-Mo Based Alloys: Part II Phase Stability”, Computer Coupling of Phase Diagrams and Thermochemistry (CALPHAD), 31 (2007) 237–248.

46. C. R. Conder, G. D. Smith, J. F. Radavich, “Microstructural and Mechanical Property Characterization of Aged Inconel Alloy 625LCF” Superalloys 718, 625,706 and Various Derivatives, ed. E. A. Loria, (TMS, Warrendale, PA, 1997), 447 – 458.

47. M. Sundararaman, P. Mukhopadhyay and S. Banerjee, "Deformation Behavior of γ" Strengthened INCONEL 718", Acta Metall. 36 (1988) 847 – 864.

48. M. Sundararaman, P. Mukhopadhyay, and S. Banerjee, "Some aspects of the precipitation of metastable intermetallic phases in INCONEL 718," Metallurgical transactions. A, 23, (1992) 2015 – 2028.

49. J. F. Radavich, A. Fort, “ Effect of Long-Time Exposure in Alloy 625 at 1200 oF, 1400 oF and 1600 oF”, Superalloys 718, 625, 706 and Various Derivatives, ed. E.A. Loria, TMS, Warrendale, PA, (1994) 635 – 647.

50. Y. Rong, S. Chen, G. Hu, M. Gao, R. P. Wei, "Prediction and Characterization of Variant Electron Diffraction Patterns for γ" and δ Precipitates in an INCONEL 718 Alloy", Met. & Mater. Trans. 30A (1999) 2297 – 2303.

51. M. Sundararaman, P. Mukhopadhyay, "Thermal Stability of Deformation Twins in γ" Strengthened Alloy 718", Defect and Diffusion Forum, 213 – 215 (2003) 61 – 74.

52. A. Niang, J. Huez, J. Lacaze, B. Viguier, " Characterizing Precipitation Defects in Nickel based 718 Alloy", Materials Science Forum, 636 – 637 (2010) 517 – 522.

53. M. Sundararaman, P. Mukhopadhyay and S. Banerjee, "Precipitation of the δ-Ni3Nb Phase in Two Nickel Base Superalloys", Met. Trans. A 19A (1988) 453 – 465.

54. M. Dehmas, J. Lacaze, A. Niang and B. Viguier, "TEM Study of High-Temperature Precipitation of Delta Phase in Inconel 718 Alloy", Advances in Materials Science and Engg. 2011 (2011) 1 – 9.

55. V. Shankar, M. Valsan, K. B. S. Rao, and S. L. Mannan, “Room Temperature Tensile Behavior of Service Exposed and Thermally Aged Service Exposed Alloy 625”, Scripta Mater 44 (2001) 2703-2711.

56. A. Iqbal, J. E. King, "The Role of Primary Carbide in Fatigue Crack Propagation in Aeroengine Bearing Steels", Int. J. of Fatigue 12 (1990) 234 – 244.

57. H. L. Eiselstein, “Advances in the Technology of Stainless Steels and Related Alloys: Metallurgy of Columbium Hardened Nickel–Chromium–Iron Alloy”, Special Technical Publication, ASTM: USA, 369 (1965) 62-79.

58. B. Radhakrishna and R. G. Thompson, "A phase diagram approach to study liquation cracking in alloy 718", Met. Trans. Vol. 22 A (1991) 887-902.

59. M. Sundararaman, P. Mukhopadhyay, S. Banerjee, “Carbide precipitation in Nickel Base Superalloys 718 and 625 and their Effect on Mechanical Properties” Superalloys 718, 625,706 and Various Derivatives, ed. E. A. Loria, TMS, Warrendale, PA, (1997) 367-378.

60. E. Balikci, R.A. Mirshams, A. Raman, "Fracture Behavior of the Superalloy IN738LC with Various Precipitate Microstructures", Mat. Sci. and Engg A, 265 (1999) 50-62.

61. A. Sengupta, S. K. Putatunda, "Influence of dynamic strain aging on the near-threshold fatigue crack growth behavior of a new single crystal nickel-based superalloy", Scripta Metallurgica et Materialia 31 (1994) 1163 – 1168.

62. M. Yamaguchi, Y. Umakosh, "The Deformation Behavior of Intermetallic Superlattice Compounds", Progress in Materials Science. 34 (1990) 1-148.

63. M. Yamaguchi, V. Vitek, D. P. Pope, Phil. Mag. A 43 (1981) 1027 – 1044.

64. M. Qian, J. C. Lippold, "Investigation of Grain Refinement during a Rejuvenation Heat Treatment of Wrought Alloy 718", Mat. Sci. and Engg A, 456 (2007) 147 – 155.

65. P. Sengupta, J. Mittra, G. B. Kale, "Interaction between borosilicate melt and Inconel", Journal of Nuclear Materials 350 (2006) 66 – 73.

66. J.P. Perdew, K. Burke, M. Ernzerhof, “Generalized Gradient Approximation Made Simple” Phys. Rev. Lett. 77 (1996) 3865 – 3868.

67. J. P. Perdew, K. Burke, M. Ernzerhof, “Errata: Generalized Gradient Approximation Made Simple”, Phys. Rev. Lett. 78 (1996) 1396.

68. G. Kresse, J. Hafner, “Ab initio molecular dynamics for open-shell transition metals”, Phys. Rev. B 48 (1993) 13115 – 13118.

69. G. Kresse, J. Furthmüller, “Efficiency of ab-initio total energy calculations for metals and semiconductors using a plane-wave basis set”, Comput. Mater. Sci. 6 (1996) 15–50.

70. G. Kresse, J. Furthmüller, “Efficient iterative schemes for ab initio total-energy calculations using a plane-wave basis set”, Phys. Rev. B 54 (1996) 11169 – 11186.

71. P. E. Blöchl, “Projector augmented-wave method”, Phys. Rev. B 50 (1994) 17953 - 17979.

72. G. Kresse, D. Joubert, “From ultrasoft pseudopotentials to the projector augmented-wave method”, Phys. Rev. B 59 (1999) 1758 - 1775.

73. J. Vaccaro, "Materials handbook", Mc Graw-Hill handbooks, fifteenth edition, New York, 2002.

74. K. Gall, N. Yang, H. Sehitoglu, Y. I. Chumlyakov, "Fracture of precipitated NiTi shape memory alloys" Int. J. of Fracture, 109 (2001) 189–207.

75. Y. –U. Heo, H. –C. Lee, " Precipitation and fracture behaviour of Fe–Mn–Ni–Al alloys", Philosophical Magazine, 93, (2013) 4519–4531.

76. J. Mittra, J. S. Dubey, U. D. Kulkarni, G. K. Dey, " Role of dislocation density in raising the stage II work-hardening rate of Alloy 625", Materials Sci and Engg. A 512 (2009) 87–91.

77. J. Mittra, S. Banerjee, R. Tewari, G. K. Dey, " Fracture behavior of Alloy 625 with different precipitate microstructures", Materials Science & Engg. A 574 (2013) 86–93.

78. D. Zhao, P. K. Chaudhury, "Effect of Starting Grain Size on As-Deformed Microstructure in High Temperature Deformation of Alloy 718", Superalloys 718, 625, 706 and Various Derivatives, ed. E.A. Loria, TMS, Warrendale, PA, (1994) 303–313.

79. B. Raj, T. Jayakumar, "Acoustic Emission During Tensile Deformation and Fracture in Austenitic Alloys", Acoustic emission: current practice and future directions, eds. W. Sachse, K. Yamaguchi, J. Roget, ASTM STP 1077 (1991) 218-241.

80. J.P. Hirth, J. Lothe, Theory of dislocations, Wiley, New York, 1982.

81. M. Sundararaman, W. Chen, R. P. Wahi, A. Wiedenmann, W. Wagner, W. Petry, Acta Metall. Mater. 40 (1992) 1023–1028.

82. J. T. Michalak, " The influence of temperature on the development of long-range internal stress during the plastic deformation of high-purity iron", Acta Metall. 13 (1965) 213–222.

83. J.A. Del Valle, A.C. Picasso, R. Romero, "Work-Hardening in Inconel X-750: study of stage II" Acta Mater. 46 (1998) 1981 – 1988.

84. A. Deschamps, M. Niewczas, F. Bley, Y. Brechet, J. D. Embury, L. Le Sinq, F. Livet, J. P. Simon, "Low-temperature dynamic precipitation in a supersaturated Al-Zn-Mg alloy and related strain hardening", Philos. Mag. A 79 (1999) 2485 – 2504.

85. S. Esmaeli, L. M. Cheng, A. Deschamps, D. J. Lloyd, W. J. Poole, " The deformation behaviour of AA6111 as a function of temperature and precipitation State", Mater. Sci. Eng. A 319–321 (2001) 461 – 465.

86. P. E. Blöchl, O. Jepsen, O. K. Anderson, "Improved tetrahedron method for Brillouin-zone integrations", Phys. Rev. B 49 (1994) 16223 -16233.

87. F. D. Murnaghan, "The Compressibility of media under extreme pressures", Proceedings of the National Academy of Sciences of the United States of America 30 9 (1944) 244 - 247.

88. F. Birch, "Finite elastic strain of cubic crystals", Phys. Rev. 71 (1947) 809 - 824.

89. A. Kokalj, "Computer graphics and graphical user interfaces as tools in simulations of matter at the atomic scale", Comp. Mater. Sci. 28 (2003) 155 - 168.

90. V. Vitek, "Theory of the core structures of dislocations in body-centred-cubic metals", Cryst. Lattice Defects, Cryst. Lattice Defects 5, (1974) 1 - 33.

91. J. A. Moriaroty, V. Vitek, V. V. Bulatov, S. Yip, "Atomistic simulations of dislocations and defects", J. of Comput. Aided Mater. Design 9 (2002) 99 - 132.

92. A. Goetz and A. B. Focke, "Density and conductivity of bismuth single crystals grown in magnetic fields with relation to their mosaic structure", Phys. Rev. 37 (1931) 1044 – 1056.